THESIS FOR THE DEGREE OF DOCTOR OF PHILOSOPHY

in

Thermo and Fluid Dynamics

Numerical Modelling of Fuel Injection and Stratified Turbulent Combustion in a Direct-Injection Spark-Ignition Engine Using an Open Source Code

CHEN HUANG

Department of Applied Mechanics
CHALMERS UNIVERSITY OF TECHNOLOGY
Göteborg, Sweden 2014

Numerical Modelling of Fuel Injection and Stratified Turbulent Combustion in a Direct-Injection Spark-Ignition Engine Using an Open Source Code
ISBN 978-91-7597-094-3

Doktorsavhandlingar vid Chalmers tekniska högskola
Ny serie nr 3775
ISSN 0346-718X

Department of Applied Mechanics
Chalmers University of Technology
SE-412 96 Göteborg
Sweden
Tel. +46-(0)31 772 1000

Cover:
A stratified turbulent flame in a gasoline direct-injection spark-ignition engine

Chalmers Reproservice
Göteborg, Sweden 2014

When one door closes, another opens.
Alexander Graham Bell

List of Publications

This thesis is based on the following five appended papers:

Paper I

Huang C, Golovitchev V and Lipatnikov A. Chemical model of gasoline-ethanol blends for internal combustion engine applications. SAE paper 2010-01-0543, 2010.

The author of this thesis carried out sensitivity analysis of chemical reactions, ignition delay and laminar flame speed calculations, data analysis and paper writing. The 2nd author assisted in chemical mechanism optimization and the 3rd author assisted in paper writing.

Paper II

Huang C and Lipatnikov A. Modelling of gasoline and ethanol hollow-cone sprays using OpenFOAM. SAE paper 2011-01-1896, 2011.

The author of this thesis carried out spray model implementations and modifications in OpenFOAM®, sensitivity study, data analysis and paper writing. The 2nd author assisted in understanding of spray models and checking the implementations and assisted in paper writing.

Paper III

Huang C, Yasari E and Lipatnikov A. A numerical study on stratified turbulent combustion in a direct-injection spark-ignition gasoline engine using an open-source code. SAE paper 2014-01-1126, 2014.

The author of this thesis carried out combustion model development and implementations, engine simulations, data analysis and paper writing. The 2nd author assisted in understanding thermophysical library and implementing combustion model in OpenFOAM®. The 3rd author assisted in model development and paper writing.

Paper IV

Huang C, Lipatnikov A, Johansen LCR and Hemdal S. A study of two basic issues relevant to RANS simulations of stratified turbulent combustion in a spray-guided direct-injection spark-ignition engine. SAE paper 2014-01-2572, 2014.

The author of this thesis carried out combustion model development and implementations, engine simulations, data analysis and paper writing. The 2nd author assisted in model development and paper writing. The 3rd and 4th authors supplied with experimental description and data.

Paper V

Huang C, Yasari E, Johansen LCR, Hemdal S and Lipatnikov A. Application of an open source code and flame speed closure model to RANS simulations of stratified turbulent combustion in a gasoline direct-injection spark-ignition Engine. Submitted to *International Journal of Engine Research* for publication.

The author of this thesis carried out combustion model development and implementations, engine simulations, data analysis and paper writing. The 2nd author assisted in understanding thermophysical library and implementing combustion model in OpenFOAM®. The 3rd and 4th authors supplied with experimental description and data. The 5th author assisted in model development and paper writing.

Other papers (not included in the thesis)

Paper VI

Huang C, Golovitchev V and Lipatnikov A. A chemical model of gasoline/ethanol blends. In: *1st Joint Meeting of the Scandinavian-Nordic and French Section of the Combustion Institute*, Copenhagen, Denmark, 9-10 Nov, 2009.

Paper VII.

Huang C. Modeling of gasoline hollow cone spray using OpenFOAM. In: *5th OpenFOAM Workshop*, Gothenburg, Sweden, 21-24 Jun, 2010.

Paper VIII

Huang C, Golovitchev V and Lipatnikov A. A semi-detailed chemical mechanism of combustion of gasoline-ethanol blends. In: *Thirty-Third International Symposium on Combustion*, Beijing, China, 1-6, Aug, 2010, Poster No. W4P014.

Paper IX

Lipatnikov A, Huang C and Golovitchev V. A semi-detailed chemical mechanism for gasoline: further validation against experimental data on laminar flame speeds of gasoline/O2/N2 and n-heptane/iso-octane/air mixtures. In: *34th International Symposium on Combustion*, Warsaw, Poland, 29 Jul - 3 Aug, 2012. Poster No. W5P079.

ABSTRACT

Stringent regulations on the emission of pollutants, especially carbon dioxide (CO_2), necessitate the development of advanced combustion technologies. Gasoline direct injection (GDI) into the combustion chamber of a Spark Ignition (SI) engine is a combustion strategy that is widely recognized as having the potential to improve fuel efficiency of internal combustion engines for passenger cars. In particular, the CO_2 emissions of GDI engines could be 20-26% lower than those of equivalent port-fuel injected (PFI) SI engines. Unfortunately, the development of combustion systems for GDI engines is very challenging because the creation of an appropriate combustion system is a major challenge. They require very precise formation of an ignitable fuel-air mixture with a steep stratification gradient right between the ignition electrodes to permit efficient operation under a wide range of operating conditions.

CFD simulations are widely used to increase the efficiency of engine R&D. This thesis aimed at development of a tool for numerically modelling of working process in a GDI engine. The work had two main objectives. First, an available CFD code should be applied to multidimensional GDI engine simulations. Second, the code should be developed by implementing advanced models of stratified turbulent combustion, followed by comparison with experimental data.

As far as a code is concerned, although there are several mature commercial CFD packages on the market, there is also a need for less expensive software. Consequently, there is growing interests from both industry and academia in the OpenFOAM® open source CFD code, whose source code is freely available so that users can implement and test new models without paying licence fees. However, it had not been used to simulate combustion in a GDI engine when the work reported herein was begun. This thesis presents an assessment of OpenFOAM® as a tool for the numerically modelling of fuel injection, spray breakup, evaporation, mixture formation, and stratified turbulent burning in the combustion chamber of a GDI engine.

OpenFOAM® was used to simulate hollow-cone sprays of gasoline and ethanol discharged by a piezo-controlled pintle-type injector. The liquid properties of gasoline were implemented in the code to enable the simulation of gasoline sprays. In addition, the implementations of various spray breakup models such as LISA, TAB, Reitz-Diwakar, and KHRT into the standard OpenFOAM® package were checked and modified in order to more closely reflect their descriptions in the original papers. Liquid penetration and SMD calculated by simulations using the revised model implementations were compared to experimental data provided by my colleagues. These comparisons showed that the best agreement between the experimental data and simulations was achieved when using a combination of the uniform droplet size and KHRT models. This model was therefore used in all subsequent engine simulations.

As far as modelling is concerned, the code's modelling capabilities were enhanced by implementing and developing models relevant to the turbulent burning of stratified gasoline-air mixtures at the elevated temperatures and pressures associated with combustion in a GDI engine. More specifically, two relevant issues were addressed.

First, a semi-detailed chemical mechanism for the combustion of a gasoline surrogate in air was developed and validated. The gasoline surrogate consisted of *iso*-octane, toluene, and *n*-heptane in volumetric proportions of 55%:35%:10%, respectively. The mechanism includes 120 species participating in 677 reactions. It was

validated against experimental data on the ignition delay times and laminar flame speeds of different mixtures at a range of pressures and temperatures. The mechanism was then used to compute laminar flame speeds for gasoline-air mixtures at equivalence ratios of $0.2 \leq \phi \leq 2.0$, unburned gas temperatures of $298 \leq T_u \leq 800K$, and pressures of $1 \leq P \leq 30\ atm$. The results of these calculations were approximated and the approximations were implemented into OpenFOAM® for subsequent CFD modelling of stratified turbulent combustion in a GDI engine.

In order to study stratified burning in a GDI engine, the Flame Speed Closure (FSC) model of premixed turbulent combustion was combined with a so-called presumed Probability Density Function (PDF) method that made it possible to account for the influence of turbulent fluctuations in local mixture composition on the local burning rate. The combined model based on the FSC and presumed PDF approach was implemented into OpenFOAM® and the roles played by its various submodels were investigated in a step-wise fashion.

Finally, the so-extended code was used to simulate a GDI engine burning a globally lean mixture. Good agreement between results computed by me and experimental data provided by my colleagues was obtained. In addition, the model's sensitivity was investigated.

Keywords: chemical mechanism, ignition delay, laminar flame speed, hollow-cone spray, KHRT, liquid penetration, SMD, gasoline surrogate, premixed/stratified turbulent combustion, Flame Speed Closure (FSC), presumed PDF, Spray-Guided Gasoline Direct Injection engine, modelling, CFD, OpenFOAM®.

Acknowledgements

First and foremost I offer my sincerest gratitude to my supervisor Dr. Andrei Lipatnikov who has supported me throughout this work with his immense knowledge and patience. I am truly grateful that Andrei takes his time in reading through my codes, papers and thesis word by word. I felt fruitful for the discussions we had especially during the second stage of my PhD study. I've always felt that I am welcome to his office and he is willing to share all his knowledge about premixed turbulent combustion.

Professor Ingemar Denbratt offered me the opportunity to work in combustion division at Chalmers University of Technology. I am especially grateful that he initiated a three-month visit to Politecnico di Milano in the beginning of this project. I not only benefited in mastering the OpenFOAM® code but also met many excellent people who work within the same field as I do. Ingemar has constantly encouraged and supported me in my project research.

I learned about Chalmers by reading articles from Dr. Valeri Golovitchev when I studied in China, and luckily for me, I had an opportunity to work with Valeri during the first period of this project. His willingness to share his deep knowledge in chemical kinetics has allowed my research to progress smoothly and made my work more rewarding than it might otherwise have been. Dr. Anders Karlsson generously shared his impressive understanding of and experience with spray simulations; his feedback was one of the driving forces in improving this work. Dr.s Stina Hemdal and Jonas Wärnberg not only provided me with important experimental data for hollow-cone spray, but also answered all my questions about experimental setups with warmth and patience. Moreover, Stina and Lars Christian provided me with invaluable measured data from optical engine. Dr. Abdurrahman Imren provided me with several different sets of computational mesh with complicated geometry of the optical engine. He also provided me data using KIVA simulations. I am grateful for his willingness to help and a lot of valuable discussions with him. Studying and discussing with Dr. Anne Kösters was an extremely enjoyable experience. I benefited a lot by discussions turbulence and combustion with Ehsan Yasari. Dr. Fabian Peng-Kärrholm spent many hours during his spare time in teaching me OpenFOAM®, and Daniele Ettorre tirelessly answered all my strange questions while I was getting to grips with it. Dr. Tommaso Lucchini showed me the path to self-learning in OpenFOAM®. I would like to thank Tommaso for being a member of grading committee.

I would like to thank the Combustion Engine Research Center (CERC) at Chalmers, and thanks to the Swedish Energy Agency for financial support of this work. I am grateful for my reference group members for all the feedbacks that I received. They are Dr. Niklas Nordin, Dr. Roy Ogink, Dr. Mattias Ljungqvist, Dr. Aristotelis Babajimopoulos. I would like to thank Aris for taking his time of reading my thesis and being a member of grading committee.

Thanks to all my previous and current colleges at Chalmers who made me feel welcome and at home here. Especially thanks to Dr. Raúl Ochoterena who encouraged and helped me when I was new comer in Sweden. Thanks to my office-mates, Ehsan, Mattias and Gunnar; we do practice Swedish now and then. Thanks to the current and

previous combustion girls: Elenor, Anne, Stina, Zhiqin, Karin, Monica and Malin. I enjoyed jogging and fikaing with you and I am proud of being a member of you. Thank Ulla Lindberg-Thieme and Blagica Smilevska for the administrative support.

Finally, I owe a deep debt to my family, especially my mother-in-law Yinghua who tried her best to help out at home during the last period of my PhD study, my mother Shoue and father Guiwen, who have always believed in me and have cared for me in every possible way, my husband Jian, who has supported me with tolerance and love, and my son Arvid, who brought me so much joy and made everything worthwhile.

Contents

Nomenclature

Roman symbols

A	a constant of the Flame Speed Closure model (see Equation (4.25))
b	combustion regress variable
c	combustion progress variable
D	diffusivity
$Da = \tau_t/\tau_c$	Damköhler number
G	scalar field
h	mixture specific enthalpy [J/kg]
$k = 3/2\,u'^2$	turbulent kinetic energy [m²/s²]
L	integral length scale of turbulence
P	probability density function
p	pressure
Pr	Prandtl number
$R^0 = 8.314$	universal gas constant [J/(mole K)]
Re	turbulent Reynolds number
Q	source term (see Equations (4.21) and (4.26))
S_L	perturbed laminar flame speed
T	temperature
t	time
t_{fd}	time since the start of ignition (see Equations (4.22) and (4.23))
t_r	reaction time scale (see Equation (4.26) and (4.27))
U_t	turbulent burning velocity in a planar one-dimensional flame
u	gas flow velocity components
u'	rms turbulent velocity fluctuation
x	spatial coordinates

Greek symbols

ε	turbulent dissipation rate [m²/s³]
ϕ	equivalence ratio
κ	heat diffusivity
μ	molecular viscosity
ν	kinematic viscosity
Θ	activation energy
ρ	density
τ_c	chemical time scale
τ_t	turbulent time scale

Subscripts

b	combustion products
u	unburned mixture
∞	fully developed, asymptotically steady quantities

Superscripts

$\bar{}$	ensemble-averaged
$\tilde{}$	Favre-averaged

Acronyms

aTDC, bTDC	after, before Top Dead Center
BML	Bray-Moss-Libby
CAD	Crank Angle Degree
CFD	Computational Fluid Dynamics
CPU	Central Processing Unit
DI	Direct-Injection
EVC, EVO	Exhaust Valve Closing, Opening
FSC	Flame Speed Closure
GDI	Gasoline Direct-Injection
IVC, IVO	Inlet Valve Closing, Opening
LHS	Left Hand Side
OpenFOAM®	Open Field Operation and Manipulation
SG	Spray-Guided
SI	Spark-Ignition

Chapter 1

Introduction

1.1. Background

The world's population in 2014 was estimated to be 7.18 billion by the United States Census Bureau (USCB), with China and India accounting for 19% and 17% of the total, respectively [1]. The population is currently growing slowly, at a rate of around 1.07% per annum as of the year 2012 [1]. Since the global recession of 2008 and 2009, there has been considerable variation in economic performance among different regions and countries. Economy in the more developed Organization for Economic Cooperation and Development (OECD) countries has generally been slower than in the non-OECD countries, especially those in Asia. The long-term economic growth of non-OECD countries and the world's vast population are pushing energy consumption to higher level. According to the United States Energy Information Administration (EIA), global energy consumption will grow by 56% between 2010 and 2040 with much of this growth occurring outside the OECD countries (Figure 1.1) [2].

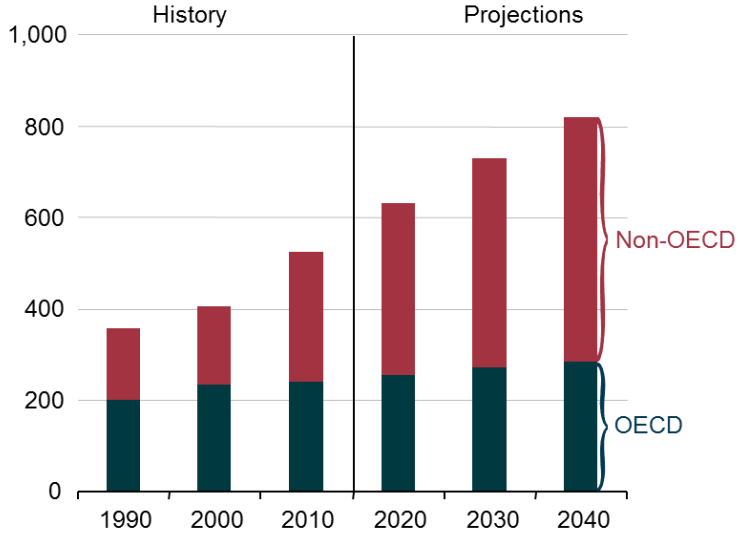

Figure 1.1: *World energy consumption between 1990 and 2040 (quadrillion Btu) [2].*

The growing demand for energy is causing two major problems, as shown in Figure 1.1 and Figure 1.2: (i) the availability of energy resources is becoming increasingly limited and (ii) rising energy consumption is creating or exacerbating a range of environmental issues. The first problem is associated with the fact that, as shown in Figure 1.2, oil, which is a non-renewable resource, accounted for 33% of world energy consumption in 2013 [2]. Total proven global oil reserves increased slowly to 1687.9 billion barrels by the end of 2013, yielding a reserves-to-production

(R/P) ratio of 53.3. Accordingly, currently proven fossil fuel reserves are only sufficient to support 53.3 years of global production [3]. Global energy consumption is largely due to three sectors: industry, transportation, and residential and commercial activity. Industrial users accounted for around half of world's energy consumption in 2010, while transportation and the residential and commercial sector consumed almost equal shares of the remainder [2]. This thesis focuses on energy transformation in the transportation sector.

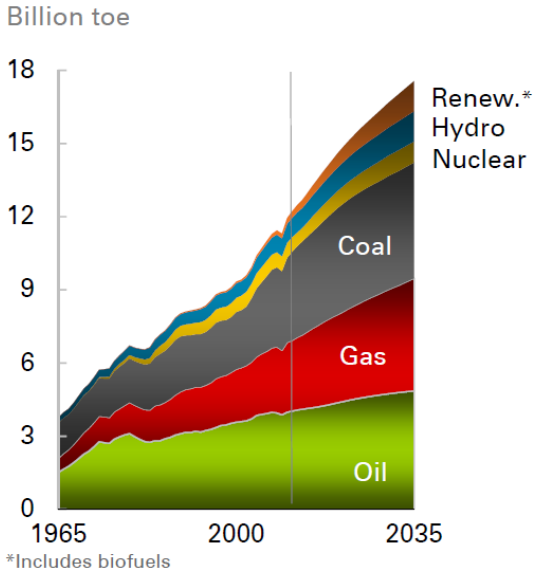

Figure 1.2: *World energy consumption [3].*

The transportation sector is devoted to the movement of people and goods by road, rail, water and pipeline. It is an important component of the global economy and has played a central role in improving standards of living over time. In the year 2013, the transportation sector consumed around 55% of global oil resources and produced around one-quarter of the global greenhouse gas (GHG) emissions due to fossil fuel combustion [2][4]. The sector's energy demand is expected to increase by 1.1% per annum on average between 2010 and 2040. In the developing non-OECD regions, the average transportation energy demand is expected to rise by 2.2% over this period as a result of relatively immature transportation systems, high projected economic growth and large populations. In contrast, the energy demand of the OECD countries' transportation sectors are expected to decline slightly over the same period due to improvements in energy efficiency, relatively slow economic growth and stable or declining in populations [2].

Light-duty vehicles (LDVs), which include passenger cars and light commercial vehicles, account for a large proportion of the transportation sector's demand for liquid fuel. For example, the LDVs accounted for around 60% of the total fuel consumed by transportation in the United States in 2012, which includes fuel consumed by LDVs, heavy-duty vehicles (HDVs), air, marine, pipeline, and rail transport, and so on. However, it should be noted that this figure is projected to drop to 47% by 2040 [5]. This thesis deals with energy transformation in LDVs.

The second problem caused by the increasing global consumption of energy resources relates to environmental issues. Emissions including carbon monoxide (CO), hydrocarbons (HC), nitrogen oxides (NO_x) and particulate matter (PM) from passenger

cars are harmful to both the environment and human health. In Europe, the European Union (EU) has proposed a series of progressively more stringent regulations on emissions. For passenger cars, the emission standard currently in force is Euro 5, which requires that PM emissions from diesel cars be reduced from 25 mg/km to 5 mg/km. A new standard Euro 6 will come into force in September 2014, and will impose stricter regulations on NO_x emissions from diesel engines, reducing the acceptable limit from 180 mg/km to 80 mg/km [6].

In addition to conventional pollutants such as CO, HC, NO_x and PM, engines produce the major GHG carbon dioxide (CO_2) emissions of which from LDVs are strictly regulated by national and supranational authorities around the world (see Figure 1.3) due to its effects on the global climate and because it is closely linked to fuel consumption. The European Commission (EC) introduced its first (voluntary) CO_2 emissions target after negotiation with European, Japanese and Korean automobile manufacturers' associations in 1998. These agreements targeted fleet-average CO_2 emissions of 140 g/km by September 2008 [7]. Later on, the commission introduced a mandatory CO_2 emissions reduction program that required each vehicle manufacture active in the EU to achieve fleet-average CO_2 emissions of 130 g/km by 2015 [8]. In addition, each manufacture is required to ensure that 95% of their new passenger cars registered in 2020 reach a long-term CO_2 emissions target of 95 g/km, rising to 100% of cars by 2021 [9].

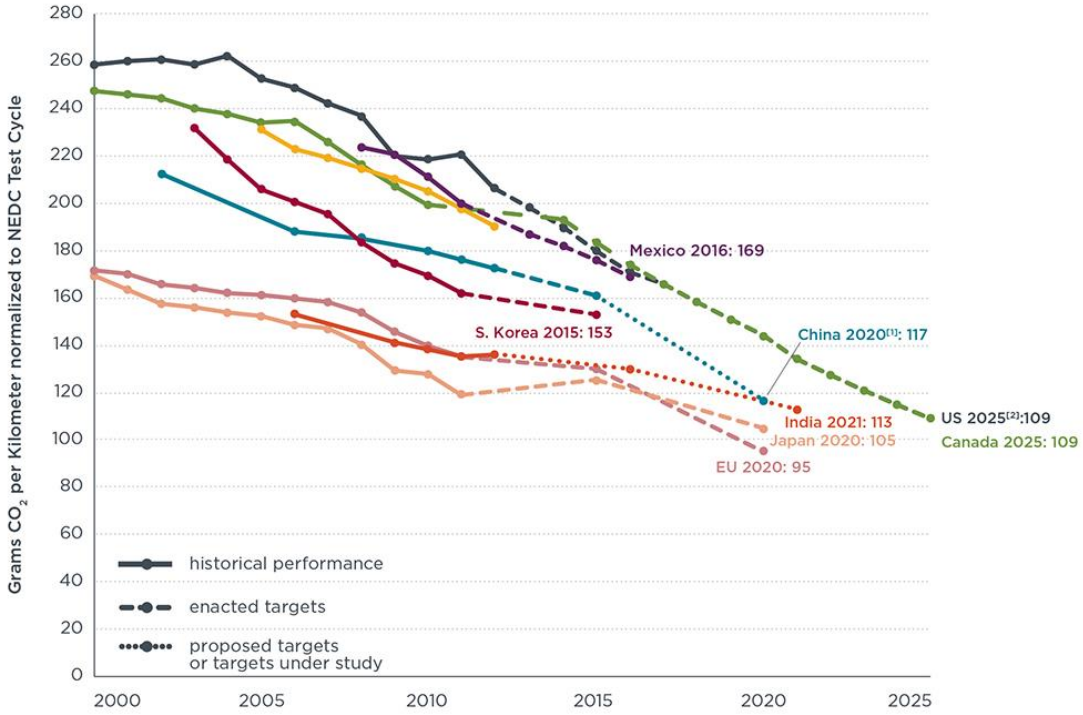

Figure 1.3: *Comparison of historical and targeted Light Duty Vehicle CO_2 emission rates [4].*

Similar legislation has been proposed in the US, which currently has two CO_2 emissions standards: (i) the corporate average fuel economy (CAFE) standards of the National Highway Traffic Safety Administration (NHTSA) and (ii) the greenhouse gas emission standards of the US Environmental Protection Agency (EPA). These standards were harmonized in 2010, which resulted in an average CAFE fuel economy target of 34.1 mpg (6.9 L/100 km) and CO_2 emissions target of 250 g/mile (155 g/km) by

2016 for LDVs. More than two years later, the EPA and NHTSA issued joint GHG and fuel economy standards for vehicles resisted during 2017-2025, requiring average GHG emissions not exceeding 163 g/mile (101 g/km) of CO_2 and an average fuel consumption of between 48.7 and 49.7 mpg (4.7 and 4.8 L/100km) by 2025 [10].

In summary, there is a need for new clean and highly efficient internal combustion engines (ICE) for transportation that is driven by the world's large population, the expected long-term economic growth especially in non-OECD countries, the limited global oil reserves, and increasingly stringent emissions regulations.

1.2. Technologies for improving the fuel economy of gasoline engines

Contemporary R&D (research and development) in the field of internal combustion engines deals with a wide spectrum of promising technological solutions aimed at improving fuel efficiency and reducing CO_2 emissions. In line with the subject of this thesis, the subsequent discussion is exclusively devoted to technologies developed for gasoline engines. Such engines are often called Spark Ignition (SI) engines and are used in gasoline cars.

It is worth noting that in the top three vehicle markets for passenger cars (China, the US and the EU), gasoline cars accounted for around 98%, 90% and 44%, respectively, of all new car sales in 2012. This situation is expected to continue in the coming decades as the market grows, especially in China where LDV sales are expected to increase by 221% between 2010 and 2030 [11]. Even though the EU market is dominated by diesels, sales of Gasoline Direct Injection (GDI) vehicles in the EU have increased sharply since 2008, giving them an estimated market share of approximately 25% in 2012 [11].

Downsizing and downspeeding, i.e. reducing the total displacement volume of an engine and operating the engine at lower speed by adjusting the transmission, are widely used by vehicle manufactures when developing modern gasoline engines. These techniques can provide significant fuel economy advantages because they shift the engine's operating point from less efficient partial load conditions to more efficient high load conditions [11]. In combination with other technologies such as (i) direct injection (DI) of fuel, which is called GDI if gasoline is directly injected into the combustion chamber of a SI engine, (ii) boosting, (iii) variable valve timing (VVT), (iv) engine friction reduction, and (v) cylinder deactivation, significant reductions in fuel consumption and CO_2 emissions can be achieved while maintaining the performance of the original engine.

GDI technology, which will be discussed in more detail later, is one of the most efficient methods for reducing fuel consumption and CO_2 emissions for SI engines. According to a report by the United States of Environmental Protection Agency (EPA), it has the potential to reduce CO_2 emissions by 20-26% for passenger cars relative to those expected for an equivalent as compared to natural aspirated port-fuel injection (PFI) spark-ignition engines [12].

Boosting means increasing the inducted air and thereby increasing the engine's specific power. This technology is realized either by turbocharging (in which the forced

induction system is powered by a turbine that is driven by exhaust gas) or by supercharging (in which forced induction is driven by the engine via a belt connected to the cam shaft). Boosting together with downsizing can potentially reduce passenger cars' fuel consumption by 5-7% beyond the reductions achieved by implementing GDI technology [12].

VVT systems are designed to optimize engines' gas exchange process to reduce knock or trapped residuals. They can reduce CO_2 emissions by 2-4% relative to those achieved with fixed valve engines [12].

Friction reduction can be applied to several of the reciprocating and rotating components of engines, including piston surfaces and rings, crankshaft, and so on. Minor improvements in these components can collectively have measurable positive effects on fuel consumption.

A final efficient method for reducing fuel consumption, especially in larger passenger cars, is cylinder deactivation. This involves shutting down half of the engine's cylinders while leaving the others operating at almost twice the load that would be required otherwise. The intake and exhaust valves of the inactive cylinders are closed and no fuel is injected into them. Pumping losses are thereby reduced significantly, which in turn reduces fuel consumption.

The remainder of this thesis deals exclusively with GDI technology.

1.3. GDI engines

1.3.1. GDI versus PFI

The major difference between a GDI engine and a conventional port fuel injection (PFI) engine is the mixture preparation, as illustrated schematically in Figure 1.4. In most PFI engines, fuel is injected to the back of the intake valve when it is closed, which creates a wall film around intake valve, especially when motoring and during cold starts; see Figure 1.4 (a). This delays fuel delivery and causes fuel metering errors, which in turn leads to either misfiring or partial burning for the first 4-10 cycles. As a result, the engine produces high unburned HC emissions and has a relatively high fuel consumption. In contrast, in GDI engines, fuel is directly injected into the combustion chamber. This avoids the formation of a wall film on the intake port, as shown in Figure 1.4 (b). In order to accelerate the fuel vaporization and reduce HC emissions, GDI engines use relatively high injection pressures of 100 - 200 bar, and produce sprays of fine droplets with typical diameters of around 16 μm; for comparative purposes, the droplets discharged to the intake valve of a PFI engine are usually around 120 μm in diameter [13].

Aside from producing significantly lower unburned HC emissions than PFI engines, GDI has the additional advantage of reducing pumping losses by using less throttling. PFI engines have a throttle located upstream of the intake system (see Figure 1.4 (a)) for basic load control: the throttle is opened wide under full load conditions and closed at low load. The pumping losses associated with throttling are substantial. GDI engines can be operated with wide open throttle or even without a throttle at part load depending on the engine design, and their load is controlled by the amount of fuel

injected. Another positive effect of wide open throttle or lack of throttle is that it improves the engine's dynamic response characteristics. When a PFI engine is suddenly switched from low to high load, the throttle is opened wide to fill up the intake system with air. Therefore, the intake pressure slowly rises to meet the load requirement. In contrast, the intake pressure in an unthrottled GDI engine is relatively stable regardless of the load, so the torque response is much faster.

Moreover, GDI engines can be operated in either stoichiometric homogeneous mode at high loads by imposing early injection or in lean stratified mode under partial loads by performing late injection. The latter mode is beneficial for fuel efficiency. With appropriate organization of the fuel spray and in-cylinder flow, a near stoichiometric fuel-air mixture is formed near the spark plug to facilitate ignition. Less heat is lost through the cylinder walls because the burning is restricted to the centre of the combustion chamber and the surrounding gas, which is mainly air, acts as an isolating layer.

A final advantage of GDI engines is that they operate with higher compression ratios than PFI engines due to the charge cooling effect associated with direct fuel injection.

While GDI technology has several benefits as listed above, it also has some drawbacks and associated challenges. For example, GDI engines suffer greater mechanical losses than their PFI counterparts due to their need for high pressure fuel pumps and the increased piston-ring friction associated with the increased in-cylinder air in the untrottled mode. GDI engines also require more costly and complicated exhaust gas aftertreatment system because conventional three-way catalytic converters lose much of their efficiency when operating under lean stratified conditions. In addition, GDI engines operating in stratified mode tend to produce relatively high soot emissions, partly as a result of pool fires. Finally, it is difficult to design a combustion system that will reliably form an ignitable mixture with a steep mixture fraction gradient in the vicinity of the spark plug at the desired ignition timing regardless of engine load and speed. To consistently achieve this target would require the consideration of many factors including the intake flow, the properties of the combustion chamber, the compression ratio, the position of injector relative to the spark plug, the injection parameters, and so on. The following subsection focuses on the various combustion systems used in GDI engines.

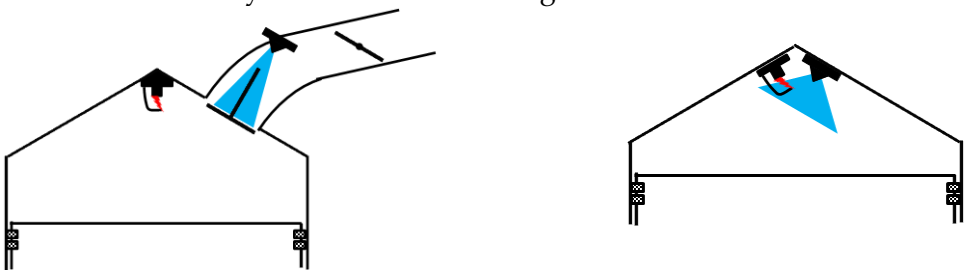

(a)PFI *(b)GDI*

Figure 1.4: *Comparison of PFI and GDI systems.*

1.3.2. The development of GDI

One of the challenges associated with the design of GDI engines has to do with the difficulty of maintaining stable combustion, which requires a suitable fuel-air mixture. The formation of the fuel-air mixture is influenced by fuel atomization, droplet breakup, vaporization, and the efficiency of mixing. Numerous gasoline direct injection combustion systems have been developed and applied in practical production. Depending on the relative position of the injector and spark plug as well as the in-cylinder air motion, three types of GDI combustion systems can be defined, as shown in Figure 1.5**:** wall-guided (WG), air-guided (AG) and spray-guided (SG).

The wall-guided configuration was commonly used in the first generation of GDI engines. A side-mounted high pressure injector discharges fuel towards a contoured piston bowl with the help of a strong tumble flow generated by the intake system; see Figure 1.5 (a). Engines of this type produce relatively high unburned HC emissions due to the decomposition of fuel on the cylinder walls and the piston crown, as well as in the squish area. Moreover, the formation of a near-stoichiometric fuel-air mixture requires the fine tuning of the fuel injection timing and piston movement, and thus the engine speed.

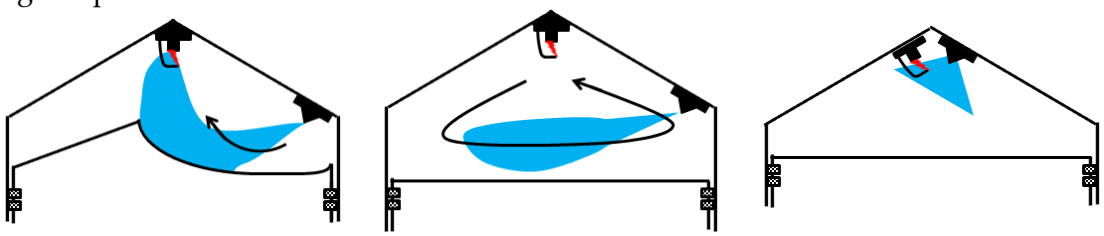

(a)wall-guided *(b)air-guided* *(c)spray-guided*

Figure 1.5: *Classification of GDI combustion system.*

In the air-guided concept, contact between the fuel spray and combustion chamber should be avoided. Ideally, the fuel accumulation on the walls is avoided completely. The fuel cloud is transported to the spark plug solely by charge motion generated in the intake side in a process that exploits a specially designed piston bowl; see Figure 1.5 (b). The fuel and air are mixed while being directed towards the spark plug. In this concept, it is essential to maintain a strong swirl or tumbling air motion until the combustion phasing is reached, which results in a relatively low engine volumetric efficiency and thus poor performance. The air-guided concept is rarely used in engine productions, but a very limited number of engines with air-guided systems are available on the market.

The spray-guided combustion system represents the second generation in the development of the modern direct injection gasoline engine. In these engines, a centrally-located high pressure injector discharges fuel into the combustion chamber, and a spark plug is positioned precisely at the edge of the spray; see Figure 1.5 (c). The narrow gap between the injector and spark plug is intended to ensure the formation of an ignitable fuel-air mixture with a steep stratification gradient in between the ignition electrodes under a wide range of operating conditions. The need for the spark plug to be positioned very precisely in relation to the spray presents a challenge when developing SG GDI engines. Moreover, a robust and repeatable spray pattern is required even in the presence of cyclic variations in back pressure and flow patterns within the combustion chamber. Optimised spray-guided systems can achieve very good fuel economy, with around 4-6% less fuel consumption than wall-guided systems

[14] while retaining comparable soot emissions and levels of combustion stability to those observed with other GDI concepts. The work presented in this thesis deals with a SG GDI engine.

1.3.3. GDI injection technology

Because fuel injection and the formation of fuel-air mixtures are crucial steps in the combustion process of a GDI engine, development of a suitable fuel injector is a very important task. Three different types of injectors have been used in modern GDI engines (see Figure 1.6).

Swirl nozzles were commonly used in purely homogeneous GDI engines and in the first generation of stratified charge wall-guided engines that had relatively low injection pressures of 50-100 bar [13]. Nozzles of this type have an internal structure that imparts an angular velocity to the fuel before it is released into the chamber. They generate sprays with a hollow cone shape and the geometries of their spray cones exhibit good atomisation characteristics with high pulse-to-pulse repeatability when a flow guiding pattern is present at the nozzle tip [13]. They are also relatively insensitive to mechanical and thermal interference as well as contamination. However, they are unsuitable for use in spray-guided engines because the spray cone angles are sensitive to the back pressure in the combustion chamber [11].

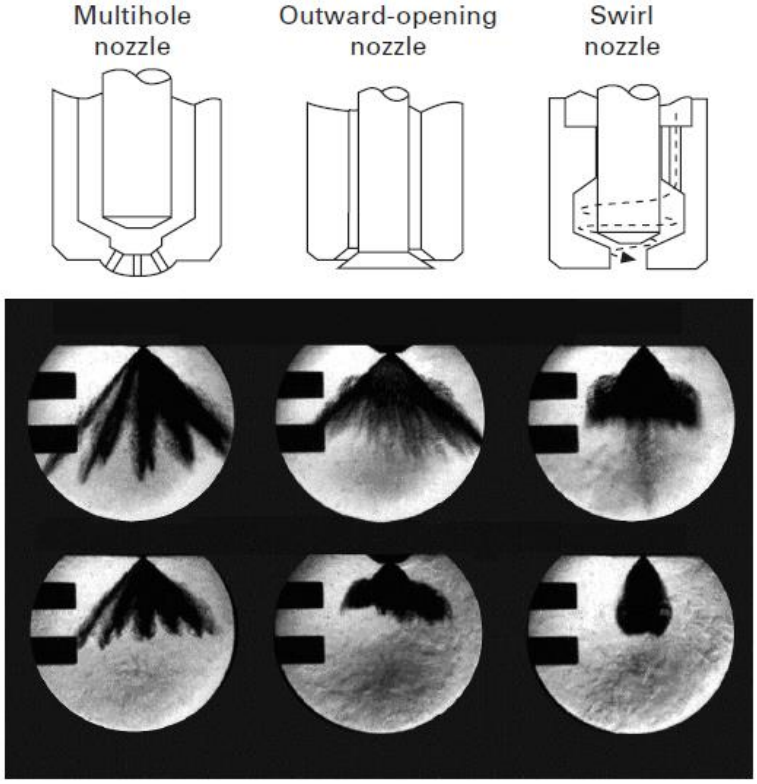

Figure 1.6: *Three types of injectors for GDI engines (from left to right: a multi-hole injector, an outward-opening pintle-type piezo-controlled injector, and an inward-opening pressure-swirl injector). Adapted from a paper by Wirth et al. [14].*

In order to achieve the spray-guided stratified charged combustion, multi-hole injectors that release sprays in the form of several plumes were developed and put into

mass production. The multi-hole injectors create flexible spray patterns by using different configurations in orientation of their nozzle holes. However, they require relatively high pressures (above 150 MPa) to achieve good atomisation. Moreover, the small nozzle diameters associated with high injection pressures increases the tendency for the nozzle hole to become blocked by soot deposits. Therefore, injectors of this sort require good cooling to avoid soot formation in their vicinity. Another disadvantage of multi-hole injectors is the problem of wall wetting associated with retarded fuel injection, which increases HC and soot emissions.

A good alternative injector type for spray-guided GDI engines is the outward-opening piezo-controlled pintle-type injector. These injectors do not produce the initial sac spray generated by most inward opening injectors as a result of the passage of fuel through the sac volume. The initial liquid sheet thickness is directly controlled by the pintle stroke rather than the angular velocity of the swirling fuel as in a swirl injector [13]. With the piezo-actuated system, the injection can be controlled with a high degree of accuracy by adjusting the pintle lift height and the opening duration. Moreover, they can achieve injection pressures of up to 200 bar, which improves fuel atomisation [15].

In my thesis work, I dealt with the outward-opening piezo-controlled pintle-type injectors.

1.3.4. Working process in a SGDI engine

In principle, SGDI engines can switch smoothly between two combustion modes: homogeneous and lean stratified modes. At high loads, fuel is injected during the intake stroke on the downward stroke of the piston, forming a homogeneous mixture. The engine is operated in a way similar to that for the homogenous PFI concept. At low loads, the fuel injection timing is retarded relative to the homogeneous mode and fuel is usually injected during the compression stroke, when the piston is close to the top dead center (TDC); see Figure 1.7.

After the fuel injection, the liquid core breaks up into smaller droplets downstream of the spray; these smaller droplets then evaporate. The resulting fuel vapour is transported towards the spark plug and mixed with air by turbulent eddies that are mainly generated as the fuel is injected. The time available for the transformation from liquid fuel to the gas phase is extremely limited, usually on the order of several hundred microseconds for a late injection. Therefore, a highly stratified fuel-air mixture is formed in the center of the combustion chamber. Directly after the end of injection or even during the injection, the spark plug starts to ignite the newly prepared mixture. Ignition may take a few crank angles, after which the turbulent flame propagates. Since the mixture is highly stratified, the flame propagates fastest in slightly rich fuel-air mixture accompanied with the formation of a large amount of CO_2. Propagation is slower in both lean and rich mixtures; the latter in particular leave substantial quantities of unburned HC. In addition, NO_x can be formed in the slightly lean products associated with high combustion temperature at 2200 K or above. After the propagation of the premixed flame, the lean and rich products burn in mixing-controlled mode. The whole burning process happens during the end of compression and most of the expansion strokes, and is followed by the exhaust process that occurs as the piston expels the burned gases.

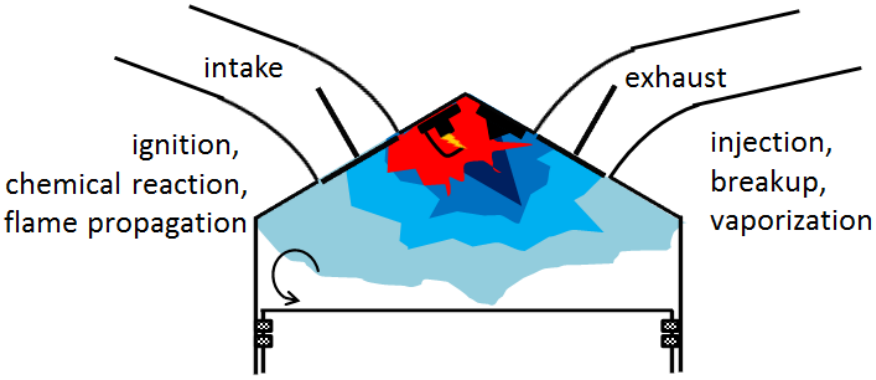

Figure 1.7: *The working process in a SGDI engine.*

1.4. Specific issues and goals of the thesis

To realize the high potential of the SG DISI technology, the automotive industry urgently requires advanced tools, both experimental and numerical, for investigating working process in SG DISI engines. In a broad sense, the work presented in this thesis aimed to develop models, methods, and a numerical platform for simulations of gasoline DISI engines. Such a platform should be based on efficient and reliable CFD code and should involve advanced models of the many important phenomena described briefly in the previous section. However, it would be impossible to make substantial contributions to the modelling of every single one of these phenomena within the framework of a single PhD thesis work. Accordingly, my work focused on a selection of important and closely related issues associated with numerically modelling of working processes in a DISI engine. My work can be broken down into three categories: (i) model development, (ii) numerical platform development, and (iii) applications of the new models and platform.

It is worth noting that this work was carried out within the framework of unsteady RANS rather than LES (Large Eddy Simulation) or DNS (Direct Numerical Simulation). One of the most important reasons for such choice is due to the relatively low computational cost associated with unsteady RANS simulations. In RANS simulations the time or ensemble averaged governing equations are solved and a relatively course grid is acceptable. In contrast, in LES simulations the large scale eddies are resolved using the spatial filtered equations leaving the small-scale eddies being modelled and a relatively fine grid is required. Moreover, valuable LES simulations in engine applications require simulations for multiple engine cycles and statistical analysis of results. Such requirements substantially increase the computational costs for LES simulations. The DNS simulations in engine application are currently beyond the capability of computational resources since the unfiltered or unaveraged instantaneous governing equations are solved using extremely fine computational grids for all scales of turbulence eddies. However, there are drawbacks associated with unsteady RANS simulations. For example, the unsteady RANS simulations cannot be applied to study the cycle-to-cycle variation as it can be studied within LES framework.

1.4.1. Model development

Due to the direct injection of gasoline into the combustion chamber of a DISI engine, the time interval between fuel injection and spark ignition is typically very short especially during a stratified lean burn under partial load. Accordingly, the flame kernel created by the spark expands in an inhomogeneously premixed mixture, with the mixture composition varying substantially in space and time. Therefore, to model stratified turbulent combustion in a DISI engine, it is necessary to accurately predict the dependence of the rate of turbulent burning on the composition of the fuel-air mixture.

The problem of predicting the influence of mixture composition on the stratified burning rate can be divided into three sub-problems. First, because a typical model of a premixed or stratified turbulent flame considers the laminar flame speed to be the primary input parameter characterizing the burning mixture [16]-[18], the dependence of the laminar flame speed on the composition of gasoline-air mixture should be well predicted under conditions associated with combustion in a DISI engine (i.e. under conditions of high and transient pressure and temperature). This requires a sufficiently accurate chemical mechanism for the combustion of gasoline-air mixtures is required.

Accordingly, **the first specific goals** of my work were to (i) further develop and thoroughly validate of a semi-detailed chemical mechanism for the combustion of a gasoline surrogate that was originally put forward by Ogink and Golovitchev [19], (ii) apply this mechanism to the evaluation of the laminar flame speeds of gasoline-air mixtures under conditions associated with combustion in a DISI engine, and (iii) to approximate the obtained flame speeds for subsequent multidimensional numerical simulations of stratified turbulent combustion in a GDI engine.

The second and third sub-problems relate to properly predicting (i) the dependence of the local turbulent burning rate on the local laminar flame speed, and (ii) the influence of turbulent fluctuations in mixture composition on the burning rate, respectively. These two sub-problems were addressed by utilizing and extending the so-called Flame Speed Closure (FSC) model of premixed turbulent combustion.

The FSC model was developed and thoroughly validated against various experimental data on premixed turbulent flames obtained under laboratory conditions [18]. These tests demonstrated the model's ability to quantitatively predict the influence of mixture composition on the turbulent burning rate in the premixed case and this feature of the FSC model makes it particularly interesting for application to stratified turbulent flames.

Because the FSC model was developed to simulate premixed turbulent flames, it does not account for the effect of turbulent fluctuations in the local mixture composition on the local burning rate. Accordingly, **the second specific goal** of the thesis was to extend the FSC model in order to take this effect into account.

1.4.2. OpenFOAM®

Although several mature commercial CFD codes (Star-CD, FIRE, FORTE, Fluent, KIVA, etc) are available on the market, industrial companies are keen to adopt less expensive software. For this reason, OpenFOAM® (Open Field Operation and

Manipulation), which is a free, open source CFD software package available at www.openfoam.com, has attracted increasing amounts of attention from both commercial and academic organizations since its first release in 2004 [20]. In particular, researchers working in the field of piston engines have shown growing interest in using this code over the past few years. However, although the number of problems relevant to piston engines that have been studied with OpenFOAM® continues to grow, there are still a great many such problems that have not yet been addressed with this code. Consequently, many more studies will be required in order to properly assess its utility in the automotive industry.

Accordingly, **the third specific goal** of the thesis was to further develop OpenFOAM® as a numerical platform for studying GDI engines. To this end, the implementation of various models in the standard OpenFOAM® package was assessed. For instance, while modern outward-opening pintle-type piezo-controlled injectors, which are commonly used in the second generation GDI engines, can discharge fuel sprays at both low (50 bar) and relatively high (200 bar) pressures**,** spray models that are typically used in CFD research into SI engines and particularly those implemented in OpenFOAM® were developed and validated primarily for simulating inward-opening pressure-swirl injectors that operate at a relatively low pressure (around 50 bar). Consequently, there was a strong need to test such models against experimental data obtained with pintle injectors operating at significantly higher pressures (up to 200 bar) so that the model that best describes such conditions could be identified. Accordingly, various spray models implemented in the standard OpenFOAM® package were assessed by (i) applying the code to numerical simulations of gasoline and ethanol sprays discharged by a pintle injector into a constant-volume rig under different pressures and (ii) comparing the computed results to experimental data obtained in our laboratory by Hemdal et al [21].

While models of many phenomena described briefly in Section 1.3.4 are implemented in the original version of OpenFOAM®, the code still requires further development. To this end, an approximation for evaluating gasoline laminar flame speeds under engine-like conditions was implemented into OpenFOAM®. Moreover, the extended FSC model which accounts for the influence of mixture composition and its fluctuations on stratified burning was also implemented.

1.4.3. Application of models and OpenFOAM®

The final goal of the thesis was to (i) apply OpenFOAM®, extended as outlined above, to multidimensional RANS simulations of fuel injection, evaporation, mixing, and stratified turbulent burning in a research SG GDI engine; and (ii) compare the results obtained in these simulations to experimental data provided by my colleagues.

1.5. Structure of the thesis

The development and validation of a chemical mechanism for the combustion of gasoline-ethanol blends is described in Chapter 2. The major results of this part of the thesis consist of semi-detailed chemical mechanism for gasoline surrogate and an approximation of the laminar flame speeds of gasoline-air mixtures under various

equivalence ratios, elevated temperatures and pressures, associated with combustion in a GDI engine.

Chapter 3 provides a detailed discussion of the simulation of hollow cone sprays of gasoline-ethanol mixtures using OpenFOAM®. The major results of this part of the thesis consist of a number of implementations into OpenFOAM® and selection of models for simulating sprays discharged by a pintle injector under high (for SI engines) pressures.

Chapter 4 describes a stratified turbulent combustion model for DISI engine, its implementation into OpenFOAM® and results of applications of the improved code to unsteady multidimensional RANS simulations of stratified turbulent combustion in a research GDI engine. The major results of this part of the thesis consist of extension of the FSC model to stratified flames, code development, and validation of the developed numerical tool against experimental data obtained by my colleagues at Chalmers.

Finally, some conclusions and suggestions for future work are presented in Chapter 5.

Chapter 2

A Chemical Model for Gasoline-Ethanol Blends

2.1. Introduction

The investigation of promising design concepts and new technologies for reciprocating combustion engines would be greatly facilitated by the availability of a chemical mechanism for the combustion of gasoline-ethanol-air mixtures under various conditions (i.e. at different equivalence ratios ϕ, initial temperatures T_u, and pressures p). For instance, ϕ, T_u and p vary in the cylinder of a GDI engine, and so to accurately model such engines one must use a combustion mechanism that can account for this variation. Moreover, by burning gasoline-ethanol blends, one can suppress engine knock at elevated compression ratios; this allows engine downsizing through the use of a turbocharger [22][23], but again can only be accurately modelled if a reliable combustion mechanism has been elucidated.

While detailed chemical mechanisms for the combustion of ethanol are available [24]-[29], the chemistry of gasoline combustion is much more complicated. Real gasoline is a blend of hundreds of different hydrocarbons, and its composition can vary greatly depending on the source of the crude oil source from which it was made, the refining processes used in its preparation, and seasonal factors. Due to the complexity of real gasoline, experimentalists typically use a surrogate fuel with a known and constant composition instead when studying engine behaviour and combustion; the various surrogate fuels that have been recommended over the years and their properties have recently been reviewed [30]. One of the most commonly-used surrogates is Primary Reference Fuel (PRF), a mixture of *n*-heptane and *iso*-octane whose octane number is similar to that of typical gasoline. Detailed [31][32], semi-detailed [33][34] and reduced [35]-[38] chemical mechanisms for PRF combustion have been developed. However, the H/C molar ratios of *n*-heptane and *iso*-octane are 2.29 and 2.25, respectively, while that of commercial gasoline is around 1.87. The local fuel/air ratio is a function of the H/C molar ratio among other variables, and so the difference between PRF and gasoline in this respect makes it an unsatisfactory surrogate fuel in some applications.

A semi-detailed mechanism for the combustion of a ternary gasoline surrogate mixture (55 mole % *iso*-octane, 35% toluene, and 10% *n*-heptane) was developed by Ogink and Golovitchev [19] and used to simulate gasoline (C_8H_{15}) combustion in HCCI engines. Detailed chemical mechanisms for the combustion of PRF-toluene blends have been reported by Andrae et al. [39], Chaos et al. [40], and by Battlin-Leclerc et al. [41][42], Bounaceur et al. [43] and Mehl et al. [44] devised detailed mechanisms for *n*-heptane/*iso*-octane/hexene/toluene blends that can be used as gasoline surrogates, while Naik et al. [45][46] reported a detailed mechanism for a gasoline surrogate with

five components (*n*-heptane, *iso*-octane, 1-pentene, toluene, and methylcyclohexane). However, these detailed mechanisms are too complex to be used in CFD engine simulations; for example that developed by Bounaceur et al. [43] features 1267 species and 5803 reactions, while that of Mehl et al. [44] features 1550 species and 8000 reactions. A semi-detailed mechanism for the combustion of gasoline-ethanol-air mixtures was recently developed by Golovitchev et al. [47] based on the chemical mechanism for the gasoline surrogate proposed by Ogink and Golovitchev [19] and that of ethanol. The chemistry of the combustion of ethanol/*iso*-octane/1-hexene/toluene blends was also addressed by Frassoldati et al. [48]. A semi-detailed (137 species, 633 reactions) mechanism for the combustion of the ternary blend proposed by Ogink and Golovitchev [19], is described by Andrae et al. [49] for the so called toluene reference fuel. The mechanism was found to perform rather well when its predictions were compared to shock-tube auto-ignition data [50] for ternary mixtures A and B, which consist of mixtures of *iso*-octane, toluene and *n*-heptane in the volumetric proportions of 63:20:17% and 69:14:17%, respectively. However, these blends have H/C ratios of around 2 and do not closely resemble commercial gasoline in this respect.

The work described in this chapter was aimed at refining and validating the gasoline-ethanol mechanism [19][47] using experimental data on the shock tube ignition delays and laminar flame speeds observed using mixtures relevant to this gasoline surrogate. The ultimate goal of work conducted along these lines is to construct a mechanism that can be used in combination with CFD engine modelling.

2.2. Methodology used in constructing reaction mechanisms

The reaction mechanism was constructed using an approach based on the principles of hierarchy and modularity [51][52]. This means that the reaction mechanism was built up starting from small blocks (modules) and the simplest sub-mechanism included was the first one in the hierarchy. The advantage of this approach is that new components can easily be added to the mechanism: once the basic elementary reactions are defined, the introduction of new species requires only the definition of new primary steps.

The first block in the overall mechanism defined a sub-mechanism for hydrogen oxidation; the next focused on the oxidation of carbon monoxide. Sub-mechanisms were then added for the oxidation of hydrocarbon species, starting with the simplest - methane - and moving on to increasingly complex hydrocarbons, up to *n*-heptane, *iso*-octane, and toluene. Finally, a sub-mechanism for ethanol oxidation was implemented. The sub-mechanisms were constructed according to established generic oxidation rules [53][54] (see Figure 2.1).

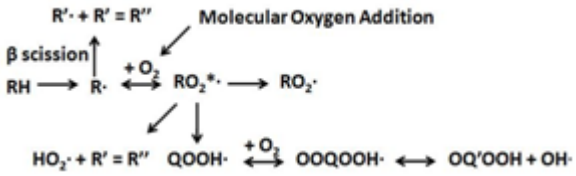

Figure 2.1: *Branching pathways for aliphatic hydrocarbon oxidation at low and intermediate temperatures.*

After the addition of each new sub-mechanism, the model's predictions were compared to experimental data for the new constituent. The information used for validation was obtained from shock-tube auto-ignition and laminar flame speed measurements. The SENKIN [55] and PREMIX [56] codes from the Chemkin-II [57] package were used for computation. If the match between experimental and simulated results was not satisfactory, a sensitivity analysis was carried out on the dataset to identify the most sensitive reactions during auto-ignition. Since the validation was done using ignition delay data, the temperature/reaction rate sensitivity was used in the analysis. The largest sensitivity occurs near the moment of ignition [55]. On the basis of this analysis, the rate coefficients of one or more reactions were adjusted to improve the agreement with the experimental data. It is worth stressing that only the newly-added reactions were tuned after adding a new sub-mechanism; this was done to avoid compromising the quality of the predictions obtained with the previously-added sub-mechanisms. A schematic diagram illustrating the construction of this chemical mechanism is shown in Figure 2.2.

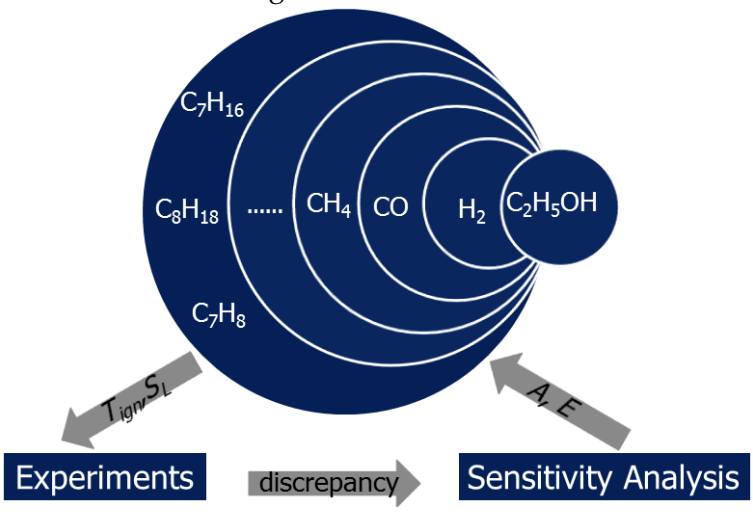

Figure 2.2: *A schematic diagram illustrating the construction of the combustion mechanism for gasoline-ethanol blends.*

The lumping procedure [52][54], which assumes that intermediate species with the same molecular formula can be represented by a single species or a reduced number of similar species, was used to keep the size of the mechanism at a computationally-tractable level. Specifically, this method was used for the *iso*-octane, *n*-heptane and toluene sub-mechanisms, where it was applied to species ranging from fuel radicals down to hydrocarbon species with a maximum of three carbon atoms. Thus, only four octyl and two heptyl radicals are considered in the mechanism, along with the appropriate intermediates involved in their decomposition and isomerization. The C_3-

species are then converted to intermediates and radicals that feature in the sub-mechanisms relating to the formation of CO and CO_2.

In this mechanism (see Figure 2.1), combustion is initiated by the decomposition of the fuel (RH) to produce alkyl radicals (R·). The dominant reactions in the low temperature auto-ignition region are those involving RO· radicals formed from small hydrocarbons and hydroperoxyalkyl radicals (QOOH·) formed from larger hydrocarbons. The intermediate temperature region is dominated by the reactions of HO_2 radicals, which result in the formation of stable alkenes, oxygenated species (e.g. aldehydes), and methane. The most important reactions in the high temperature region are those of the OH, O, and H radicals and beta-scission reactions.

Fourteen cross-interaction reactions between the components of the gasoline surrogate are considered in the mechanism. These are all of the form

AH + B < = > A + BH

AH + C < = > A + CH

BH + C < = > B + CH

where AH denotes *iso*-octane, BH denotes toluene, and CH denotes *n*-heptane.

This methodology was used to create a comprehensive mechanism for the combustion of gasoline-like fuels, featuring 111 species and 616 reactions. The gasoline surrogate that was modelled consists of *iso*-octane, toluene, and *n*-heptane in volumetric proportions of 55%:35%:10%, respectively [19]. The H/C molar ratio of this mixture is similar to that of for real gasoline, i.e. 1.87, and it also has a realistic equivalence ratio. The mechanism for gasoline-ethanol blends includes 120 species and 677 reactions after the addition of the ethanol combustion sub-mechanism [58]. Six reactions taken from a previously-developed detailed mechanism for the combustion of dimethyl ether [59] were also incorporated into the ethanol sub-mechanism (see Table 2.1); the rate constants for these reactions can be found in [58][59]. The thermal and transport properties of the species used in the model were obtained from published data [60][61][62].

Table 2.1: *Six reactions adapted from a previously-published mechanism for the combustion of dimethyl ether*

$C_2H_5OH + O_2 <=> C_2H_4OH + HO2$
$C_2H_5OH + CH_3 <=> C_2H_4OH + CH_4$
$C_2H_5OH+CH_3 <=> C_2H_4OH+CH_4$
$C_2H_4OH<=> C_2H_4+OH$
$HOC_2H_4O_2<=> C_2H_4OH+O_2$
$HOC_2H_4O_2<=>OH+CH_2O+CH_2O$

The mechanism that was ultimately developed describes the combustion of fuel blends containing four components: *iso*-octane, *n*-heptane, toluene, and ethanol. It is an order of magnitude smaller than existing typical detailed mechanisms for the combustion of mixtures of *iso*-octane and *n*-heptane. For example, the PRF mechanism developed by [62] involves 1024 species and 4237 reactions, the gasoline surrogate mechanism developed by [39] features 1083 species and 4535 reactions, and that developed by [45] involves 1214 species and 5401 reactions.

The next section describes studies in which predictions made using this new mechanism (which is henceforth referred to as the Chalmers mechanism) were compared to experimental data on ignition delay times and laminar flame speeds.

2.3. Results and discussions

2.3.1. Model validation

This section details with the most important results obtained during the validation of the Chalmers mechanism; interested readers are directed to Paper I for a more detailed discussion of this work.

The measured [50] (filled symbols) and calculated (open symbols) ignition delays for a stoichiometric *n*-heptane-air mixture are shown in Figure 2.3. The Chalmers mechanism accurately predicts the experimental behaviour at both low (p=15-25 atm) and high (p=45-60 atm) pressures. The mechanism also reproduces the ignition delay times observed in the negative temperature coefficient (NTC) region measured by [64] at p =13.3 atm.

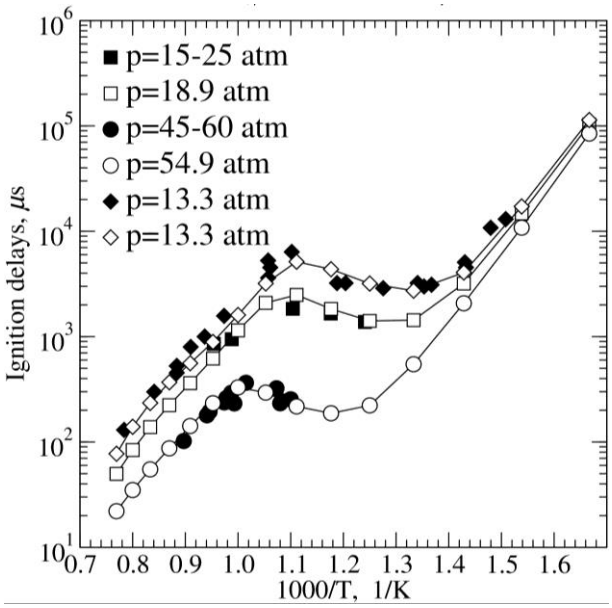

Figure 2.3: *Computed (open symbols) and measured (filled symbols) ignition delay times for a stoichiometric mixture of n-heptane and air. The experimental data obtained by Gauthier et al. [50] is shown with filled circles and squares; that obtained by Ciezki and Adomeit [64] is shown with filled diamonds.*

I next examined the mechanism's ability to predict the results obtained with gasoline. Figure 2.4 shows the measured [50] (filled symbols) and calculated (open symbols) ignition delays for a stoichiometric mixture of air and a gasoline surrogate consisting of *iso*-octane, toluene, and *n*-heptane in a volumetric ratio of 55%:35%:10%, respectively. The Chalmers mechanism accurately predicts the experimental observations at both low (p=15-25 atm) and high (p=45-60 atm) pressures.

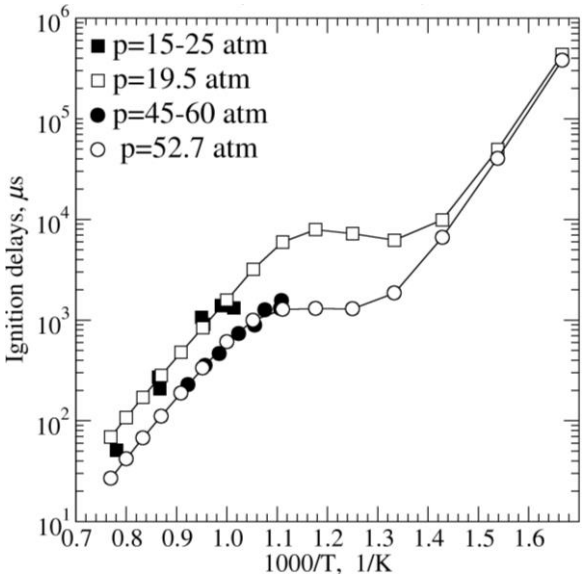

Figure 2.4: *Computed (open symbols) and measured [50] (filled symbols) ignition delay times for the stoichiometric gasoline-air mixture.*

Figure 2.5 shows the measured (filled symbols) and computed (open symbols) dependency of the laminar flame speed S_L on the equivalence ratio ϕ for gasoline-air mixtures. The mechanism accurately predicts the dependencies of S_L on ϕ which have been documented by Metghalchi et al. [65] at p=1 bar, T_u=298 K (circles in Figure 2.5) and by Zhao et al. [66] at p=1 bar, T_u=353 K (squares) and T_u=500 K (diamonds). The computed results at T_u =500 K closely resemble those predicted using the approximation proposed by Metghalchi et al. [65] (dashed line).

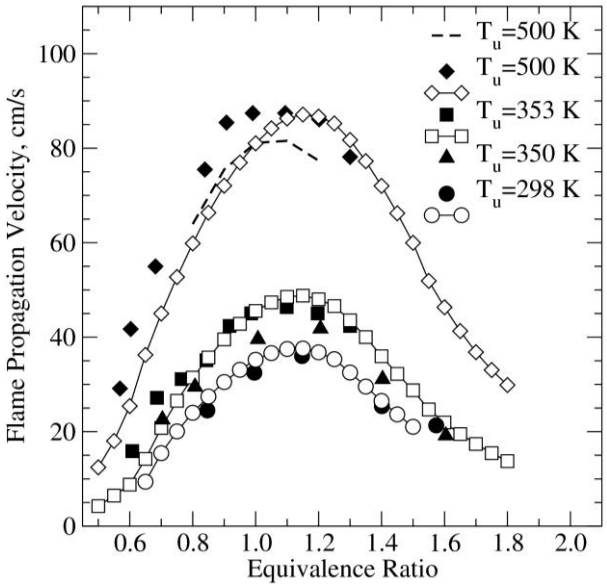

Figure 2.5: *Computed (open symbols) and measured (filled symbols) laminar flame speeds for gasoline-air mixtures at p=1 atm. Filled circles and triangles show the data reported by Metghalchi et al. [65]. The experimental data obtained by Zhao et al. [66] is shown using filled squares and diamonds. The dashed line indicates the predicted results obtained using the high-temperature approximation proposed by Metghalchi et al. [65] at T_u=500 K and p=1 atm.*

Jerzembeck et al. [38] reported flame speed data for gasoline-air mixtures at elevated pressures, p=10-25 bar. Figure 2.6 indicates that the mechanism accurately predicts the effects of pressure on the laminar flame speed for gasoline-air mixtures at ϕ=0.8, 1.0, and 1.2.

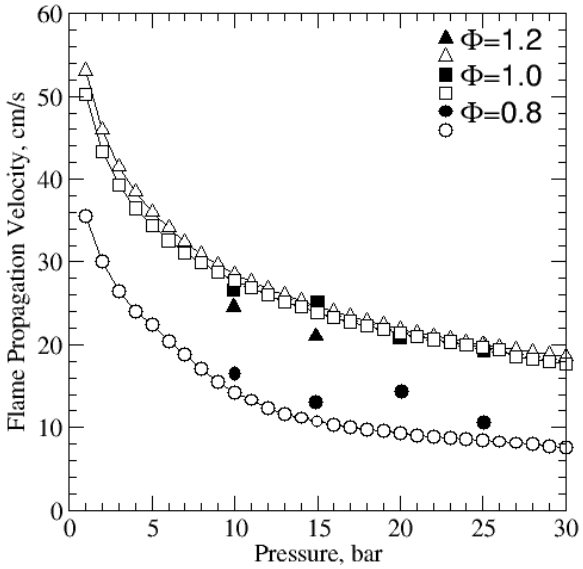

Figure 2.6: *Computed (open symbols) and measured [38] (filled symbols) laminar flame speeds for gasoline-air mixtures at $T_u = 373\ K$ and elevated pressures.*

It is worth noting that the semi-detailed chemical mechanism has been extensively validated (see Ref. [67]) against a large set of experimental data for ignition delay times and the few measured data sets for $S_L(\phi)$ that were available in 2010. New experimental results on laminar flame speeds in gasoline-air mixtures were recently reported by two research groups [68][69]. The semi-detailed chemical mechanism predicts the results obtained for lean and near-stoichiometric flames very accurately, but moderately overpredicts the speeds of rich flames (cf. the curves and symbols shown in Figure 2.7). It is worth stressing, however, that (i) alternative chemical mechanisms tested in Ref. [68] did not perform better than the semi-detailed mechanism even when applied to individual gasoline components (either *n*-heptane, or *iso*-octane, or toluene), but (ii) a larger chemical mechanism (304 species and 2234 reactions) tested in Ref. [69] under-predicts the S_L values obtained from rich flames. We are not aware of any chemical mechanism that is demonstrably capable of predicting the laminar flame speeds of rich gasoline-air mixtures at the elevated pressures and temperatures associated with combustion in SI engines and this issue should be borne in mind when invoking an approximation for S_L in order to simulate combustion in a SI engine. There is an urgent need for reliable experimental data obtained at the elevated temperatures and pressures associated with combustion in a SI engine in order to further access various available chemical mechanisms.

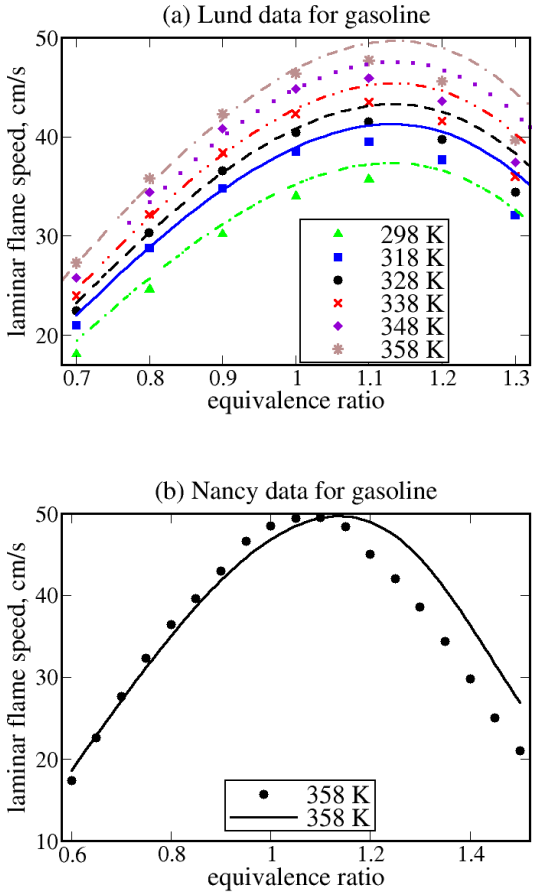

Figure 2.7: *Comparison of laminar flame speeds computed using the Chalmers chemical mechanism (lines) to recent experimental data (symbols) reported by (a) Sileghem et al. [68] and (b) Dirrenberger et al. [69].*

2.3.2. Parameterizations of laminar flame speed, burned temperature and density

To evaluate the laminar flame speeds under conditions associated with combustion in a DI SI engine, numerical simulations of stationary, planar, one-dimensional, laminar premixed flames were performed using the PREMIX code [56] from the Chemkin-II package [57] with the Chalmers semi-detailed chemical mechanism for a gasoline surrogate [67][19], i.e. a blend of *iso*-octane, toluene, and *n*-heptane in a volumetric ratio of 55%:35%:10%, respectively. The mechanism involves 120 species and 677 reactions.

The simulations were conducted under engine-like conditions, i.e. at pressures of 1 to 30 bar, temperatures of 298 to 800 K, and equivalence ratios of 0.2 to 2.0. Calculations were performed for a total of 4009 sets of conditions. Certain informative results are shown by the solid lines in Figure 2.8. The calculated values of S_L were fitted (see dashed lines) using the following expression

$$S_L = S_{L,0}\alpha\left[\left(\frac{T_u}{T_0}\right)^{\beta} + \gamma\right]\left[\left(\frac{p}{p_0}\right)^{\delta} + \varepsilon\right] \tag{2.1}$$

where $T_0 = 298$ K and $p_0 = 1$ atm are the reference temperature and pressure, $S_{L,0} = 0.37$ m/s is the laminar flame speed under the reference conditions, α, β, γ, δ, ε are sixth-order polynomials of the equivalence ratio φ, e.g.

$$\alpha(\varphi) = \alpha_n\varphi^n + \alpha_{n-1}\varphi^{n-1} + \cdots + \alpha_1\varphi + \alpha_0 \tag{2.2}$$

where $n = 6$, etc. The coefficients of these polynomials are reported in Table 2.2. A comparison of the laminar flame speeds computed by running PREMIX to the values of S_L given by Equations (2.1) and (2.2) yielded a mean error of 5%.

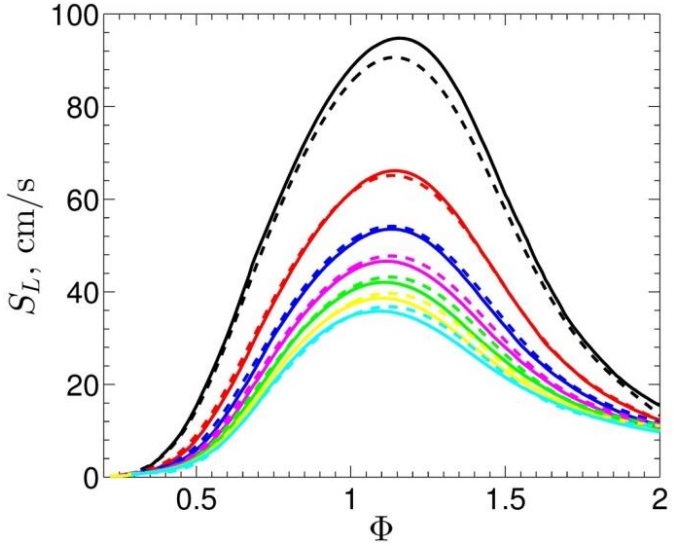

Figure 2.8: *Comparison of calculated (solid lines) and approximated (dashed lines) laminar flame speed at different pressures. Black lines: p=1 atm, red lines: p=5 atm, blue lines: p=10 atm, magenta lines: p=15 atm, green lines: p=20 atm, yellow lines: p=25 atm, cyan lines: p=30 atm. T_u=500 K.*

Table 2.2: *Coefficients for approximating α, β, γ, δ, ε*

k	0	1	2	3	4	5	6
α_k	3.16E+01	-3.25E+02	9.32E+02	-3.73E+02	-2.90E+02	2.09E+02	-3.38E+01
β_k	8.00E+00	-1.59E+01	2.36E+01	-2.75E+01	2.20E+01	-9.09E+00	1.46E+00
γ_k	-3.13E+01	1.61E+02	-3.19E+02	3.18E+02	-1.66E+02	4.16E+01	-3.63E+00
δ_k	8.84E-04	-5.54E-03	1.17E-02	-1.62E-02	1.28E-02	-5.05E-03	7.65E-04
ε_k	-9.97E-01	-2.06E-02	5.15E-02	-3.68E-02	1.88E-04	7.84E-03	-1.98E-03

Figure 2.9 shows the variation of the coefficients α, β, γ, δ and ε with the equivalence ratio when they are calculated using Equation (2.2) and constants in Table 2.2. The curves for coefficients α, β, δ and ε are parabolas whereas that for γ is flat except under very lean or rich conditions. It should be noted that Equation (2.1) differs slightly from the formula used by Metghalchi and Keck [65] due to the introduction of the coefficients γ and ε, whose purpose is to increase the accuracy of the approximations given by Equation (2.1).

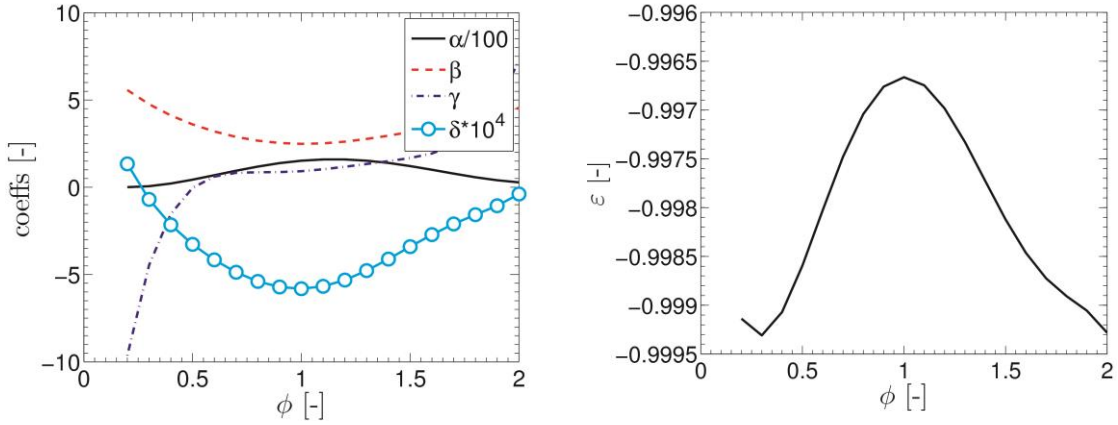

(a) α, β, γ, δ (b) ε

Figure 2.9: *Variation of the coefficients $\alpha, \beta, \gamma, \delta,$ and ε with the equivalence ratio.*

The combustion temperature T_b was approximated as a function of the product enthalpy, pressure and mixture composition. The use of the product enthalpy makes it possible to account for the influence of wall heat losses on T_b. The product enthalpy was computed using a method implemented in the original version of OpenFOAM®, which invokes the BML approach, a balance equation for the enthalpy that is conditioned on data for unburned gas, and a balance equation for the Favre-averaged enthalpy.

The equilibrium calculations were conducted under engine-like conditions, i.e. pressures of 1 to 50 bar, an enthalpy of -1800 to 1000 kJ/mol (fuel), and equivalence ratios of 0.2 to 4.0. Calculations were performed for 66 842 sets of conditions in total; illustrative results are shown in Figure 2.10. The calculated equilibrium combustion temperatures, T_b, were fitted (see lines) using the following expression

$$\begin{aligned} T_b = {} & [(\zeta_{16}p + \zeta_{06})\varphi^6 + (\zeta_{15}p + \zeta_{05})\varphi^5 + \cdots + (\zeta_{10}p + \zeta_{00})]h_b^2 \\ & + [(\eta_{16}p + \eta_{06})\varphi^6 + (\eta_{15}p + \eta_{05})\varphi^5 + \cdots \\ & + (\eta_{10}p + \eta_{00})]h_b \\ & + [(\theta_{16}p + \theta_{06})\varphi^6 + (\theta_{15}p + \theta_{05})\varphi^5 + \cdots \\ & + (\theta_{10}p + \theta_{00})] \end{aligned} \qquad (2.3)$$

where, ζ, η and θ are constants whose values are listed in Table 2.3. The maximum error in the values of T_b given by Equation (2.3) relative to combustion temperatures computed using Chemkin-II was 6.5%.

Table 2.3: *Coefficients for approximating ζ, η, θ*

k	0	1	2	3	4	5	6
ζ_{0k}	-1.76E-04	1.64E-03	-5.30E-03	8.22E-03	-6.78E-03	2.84E-03	-4.73E-04
η_{1k}	7.95E-07	-6.75E-06	2.04E-05	-2.93E-05	2.25E-05	-8.74E-06	1.35E-06
θ_{0k}	1.42E-01	-1.53E+00	9.23E+00	-1.81E+01	1.65E+01	-6.99E+00	1.12E+00
β_{1k}	-2.49E-03	2.59E-02	-9.87E-02	1.73E-01	-1.47E-01	5.90E-02	-9.02E-03
γ_{0k}	3.45E+02	3.73E+03	-7.64E+03	1.72E+04	-1.83E+04	8.43E+03	-1.40E+03
γ_{1k}	-2.93E+00	3.01E+01	-1.13E+02	1.98E+02	-1.69E+02	6.93E+01	-1.08E+01

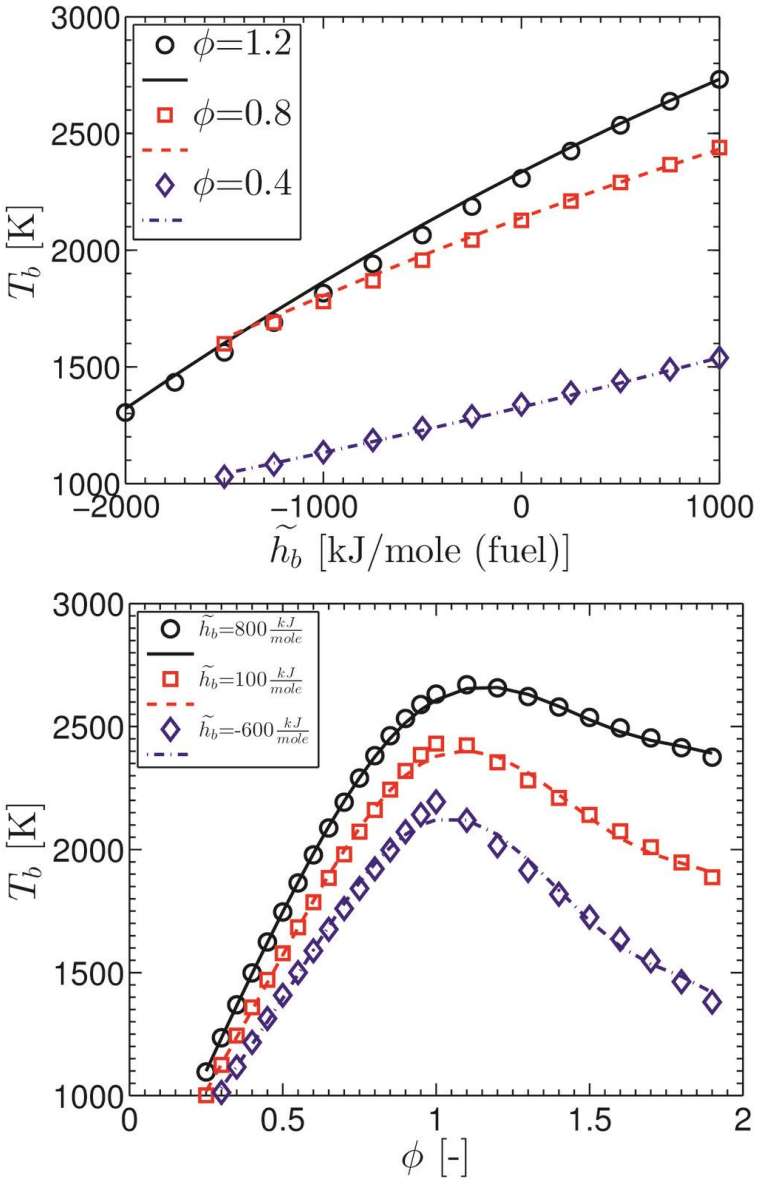

Figure 2.10: *Comparison of calculated (symbols) and approximated (lines) adiabatic flame temperatures at p=15 bar.*

2.4. Conclusion

A semi-detailed (120 species, 677 reactions) chemical mechanism for the combustion of gasoline-ethanol blends in air was developed and validated against experimental data for a gasoline surrogate consisting of *iso*-octane, toluene, and *n*-heptane in a volumetric ratio of 55%:35%:10%, respectively.

Ignition delay times computed for various gasoline surrogates, including ternary mixtures A and B, at various equivalence ratios, initial temperatures, pressures, and EGR dilutions agree reasonably well with the detailed sets of experimental data obtained under engine-like conditions by the Stanford group [50].

The chemical mechanism accurately predicts the laminar flame speeds of gasoline-air mixtures at various equivalence ratios and temperatures, at both atmospheric and elevated pressures.

A correlation for evaluating gasoline laminar flame speeds under engine-like conditions was developed aiming at calculating flame propagation in a SGDI engine by using the aforementioned mechanism.

Chapter 3

Numerical Simulations of Hollow-Cone Sprays

In order to accurately simulate the energy transformation process in the chamber of a DISC SI engine, several phenomena must be modeled, including (i) fuel sprays, (ii) turbulent mixing, (iii) spark ignition, and (iv) turbulent combustion. This chapter describes the results of an investigation into the ability of OpenFOAM® and the spray breakup models it implements to predict the principal properties of hollow-cone sprays discharged by a piezo-actuated outward-opening pintle injector.

This particular problem was primarily chosen because of the availability of detailed experimental data concerning such sprays obtained using Chalmers' spray chamber by my colleagues Stina Hemdal, Jonas Wärnberg, Mats Andersson, and Petter Dahlander. It is also worth noting that the pintle injector is considered to be one of the most promising technological solutions in the field of fuel injection into a gasoline engine. Such injectors (i) are very fast, thus generating a high rate of spray atomization with precise control over the rate and duration of injection, (ii) produce a stable hollow-cone spray that is only weakly sensitive to variations in the in-cylinder temperature and pressure, and (iii) make it possible to minimize wall wetting by tailoring the properties of the injected spray so that it exhibits low penetration, etc. Because the vast majority of numerical simulations of hollow-cone sprays have been performed for swirl injectors, it is of interest to assess the applicability of various spray models that are widely used in the automotive industry to the simulation of sprays discharged by a pintle injector.

The next Section of this chapter discusses the spray models implemented into the standard version of OpenFOAM®. Section 3.2 describes the modifications to the standard version of OpenFOAM® that were made during this project. The test problem, computational mesh, boundary and initial conditions, input parameters, etc. are discussed in Section 3.3. The results of sensitivity studies are reported in Section 3.4, along with comparisons between the results computed using various spray models and experimental data. Finally, the conclusions drawn on the basis of these studies are discussed in Section 3.5.

3.1. Spray models implemented in the standard version of OpenFOAM®

OpenFOAM® uses the discrete Lagrangian method to simulate sprays. A liquid spray is represented by one or a set of different parcels, with each parcel containing a number of physically identical droplets having the same diameter, velocity, pressure, temperature, etc. Each parcel is tracked using the Lagrangian approach, with the droplets from this parcel exchanging momentum and heat with the surrounding gas, being affected by turbulent dispersion, colliding with other droplets, undergoing secondary breakup , evaporating, etc. The simulation of these processes requires the

use of a number of models, including: (i) a model of liquid injection, (ii) a model of primary atomization, (iii) a model of the influence of the gas on droplet motion, (iv) a model of the influence of droplets on turbulent gas flow, (v) a model of droplet collision and coalescence, and (vi) a model of secondary breakup. The work described in this chapter focused exclusively on assessing and comparing various new models of injection, primary droplet atomization, secondary breakup, and collision, that were implemented in OpenFOAM®; the default models for droplet-flow interaction, evaporation, and other processes were used in all the simulations discussed herein.

3.1.1. Simulation of injection and primary atomization

In these studies, the values taken by a number of important parameters were specified on the basis of experimental data. These parameters included the position and the area of the injector nozzle's aperture, the direction of injection (i.e. the injection angle, θ, which was uniformly and randomly distributed between specified inner and outer angles of the hollow-cone spray), the fuel temperature and composition, the total mass of injected fuel (m), and the injection pressure p_{inj}. Three different methods for simulating primary atomization were examined.

Presumed PDF approach

The simplest approach to modelling primary atomization involves seeding a number, N_p, of different parcels at the position of the injector nozzle. The radii of the droplets in the individual parcels are determined using a suitable probability density function (PDF). In OpenFOAM®, the Rosin-Rammler PDF

$$f(D) = \frac{n}{\delta}\left(\frac{D}{\delta}\right)^{n-1} e^{-\left(\frac{D}{\delta}\right)^{n}} \tag{3.1}$$

is implemented for this purpose. The input parameters in this case are the number of parcels (N_p), the factor q, and the droplet radius r_m

Typically, the above PDF is truncated, i.e. the range of allowed droplet radii is restricted ($r_{min} < r < r_{max}$) with r_{max} being controlled by the nozzle length scale) and the right hand side (RHS) of Equation (3.1) is multiplied by a constant

$$C(r_{\min}, r_{\max}) = \left\{ \exp\left[-\left(\frac{r_{\min}}{r_m} \right)^q \right] - \exp\left[-\left(\frac{r_{\max}}{r_m} \right)^q \right] \right\}^{-1} \tag{3.2}$$

in order to normalize the expression:

$$\int_{r_{\min}}^{r_{\max}} C \frac{q r^{q-1}}{r_m^q} \exp\left[-\left(\frac{r}{r_m} \right)^q \right] dr = 1. \tag{3.3}$$

Using this simple model of primary atomization, the absolute value w of the injection velocity can be calculated by first solving the following equations

$$w = \frac{\dot{m}}{C_d \rho_f A_i}, \tag{3.4}$$

$$p_{inj} = p_{air} + \frac{\rho_f w^2}{2}, \tag{3.5}$$

then invoking an estimated mass flow rate $\dot{m}(t)$ that satisfies the mass conservation constraint:

$$m = \int_0^\infty \dot{m}(t)dt, \tag{3.6}$$

and finally tuning the discharge coefficient C_d in Equation (3.4) so that Equation (3.5) holds. Here, A_i is the area of the aperture of the injector nozzle, ρ_f is the density of the injected fuel, and p_a is the pressure of the ambient air.

Wave breakup model

The wave breakup model [70][71] was proposed for the simulation of high-pressure fuel jets in diesel engines and appears to be a more sophisticated approach for simulating primary atomization. Within the framework of the model, only one parcel is seeded just at the nozzle, with the droplet diameter and number being controlled by the nozzle diameter and mass injection rate, respectively. Subsequently, primary atomization is simulated by treating the Kelvin-Helmholtz (KH) instability as the driving force behind the breakup of the parent droplets. This model is also used to simulate the secondary breakup of child droplets, as will be discussed later.

The model is based on the theoretical results obtained by Reitz and Bracco [70]. These workers considered a cylindrical liquid surface over which an inviscid gas flows with a velocity U, and performed a linear analysis of the stability of this surface with respect to infinitesimal wave perturbations of the cylinder's radius. The analysis yielded a complicated dispersion relation between the growth rate ω of the perturbation amplitude and its wavenumber k, with an $\omega(k)$-curve having a single positive maximum. In a subsequent paper, Reitz [71] derived a numerical approximation of these theoretical results and, notably, reported the following curve-fits

$$\Omega_{\mathrm{KH}} = \frac{0.34 + 0.38\mathrm{We}_g^{1.5}}{(1+Z)(1+1.4\mathrm{T}^{0.6})}\sqrt{\frac{\sigma}{\rho_f r^3}}, \tag{3.7}$$

$$\frac{\Lambda_{\mathrm{KH}}}{r} = 9.02\frac{(1+0.45Z^{0.5})(1+0.4\mathrm{T}^{0.7})}{(1.+0.87\mathrm{We}_g^{1.67})^{0.6}} \tag{3.8}$$

for the maximum growth rate ω_{KH} and the corresponding wavelength $\Lambda_{KH} = 2\pi/k_{max}$ as functions of the droplet radius r, the Weber number $We_g = \rho_g U^2 r/\sigma$ calculated for the gas, and the Ohnesorge parameter $Z \equiv \sqrt{We_g}/Re_f$ evaluated for the liquid fuel. Here, ρ is the density, σ is the surface tension coefficient of the fuel, $Re = Ur/\nu$ is the Reynolds number, ν_f is the kinematic viscosity of the fuel, $T = Z\sqrt{We_g}$ is the Taylor number, and the subscripts g and f designate the gas and the liquid fuel, respectively. The fastest growing surface wave was hypothesized to cause liquid atomization and subsequent secondary breakup [71].

In keeping with the recommendations of Reitz and Diwakar [72][73], the simulation of primary atomization in the wave breakup model begins with the injection of spherical droplets whose radius is equal to that of the nozzle aperture, while the number of droplets is calculated based on the fuel mass injection rate $\dot{m}(t)$. The rate at which the droplet radius decreases due to wave breakup is then modeled using the following equation

$$\frac{dr}{dt} = -\frac{r - r_{\mathrm{KH}}}{\tau_{\mathrm{KH}}}, \tag{3.9}$$

where the relaxation time is parameterized as follows

$$\tau_{\mathrm{KH}} = 3.726 B_1 \frac{r}{\Omega_{\mathrm{KH}} \Lambda_{\mathrm{KH}}} \tag{3.10}$$

and the radius of child droplets scales as the wavelength of the fastest growing surface wave, i.e.

$$r_{\mathrm{KH}} = B_0 \Lambda_{\mathrm{KH}} \tag{3.11}$$

if it is smaller than the radius of the parent droplet. If $B_0 \Lambda_{KH} > r$, then Reitz [71] assumed that the volume of a child droplet is equal to $\pi r^2 L$, where $L = min\{\Lambda_{KH}, 2\pi U/\Omega_{KH}\}$, i.e.

$$r_{\mathrm{KH}} = \left[\frac{3r^2 \min\left\{\Lambda_{\mathrm{KH}}, 2\pi U/\Omega_{\mathrm{KH}}\right\}}{4} \right]^{1/3}, \tag{3.12}$$

In most of the studies using this model, the value of the constant B_0 is taken to be 0.61 [71],[74]-[76]. However, a wide range of different values of B_1 have been examined, ranging from 10 [71][75] to 30 [74] or 40[76]. This large variation in the tuned values of the latter constant is a consequence of the different conditions generated by the different injector nozzles considered in these studies.

Within the framework of the KH model, the radius of a parent droplet decreases continuously with time according to Equation (3.9). Furthermore, a new parcel of spherical child droplets of radius r_{KH} is created when (i) the mass $4\pi N_0 \rho_f (r_0^3 - r^3)$ of the liquid stripped off the parent droplets exceeds 3% of the mass of the parent parcel and (ii) the number of child droplets, evaluated using the mass conservation law, exceeds the number of parent droplets [71]. Here, the subscript 0 denotes the moment at which the parent parcel was created. When the child droplets are created, their initial temperature and velocity in the direction of the parent droplet's velocity vector are set equal to the corresponding characteristics of the parent droplet. Moreover, the child droplets are also given a random velocity vector in the tangential direction [71]. Until the above breakup criteria are satisfied, mass conservation is enforced by increasing the number of droplets in the parent parcel ($Nr^3 = N_0 r_0^3$). Note that if $B_0 \Lambda_{KH} > r$, Reitz [71] proposed (i) to replace "the parent parcel by a new parcel containing drops with size given by" Equation (3.12) and (ii) to allow such a "breakup" only once for each injected parcel.

Patterson and Reitz [75] pointed out that the radius of the parent droplets should also be changed during a breakup event in order to ensure that the average Sauter mean radius (SMR, i.e. $\overline{r^3}/\overline{r^2}$) of the parent and child droplets after the breakup

remains equal to the SMR of the parent droplets before the breakup. Using this constraint and the law of mass conservation, Patterson and Reitz [75] derived the following two equations

$$Nr^2\left(r - r_{\mathrm{KH}}\right) = N_0 r_b^2\left(r_b - r_{\mathrm{KH}}\right), \tag{3.13}$$

$$n = \frac{Nr^3 - N_0 r_b^3}{r_{\mathrm{KH}}^3}, \tag{3.14}$$

for calculating the number n of smaller child droplets with radius r_{KH} and the radius r_b of larger child droplets. Here, the subscript b designates larger droplets formed after the breakup, with the number of larger droplets being equal to the number N_0 of parent droplets before the breakup process.

The wave model features only one tuneable parameter, namely B_1 in Equation (3.10).

OpenFOAM® does not use Equations (3.12)-(3.14). Instead, breakup is allowed only if $B_0\Lambda_{KH} < r$; the second of the aforementioned breakup criteria, i.e. $n \geq N_0$, is not invoked. The radius of parent droplets is not changed during breakup event, but their number is decreased due to the reduction of the mass of the parent parcel during the breakup event. The standard number n of child droplets is calculated on the basis that mass is conserved. When a child droplet is created, its temperature and velocity vector are set equal to the temperature and velocity vector of the parent droplets. Before the breakup, a decrease in the radius of the parent droplets is simulated by solving Equation (3.9) invoking an implicit scheme, i.e.

$$r = \frac{r^0 + r_{KH}\dfrac{\Delta t}{\tau_{KH}}}{1 + \dfrac{\Delta t}{\tau_{KH}}} \tag{3.15}$$

where r^0 is the droplet radius at the previous time step $t - \Delta t$.

For unknown reasons, the wave breakup model implemented in OpenFOAM® calculates the mass stripped off a parent droplet as being equal to $4\pi\rho_f r_{KH}^3/3$ during each time step, with the restriction that this stripped mass cannot exceed half the mass of the parent droplet.

In the present work, Equations (3.4)-(3.6) were used to evaluate the injection velocity in the wave model.

The LISA Model

The Linearized Instability Sheet Atomization (LISA) model was developed by Reitz et al. [77][78], on the basis of earlier work by Dombrowski and Johns [79] and Clark and Dombrowski [80]. Like the wave breakup model discussed above, it focuses on the growth of perturbations on a liquid surface due to the KH instability as the driving force of primary atomization, and associates the breakup with the fastest growing surface waves. However, unlike the wave model, which considers a cylindrical liquid volume, the LISA model deals with the instability of a planar liquid sheet of thickness $2h$, because the latter problem was hypothesized to be more relevant to the atomization of a hollow-cone spray produced by a pressure-swirl injector. Therefore, the wave and LISA models are based on the same physical mechanism (the KH

instability), manifesting itself in two different geometrical configurations - a liquid jet and a hollow-cone spray, respectively.

Senecal et al. [77] examined a liquid sheet, over which a viscid gas is flowing with a velocity U. A linear analysis of the stability of the sheet with respect to infinitesimal wave perturbations of the surface height yielded complicated dispersion relations between the growth rate ω of perturbation amplitude and its wavenumber k for two unstable modes, one sinuous and the other various. In the former case, the waves at the upper and lower liquid-gas interfaces are exactly in phase and the sheet thickness is constant; in the latter, the thickness oscillates because the maximum height of the upper interface corresponds to the minimum height of the lower interface and vice versa. Numerical investigation of simplified dispersion relations obtained by examining these general relations in the limiting case of an inviscid gas showed that each $\omega(k)$-curve has a single peak, with the maximum growth rate of the sinuous mode being greater (when the calculated Weber number $We_g = \rho_g U^2 r/\sigma$ of the gas is low) or equal (when We_g is large) to the maximum growth rate of the various mode. On the basis of this observation, the LISA model focuses exclusively on the sinuous mode.

Subsequently, Senecal et al. [77] analyzed the dispersion relation for the sinuous mode (again in the inviscid-gas limit) in cases involving, long ($kh \ll 1$) and short ($kh \gg 1$) waves. The numerical results reported in the cited paper indicate that the simplified dispersion relation obtained for long (short) waves provides a reasonably approximation of the more rigorous dispersion relation (valid for all kh, but ν_g=0) in the case of a low (large) We_g. Furthermore, the theoretical expressions derived for the limiting case of ν_g=0 and $\rho_g \ll \rho_f$ show that (i) the ratio of the growth rates of the short and long waves scales as $\sqrt{kh}$, i.e. the short waves grow faster than the long waves if $kh > 1$, and (ii) the maximum growth rates for the long and short waves are equal to one another if We_g=27/16.

Finally, numerical investigation of the general (ν_g>0, arbitrary kh) dispersion relation indicated that the simplification of ν_g=0 was justified for the long waves, whereas the growth of the short waves was substantially affected by the gas viscosity.

On the basis of the above theoretical results, the following model for sheet breakup was proposed.

First, the breakup occurs when the amplitude of the fastest growing wave reaches a critical value η_b.

Second, if $We_g > 27/16$, the fastest growth rate is calculated using the following dispersion relation

$$\omega = -2\nu_g k^2 + \sqrt{4\nu_g^2 k^4 + QU^2 k^2 - \frac{\sigma k^3}{\rho_f}} \tag{3.16}$$

derived for the short waves. Here, $Q = \rho_g/\rho_f$. Because ω does not depend on the sheet thickness, the growth of the perturbation amplitude is modeled as follows

$$\eta(t) = \eta_0 \exp(\Omega_s t) \tag{3.17}$$

in the linear limit. Here, Ω_s is the maximum growth rate for the short waves, calculated using Equation (3.16). Consequently, the breakup time and length scales are equal to

$$\tau_s = \frac{1}{\Omega_s} \ln\left(\frac{\eta_b}{\eta_0}\right) \tag{3.18}$$

and

$$L_s = \frac{V}{\Omega_s} \ln\left(\frac{\eta_b}{\eta_0}\right), \tag{3.19}$$

respectively, with $ln(\eta_b/\eta_0)$ being assumed to be equal to 12 [77][78]. Here, V is the magnitude of the velocity of the liquid sheet, while U is the magnitude of the velocity of the sheet with respect to the surrounding gas. Schmidt et al. [78] pointed out that, $V \approx U$, because the sheet velocity is much higher than the gas velocity in the vicinity of a hollow-cone injector.

If $We_g < 27/16$, the fastest growth rate is calculated from the following dispersion relation

$$\omega = \sqrt{\frac{QU^2k}{h} - \frac{\sigma k^2}{\rho_f h}} \tag{3.20}$$

derived for the long waves and inviscid gas. The maximum growth rate

$$\Omega_l = \frac{\rho_g U}{2\sqrt{\rho_f \sigma h}} \tag{3.21}$$

is reached for

$$K_l = \frac{\rho_g U^2}{2\sigma}. \tag{3.22}$$

Because the maximum growth rate of long waves depends on the sheet thickness, which decreases with the distance X between the sheet and the nozzle due to mass conservation ($Rh = R_0 h_0$), where $R = R_0 + cos\theta$, and θ is the cone angle), Equation (3.17) should be replaced with the following equation

$$\ln\left(\frac{\eta_b}{\eta_0}\right) = \int_0^t \Omega_l d\vartheta \tag{3.23}$$

for the long waves. Senecal et al. [77] assumed that $h = J/t$, where J is a dimensional constant (if $X = Vt \gg R_0$, then $J = R_0 h_0 / V\, cos\theta$). In this case, Equations (3.21) and (3.23) yield

$$L_l = V\tau_l = V\left[3\ln\left(\frac{\eta_b}{\eta_0}\right)\right]^{2/3}\left(\frac{\rho_f \sigma J}{\rho_g^2 U^4}\right)^{1/3}. \tag{3.24}$$

Third, as soon as the distance X moved by the liquid sheet exceeds either L_s (if $We_g > 27/16$) or L_l (if $We_g < 27/16$), the sheet breaks up and forms ligaments (elongated cylindrical volumes whose axis of symmetry is perpendicular to the direction of the motion of the sheet). The diameter d_L of the ligaments is calculated on

the assumption that mass is conserved and that ligaments are formed once per short wavelength, but twice per long wavelength. Therefore, if $We_g > 27/16$,

$$d_L = \sqrt{\frac{16h}{K_s}}, \tag{3.25}$$

where K_s is associated with the maximum of an $\omega(k)$-curve calculated using Equation (3.16). If $We_g < 27/16$,

$$d_L = \sqrt{\frac{8h}{K_l}}, \tag{3.26}$$

where K_l is calculated using Equation (3.22). The thickness $2h$ of the liquid sheet in Equations (3.25) and (3.26) can be evaluated as follows

$$\dot{m}_{inj}(t-\tau) = 4\pi\rho_f RhU, \tag{3.27}$$

where $\dot{m}_{inj}(t-\tau)$ is the fuel mass flow injected $\tau = X/V$ seconds before the breakup.

Fourth, following Dombrowski and Johns [79], Reitz et al. [77][78] assumed that the breakup of the ligaments is controlled by the instability of a cylindrical, viscous liquid column in a quiescent gas (note that the flow velocity along the ligaments is low, because they are oriented transversely to the direction of the sheet motion), and that ligament breakup occurs when the amplitude of the fastest growing wave is equal to the radius of the ligament. Accordingly, the child droplet radius is calculated from a mass balance

$$r^3 = \frac{3\pi d_L^2}{8K_W}, \tag{3.28}$$

where the wavenumber

$$K_W d_L = \left(\frac{1}{2} + \frac{3\rho_f \nu_f}{2\sqrt{\rho_f \sigma d_L}}\right)^{-1/2} \tag{3.29}$$

of the fastest growing wave is calculated by invoking the classical solution proposed by Weber [81].

Fourth, the time scale of the ligament breakup is assumed to be much shorter than the time scale of the sheet breakup; in modelling applications, it is assumed that spherical droplets are formed directly from the liquid sheet, and no attempt is made to simulate the ligaments.

Fifth, during the breakup event, the radius of the child droplets is randomly selected using a Rosin-Rammler distribution, with either the mean radius [77] or the SMD [78] being evaluated using Equation (3.28).

Sixth, models of the interaction between the liquid sheet and the gas, collisions, and secondary breakup are switched off in simulations until the breakup event [78].

Finally, Reitz et al. [77][78] proposed the use of the following equations

$$w = k_w \sqrt{\frac{2(p_{inj} - p_a)}{\rho_f}}, \tag{3.30}$$

$$k_w = \min\left\{1, \max\left[0.7, \frac{\dot{m}}{\rho_f A_i \cos\theta}\sqrt{\frac{\rho_f}{2\left(p_{inj} - p_a\right)}}\right]\right\} \tag{3.31}$$

for evaluating the injection velocity for a liquid sheet.

The LISA model was successfully used (in conjunction with the so-called TAB model of secondary breakup, which is discussed later in this thesis) by Reitz et al. [77][78] to simulate the penetration length and SMD for hollow-cone sprays injected at pressures ranging from 4.76 to 10 MPa. Chryssakis et al. [82] and Gao et al. [83] also used the LISA-TAB model to predict penetration length and SMD for gasoline hollow-cone sprays discharged by different swirl injectors at 5 MPa. Park et al. [84] used the LISA-TAB model to predict SMD for gasoline and bioethanol sprays discharged by a swirl injectors at 7 MPa.

In order to allow for the damping effect of a denser gas on the growth of surface waves and the influence of superheating of fuel droplets on their breakup, OpenFOAM® incorporates an empirical extension of Equation (3.28) [85]

$$r^3 = \frac{3\pi d_L^2}{8K_W}\left(\frac{p}{p_{atm}}\right)^{0.27}\left[1 - \chi\left(\frac{p}{p_{atm}}\right)^{-0.135}\right] \tag{3.32}$$

of the kind proposed by Zuo et al. [86] Here, p_{atm} is the atmospheric pressure,

$$\chi = \frac{I\left(T_f\right) - I\left(T_b\right)}{L\left(T_b\right)} \tag{3.33}$$

is the superheat parameter, I and L are the internal energy of the liquid particle and the latent heat of the liquid, respectively, and T_b is the local boiling temperature.

Lucchini et al. [85] used OpenFOAM® to predict the penetration length and SMD for four different hollow-cone sprays discharged by swirl injectors under injection pressures ranging from 4.76 to 7MPa. In these simulations, the LISA model of primary breakup was combined with the so-called Reitz-KHRT model of the secondary breakup, which will be discussed later.

3.1.2. Secondary breakup models

Secondary breakup models are designed to simulate the formation of smaller droplets in the downstream of a spray. This process is mainly caused by aerodynamic forces acting on droplets from the surrounding gas. This section discusses three secondary breakup models that are implemented in OpenFOAM®, namely the Reitz-Diwakar, Taylor Analogy Breakup (TAB), and Kelvin-Helmholtz, Rayleigh-Taylor (KHRT) models.

The Reitz-Diwakar model

Reitz and Diwakar [73] reduced the problem of secondary breakup to a process involving a continuous decrease in droplet radii, simulated using the following equation

$$\frac{dr}{dt} = -\frac{r - r_{\mathrm{RD}}}{\tau_{\mathrm{RD}}}, \tag{3.34}$$

closed by invoking the following empirical correlations [72]

$$\tau_{\mathrm{RD}} = B_{\mathrm{RD}} \frac{r}{U} \sqrt{\frac{\rho_f}{\rho_g}}, \tag{3.35}$$

$$r_{\mathrm{RD}} = \frac{\sigma^2}{2\rho_g U^3 \nu_g} \tag{3.36}$$

if $We_g > 0.5\sqrt{Re_g}$, while

$$\tau_{\mathrm{RD}} = \pi \sqrt{\frac{\rho_f r^3}{2\sigma}}, \tag{3.37}$$

$$r_{\mathrm{RD}} = \frac{6\sigma}{\rho_g U^2} \tag{3.38}$$

if $6 < We_g < 0.5\sqrt{Re_g}$. The droplet radius is assumed to be constant if $We_g < 6$. Here, $We_g = \rho_g U^2 r/\sigma$ and $Re_g = Ur/\nu_g$ are the Weber and Reynolds numbers, respectively, both of which are calculated for the gas. ρ is the density and σ is the surface tension coefficient of the fuel, ν is the kinematic viscosity, U is the magnitude of the gas velocity vector with respect to the droplet, and the subscripts g and f designate the gas and liquid fuel, respectively. The default value of the constant B_{RD} is 20 [72].The number N of smaller droplets is calculated by assuming that the mass of the droplets in the parcel is conserved, i.e. $Nr^3 = N_0 r_0^3$.

It is worth noting that the scaling given by Equations (3.35) and (3.37) is similar to that predicted by the KH model for breakup time [71]. Indeed, in the inviscid limit, we have Z=0, T=0, while Equations (3.7) and (3.8) give $\Lambda_{KH} \to 9.02$ and $\Omega_{KH}\sqrt{\rho_f r^3/\sigma} \to 0.34$ if $We_g \to 0$, while $\Lambda_{KH} \to 9.806/We_g$ and $\Omega_{KH}\sqrt{\rho_f r^3/\sigma} \to 0.38We_g^{1.5}$ if $We_g \to \infty$. Consequently, Equation (3.10) yields

$$\tau_{\mathrm{KH}} = 1.72 B_1 \sqrt{\frac{\rho_f r^3}{2\sigma}} \tag{3.39}$$

if $We_g \to \infty$ and

$$\tau_{\mathrm{KH}} = B_1 \sqrt{\frac{\rho_f}{\rho_g}} \frac{r}{U} \tag{3.40}$$

if $We_g \to \infty$. Equation (3.39) reduces to Equation (3.37) if $1.72B_1 = \pi$, while Equation (3.40) reduces to Equation (3.37) if $B_1 = B_{RD}$. Furthermore, if Z0, T=0, and $We_g \to \infty$, Equation (3.11) results in $We_g = 6$, again in line with the Reitz-Diwakar model.

In OpenFOAM®, Equation (3.34) is solved using an implicit scheme, i. e.

$$r = \frac{r^0 + r_{KH}\frac{\Delta t}{\tau_{RD}}}{1 + \frac{\Delta t}{\tau_{RD}}} \tag{3.41}$$

where r^0 is the droplet radius at the previous time step $t - \Delta t$.

The TAB model

The TAB model developed by O'Rourke and Amsden [87] treats breakup as a consequence of oscillations in the shape of a droplet, caused by aerodynamic forces. While the equilibrium shape of the droplet surface is spherical, it becomes ellipsoidal and oscillates under the influence of aerodynamic forces and surface tension. The model considers the oscillation of the normalized coordinate $y = \frac{x}{2r}$ of the point at the droplet surface that that is furthest upstream. This is the west pole of the droplet surface, provided that the gas velocity with respect to the droplet is directed along the x-direction and is positive. Breakup is postulated to occur if $|y| = 1$.

O'Rourke and Amsden [87] modelled these oscillations by invoking the following equation

$$\frac{d^2y}{dt^2} = 2C_F\frac{\rho_g U^2}{\rho_f r^2} - \frac{C_k\sigma}{\rho_f r^3}y - \frac{C_d\nu_f}{r^2}\frac{dy}{dt}, \tag{3.42}$$

in which the three terms on the right hand side (RHS) model, respectively, (i) aerodynamic forces, which act to increase y and cause the oscillations, (ii) surface tension, which counteracts the aerodynamic forces and acts to restore the spherical shape of the drop surface, and (iii) viscous forces, which damp the oscillations. In the case of negligible viscous forces, Equation (3.42) is mathematically similar to the well-known equation $\ddot{x} = F - kx$, which describes the well-known harmonic oscillator. This analogy between the pulsating droplet and the harmonic oscillator was suggested by Taylor; O'Rourke and Amsden [87] consequently named their model the Taylor Analogy Breakup (TAB) model.

Equation(3.42) involves three constants, C_F, C_k, and C_d. Two of them, C_k=8 and C_d=5 were determined by O'Rourke and Amsden [87] by comparing their model's output to known theoretical solutions. The third constant, C_F=1/3, was evaluated by comparison with experimental data, which showed that a break could occur if $We_g > 6$. Note that the same empirical criterion is invoked in the Reitz and Diwakar [72][73] model.

If the relative velocity U of the droplet with respect to the gas is assumed to be constant, the solution to Equation(3.42) is as follows

$$y(t) = \frac{\mathrm{We}_g}{12} + \left\{\left(y_0 - \frac{\mathrm{We}_g}{12}\right)\cos\omega t + \frac{1}{\omega}\left[\dot{y}_0 + \frac{1}{t_d}\left(y_0 - \frac{\mathrm{We}_g}{12}\right)\right]\sin\omega t\right\}\exp\left(-\frac{t}{t_d}\right), \tag{3.43}$$

where $y_0 \equiv y(0)$, $\dot{y}_0 \equiv dy/dt(0)$,

$$\frac{1}{t_d} = \frac{5}{2}\frac{\nu_f}{r^2}, \tag{3.44}$$

$$\omega^2 = \frac{8\sigma}{\rho_f r^3} - \frac{1}{t_d^2}, \tag{3.45}$$

and the above values of the model constants are used.

Note that in contrast to the unstable waves of increasing amplitude addressed by the Reitz-KHRT and LISA models, the TAB model deals with oscillations that decay due to viscous forces, simulated by the last exponential term on the RHS of Equation (3.43). Nevertheless, certain scalings predicted by the TAB model resemble those associated with the KH model. For instance, if viscous forces are neglected and $y_0 = \dot{y}_0 = 0$, then Equation (3.43) becomes

$$y(t) = \frac{\mathrm{We}_g}{12}(1 - \cos \omega t). \tag{3.46}$$

At the instant breakup occurs, which is characterized by y=1, Equation (3.46) becomes

$$1 = \frac{\mathrm{We}_g}{24}(\omega t_b)^2 \tag{3.47}$$

if $We_g \gg 1$. Subsequently, Equation (3.45) and (3.47) result in

$$t_b = \sqrt{3}\sqrt{\frac{\rho_f}{\rho_g}}\frac{r}{U}, \tag{3.48}$$

which is basically similar to Equation (3.37) and (3.39), but involves a significantly smaller constant. If $We_g \approx 6$, Equation (3.46) will predict a breakup only if $\omega t \approx \pi$. Consequently, using Equation (3.45), we have

$$t_b = \frac{\pi}{\omega} = \pi\sqrt{\frac{\rho_f r^3}{8\sigma}}, \tag{3.49}$$

which is basically similar to Equations (3.37) and (3.39), but involves a smaller constant.

O'Rourke and Amsden [87] proposed that the normalized coordinate $y(t_n + 1)$ at $(n + 1)$-th time step could be calculated using Equation (3.43), with $y_0 = y_n \equiv y(t_n)$ and $\dot{y}_0 = \dot{y}_n \equiv dy/dt(t_{n+1})$. If the amplitude

$$A^2 = \left(y_n - \frac{\mathrm{We}_g}{12}\right)^2 + \left(\frac{\dot{y}_n}{\omega}\right)^2 \tag{3.50}$$

of an undamped oscillation (i.e. $t_d \to \infty$ in Equation (3.43)) is low, i.e.

$$\frac{\mathrm{We}_g}{12} + A \le 1, \tag{3.51}$$

then breakup cannot occur during time interval $\Delta t = t_{n+1} - t_n$ and the next time step (t_{n+2}) is considered, with y_{n+1} and $\dot{y}_{n+1}$ being calculated using Equation (3.43).

If Equation (3.51) does not hold, then the following equation

$$1 = \frac{\mathrm{We}_g}{12} + A\cos\left[\omega\left(t - t_n\right) + \phi\right], \tag{3.52}$$

which results from Equation (3.43) provided that $t_d \to \infty$ and y=1, is solved to evaluate the smallest root t_{bu} greater than t_n. Here,

$$\cos\phi = \frac{1}{A}\left(y_n - \frac{\mathrm{We}_g}{12}\right) \tag{3.53}$$

and

$$\sin\phi = -\frac{\dot{y}_n}{A\omega}. \tag{3.54}$$

If $t_{bu} > t_{n+1}$, then breakup cannot occur during time interval $\Delta t = t_{n+1} - t_n$ and the next time step (t_{n+2}) is considered, with y_{n+1} and $\dot{y}_{n+1}$ being calculated using Equation (3.43). If $t_{bu} < t_{n+1}$, then the droplet breaks up and the radius of the child droplet is randomly generated using the following distribution of the droplet mass

$$g(r) = \frac{r^3}{6r_m^4}\exp\left(-\frac{r}{r_m}\right) \tag{3.55}$$

with the Sauter mean radius r_{32}

$$\frac{r}{r_{32}} = 1 + \frac{8K}{20} + \left(\frac{6K-5}{120}\right)\frac{\rho_f r^3}{\sigma}\dot{y}\left(t_{bu}\right) \tag{3.56}$$

being determined using the energy balance [87] and $r_m = r_{32}/6 = \bar{r}/4$. Here, K=10/3 is a constant and r_n is the radius of the parent droplet at time step t_n.

The number of child droplets

$$N_{n+1} = N_n\left(\frac{r_n}{r_{n+1}}\right)^3 \tag{3.57}$$

is calculated by assuming conservation of mass.

Finally, child droplets are assumed to acquire a velocity normal to the path of the parent drop during the breakup event. O'Rourke and Amsden [87] assumed that this normal velocity is equal to $\dot{x}(t_{bu}) = 0.5r\dot{y}(t_{bu})$, which is calculated at the moment of breakup t_{bu} using Equation (3.43).

As mentioned above, the TAB model for secondary breakup has been successfully used in conjunction with the LISA model of primary atomization by several research groups interested in simulating the penetration length and/or SMD of hollow-cone sprays injected at pressures ranging from 4.76 to 10MPa [77][78][82][83]. In some of these papers, following a proposal by Han et al. [88], the χ-squared distribution given by Equation (3.55) was replaced with the Rosin-Rammler distribution

$$f(r) = \frac{qr^{q-1}}{r_m^q}\exp\left[-\left(\frac{r}{r_m}\right)^q\right] \tag{3.58}$$

For a PDF given by Equation (3.58), we have

$$r_{32} \equiv \frac{\overline{r^3}}{\overline{r^2}} = \frac{3}{2}\frac{\Gamma(3/q)}{\Gamma(2/q)} r_m = \frac{3}{2}\frac{q\Gamma(3/q)}{\Gamma(1/q)\Gamma(2/q)}\bar{r}, \tag{3.59}$$

where Γ is the gamma function. For instance, if q=2, then $r_{32} = 0.75\sqrt{\pi}\bar{r}$. Note that the mean radius is equal to $q^{-1}\Gamma(q^{-1})r_m$.

The Rosin-Rammler distribution is supposedly used in OpenFOAM®.

The Reitz-KHRT model

The Reitz-KHRT model treats droplet breakup as a consequence of the growth of two instabilities: the KH instability addressed by the wave model, which has already been already discussed, and the Rayleigh-Taylor (RT) instability that develops on the droplet surface under the influence of the flow acceleration. The two instabilities are assumed to be independent of and to compete with one another. Conceptually, the submodels of the two instabilities are similar, i.e. breakup is associated with the fastest growing perturbation and the child droplet radius is associated with the wavelength of that perturbation. Because the KH submodel is identical to the wave model already discussed above, the remainder of this section focuses exclusively on the RT submodel [74]-[76], which is based on the theoretical results of a linear analysis of the evolution of an infinitesimally small perturbation on a planar interface between two viscous incompressible fluids of infinite depth, with the fluids being accelerated in a direction perpendicular to the interface [89].

For the limiting where the fluids' viscosities are negligible, Bellman and Pennington [89] derived the following equations for the wavenumber

$$K = \sqrt{\frac{-a(\rho_f - \rho_g)}{3\sigma}} \tag{3.60}$$

and growth rate

$$\Omega_{\mathrm{RT}} = \sqrt{\frac{2}{3\sqrt{3\sigma}}\frac{\left[-a(\rho_f - \rho_g)\right]^{3/2}}{\rho_f + \rho_g}} \tag{3.61}$$

of the most unstable perturbation. Here, a is the acceleration directed from a less dense to a more dense fluid. For the interface to be unstable, this acceleration should be negative (point to the less dense fluid).

Patterson and Reitz [75] associated the acceleration a with the drag force. For the trailing edge of a droplet, this acceleration is negative, i.e.

$$a = -\frac{3}{8}C_D\frac{\rho_g U^2}{\rho_f r}, \tag{3.62}$$

while a different expression was used by Su et al. [74].

Reitz et al. [74]-[76] hypothesized that the RT instability will grow and cause droplet breakup after a period of time

$$\tau_{\mathrm{RT}} = \frac{C_\tau}{\Omega_{\mathrm{RT}}} \tag{3.63}$$

only if the length of the fastest growing perturbation is smaller than the droplet diameter, i.e.

$$2r > \Lambda_{\mathrm{RT}} = \frac{2\pi C_{\mathrm{RT}}}{K_{\mathrm{RT}}}. \tag{3.64}$$

Different values of the tuning constants C_τ and C_{RT} have been reported in different papers. For diesel spray simulations, Su et al. [74], Patterson and Reitz [75] set C_τ=1 and C_{RT}=5.33. For hollow-cone sprays, Beale and Reitz [76] used C_τ=10 and C_{RT}=0.1.

Different methods have been proposed for simulating the radii of child droplets in diesel and hollow-cone sprays [74]-[76]. In the former case, the radius scales as r_{RT} [74][75], while the Rosin-Rammler distribution with the mean radius being equal to r_{RT} and q=10 was invoked by Beale and Reitz [76] to simulate the penetration and SMD of hollow-cone sprays injected under pressures from 3.4 to 6.12 MPa.

In the latter simulations, the RT model was switched off until the distance travelled by a parcel exceeded a primary breakup length evaluated as follows

$$L_{CD} = B\left(\frac{\rho_f \sigma h \cos\theta}{\rho_g^2 U^2}\right)^{1/2}, \tag{3.65}$$

where B=10.4. Equation (3.65) models the breakup of a liquid sheet under the influence of the fastest growing long surface waves, a phenomenon that is also addressed by the LISA model; it is instructive to compare Equation (3.65) with Equation (3.24) where $J \propto hL_t/U$.

Thus, for a hollow-cone spray, the Reitz-KHRT model involves four tuning constants; B_1 in Equation (3.10), C_τ, C_{RT}, and B.

In OpenFOAM®, following the proposal of Su et al. [74], the number n_c and radius r_c of child droplets are calculated as follows

$$n_c = N\frac{rK_{RT}}{\pi} \tag{3.66}$$

$$n_c r_c^3 = Nr^3 \tag{3.67}$$

The drag coefficient C_D is evaluated for a non-spherical droplet by invoking the following expression [90]

$$C_D = C_{D,sphere}(1 + B_D y) \tag{3.68}$$

where $C_{D,sphere}$ is the drag coefficient for a spherical droplet, B_D is a constant, and the TAB model is invoked to evaluate the normalized deviation y of the droplet's shape from a sphere, i.e. y is calculated using Equation (3.43). Following a proposal by Patterson and Reitz [75], the criteria for RT breakup are checked first and KH breakup is considered only if these criteria are not satisfied.

The VSB2 spray model

The VSB2 spray model, which was implemented in OpenFOAM® by Kösters and Karlsson [91], is a stochastic separate flow (SSF) model in which the Lagrangian equations of drop position, momentum, mass and energy are solved. The main differences between this model and traditional SSF models are that the parcel

containing identical droplets is replaced with an irregular lump of liquid, referred to as a blob, that carries droplets of various sizes, and that all interactions between the blob and its surroundings take place in a bubble that engulfs it rather than across the entire computational cell that the blob currently occupies. The advantages of this spray model are that (i) it has relatively few tuning constants and (ii) it exhibits unconditional robustness. The VSB2 spray model has successfully been used to predict the behavior of diesel sprays under various ambient pressures and injection pressures [91].

3.1.3. Collision models

Two collision models are implemented in OpenFOAM®. These are the classical O'Rourke model [92]-[94], which is widely used in engine spray simulations, and a trajectory model developed recently by [95] that is based on the O'Rourke model.

The O'Rourke model

The O'Rourke collision model [92]-[94] states that the probability of a collision between a larger droplet from parcel i and n_j identical smaller droplets from parcel j is described by a Poisson distribution

$$P_{n_j} = \frac{(\upsilon \Delta t)^{n_j}}{n_j!} \mathrm{e}^{-\upsilon \Delta t} \tag{3.69}$$

provided that the two parcels occupy the same computational cell (otherwise, the collision probability is zero). Here,

$$\upsilon = N_j \frac{\pi (r_i + r_j)^2}{V_{ij}} \left| \mathbf{u}_i - \mathbf{u}_j \right| \tag{3.70}$$

is the collision frequency for a single droplet from the i-th parcel, N_j is the number of droplets in the j-th parcel, V_{ij} is the volume of the cell occupied by both parcels, and $\mathbf{u}_i$ is the velocity vector of the i-th parcel.

Subsequently, if a random number b uniformly distributed between zero and unity is less than

$$b_{cr} = \min\left\{1.0, \frac{2.4}{\mathrm{We}_j}\left[\left(\frac{r_i}{r_j}\right)^3 - 2.4\left(\frac{r_i}{r_j}\right)^2 + 2.7\frac{r_i}{r_j}\right]\right\}, \tag{3.71}$$

the colliding droplets are assumed to coalesce, with the temperature, velocity, and radius of large droplet formed by this coalescence being evaluated as follows

$$\begin{aligned} T &= \frac{T_i r_i^3 + T_j n_j r_j^3}{r_i^3 + n_j r_j^3}, \\ \mathbf{u} &= \frac{\mathbf{u}_i r_i^3 + \mathbf{u}_j n_j r_j^3}{r_i^3 + n_j r_j^3}, \\ r^3 &= r_i^3 + n_j r_j^3. \end{aligned} \tag{3.72}$$

Here, the Weber number

$$We_j = \frac{\rho_f \left|\mathbf{u}_i - \mathbf{u}_j\right| r_j}{\sigma\left(\overline{T}_V\right)} \tag{3.73}$$

is calculated for the j-th (smaller) colliding droplets, with the surface tension being evaluated at the mean volume temperature

$$\overline{T}_V = \frac{T_i r_i^3 + T_j r_j^3}{r_i^3 + r_j^3}. \tag{3.74}$$

If the random number b is larger than b_{cr}, the colliding droplets do not coalesce but exchange momentum with one another, in a so-called grazing collision, i.e.

$$\begin{aligned} \mathbf{u}_k' &= \mathbf{v}_k, \\ \mathbf{u}_l' &= \frac{N_k \mathbf{v}_l + \left(N_l - N_k\right)\mathbf{u}_l}{N_l} \end{aligned} \tag{3.75}$$

after the collision. Here,

$$\begin{aligned} \mathbf{v}_k &= \frac{\mathbf{u}_i r_i^3 + \mathbf{u}_j r_j^3 + \zeta\left(\mathbf{u}_i - \mathbf{u}_j\right) r_j^3}{r_i^3 + r_j^3}, \\ \mathbf{v}_l &= \frac{\mathbf{u}_i r_i^3 + \mathbf{u}_j r_j^3 - \zeta\left(\mathbf{u}_i - \mathbf{u}_j\right) r_i^3}{r_i^3 + r_j^3}, \end{aligned} \tag{3.76}$$

$k = i$ and $l = j$ if $N_i \le N_j$, but $k = j$ and $l = i$ if $N_i > N_j$, and

$$\zeta = \frac{\sqrt{b} - \sqrt{b_{cr}}}{1 - \sqrt{b_{cr}}}. \tag{3.77}$$

Readers seeking a rigorous justification for Equations (3.69)-(3.77) are referred to the Ph.D. thesis of O'Rourke [92].

The trajectory model

Within the framework of the trajectory model [95], droplets from i-th and j-th parcels may collide even if they occupy different cells at a given instant t_n, but (i) are moving towards one another, i.e.

$$U_{ij} \equiv \left[\mathbf{u}_i\left(t_n\right) - \mathbf{u}_j\left(t_n\right)\right] \cdot \frac{\mathbf{x}_j\left(t_n\right) - \mathbf{x}_i\left(t_n\right)}{\left|\mathbf{x}_i\left(t_n\right) - \mathbf{x}_j\left(t_n\right)\right|} > 0, \tag{3.78}$$

and (ii) will pass through the same point during time step Δt, i.e.

$$U_{ij}\Delta t > \left|\mathbf{x}_i\left(t_n\right) - \mathbf{x}_j\left(t_n\right)\right| - \left(r_i + r_j\right). \tag{3.79}$$

If both of these conditions are satisfied, the grid-dependent PDF given by Equations (3.69) and (3.70) is replaced with the following collision probability

$$P = \left(\frac{r_i + r_j}{\max\left\{r_i + r_j, \Delta_{ij}\right\}}\right)^{C_1} \exp\left(-C_2 \frac{\left|\alpha_m - \beta_m\right|}{\Delta t}\right). \tag{3.80}$$

Here, C_1 and C_2 are model constants, and $\Delta_{ij} = \left|\mathbf{p}_j(\beta_m) - \mathbf{p}_i(\alpha_m)\right|$ is the minimum distance between the trajectories $\mathbf{p}_i = \mathbf{x}_i(t_n) + \alpha\mathbf{u}_i$ and $\mathbf{p}_j = \mathbf{x}_j(t_n) + \beta\mathbf{u}_j$, determined using the following constraint

$$\frac{\partial\left|\mathbf{p}_i - \mathbf{p}_j\right|}{\partial\alpha}(\alpha_m, \beta_m) = \frac{\partial\left|\mathbf{p}_i - \mathbf{p}_j\right|}{\partial\beta}(\alpha_m, \beta_m) = 0. \tag{3.81}$$

Equation (3.81) yields the following two linear equations

$$\begin{aligned} -\alpha_m\mathbf{u}_i\cdot\mathbf{u}_j + \beta_m\mathbf{u}_j\cdot\mathbf{u}_j &= (\mathbf{x}_i - \mathbf{x}_j)\cdot\mathbf{u}_j, \\ \alpha_m\mathbf{u}_i\cdot\mathbf{u}_i - \beta_m\mathbf{u}_i\cdot\mathbf{u}_j &= -(\mathbf{x}_i - \mathbf{x}_j)\cdot\mathbf{u}_i \end{aligned} \tag{3.82}$$

for calculating α_m and β_m.

If a random number q uniformly distributed between zero and unity is less than the collision probability given by Equation (3.80), droplets from the two parcels are considered to collide with one another and O'Rourke's Equations (3.71)-(3.77), with r_i^3 and r_j^3 being replaced by M_i and M_j in OpenFOAM®, are invoked to simulate coalescence and grazing collisions.

3.2. Modifications of spray models implemented in OpenFOAM®

Because the implementation of certain aforementioned spray models into the standard version of OpenFOAM® does not completely follow the original papers, certain modifications of the code have been made. These modifications are discussed in this section. In the following discussion, the spray models implemented in the standard version of OpenFOAM® are referred to as the standard models.

3.2.1. The pintle injector model

The default injector model in OpenFOAM® is a unit injector model, as illustrated in Figure 3.1. The parcels are randomly injected on a circle and the direction of injection is restricted so as to always fall within certain cone angles, i.e. between the inner and outer cone angles. This injector model is not suitable for simulating an outward opening piezo injector. If a parcel is randomly generated at the left edge of the injector, it is equally likely to move in either the southwest or the southeast direction. That means that the air below the injector will be dragged downwards by the parcel if it moves towards southeast. Moreover, the air above the injector will also be dragged downwards due to the continuity equation. This would results in the formation of an unrealistically large velocity field below the injector, as shown in Figure 3.2. The magnitude of the velocity is the largest along the direction of the injection cone angle, while the magnitude of the velocity in the central part of the spray is unrealistically small for pintle injector.

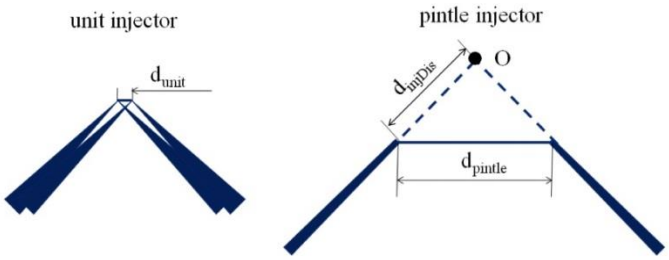

Figure 3.1: *Illustration of the unit and pintle injector models.*

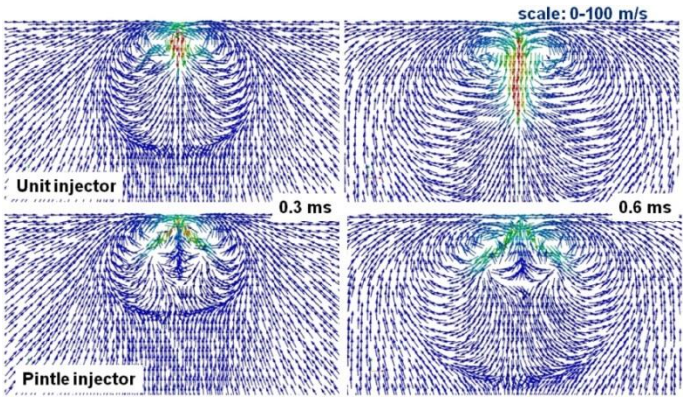

Figure 3.2: *The calculated velocity vector fields of a hollow cone spray of gasoline at 0.3 ms and 0.6 ms after the start of injection. First row: unit injector model; second row: pintle injector model, generated using the Rosin-Rammler distribution (r_m=15 μm, q=2) and the standard Reitz-Diwakar model with a coarse mesh (1x1.6x1.6 mm near the injector) at T_a=350 K, T_f=243 K, p_{inj}=200 bar, p_a=5 bar, d_{inj}=3 mm.*

One way to overcome this problem is to use a pintle injector model of the kind illustrated in Figure 3.1. This injector model is designed to simulated the pintle-type injectors commonly used in GDI engines. In this model, the spray originates at a point O, referred to as the injection origin, and the injection direction is restricted to lie within the cone angles, i.e. between the inner cone angle and the outer cone angle. The real injection position is somewhere on the surface of a ring located at a distance d_{injDis} from the virtual injection origin (point O in Figure 3.1), defined by the intersection of the cone with a plane.

The effect of different injector models on the calculated liquid penetration of gasoline is shown in Figure 3.3. The liquid penetration calculated using the pintle injector model is slightly higher than that predicted using the unit injector model between 0 and 1ms. The liquid penetration calculated using the unit injector model is much higher than that predicted by the pintle injector model between 1 and 4 ms, which indicates that the hollow cone collapses in the former case. The SMD is approximately the same for the both injector models.

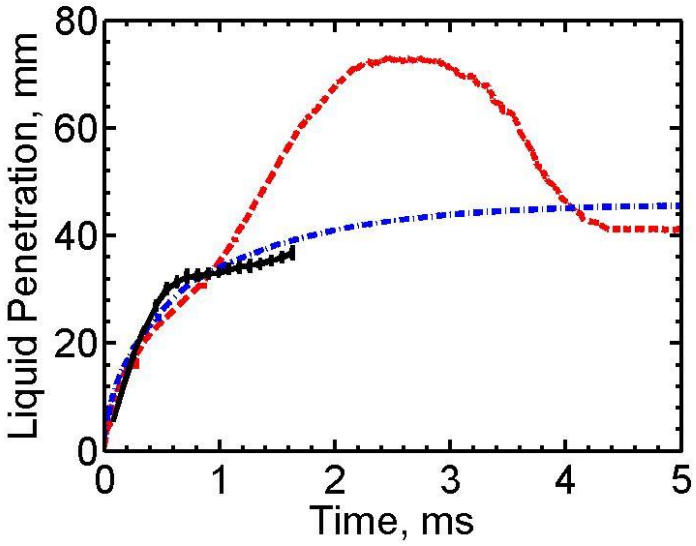

Figure 3.3: *Comparison of the liquid penetration calculated using the unit injector (black solid lines) and pintle injector (red dashed lines) models, using the Rosin-Rammler distribution (r_m=15 μm}, q=2) and the standard Reitz-Diwakar model with a coarse mesh (1.60×1.60×2.73 mm near the injector) at T_a=350 K, T_f=243 K, , p_{inj}=200 bar, p_a=5 bar, d_{inj}=3 mm.*

3.2.2. The coefficient of discharge

The coefficient of discharge, C_d, compares the ratio of the mass flow rate at the exit of the nozzle to that of an ideal nozzle out of which an identical working fluid expands under the same initial conditions and the same exit pressure. The effect of treating C_d as a constant and of varying it was examined, in terms of its influence on liquid penetration and SMD. When C_d is treated as a constant, the injection velocity and the injection pressure depend on the mass injection rate (see Equations (3.4) and (3.5)). If C_d is allowed to vary, for instance if $\frac{C_d(t)}{\dot{m}(t)} = \text{const}$, the injection velocity is constant during the injection. Consequently, under these conditions, the injection pressure also remains unchanged.

Two cases were considered: (i) a pintle injector with a variable C_d (i.e. $\frac{C_d(t)}{\dot{m}(t)} = \text{const}$), and (ii) a pintle injector with a constant C_d. The influence of C_d on liquid penetration is shown in Figure 3.4. When C_d is allowed to vary, both C_d and $\dot{m}(t)$ are very small in the beginning of the injection and the magnitude of the injection velocity is high. On the other hand, when C_d is treated as a constant and $\dot{m}(t)$ is low at the beginning of the injection, the injection velocity is lower. Hence the liquid penetration at the beginning of the injection is lower than in the case where C_d is variable, as shown in Figure 3.4 (a), whereas the liquid penetration in the later period of injection is unaffected by C_d (Figure 3.4 (b)). The SMD is largely independent of the nature of C_d. The flow fields are also more or less unchanged, as can be seen in Figure 3.5.

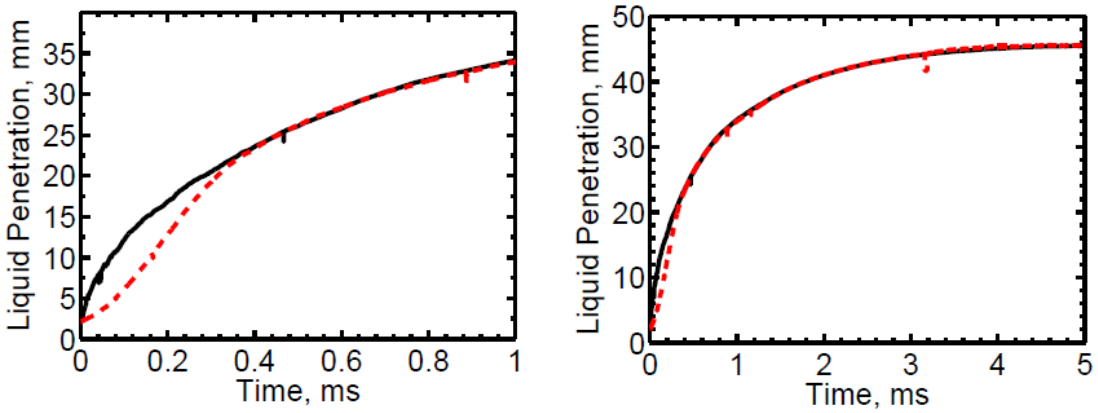

(a)0-1ms (b)0-5ms

Figure 3.4: *Comparison of the liquid penetration calculated using a variable C_d (black solid lines) and a constant C_d (red dashed lines), using a Rosin-Rammler distribution (r_m=15 μm, q=2) and the standard Reitz-Diwakar model with a coarse mesh (1×1.6×1.6 mm near the injector) at T_a=350 K, T_f=243 K, p_{inj}=200 bar, p_a=5 bar, d_{inj}=3 mm.*

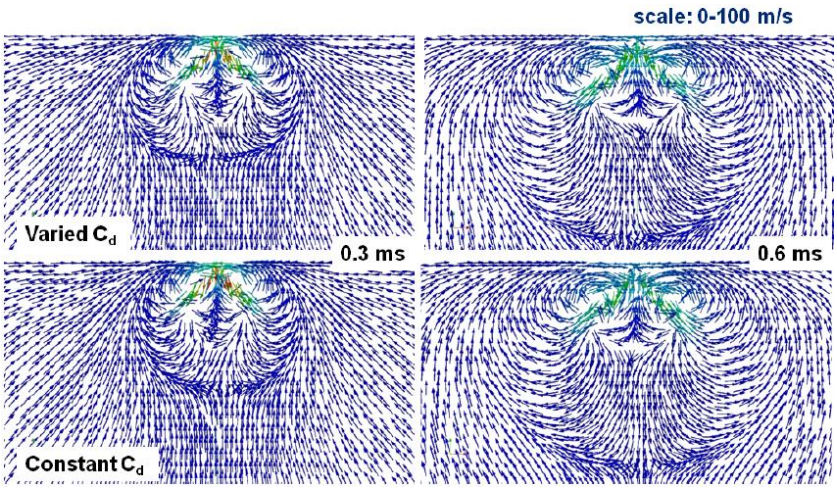

Figure 3.5: *The calculated velocity vector fields of a hollow cone spray of gasoline at 0.3 ms and 0.6 ms after the start of injection. First row: constant C_d; second row: varied C_d. Calculated using a Rosin-Rammler distribution (r_m=15 μm, q=2) and the standard Reitz-Diwakar model, with a coarse mesh (1×1.6×1.6 mm near the injector) at T_a=350 K, T_f=243 K, p_{inj}=200 bar, p_a=5 bar, d_{inj}=3 mm.*

3.2.3. The Rosin-Rammler distribution

Although the Rosin-Rammler PDF is implemented into OpenFOAM-1.6.x and the previous versions, the actual implemented PDF differs from the original Rosin-Rammler PDF given by Equation (3.1), see Figure 3.6 (a). The modified Rosin-Rammler distribution agrees well with the PDF calculated by Equation (3.1), see Figure 3.6 (b). This bug was fixed in the latest version of OpenFOAM-1.7.1 released on 26/08/10, after the author of this thesis reported the bug at the fifth OpenFOAM® workshop on 23/06/10. Moreover, other spray submodels (i.e. LISA and TAB) that use the Rosin-

Rammler distribution still incorporate the incorrect version of the Rosin-Rammler distribution in the latest release of OpenFOAM-1.7.1, as is described later.

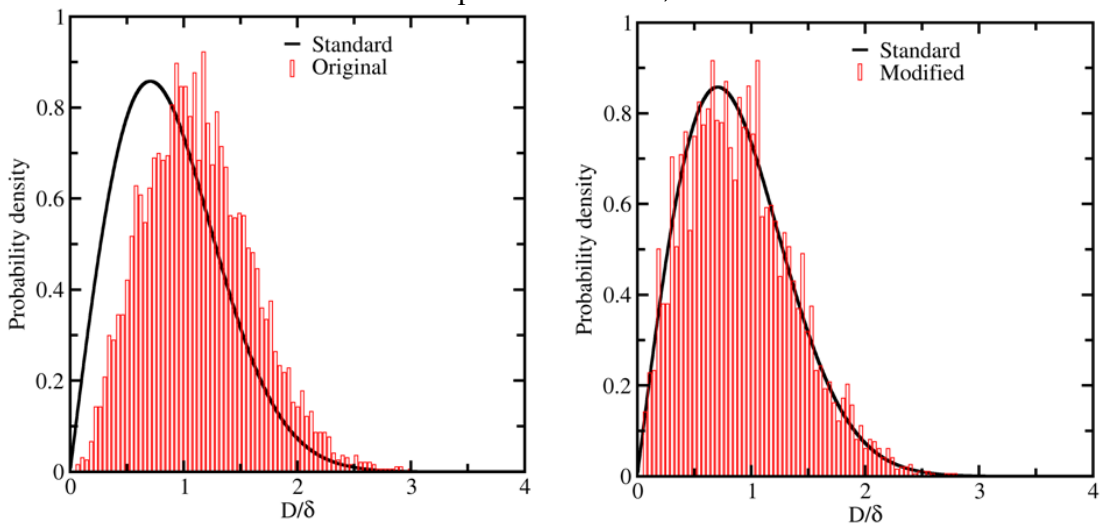

(a) Droplet size distribution in standard version of OpenFOAM® 1.6.x

(b) Rosin-Rammler distribution in modified OpenFOAM®

Figure 3.6: *Comparison of the probability densities calculated using Equation (3.1) (black solid lines), the droplet size distribution obtained using standard version of OpenFOAM-1.6.x (red bars in sub-figure (a)) and the Rosin-Rammler distribution in modified OpenFOAM® (red bars in sub-figure (b)). 5000 samples, r_m=15 μm, q=2.*

3.2.4. The LISA model

Several modifications were made to the default LISA model.

First, in the standard version of OpenFOAM®, the gas density is calculated for an average temperature

$$\hat{T}_g = \frac{T_g + 2T_f}{3}. \tag{3.83}$$

Because neither Senecal et al. [77] nor Schmidt et al. [78] mentioned $\hat{T}_g$, it was replaced with the gas temperature T_g in the LISA.C routine. This modification affects the computed penetration length and SMD very weakly under the conditions of the simulations discussed in this thesis.

Second, the correct Rosin-Rammler distribution, see Equation (3.1), was implemented into the LISA.C routine.

Third, the effect of d_{max} (i.e. maximum diameter for Rosin-Rammler distribution after the ligaments breakup) was studied (see Figure 3.7). The black solid lines show the results calculated for d_{max} limited by parcel diameter d_p, and the red dashed lines show the results calculated for d_{max} limited by $8r_m$. Here r_m is the radius of the Rosin-Rammler distribution. The liquid penetration was greatly increased in the latter case, and the SMD during the injection period was greatly increased as well. Note that the SMD in the simulation is calculated based on the droplets within a 1 mm thick plane which is horizontally located in the computational domain at a distance of 18 mm from the injection origin; we have taken to referring to it as the SMD at plane.

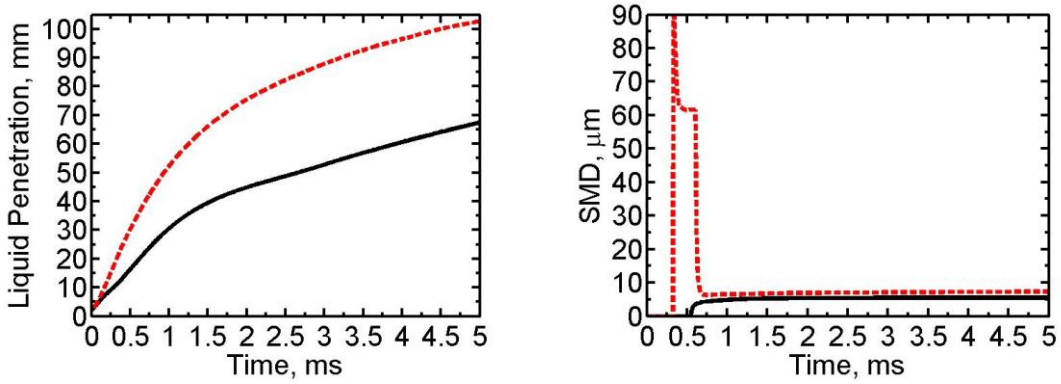

(a)Liquid penetration *(b)SMD at plane*

Figure 3.7: *The effect of d_{max} on the LISA model (using the correct Rosin-Rammler distribution, q=2) on the liquid penetration and SMD of ethanol. d_{max}=d_p, black solid lines; $d_{max} = 8r_m$, red dashed lines. Standard TAB model, coarse mesh (1×1.6×1.6 mm near the injector) at T_a=350 K, T_f=243 K, p_{inj}=200 bar, p_a=5 bar, d_{inj}=3 mm.*

Fourth, in order to identify a suitable exponential factor q for the Rosin-Rammler distribution after ligament breakup, the effect of q on liquid penetration and SMD was studied. The factor q was varied from 3 to 10. As q increases, the calculated liquid penetration and SMD also increase slightly (see Figure 3.8). On the basis of these results, the value of q was taken to be 3 in subsequent calculations using the LISA model.

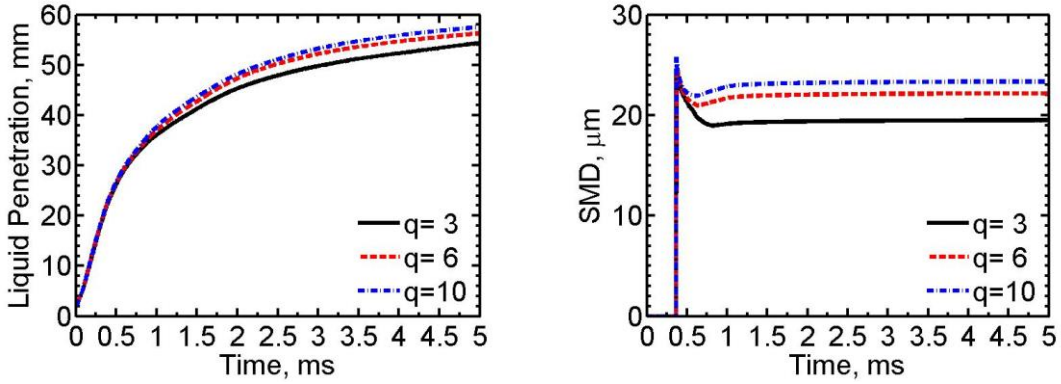

(a)Liquid penetration *(b)SMD at plane*

Figure 3.8: *The effect of factor q in LISA model on the liquid penetration and SMD of ethanol. q=3, black solid lines; q=6, red dashed lines; q=10, blue dot-dashed lines. Standard Reitz-Diwakar model, coarse mesh (1×1.6×1.6 mm near the injector) at T_a=350 K, T_f=243 K, p_{inj}=200 bar, p_a=5 bar, d_{inj}=3 mm.*

Fifth, a bug in the implementation of an expression for J in Equation (3.24) has been corrected.

3.2.5. The TAB model

The Rosin-Rammler distribution is implemented in the routine TAB.C that performs TAB calculations in the standard version of OpenFOAM®. However, the PDF that is

actually implemented is the χ-squared distribution given by Equation (3.55). Therefore, the TAB.C routine was modified so as to correctly implement the Rosin-Rammler PDF.

Moreover, the following additional modifications were made to the TAB.C routine. First, in the modified code, if the child droplet is larger than the parent droplet, the total size of the parent and child droplets remains equal to that of the parent droplets. This is not the case in the standard version of OpenFOAM®. Second, in the standard version of OpenFOAM®, droplet size deformation is not considered if breakup does not occur; in the modified version, droplet deformation is accounted for using Equation (3.43).

Figure 3.9 shows the influence of these modifications on the computed liquid penetration and SMD. Although the modifications only weakly affect the computed liquid penetration (see Figure 3.9 (a)), the SMDs calculated using the modified TAB models are much smaller than those predicted by the standard version between 0.3 and 0.5 mm (see Figure 3.9 (b)). Note that all versions of TAB model examined always yielded very small droplet sizes (less than 4 μm) in these simulations.

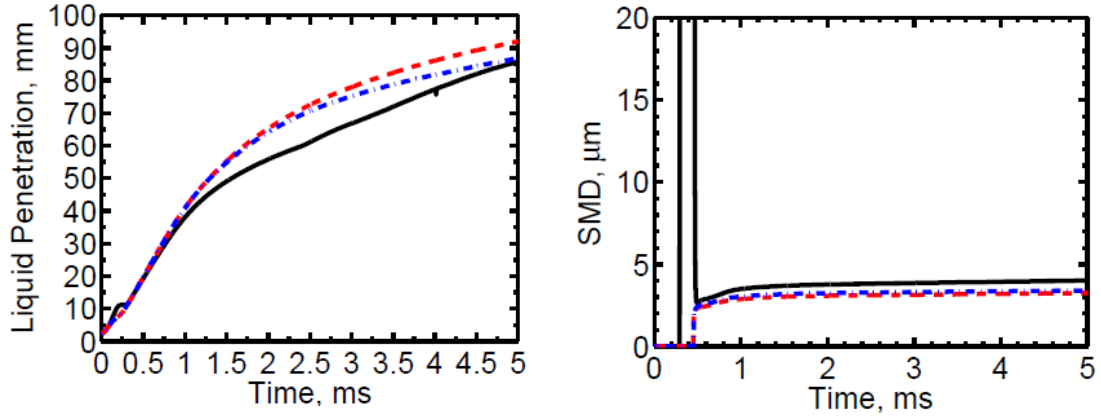

(a)Liquid penetration *(b)SMD at plane*

Figure 3.9: *Liquid penetration and SMD of hollow cone spray of ethanol computed using different versions of the TAB model. Standard TAB model, black solid lines; TAB model modified to account for droplet deformation, red dashed lines; TAB with limited child droplet radius, blue dash-dotted lines. Calculations performed using the Rosin-Rammler distribution (r_m=15 μm, q=2) with a coarse mesh (1×1.6×1.6 mm near the injector) at T_a=350 K, T_f=243 K, p_{inj}=200 bar, p_a=5 bar, d_{inj}=3 mm.*

3.2.6. The Reitz-Diwakar model

In the standard version of OpenFOAM®, the gas density is calculated for an average temperature using Equation (3.83). Because neither Senecal et al. [77] nor Schmidt et al. [78] mentioned $\hat{T}_g$, it was replaced with the gas temperature T_g in the reitzDiwakar.C routine. The effect of basing this calculation on the average temperature was tested for two different primary atomization methods: (i) the Rosin-Rammler distribution (r_m=15 mm, q=3), the results of which are shown in Figure 3.10; and (ii) the LISA model (see Figure 3.11). This modification had a modest effect on the computed penetration length and SMD under the conditions used in these simulations.

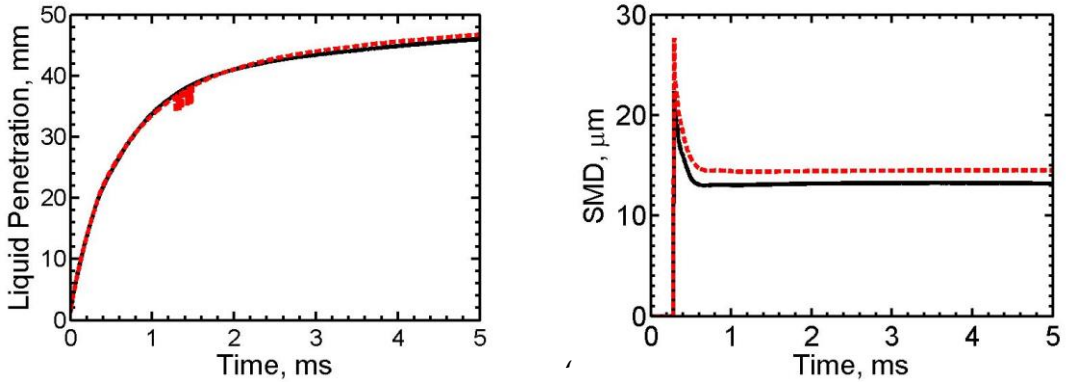

(a)Liquid penetration *(b)SMD at plane*

Figure 3.10: *The effect of using the average temperature to calculate the gas density in Reitz-Diwakar model on the liquid penetration and SMD of ethanol. $\hat{T}_g$ in Equation (3.83), black solid lines; gas temperature, red dashed lines. Calculations performed using the Rosin-Rammler distribution (r_m=15 μm, q=2) with a fine mesh (0.78×0.78×0.85 mm near the injector) at T_a=350 K, T_f=243 K, p_{inj}=200 bar, p_a=6 bar, d_{inj}=4 mm.*

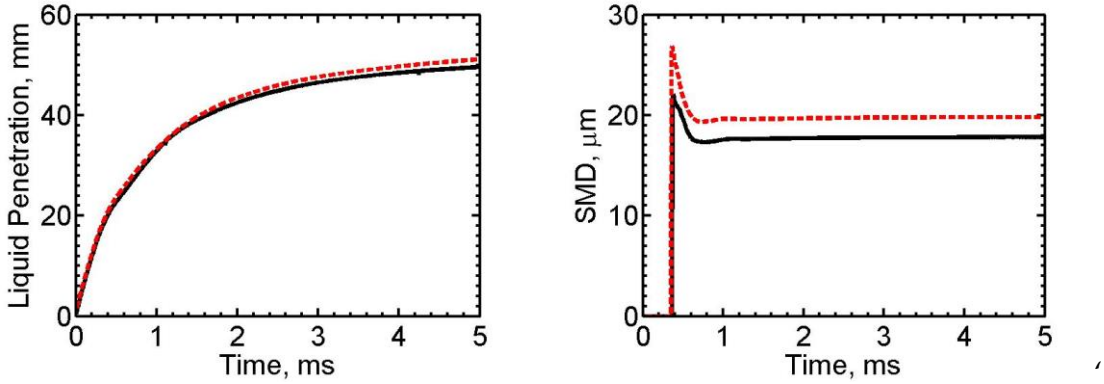

(a)Liquid penetration *(b)SMD at plane*

Figure 3.11: *The effect of using the average temperature to calculate the gas density in Reitz-Diwakar model on the liquid penetration and SMD of ethanol. $\hat{T}_g$ in Equation (3.83), black solid lines; gas temperature, red dashed lines. Calculations performed using the LISA model with a fine mesh (0.78×0.78×0.85 mm near the injector) at T_a=350 K, T_f=243 K, p_{inj}=200 bar, p_a=6 bar, d_{inj}=4 mm.*

3.2.7. The Reitz-KHRT model

The following differences were found between the implementation of the wave breakup (KH) model in OpenFOAM® and the model described by Reitz [71], Su et al. [74], and Patterson and Reitz [75].

First, in the standard version of Open-FOAM, the mass stripped off a parent droplet due to the KH instability is equal to $4\pi\rho_f r_{KH}^3/3$ during each time step and a new parcel of spherical child droplets is created when the mass of the liquid stripped off the parent droplets exceeds 20% of the average injected parcel mass $\bar{m}_{inj}$.

According to Reitz [71], the mass of the liquid stripped of the parent droplets should be equal to

$$m_s = 4\pi N_0 \rho_f \left(r_0^3 - r^3\right)/3. \tag{3.84}$$

and a breakup event occurs when

$$m_s = 0.03\overline{m}_{inj} \tag{3.85}$$

Here, the subscript *0* designates the moment at which the parent parcel is created.

Second, in the standard version of Open-FOAM, Equations (3.12)-(3.14) are not used and the radius of the parent droplets is not changed during breakup event; instead, all that happens is that their number is decreased due to the reduction of the mass of the parent parcel.

Third, the second breakup criterion introduced by Reitz [71] (that "the number of product drops was greater than or equal to the number of parent drops") is not invoked.

The three points emphasized above were addressed by us, i.e. Equations (3.13)-(3.14); these together with the criterion $n > N_0$ were implemented into reitzKHRT.C routine of the OpenFOAM® library. The corrected implementation is henceforth referred to as Reitz-KHRT-1.

Fourth, in the event case that $B_0\Lambda_{KH} > r$, Reitz [71] suggested that (i) the parent parcel should be replaced by a new parcel containing drops with size given by Equation (3.12) and (ii) that a "breakup" of this kind should be permitted only once for each injected parcel. This proposal was omitted from the implementation in the standard version of OpenFOAM® but was later implemented by us. This extended version of Reitz-KHRT-1 is henceforth referred to as Reitz-KHRT-2.

As regards the implementation of the RT submodel in the standard version of OpenFOAM®, the number and radius of the child droplets are calculated using Equations (3.66) and (3.67) as used in diesel spray studies [74][75]. Because Beale and Reitz [76] generated child droplets by invoking the Rosin-Rammler distribution (with r_m being equal to r_{RT} and q=3.5) when simulating hollow-cone sprays, we chose to adopt this method and implemented it in the reitzKHRT.C routine of the OpenFOAM® library; this extended version of Reitz-KHRT-2 is henceforth referred to as Reitz-KHRT-3.

Finally, when simulating diesel and hollow-cone sprays, Reitz et al. used different values for the model constants, namely C_τ=1, C_{RT}=5.33 [74][75] and C_τ=10, C_{RT}=0.1 [76]. For unknown reasons, in the standard version of OpenFOAM®, the default values are C_τ=1 and C_{RT}=0.1, i.e. the former set of constants are those deemed appropriate for diesel sprays while the latter are those used for hollow-cone sprays. In the present work, these constants were set at C_τ=1 and C_{RT}=5.33 when used in conjunction with Equations (3.66) and (3.67) as described by Su et al. [74] and Patterson and Reitz [75]. When working with the Rosin-Rammler distribution, the constants were set at C_τ=10 and C_{RT}=0.1, as described by Beale and Reitz [76].

Figure 3.12 shows the liquid penetration and SMD predicted by these four variations on the Reitz-KHRT model. A uniform droplet radius 15 μm was chosen to match the length scale of the injector needle lift height. The default Reitz-KHRT model crashed before the end of simulation, demonstrating that it is not robust. The Reitz-

KHRT-1 and Reitz-KHRT-2 models predicted somewhat greater liquid penetrations and SMDs than were observed with the standard model. The Reitz-KHRT-3 model, which is the version that was used in subsequent studies, predicted slightly shorter liquid penetration and smaller SMD values because it employs the Rosin-Rammler distribution when generating child droplets. Note that the computed SMD is sampled at the same height (18 μm from the injection origin) but in a 1mm thick ring with an outer radius of 16 mm (for p_{inj}=50 bar) or 20 mm (for p_{inj}=200 bar), depending on p_{inj}, and that this method of calculating SMD produces results that are more consistent with the experimental data than any of the alternatives, as described in more detail later on in this thesis.

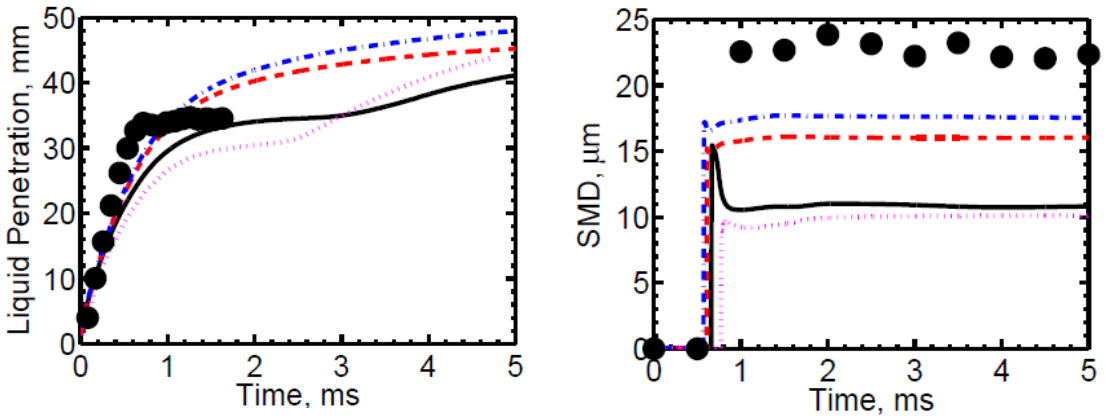

(a)Liquid penetration *(b)SMD at plane*

Figure 3.12: *Comparison of the measured (symbols) and calculated (lines) liquid penetration and SMD of ethanol. Black circles: experimental measurements; black solid lines: standard Reitz-KHRT; red dashed lines: Reitz-KHRT-1; blue dot-dashed lines: Reitz-KHRT-2; magenta dotted lines: Reitz-KHRT-3. Calculations performed using a uniform droplet radius of 15 μm and a fine mesh (0.78×0.78×0.85 mm near the injector) at T_a=350 K, T_f=243 K, p_{inj}=200 bar, p_a=6 bar, d_{inj}=4 mm.*

Similar trends were observed when using the Rosin-Rammler distribution (r_m=15 μm, q=3) with different implementations of the Reitz-KHRT model (see Figure 3.13). The liquid penetrations computed using the Reitz-KHRT-1 and Reitz-KHRT-2 models show acceptable agreement with experimental data (see Figure 3.12 (a), Figure 3.13 (a) and Figure 3.14 (a)), whereas the SMDs are underpredicted (see Figure 3.12 (b), Figure 3.13 (b) and Figure 3.14 (b)). Note that the default constants used in the Rietz-KHRT model implemented in OpenFOAM® (C_τ=1, C_{RT}=0.1, $msLimit$=0.2) were applied in these simulations. Studies of the model's sensitivity to these constants are discussed in section 3.4.1.

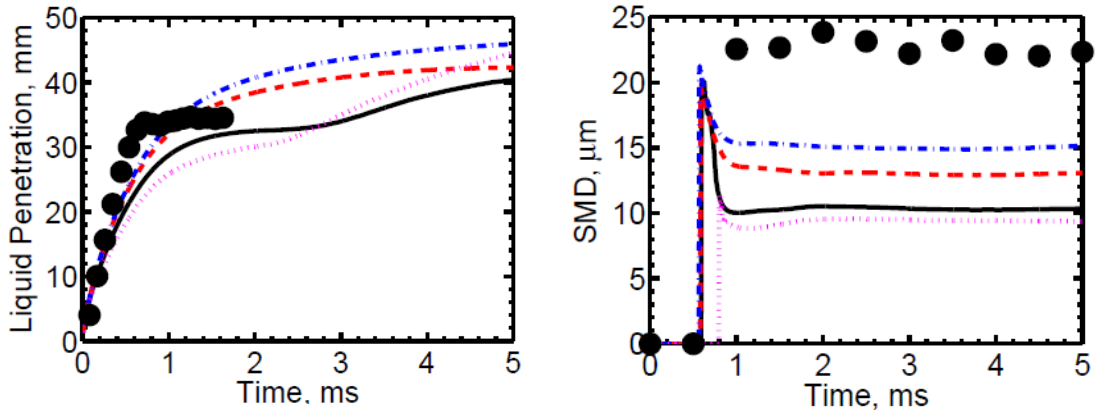

(a)Liquid penetration *(b)SMD at plane*

Figure 3.13: *Comparison of measured (symbols) and calculated (lines) liquid penetration and SMD of ethanol. Black circles: experimental measurements; black solid lines: standard Reitz-KHRT; red dashed lines: Reitz-KHRT-1; blue dot-dashed lines: Reitz-KHRT-2; magenta dotted lines: Reitz-KHRT-3. Calculations performed using the Rosin-Rammler distribution (r_m=15 μm, q=3) with a fine mesh (0.78×0.78×0.85 mm near the injector) at T_a=350 K, T_f=243 K, p_{inj}=200 bar, p_a=6 bar, d_{inj}=4 mm.*

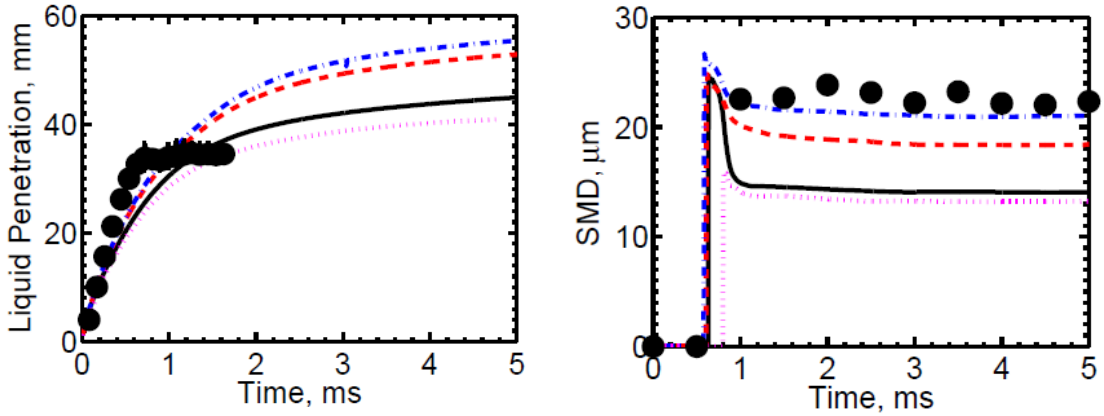

(a)Liquid penetration *(b)SMD at plane*

Figure 3.14: *Comparison of measured (symbols) and calculated (lines) liquid penetration and SMD of ethanol. Black circles: experimental measurements; black solid lines: standard Reitz-KHRT; red dashed lines: Reitz-KHRT-1; blue dot-dashed lines: Reitz-KHRT-2; magenta dotted lines: Reitz-KHRT-3. Calculations performed using the LISA model with a fine mesh (0.78×0.78×0.85 mm near the injector) at T_a=350 K, T_f=243 K, p_{inj}=200 bar, p_a=6 bar, d_{inj}=4 mm.*

Figure 3.15 compares the performance of the Reitz-KHRT-2 the standard Reitz-KHRT models in predicting the liquid penetration and SMD for gasoline. A uniform droplet radius of 15 μm was used as it was the same as the length scale of the injector needle lift height. Note that the values of the constants recommended by Su et al. [74] and Patterson and Reitz [75] (C_τ=1.0 and C_{RT}=5.33) were applied in Reitz-KHRT-2 model, whereas the default values of the constants in OpenFOAM® (C_τ=1 and C_{RT}=0.1) were applied in the standard Reitz-KHRT model. The Reitz-KHRT-2 model yields good agreement with the experimental data for liquid penetration and SMD. The

standard Reitz-KHRT model with the default constants yields lower liquid penetration and smaller SMD than was observed experimentally.

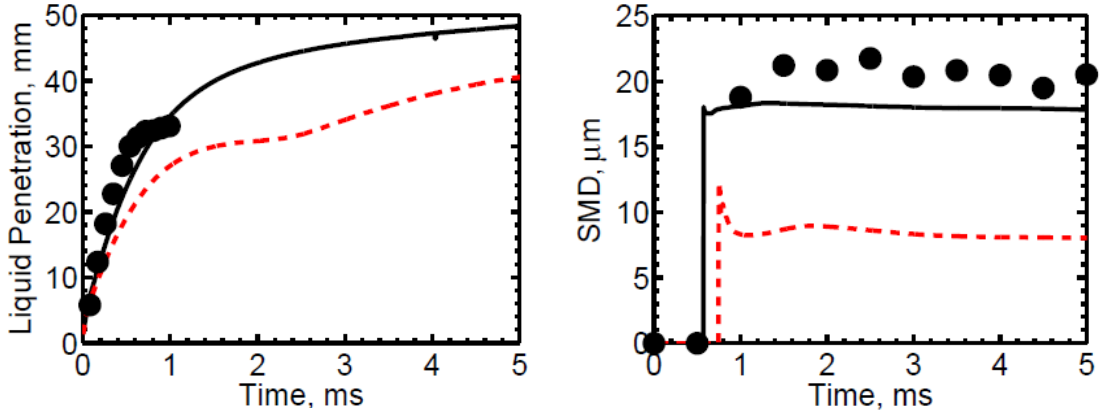

(a)Liquid penetration *(b)SMD at plane*

Figure 3.15: *Comparison of measured (symbols) and calculated (lines) liquid penetration and SMD for gasoline. Black circles: measurements; red dashed lines: Reitz-KHRT-2 (B_1=40, C_τ=1.0, C_{RT}=5.33, $msLimit$=0.03); blue dot-dashed lines: standard Reitz-KHRT (B_1=40, C_τ=1, C_{RT}=0.1, $msLimit$=0.2). Calculations performed with a uniform droplet size distribution (r=15 μm) and a fine mesh (0.78×0.78×0.85 mm near the injector) at T_a=350 K, T_f=243 K, p_{inj}=200 bar, p_a=6 bar, d_{inj}=4 mm.*

3.2.8. The O'Rourke and trajectory collision models

For unknown reasons, in the standard version of OpenFOAM®, the radii r_i^3 and r_j^3 in Equations (3.72), (3.74), and (3.76) are replaced by the parcel masses M_i and M_j, respectively. Because the two sets of equations are equivalent to one another only if the numbers of droplets in the two parcels are the same, i.e. $N_i = N_j$, we rectified this error and implemented the original equations of O'Rourke, i.e. equations (3.72), (3.74), and (3.76) in OpenFOAM®. This modification has minor effects on the calculated liquid penetration and SMD under the conditions used in our simulations.

Moreover, the standard implementation of Equation (3.73) in the trajectoryCM.H routine (the trajectory model) uses a mean radius $\sqrt{r_i r_j}$ instead of the radius r_j of the smaller droplet. We rectified this by implementing the equation originally proposed by O'Rourke, Equation (3.73), in OpenFOAM®. This modification had minor effects on the calculated liquid penetration and SMD under the conditions used in our simulations.

Finally, a few bugs in the two aforementioned routines were identified by the author and have been corrected in OpenFOAM-1.6.x. Note that before correcting the bugs it was not possible to perform a complete simulation with either the standard O'Rourke model or the standard trajectory model under the conditions used in our simulations.

3.2.9. The physical properties of gasoline

The physical properties of real gasoline, such as its surface tension, dynamic viscosity, and heat of vaporization strongly affect spray formation in gasoline direct injection

engines. Therefore, it was decided that the liquid properties of gasoline should be included in the OpenFOAM® libraries.

Some physical properties, namely the vapour pressure, latent heat, liquid viscosity, liquid heat conductivity, and surface tension were obtained from the KIVA fuel library and were implemented in OpenFOAM® in a form of a lookup table. As recommended by KIVA, the enthalpy, heat capacity, and second virial coefficient are the same as those of *n*-octane. The values for the molecular weight and critical temperature of gasoline were also taken from the KIVA fuel library. The density of gasoline was taken from [96] in the form of a table. The gasoline surrogate consists of *iso*-octane (iC$_8$H$_{18}$), toluene (C$_7$H$_8$) and *n*-heptane (nC$_7$H$_{16}$) in a volumetric ratio of 55%:35%:10% [19][67]. Therefore, an average of the chemical formulae of these species, C$_8$H$_{15}$, was used to represent gasoline in the gas phase. The rest of the properties of gasoline, including its vapour dynamic viscosity, vapour heat conductivity, critical pressure, critical volume, critical compressibility factor, triple point temperature, triple point pressure, normal boiling temperature, dipole moment, Pitzer's acentric factor, and solubility parameter, were approximated using the mixing rule [97]

$$Q_m = \sum_{k=1}^{3} X_k Q_k \tag{3.86}$$

for the above-mentioned ternary mixture.

Here, Q_m is a mixture parameter; y_i is a liquid or vapor mole fraction; Q_i is a property of a pure liquid or vapor.

3.3. Experimental and computational setup

3.3.1. Experimental setup

The code and the spray models it implements were assessed by comparing its predictions to recent experimental data on gasoline and ethanol hollow-cone sprays discharged from a piezo-actuated outward-opening pintle injector into the Chalmers spray chamber [21]. The chamber is a cylinder with an inner diameter of 170 mm and a height of 270 mm. The air inside the chamber can be pressurized up to 6 bar and heated up to 350 K. The injector was mounted 2 mm below the cylinder head, with the injection temperature being varied between 243 and 320 K in different experiments.

The chamber has good optical access via four large circular windows located on the cylinder's wall. Sprays were illuminated through two opposite windows utilizing two 250 W Dedocool floodlights. The light scattered by the spray passed through another window and was recorded using a 12 bit monochrome Vision Research Phantom V 7.1 high speed camera with an Al Nikkor 500 mm f/2.0 lens, at an exposure time of 5 ms and an acquisition rate of 11000 images per second. Ten sequential images of each investigated spray were captured and processed in order to evaluate its vertical penetration. The sizes of drops in a spray were measured using a two-dimensional TSI phase Doppler anemometry (PDA) system operating with two light beams (λ=488 and 514 nm) produced by an argon-ion laser. By processing the recorded PDA signal using Flowsizer software, the Sauter mean diameter (SMD) of droplets in the spray was

evaluated at a single probe volume, located 15 mm downstream from the injector nozzle and 14-22 mm away from the symmetry axis. The SMD was calculated during the time interval 1-4 ms after the start of injection.

A schematic diagram of the experimental set-up is shown in Figure 3.16; the interested reader is referred to the paper by Hemdal et al. [21] for further details.

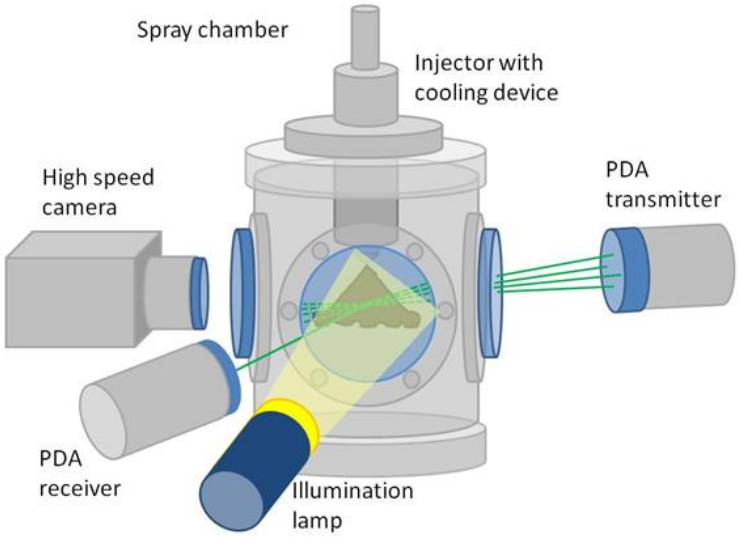

Figure 3.16: *Schematic diagram of the experimental setup (courtesy of Hemdal et al. [21]).*

3.3.2. Computational setup

In the simulations, a cylindrical computational domain with a radius of 85 mm and a height of 205 mm was employed to represent the combustion chamber. Three computational meshes were used; (i) a coarse mesh (1.60×1.60×2.73 mm near the injector with 131 250 cells, see Figure 3.17), (ii) a medium mesh (0.98×0.98×1.34 mm near the injector with 1 108 230 cells), and (iii) a fine mesh (0.78×0.78×0.85 mm near the injector with 1 754 400 cells, see Figure 3.18). For all the meshes, the center of the computational domain (40×40×205 mm) was refined to better resolve the flow field. The size of the mesh gradually increases along the injection direction so as to smoothly decrease the numbers of cells in the mesh without sacrificing detail.

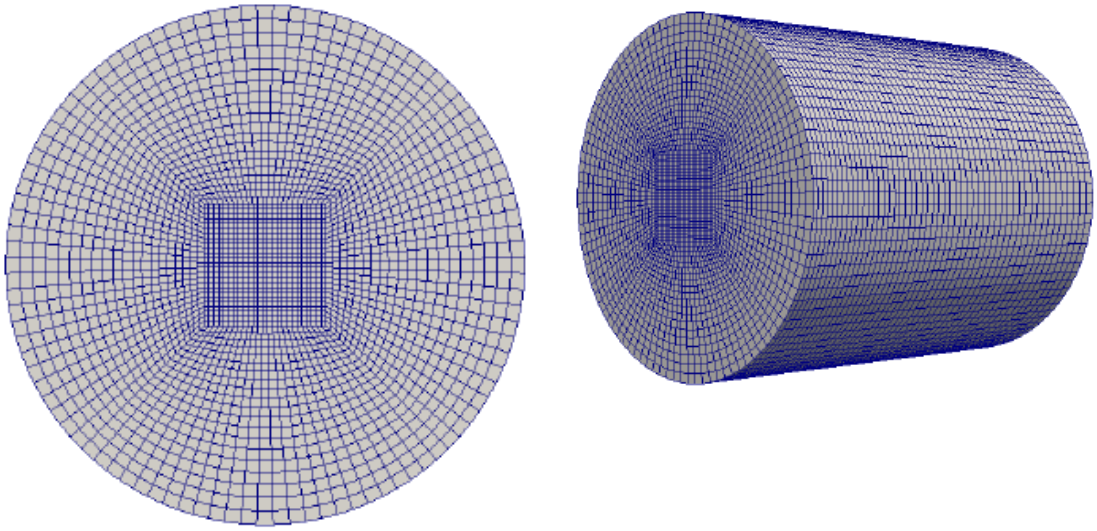

(a)View 1 *(b)View 2*

Figure 3.17: *Computational mesh (coarse) for the Chalmers spray chamber*

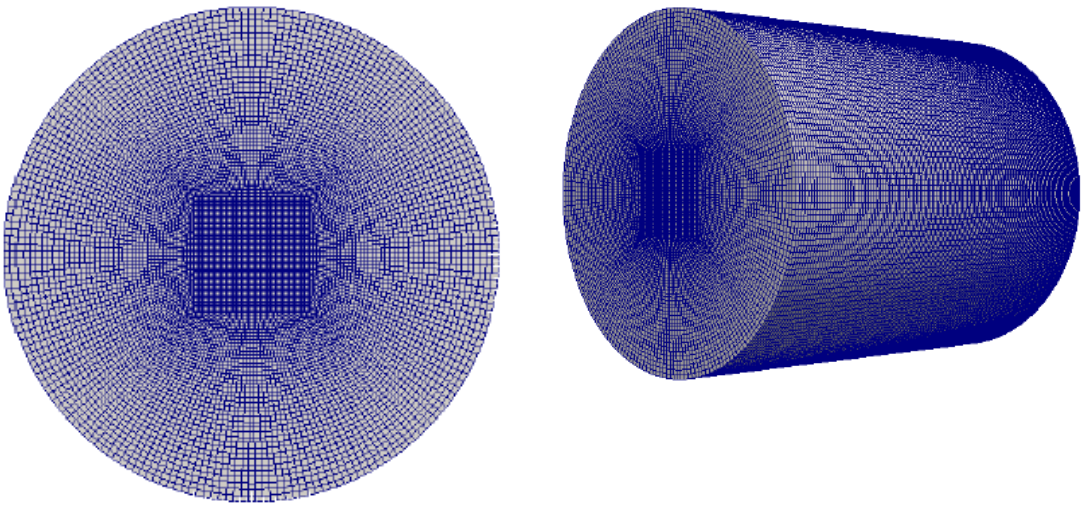

(a)View 1 *(b)View 2*

Figure 3.18: *Computational mesh (fine) for the Chalmers spray chamber*

Since the experimental air velocity is very low, i.e. around 0.06 m/s [21], the initial air velocity in the computational domain was estimated as 0 m/s. The initial turbulent kinetic energy k and turbulence length scale l_t were not measured in the experiments, but the initial k and the initial turbulent dissipation rate $\varepsilon = C_\mu k^{1.5}/l_t$, are necessary input parameters for $k-\varepsilon$ model. Due to the slow air motion in the combustion chamber, the initial k was estimated to be 0.1 m^2/s^2, whereas the initial ε was estimated to be 10 m^2/s^3 (see Table 3.1). Sensitivity studies were performed (as described in section 3.4.1) to determine the initial values of k and l_t due to the uncertainty in the above estimations.

Table 3.1: *The values of the constants in the spray models, the initial and boundary conditions used, and other `default' numerical parameters used in the simulations.*

	Type	Name	constants
Models	Injector	Pintle injector	$d_{inj} = 4\ mm, d_{gap} = 30\mu m, C_d = 0.418$
	Primary breakup	Rosin-Rammler	$r_m = 15\mu m, q = 3$
		LISA	$C_l = 1, C_\tau = 12, Q = 0.001, J = 1.5E-4$
	Secondary breakup	TAB	$y_0 = 0, \dot{y}_0 = 0, C_\mu = 5, C_\omega = 8, We_{crit} = 12$
		Reitz-Diwakar	$C_{bag} = 6, C_b = 0.785, C_{strip} = 0.5, C_s = 40$
		KHRT	$B_0 = 0.61, B_1 = 40, C_\tau = 10, C_{RT} = 0.1$
	Turbulence	standard $k-\varepsilon$	$C_\mu = 0.09, C_1 = 1.44, C_2 = 1.92, C_3 = -0.33, \sigma_k = 1.0, \sigma_\varepsilon = 1.3, Pr_t = 1.0$
	Initial internal field	Boundary type	Numerical div-schemes
k [m²/s²]	1	kqRWallFunction	Gauss limitedLinear 1
ε [m²/s³]	10	epsilonWallFunction	Gauss limitedLinear 1
T [K]	350	zeroGradient	
p [bar]	6	buoyantPressure	Gauss linear
U [m/s]	0	fixedValue	Gauss limitedLinearV 1
Other parameters	Number of parcels	19 200	
	Spray cone angles	Inner cone angle 80°; outer cone angle 90°	
	Time step	5 μs	
	Maximum Courant number	0.5	
	Mesh	0.78×0.78×0.85 mm near the injector with 1 754 400 cells	

Table 3.2: *Initial values of T_a, T_f and p_{inj} used in the simulations*

	T_a [K]	T_f [K]	p_{inj} [bar]
gasoline	350	243	50/125/200
	295	295	200
	350	320	200
	295	243	200
Ethanol	350	243	50/125/200
	295	295	200

The experimental study focused on engine operation under stratified cold start conditions (SCSC, i.e. T_a=350 K and T_f=243 K) with gasoline and ethanol, but other ambient air and fuel temperatures have been studied as well. The injection pressure p_{inj} was varied from 50 bar to 200 bar while the air pressure was kept the same (i.e. p_a =6 bar). The simulations primarily focused on the conditions studied in the experiments, as summarized in Table 3.2. The results reported in this thesis were computed under at simulated temperatures of T_a =350 K and T_f =243 K, and for pressures of p_a=6 bar and p_{inj}=200 bar unless otherwise specified.

The injection pressure profile was not measured in the experiments by Hemdal et al. [21] but the duration of electrical pulse was documented to be 0.4 ms for a single injection. Two injection pressure profiles were estimated and studied numerically. The first had an injection duration of 0.6 ms and a maximum injection pressure of 190 bar (see the black solid line in Figure 3.19). The second had an injection duration of 0.4 ms and a constant injection pressure of 200 bar (see the red dashed line in Figure 3.19). In the measurements the duration of electrical pulse is 0.4 ms so the actual injection rate should be between the aforementioned two profiles. In other words, these two profiles represent the two possible extremes of $p_{inj}(t)$. The results reported in the following sections were computed using the first of these injection pressure profiles unless otherwise specified. A sensitivity study of the aforementioned injection pressure profiles is discussed in section 3.4.1.

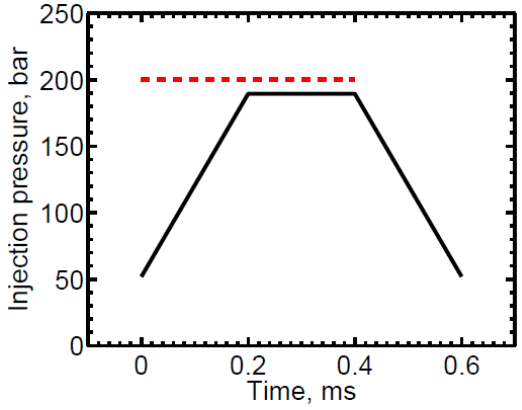

Figure 3.19: *Injection pressure profiles studied in the simulations.*

In the experiments, only the injected gasoline mass for p_{inj}=200 bar was measured (i.e. m=13 mg). For p_{inj}=50 bar, the injected gasoline mass was estimated as follows

$$m_2 = m_1 \frac{\sqrt{p_{inj,2} - p_a}}{\sqrt{p_{inj,1} - p_a}} \tag{3.87}$$

Here, subscripts 1 and 2 represent the parameters for p_{inj} =200 and 50 bar, respectively.

Moreover, for the purposes of simulation, the injected mass of ethanol, m_e, was estimated as

$$m_e = m_g \frac{\rho_e}{\rho_g} \tag{3.88}$$

where the subscripts e and g represent the parameters for ethanol and gasoline, respectively.

The first step taken when performing simulations was to define a threshold value, which was typically 90% or 95% of the total injected fuel mass, and to identify the volume of space containing that quantity of fuel. The position of the parcel most distant from the injector within that space was then recorded, and the projection of this parcel's position vector onto the injection axis was taken to be the depth of liquid penetration. The sensitivity of the computed results to the value of the threshold used in defining the depth of liquid penetration is discussed in section 3.4.1.

In the experiments, SMD was measured at a certain location in the spray cloud (i.e. 15 mm vertically below the injector and at either 16 or 20 mm in the radial direction for p_{inj}=50 bar and p_{inj}=200 bar, respectively). In the simulations, two methods for sampling the SMD were examined. The first method involved sampling the SMD at the same height but in a 1 mm thick ring with an outer radius of 16 mm (for p_{inj}=50 bar) or 20 mm} (for p_{inj}=200 bar). This guaranteed that sufficient statistical data to reliably compute the SMD was obtained. The second method involved calculating the SMD on the basis of the droplets within a 1 mm thick horizontal plane located in the computational domain, at a distance of 18 mm from the injection origin. The predicted SMD results reported in this thesis were computed using the first of these methods unless otherwise stated.

The default values assigned to the constants used in the LISA model by OpenFOAM® are shown in Table 3.1. Note that the Rosin-Rammler exponential factor q=3 is used in the modified LISA model.

The TAB model features five constants. In OpenFOAM®, the default values of these constants are as follows: y_0=0, $\dot{y}_0$=0, C_μ=10, C_ω=8, We_{crit}=12. Two of them, C_μ=5 and C_ω=8, were determined by O'Rourke and Amsden [87] by comparing their model's output to known theoretical solutions. Note that the default value of the constant C_μ differs from that recommended by O'Rourke and Amsden [87]. The sensitivity of the computed results to this constant is discussed in section 2.4.1. Note that the Rosin-Rammler exponential factor is taken to be q=2 in the modified TAB model.

The Reitz-Diwakar model features four constants. In OpenFOAM®, the default values of these constants are in line with the literature [73]. Note that the author found that one of the constant C_s has substantial influence on computed liquid penetration under certain conditions. The sensitivity study of the computed results to this constant will be discussed in section 3.4.1.

The Reitz-KHRT model involves six constants. In OpenFOAM®, the default values of these constants are as follows B_0 =0.61, B_1 =40, C_τ =1, C_{RT} =0.1, $msLimit$ =0.2, $WeberLimit$=6. Note that substantially different values of B_1, e.g. 10 [71][75], or 30 [74], or 40 [76] have been used in different simulations. Moreover, Su et al. [74] and Patterson and Reitz [75] tuned the multiple constants (C_τ =1, C_{RT} =5.33) in their simulations of diesel spray, and Beale and Reitz [76] adjusted the value of C_τ=10 and C_{RT}=0.1 when simulating hollow cone sprays. It should also be noted that the default value of the constant $msLimit$=0.2 differs from that recommended by Reitz [71], i.e. $msLimit$=0.03. The sensitivity of the computed results to these constants is discussed in section 3.4.1.

Unless otherwise specified, the results reported in the next section were obtained using the default input parameters listed in Table 3.1.

3.4. Results

3.4.1. Sensitivity studies

Initial conditions

Since the initial velocity fluctuation u' was not measured in the experiments, the sensitivity of the models to the initial u' was analyzed (see Figure 3.20). Two case studies were conducted, using a medium mesh (0.98×0.98×1.34 mm) and a hollow cone injector with a Rosin-Rammler distribution (r_m=15 μm, q=2) and the standard Reitz-Diwakar breakup model. The initial dissipation rate ε was the same in both cases, i.e. 90 m²/s³, whereas the initial turbulent kinetic energy k was varied from 1 m²/s² (black solid line) to 0.5 m²/s² (red dashed line). The liquid penetration was found to increase slightly as u' decreased, while the SMD (not shown) was only weakly affected by such variations in k.

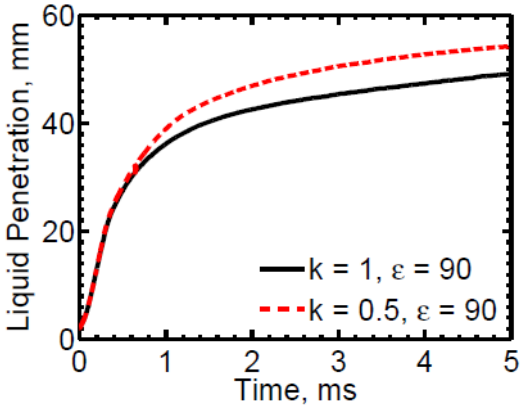

Figure 3.20: *The effect of varying the initial u' on the liquid penetration of gasoline. Black solid lines: k=1 m²/s², ε =90 m²/s³, red dashed lines: k=0.5 m²/s² , ε =90 m²/s³. Calculations were performed using the Rosin-Rammler distribution (r_m=15 μm, q=2) with the standard Reitz-Diwakar model and a medium mesh (0.98×0.98×1.34 mm near the injector), at p_a=5 bar, d_{inj}=3 mm.*

Figure 3.21 also shows the effect of varying the initial u' on the computed liquid penetration when the turbulent length scale l_t is fixed (i.e. l_t =1 mm). Two cases were examined using the medium mesh (0.98×0.98×1.34 mm). As before, the hollow cone injector with a Rosin-Rammler distribution (r_m=15 μm, q=2) and the standard Reitz-Diwakar breakup model were used. The initial k was varied from 1 (black solid line) to 0.5 (red dashed line) m²/s². In order to maintain the same turbulent length scale, the corresponding initial ε was set at either 90 or 32 m²/s³, respectively. The liquid penetration is not affected by u' when l_t is fixed.

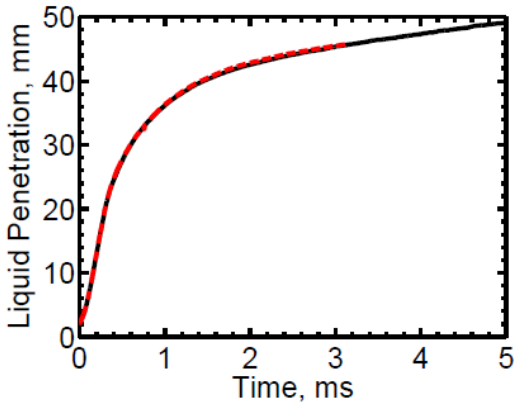

Figure 3.21: *The effect of varying the initial u' on the liquid penetration of gasoline. Black solid lines: k=1 m²/s², ε =90 m²/s³, red dashed lines: k=0.5 m²/s² , ε =32 m²/s³. Calculations were performed using the Rosin-Rammler distribution (r_m=15 μm, q=2) with the standard Reitz-Diwakar model and a medium mesh (0.98×0.98×1.34 mm near the injector), at p_a=5 bar, d_{inj}=3 mm.*

Since the initial l_t was not measured in the experiments, the effect of varying the initial l_t on liquid penetration was examined; the results are shown in Figure 3.22. Three cases were studied using the medium mesh (0.98×0.98×1.34 mm). Once again, the hollow cone injector with a Rosin-Rammler distribution (r_m=15 μm, q=2) and the standard Reitz-Diwakar model were used. In these runs, k was frozen at its initial value of 1 m²/s², whereas the initial l_t was decreased by increasing the initial ε from 90 (black solid line) to 180 (red dashed line) or 360 (blue dot-dashed line) m²/s³. The liquid penetration increased slightly as the initial l_t decreased; the SMD (not shown) was only weakly affected by these adjustments of ε.

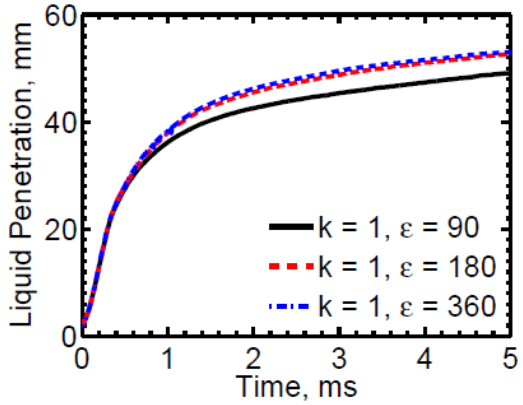

Figure 3.22: *The effect of the initial l_t on the liquid penetration of gasoline. Black solid lines: k=1 m²/s², ε =90 m²/s³, red dashed lines: k=1 m²/s², ε =180 m²/s³, blue dot-dashed lines: k=1 m²/s², ε =360 m²/s³. Calculations performed using the Rosin-Rammler distribution (r_m=15 μm, q=2) and the standard Reitz-Diwakar model with a medium mesh (0.98×0.98×1.34 mm near the injector), at p_a=5 bar, d_{inj}=3 mm.*

The effects of both the u' and l_t on liquid penetration are shown in Figure 3.23. Two cases were examined using the medium mesh (0.98×0.98×1.34 mm), along with a hollow cone injector with a Rosin-Rammler distribution (r_m=15 μm, q=2) and the standard Reitz-Diwakar model. The initial value of k was set at either 0.1 (black solid

line) or 1 (red dashed line) m^2/s^2, and the initial l_t was varied by setting the ε to either 170 (black solid line) or 90 (red dashed line) m^2/s^3. The liquid penetration was found to decrease slightly as k and l_t decreased; the SMD was largely unaffected by these changes.

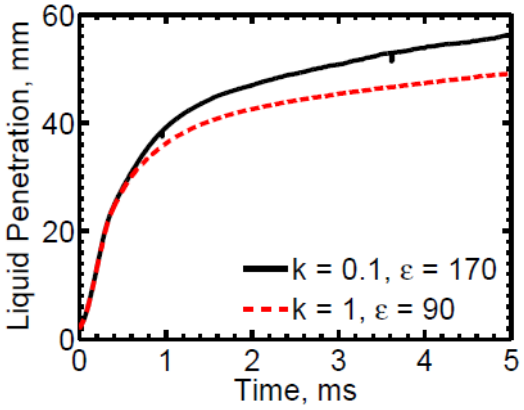

Figure 3.23: *The effect of varying the initial u' and l_t on the liquid penetration of gasoline. Black solid lines: k=0.1 m^2/s^2, ε =170 m^2/s^3, red dashed lines: k=1 m^2/s^2, ε =90 m^2/s^3. Calculations performed using the Rosin-Rammler distribution (r_m=15 μm, q=2) and the standard Reitz-Diwakar model with a medium mesh (0.98×0.98×1.34 mm near the injector), at p_a=5 bar, d_{inj}=3 mm.*

Because the optimal value of the injector diameter d_{inj} in the simulation was not known, a study of the sensitivity of the predicted liquid penetration and SMD to d_{inj} was undertaken (see Figure 3.24). Two situations were examined using the coarse mesh (1.60×1.60×2.73 mm) and the default LISA and standard Reitz-Diwakar models. The injector diameter was set to either 3 mm (black solid line) or 4 mm (red dashed line); it was found that liquid penetration and SMD decreased slightly as d_{inj} increased.

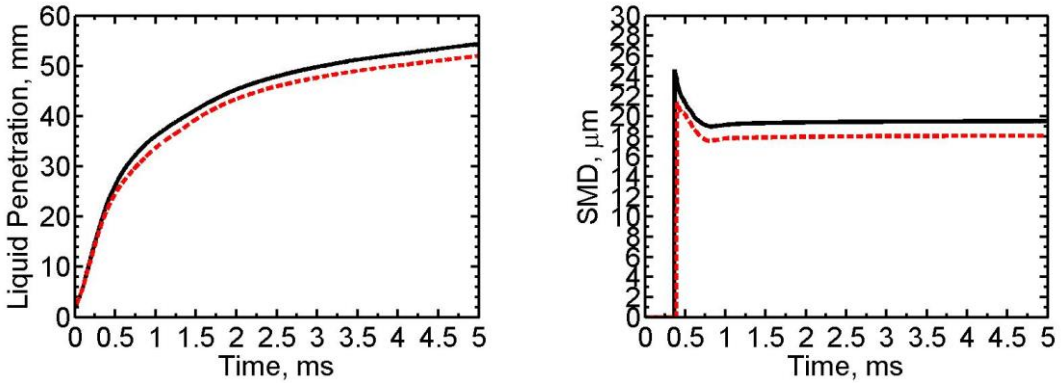

(a)Liquid penetration *(b)SMD at plane*

Figure 3.24: *The effect of varying d_{inj} on the liquid penetration and SMD of gasoline. Black solid lines: d_{inj}=3 mm, red dashed lines: d_{inj}=4 mm. Calculations performed using the LISA and standard Reitz-Diwakar models, with a coarse mesh (1.60×1.60×2.73 mm near the injector), at p_a=5 bar.*

The effect of the initial ambient air pressure p_a on liquid penetration and SMD is shown in Figure 3.25. Two cases were examined using the coarse mesh (1.60×1.60×2.73 mm) along with the LISA and standard Reitz-Diwakar models. The initial p_a was set at

either 5 bar (black solid line) or 6 bar (red dashed line in); it was found that the liquid penetration and SMD decreased slightly as p_a increased.

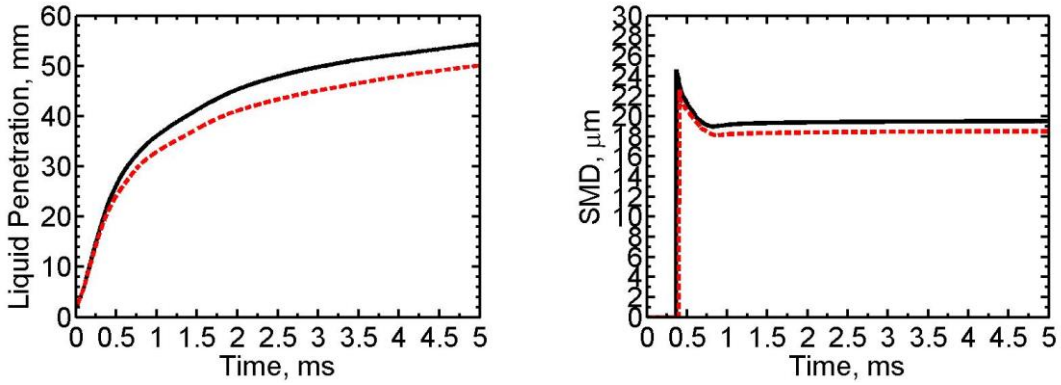

(a)Liquid penetration *(b)SMD at plane*

Figure 3.25: *The effect of varying the initial p_a on the liquid penetration and SMD of gasoline. Black solid lines: p_a=5 bar, red dashed lines: p_a=6 bar. Calculations were performed using the LISA and standard Reitz-Diwakar models, with a coarse mesh (1.60×1.60×2.73 mm near the injector), at d_{inj}=3 mm.*

Model constants

Since the initial droplet size distribution at the nozzle exit was not measured experimentally, the sensitivity of the model's output to variation of the Rosin-Rammler parameters, r_m and q, was analyzed. The effect of varying the Rosin-Rammler radius, r_m (see Equation (3.1)), on liquid penetration and SMD was tested for two different spray models: the standard Reitz-Diwakar model (see Figure 3.26), and VSB2 (see Figure 3.27). Note that the former tests were carried out on the coarse mesh (1.60×1.60×2.73 mm). The Rosin-Rammler exponential factor was treated as a constant in both cases, i.e. q=2, whereas the Rosin-Rammler radius r_m was set at one of 10 μm (black solid lines), 20 μm (red dashed lines), 30 μm (blue dot-dashed lines), or 40 μm (magenta dotted lines). The liquid penetration and SMD were found to increase with r_m in both cases.

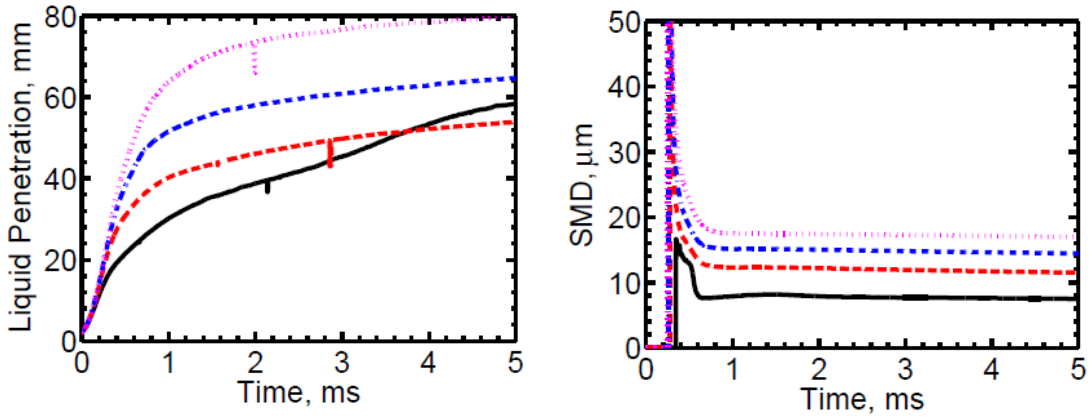

(a)Liquid penetration *(b)SMD at plane*

Figure 3.26: *The effect of altering the Rosin-Rammler radius, r_m, on the liquid penetration and SMD of gasoline. Black solid lines: r_m=10 μm, red dashed lines: r_m=20 μm, blue dot-dashed lines: r_m=30 μm, magenta dotted lines: r_m=40 μm). Calculations were performed using the Rosin-Rammler distribution (q=2) and the standard Reitz-Diwakar model, with a coarse mesh (1.60×1.60×2.73 mm), at p_a=5 bar, d_{inj}=3 mm.*

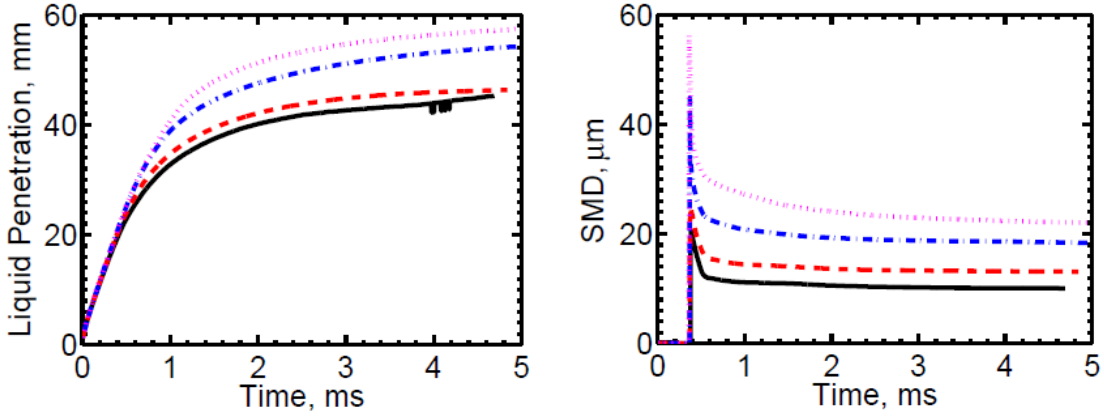

(a)Liquid penetration *(b)SMD at plane*

Figure 3.27: *The effect of Rosin-Rammler radius (black solid lines: 7.5 μm, red dashed lines: 10 μm, blue dot-dashed lines: 15 μm, magenta dotted lines: 20 μm) on ethanol liquid penetration and SMD. VSB2 model.*

The effect of Rosin-Rammler exponential factor q on liquid penetration and SMD was tested for two spray models: the standard Reitz-Diwakar model (see Figure 3.28 and the VSB2 model (see Figure 3.29). Note that the former tests were carried out on the coarse mesh (1.60×1.60×2.73 mm). The Rosin-Rammler radius was treated as a constant (i.e. r_m=10 μm), while q was set at 3 (black solid lines), 6 (red dashed lines), or 10 (blue dot-dashed lines). The Rosin-Rammler exponential factor q was found to weakly affect the liquid penetration and SMD in both cases.

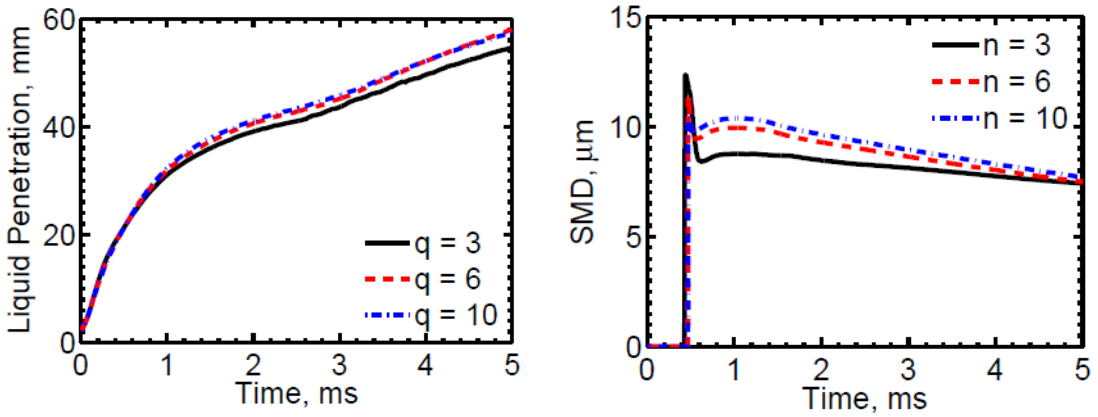

(a)Liquid penetration *(b)SMD at plane*

Figure 3.28: *The effect of varying the Rosin-Rammler exponential factor q (black solid lines: q=3, red dashed lines: q=6, blue dot-dashed lines: q=10) on liquid penetration and SMD. Rosin-Rammler (r_m=10 μm), standard Reitz-Diwakar model and coarse mesh (1.60×1.60×2.73 mm), at p_a=5 bar, d_{inj}=3 mm.*

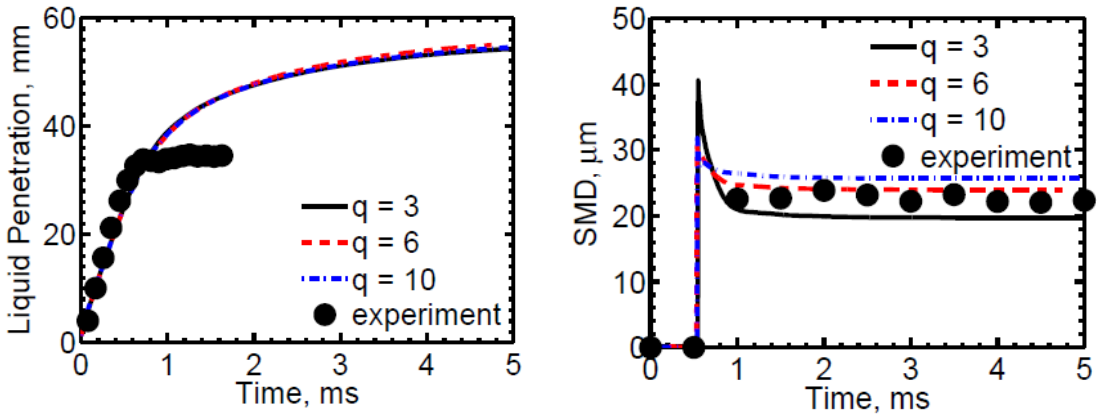

(a)Liquid penetration *(b)SMD at plane*

Figure 3.29: *Comparison of measured (symbols) and calculated (lines) ethanol liquid penetration and SMD. Black circles: measurements; black solid lines: q=3; red dashed lines: q=6; blue dot-dashed lines: q=10. VSB2 model.*

To study the sensitivity of the computed results to the constant C_s of the Reitz-Diwakar model, two cases (C_s=40 and C_s=20) were examined using the coarse mesh (1.60×1.60×2.73 mm), in conjunction with the hollow cone injector and the Rosin-Rammler distribution (r_m=15 μm, q=2). C_s was set to either 40 (black solid lines) or 20 (red dashed lines). Figure 3.30 shows that increasing C_s caused slight increases in the liquid penetration and SMD.

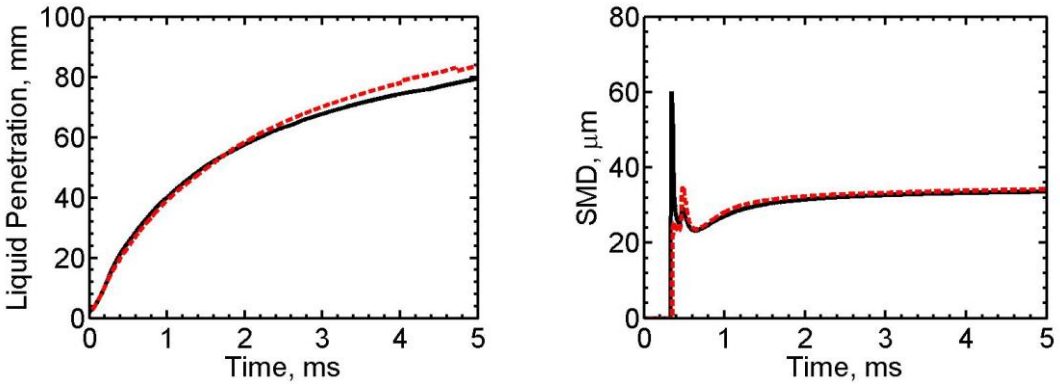

(a)Liquid penetration *(b)SMD at plane*

Figure 3.30: *The effect of varying the parameter C_s from the Reitz-Diwakar model (black solid lines: 40, red dashed lines: 20) on ethanol liquid penetration. Rosin-Rammler distribution (r_m=15 μm, q=2), coarse mesh (1.60×1.60×2.73 mm), p_a=5 bar, d_{inj}=3 mm.*

Since the default value of the constant C_μ in the TAB model differs from that proposed in the original paper [87], the influence of this constant on liquid penetration and SMD was studied; the results of this analysis are shown in Figure 3.31. Two cases were examined using the coarse mesh (1.60×1.60×2.73 mm) and the LISA + TAB spray models. When using the TAB model, C_μ was set to either 10 (black solid lines) or 5 (red dashed lines); liquid penetration and SMD were found to be weakly affected by C_μ.

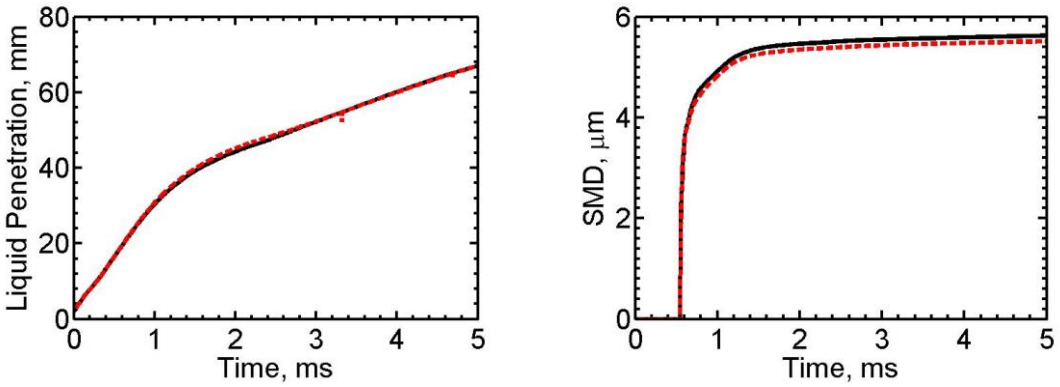

(a)Liquid penetration *(b)SMD at plane*

Figure 3.31: *The effect of varying the constant C_μ on the liquid penetration and SMD values for ethanol predicted using the TAB model (black solid lines: C_μ=10, red dashed lines: C_μ=5). Calculations performed using the LISA and standard TAB models, with a coarse mesh (1.60×1.60×2.73 mm), at p_a=5 bar, d_{inj}=3 mm.*

Substantially different values of B_1, e.g. 10 [71][75], or 30 [74], or 40 [76], have been used in different simulations. Therefore, the sensitivity of two of the Reitz-KHRT models, namely Reitz-KHRT-2 (see Figure 3.32) and Reitz-KHRT-3 (see Figure 3.33) to this parameter was examined. The initial droplet radius in these runs was equal to r=15 μm. In both cases, the parameter B_1 in the Reitz-KHRT model was set at either 40 (black solid lines) or 10 (red dashed lines). The liquid penetration and SMD computed using Reitz-KHRT-2 model decrease slightly with decreases in B_1 (see Figure 3.32). The computed liquid penetrations agree well with the experimental data, but the SMD is slightly underpredicted. The liquid penetration and SMD values predicted when using

the Reitz-KHRT-3 model are weakly affected by B_1 (see Figure 3.33); this model slightly underestimates both liquid penetration and SMD. It is worth remembering, however, that the default constants implemented in OpenFOAM® were used in these sensitivity analyses and that the agreement between the results computed using the Reitz-KHRT model and the experimental data can be improved by adjusting the values of other constants in the models, as is shown later.

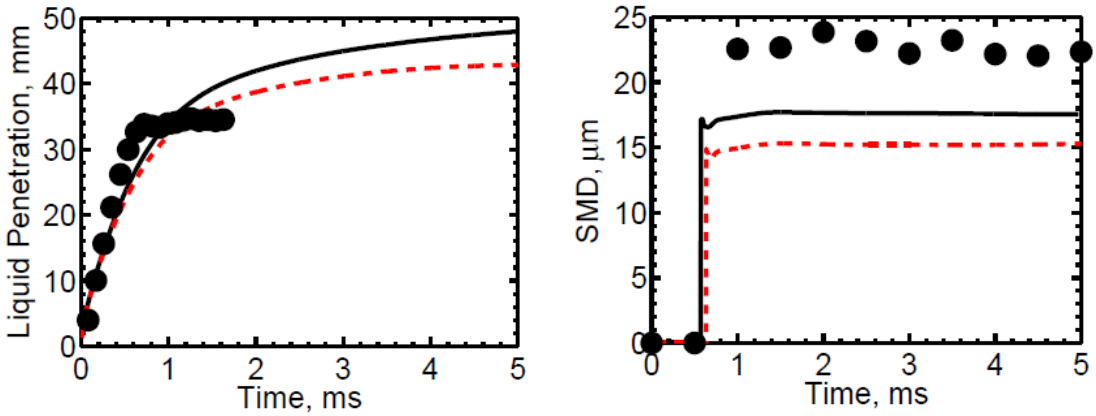

(a)Liquid penetration *(b)SMD at plane*

Figure 3.32: *Comparison of measured (symbols) and calculated (lines) ethanol liquid penetration and SMD. Black circles: measurements; black solid lines: B_1=40; red dashed lines: B_1=10 in Reitz-KHRT-2 model (C_τ=1, C_{RT}=0.1, $msLimit$=0.2). Injection of droplets with radius 15 μm.*

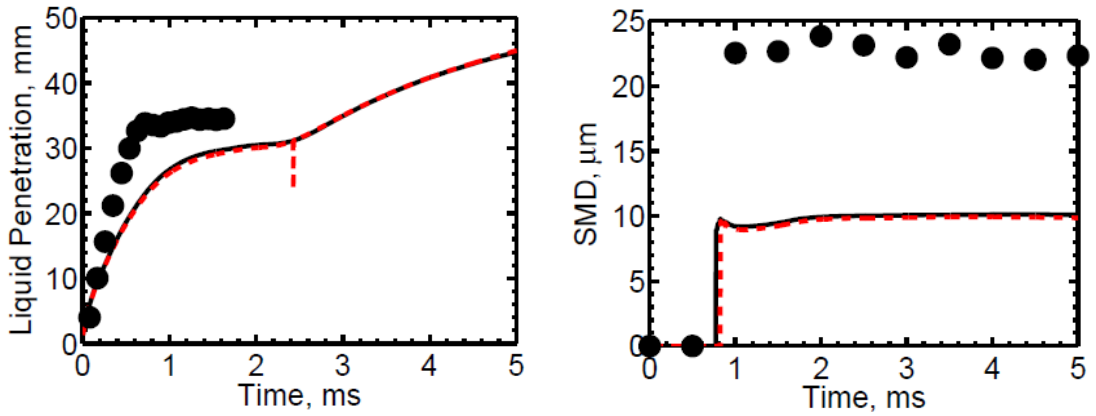

(a)Liquid penetration *(b)SMD at plane*

Figure 3.33: *Comparison of measured (symbols) and calculated (lines) ethanol liquid penetration and SMD. Black circles: measurements; black solid lines: B_1=40; red dashed lines: B_1=10 in Reitz-KHRT-3 model (C_τ=1, C_{RT}=0.1, $msLimit$=0.2). Injection of droplets with radius 15 μm.*

Different combinations of the constants C_τ and C_{RT} in the Reitz-KHRT model have been used in different sprays. Su et al. [74] and Patterson and Reitz [75] used C_τ=1, C_{RT}=5.33, while Beale and Reitz [76] used C_τ=10, C_{RT}=0.1. Therefore, studies of the sensitivity of the models' output to the values of these constants were performed for two versions of Reitz-KHRT model, i.e. Reitz-KHRT-2 and Reitz-KHRT-3.

The effects of varying the constant C_τ on the liquid penetration and SMD predicted by the two versions of the Reitz-KHRT breakup model are shown in Figure 3.34 and Figure 3.35. The initial droplet radius is equal to r=15 μm. In both cases, the constant C_τ in the Reitz-KHRT model was set to either 1 (black solid lines) or 10 (red dashed lines). For the Reitz-KHRT-2 model, the liquid penetration and SMD are weakly affected by C_τ (see Figure 3.34), whereas for the Reitz-KHRT-3 model the liquid penetration curve becomes more saturated and smooth and SMD increases with C_τ (see Figure 3.35).

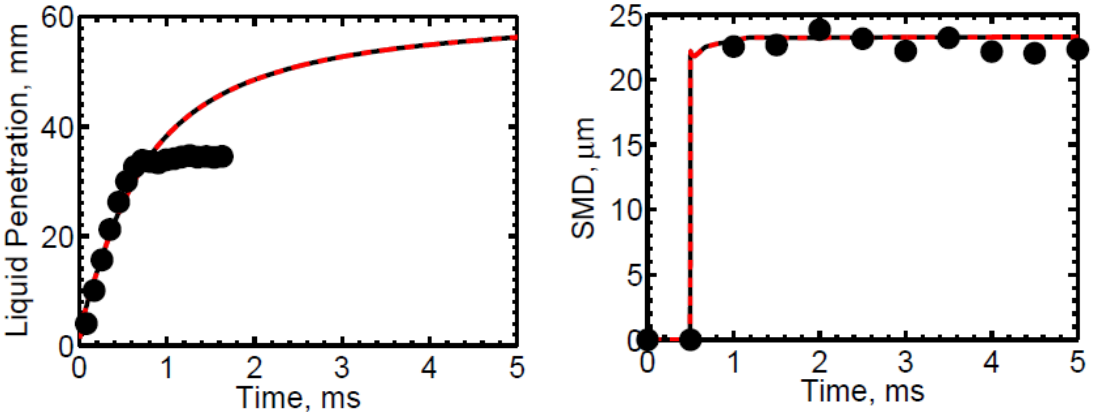

(a)Liquid penetration *(b)SMD at plane*

Figure 3.34: *Comparison of measured (symbols) and calculated (lines) ethanol liquid penetration and SMD. Black circles: measurements; black solid lines: C_τ=1; red dashed lines: C_τ=10 in Reitz-KHRT-2 model (B_1=40, C_{RT}=5.33, $msLimit$=0.03). Injection of droplets with radius 15 μm.*

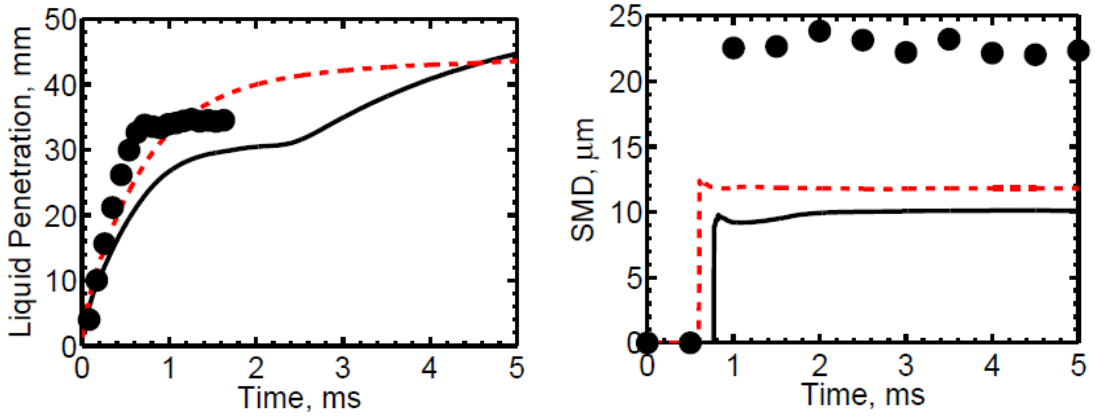

(a)Liquid penetration *(b)SMD at plane*

Figure 3.35: *Comparison of measured (symbols) and calculated (lines) ethanol liquid penetration and SMD. Black circles: measurements; black solid lines: C_τ=1; red dashed lines: C_τ=10 in Reitz-KHRT-3 model (B_1=40, C_{RT}=0.1, $msLimit$=0.2). Injection of droplets with radius 15 μm.*

The effects of the constant C_{RT} on the liquid penetration and SMD predicted using these two versions of the Reitz-KHRT breakup model are shown in Figure 3.36 and Figure 3.37. The initial droplet radius is equal to r=15 μm. In both cases, the value of C_{RT} from the Reitz-KHRT model was set to either 0.1 (black solid lines) or 5.33 (red dashed lines). For both versions of Reitz-KHRT model, the liquid penetration and SMD

increased with an increase in C_{RT}. Note that the Reitz-KHRT-3 model is more sensitive to C_{RT} than the Reitz-KHRT-2 model.

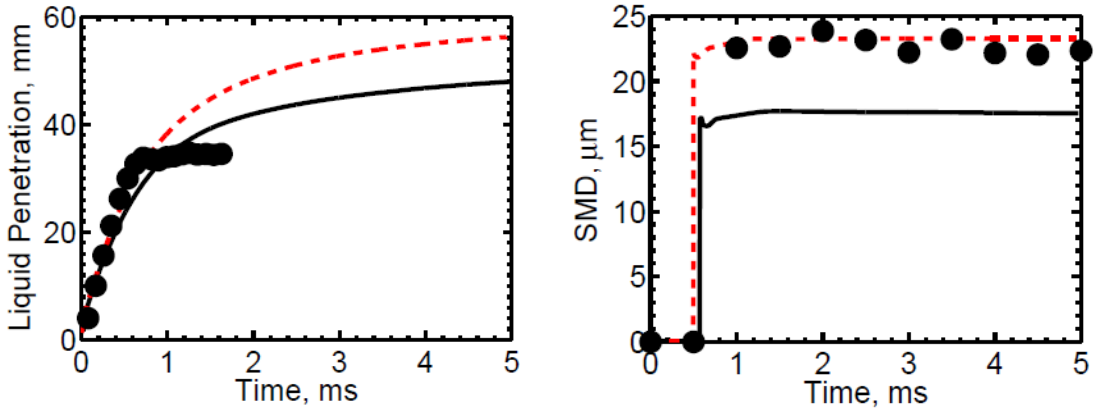

(a)Liquid penetration *(b)SMD at plane*

Figure 3.36: *Comparison of measured (symbols) and calculated (lines) ethanol liquid penetration and SMD. Black circles: measurements; black solid lines: C_{RT}=0.1; red dashed lines: C_{RT}=5.33 in Reitz-KHRT-2 model (B_1=40, C_τ=1, $msLimit$=0.2). Injection of droplets with radius 15 μm.*

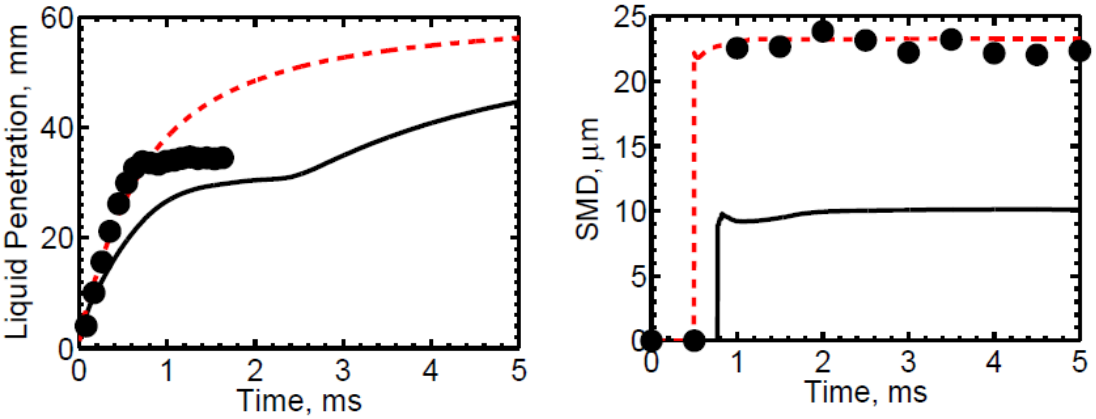

(a)Liquid penetration *(b)SMD at plane*

Figure 3.37: *Comparison of measured (symbols) and calculated (lines) ethanol liquid penetration and SMD. Black circles: measurements; black solid lines: C_{RT}=0.1; red dashed lines: C_{RT}=5.33 in Reitz-KHRT-3 model (B_1=40, C_τ=1, $msLimit$=0.2). Injection of droplets with radius 15 μm.*

The value of the constant *msLimit* recommended by Reitz [71], i.e. *msLimit*=0.03, differs from the default value in OpenFOAM®, i.e. *msLimit* =0.2. Therefore, the sensitivity of two versions of the Reitz-KHRT model, i.e. Reitz-KHRT-2 and Reitz-KHRT-3 to variation *msLimit* was examined. The initial droplet radius in these runs was equal to 15 μm; *msLimit* was set at either 0.2 or 0.03. For both versions of the Reitz-KHRT model, the liquid penetration and SMD (not shown) were weakly affected by *msLimit*.

Other parameters

Grid size dependency is a common problem for many spray atomization and breakup models. Figure 3.38 shows the effect of varying the grid size on the calculated liquid penetration and SMD. Results are shown for a grid size near the injector of 1.60×1.60×2.73 mm (black solid lines) with 131 250 cells and for a grid size of 0.98×0.98×1.34 mm(red dashed lines) with 1 108 230 cells. The hollow cone injector with a Rosin-Rammler distribution (r_m=15 μm, q=2) and the standard Reitz-Diwakar breakup model were applied in both cases. The results show that the calculated liquid penetration increases as the grid size decreases and that the SMD is weakly affected by such variations in grid size.

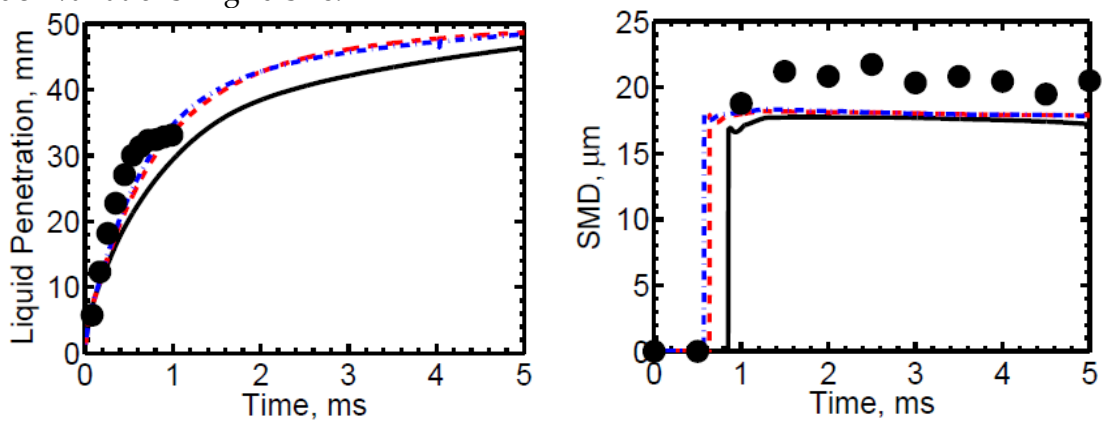

(a)Liquid penetration *(b)SMD at plane*

Figure 3.38: *The effect of changing the grid size (black solid lines: 1.60×1.60×2.73 mm, red dashed lines: 0.98×0.98×1.34 mm on the liquid penetration and SMD of gasoline. Rosin-Rammler distribution (r_m=15 μm, q=2), standard Reitz-Diwakar breakup model, p_a=5 bar, d_{inj}=3 mm.*

If an increased time step yields the same result as the original time step, the computational time by each simulation is substantially reduced. The effect of time step on the calculated liquid penetration and SMD is shown in Figure 3.39. Three test cases were run using the medium mesh (0.98×0.98×1.34 mm) with the hollow cone injector, the Rosin-Rammler distribution (r_m=15 μm, q=2), and the standard Reitz-Diwakar model. For these cases the time step was set to 1 ms (black solid lines), 2.5 ms (red dashed lines), or 5 ms (blue dot-dashed lines). The calculated liquid penetration and SMD were found to be weakly affected by such variations in the time step.

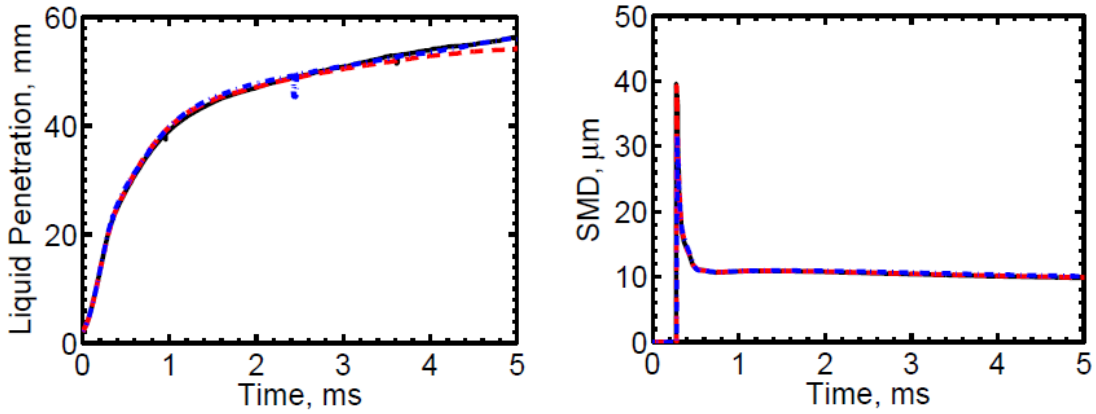

(a)Liquid penetration *(b)SMD at plane*

Figure 3.39: *The effect of varying the time step on the liquid penetration and SMD of gasoline (black solid lines: 1 ms, red dashed lines; 2.5 ms, blue dot-dashed lines: 5 ms) . Rosin-Rammler distribution (r_m=15 μm, q=2), standard Reitz-Diwakar model, medium mesh (0.98×0.98×1.34 mm), p_a=5 bar, d_{inj}=3 mm.*

The accurate simulation of turbulence is essential in spray modeling. The effect of using different turbulence models on the calculated liquid penetration and SMD is shown in Figure 3.40. Three cases were examined using the coarse mesh (1.60×1.60×2.73 mm) with the hollow cone injector, the Rosin-Rammler distribution (r_m=15 μm, q=2), and the standard Reitz-Diwakar breakup model. Three turbulence models were examined: the standard $k-\varepsilon$ model (black solid lines), the RNG $k-\varepsilon$ model [98] (red dashed lines), and the $k-\omega$-SST model [99] (blue dot-dashed lines); the calculated liquid penetration and SMD were weakly affected by these changes.

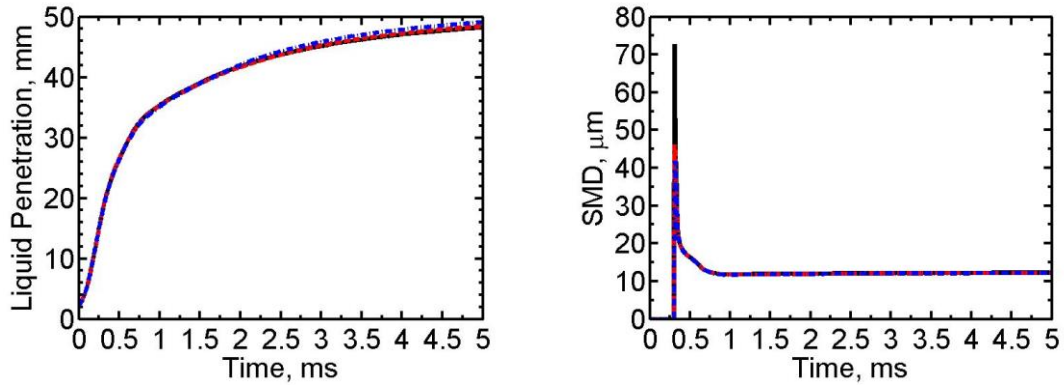

(a)Liquid penetration *(b)SMD at plane*

Figure 3.40: *The effect of changing the turbulence model on the liquid penetration and SMD of ethanol (black solid lines: $k-\varepsilon$, red dashed lines: RNG $k-\varepsilon$, blue dot-dashed lines: $k-\omega$-SST). Rosin-Rammler distribution (r_m=15 μm, q=2), standard Reitz-Diwakar model, coarse mesh (1.60×1.60×2.73 mm), p_a=5 bar, d_{inj}=3 mm.*

Since the methods used to calculate liquid penetration in the experiments and calculations are similar but not identical, it was considered important to check the sensitivity of the computed results to the threshold used to define the depth of liquid penetration. The penetration depths calculated using thresholds of 90% and 95% of the injected fuel mass are shown in Figure 3.41, as calculated using the Rosin-Rammler

droplet distribution (r_m=15 μm, q=2), the Reitz-Diwakar model and the O'Rourke collision model. Before 1 ms the liquid penetrations calculated using the two thresholds are very similar; at later timesteps, the liquid penetration calculated using a threshold of 90% is lower than that obtained with a threshold of 95%.

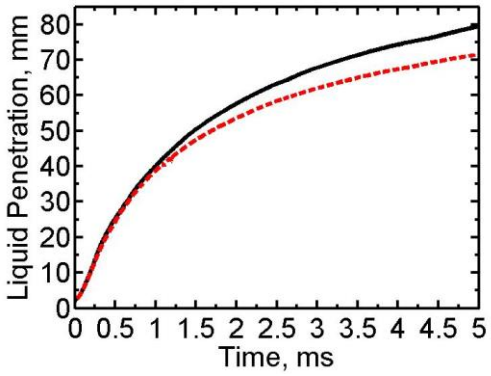

Figure 3.41: *The effect of varying the threshold used to define the depth of liquid penetration on the predicted liquid penetration for ethanol (black solid line: 95%, red dashed line: 90%). Rosin-Rammler droplet distribution (r_m=15 μm, q=2), standard Reitz-Diwakar breakup model, O'Rourke collision model, coarse mesh (1.60×1.60×2.73 mm), p_a=5 bar, d_{inj}=3 mm.*

Finally, since the mass injection rate $\dot{m}(t)$ is usually unknown in the experiments, it was important to test the effect of varying the mass injection profile on the calculated liquid penetration and SMD. Two profiles which have the same shapes as in Figure 3.42 were tested using the VSB2 model. The differences between the two injection profiles were found to weakly affect the liquid penetration and SMD (see Figure 3.42.

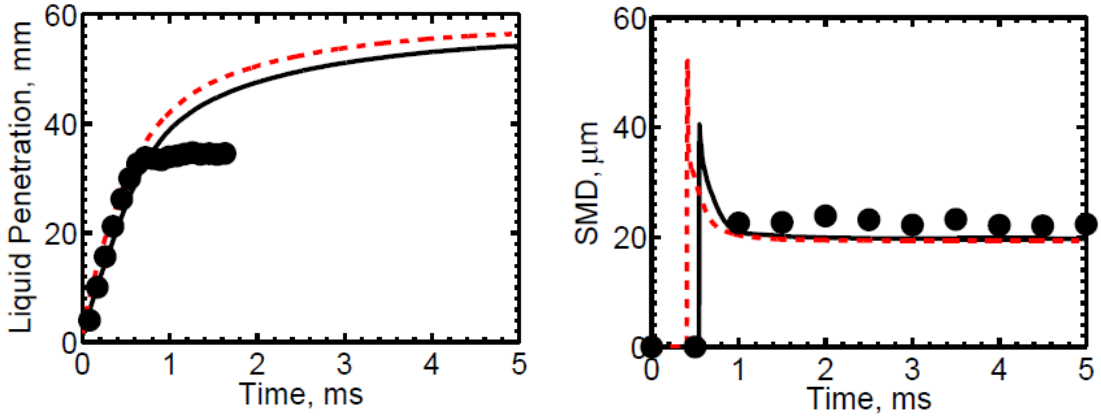

(a)Liquid penetration *(b)SMD at plane*

Figure 3.42: *Comparison of the measured (symbols) and calculated (lines) liquid penetration and SMD of ethanol. Black circles: measurements; black solid lines: trapezoidal shape with 0.6 ms injection duration; red dashed lines: rectangular shape with 0.4 ms injection duration. Rosin-Rammler distribution, VSB2 model.*

3.4.2. Model comparison

Comparative evaluation of the models

In order to identify a suitable secondary breakup model for the desired simulations, the influence of various secondary breakup models (i.e. TAB and Reitz-Diwakar) on the liquid penetration and SMD calculated using two different primary atomization models were studied: the LISA model (see Figure 3.43) and the Rosin-Rammler distribution (r_m=15 μm, q=2); see Figure 3.44. The SMDs were less than 5 μm for both LISA + TAB and Rosin-Rammler + standard TAB. The liquid penetration is more saturated for both (i) LISA + standard Reitz-Diwakar and (ii) Rosin-Rammler + standard Reitz-Diwakar as compared to those obtained using the standard TAB model, and the SMD calculated using the standard Reitz-Diwakar model is larger than that obtained using the standard TAB model in both cases.

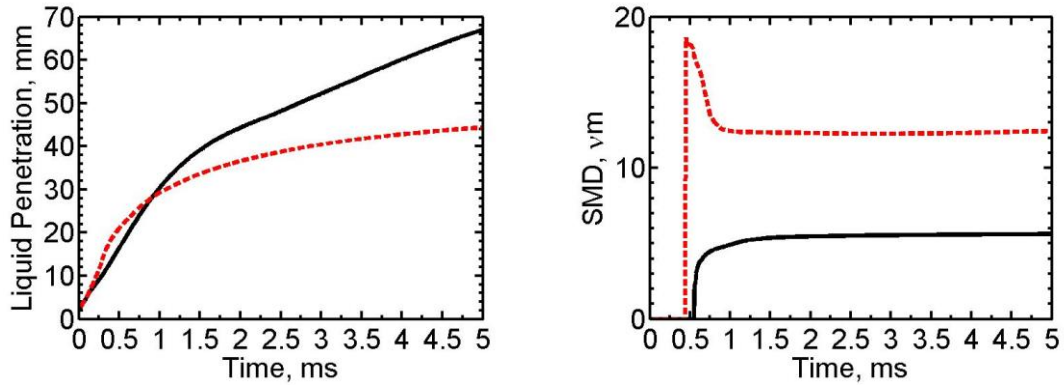

(a)Liquid penetration *(b)SMD at plane*

Figure 3.43: *The effect of using different secondary breakup models (black solid lines: standard TAB, red dashed lines: standard Reitz-Diwakar) on the liquid penetration and SMD of ethanol. LISA (gas temperature and correct Rosin-Rammler with q=2), coarse mesh (1.60×1.60×2.73 mm), p_a=5 bar, d_{inj}=3 mm.*

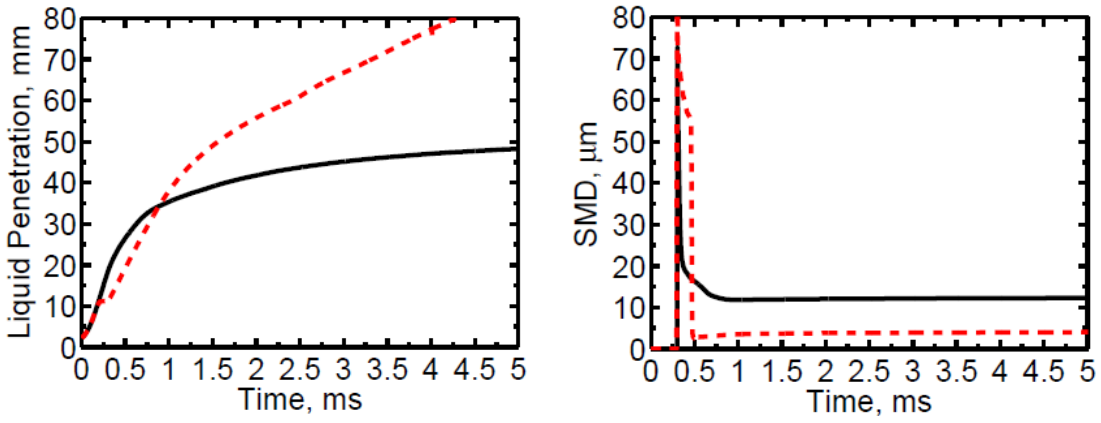

(a)Liquid penetration *(b)SMD at plane*

Figure 3.44: *The effect of using different secondary breakup models (black solid lines: standard TAB, red dashed lines: standard Reitz-Diwakar) on the liquid penetration and SMD of ethanol. Rosin-Rammler distribution (r_m=15 μm, q=2), coarse mesh (1.60×1.60×2.73 mm), p_a=5 bar, d_{inj}=3 mm.*

The effect of varying the collision model

The effect of varying the collision model (i.e. using the modified O'Rourke or the modified trajectory model) on liquid penetration and SMD is shown in Figure 3.45 for calculations using the LISA + standard TAB models. The liquid penetration and SMD obtained when using the modified O'Rourke model (red dashed lines) are considerably greater than those obtained when no collision model is used (black solid lines). The modified trajectory model (blue dot-dashed lines) had a modest effect on both liquid penetration and SMD; the plot of the results obtained using this collision model closely resembles that generated by using no collision model whatsoever.

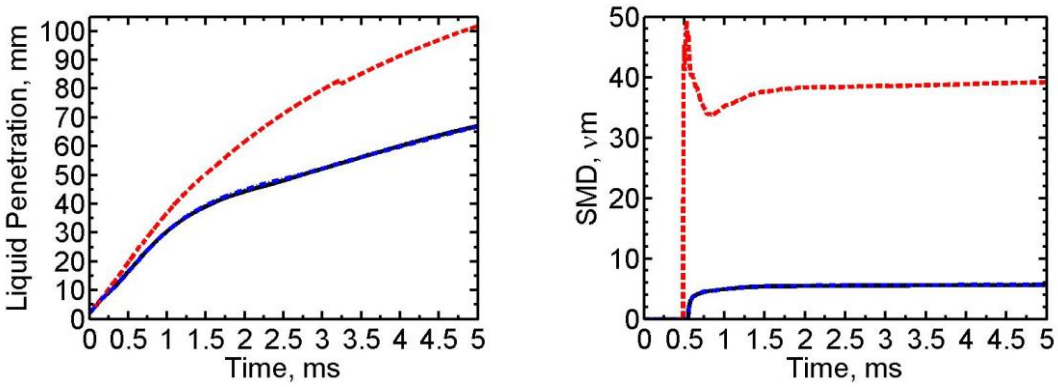

(a)Liquid penetration *(b)SMD at plane*

Figure 3.45: *The effect of varying the collision model (black solid lines: w/o collision model; red dashed lines: modified O'Rourke, blue dot-dashed lines: modified trajectory) on the liquid penetration and SMD of ethanol. LISA and standard TAB models, coarse mesh (1.60×1.60×2.73 mm), p_a=5 bar, d_{inj}=3 mm.*

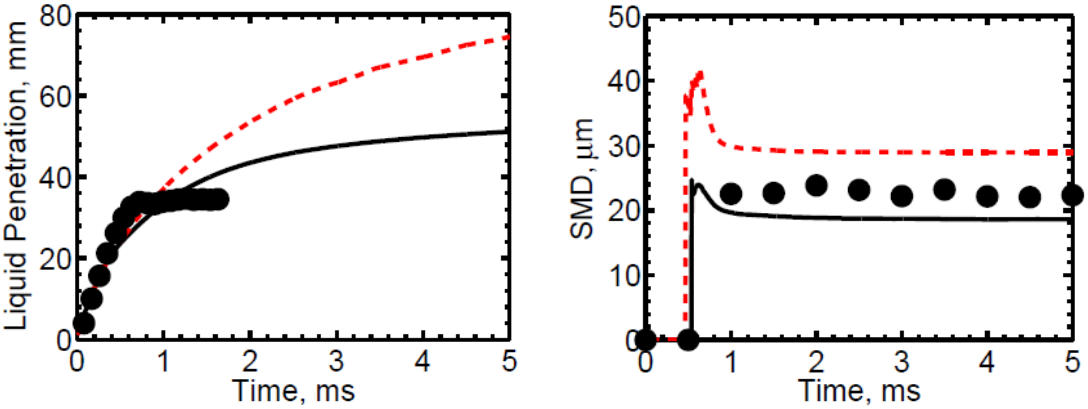

(a)Liquid penetration *(b)SMD at plane*

Figure 3.46: *The effect of including the O'Rourke collision model (black solid lines: w/o O'Rourke, red dashed lines: w O'Rourke) on the liquid penetration and SMD of ethanol. LISA + Reitz-Diwakar models.*

The effect of using the modified O'Rourke collision model on the liquid penetration and SMD calculated with the following different combinations of spray models was studied: (i) LISA + Reitz-Diwakar (see Figure 3.46), (ii) Rosin-Rammler distribution + Reitz-Diwakar (see Figure 3.47), (iii) uniform droplet size distribution (r=15 µm) + Reitz-KHRT-3 (see Figure 3.48, (iv) uniform droplet size distribution (r=15 µm) + Reitz-

KHRT-1 (see Figure 3.49). In all of these cases, the calculated liquid penetration and SMD were substantially increased when the O'Rourke model was used.

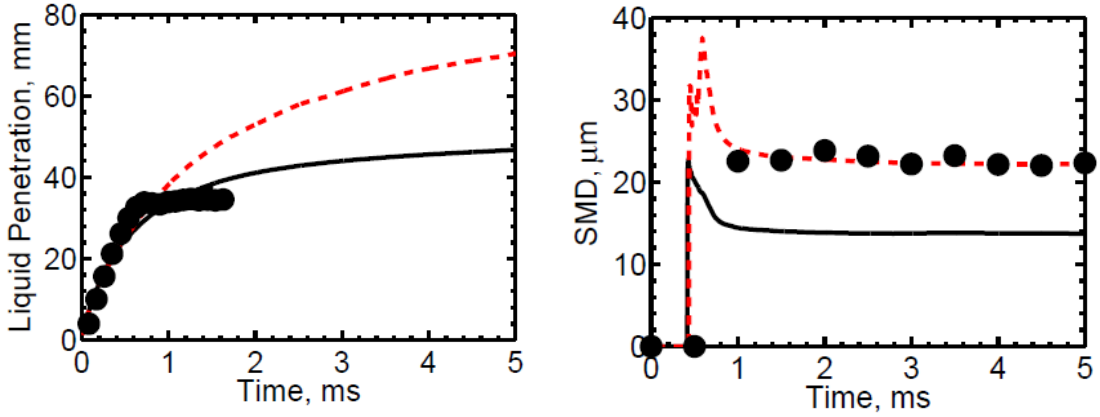

(a)Liquid penetration *(b)SMD at plane*

Figure 3.47: *The effect of including the O'Rourke collision model (black solid lines: w/o O'Rourke, red dashed lines: w O'Rourke) on the liquid penetration and SMD of ethanol. Rosin-Rammler distribution + Reitz-Diwakar model.*

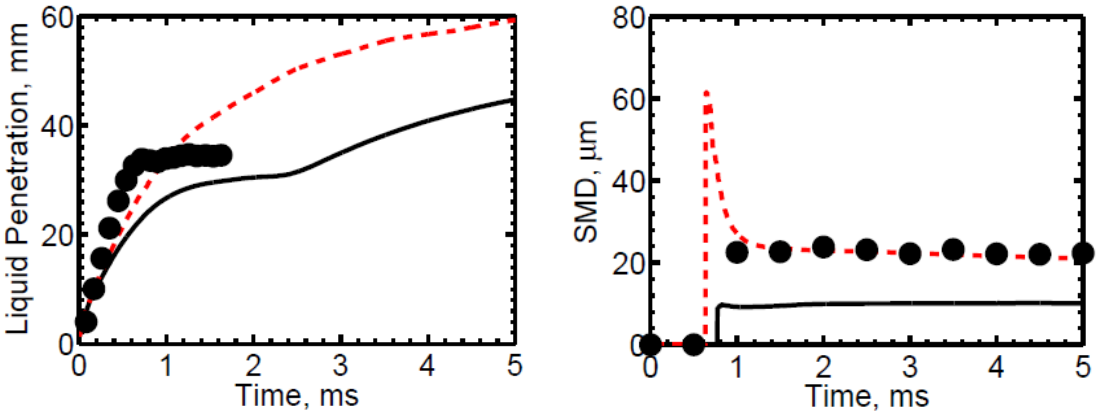

(a)Liquid penetration *(b)SMD at plane*

Figure 3.48: *The effect of including the O'Rourke collision model (black solid lines: w/o O'Rourke, red dashed lines: w O'Rourke) on the liquid penetration and SMD of ethanol. Uniform droplet radius 15 µm and Reitz-KHRT-3 model (B_1=40, C_τ=1, C_{RT}=0.1, $msLimit$=0.2).*

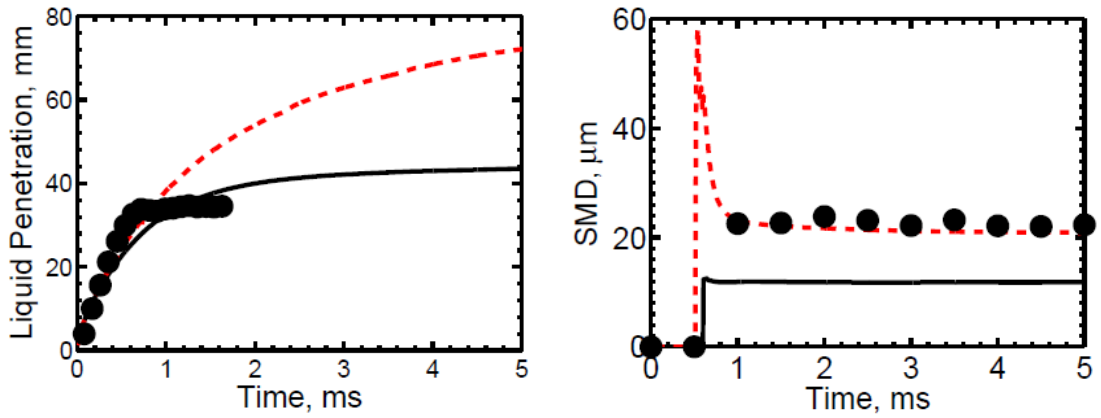

(a)Liquid penetration *(b)SMD at plane*

Figure 3.49: *The effect of using the O'Rourke collision model (black solid lines: w/o O'Rourke, red dashed lines: w O'Rourke) on the liquid penetration and SMD of ethanol. Uniform droplet radius 15 µm and Reitz-KHRT-1 model (B_1=40, C_τ=10, C_{RT}=0.1, $msLimit$=0.2).*

3.4.3. Validation

Uniform droplet size distribution (r=15 µm) + Reitz-KHRT-2 model

A comparison of the measured (symbols) and calculated (lines) gasoline liquid penetration and SMD for different injection pressures, i.e. p_{inj}=50, 125, 200 bar, is shown in Figure 3.50. The calculated liquid penetrations and SMDs show acceptable agreement with the measurements, and both simulation and measurement show that the liquid penetration increases with the injection pressure. However, the calculated SMD for p_{inj}=50 bar is larger than that measured at the end of the spray. This discrepancy might be due to several factors. First, there is difference in locations when acquiring data. In the measurements the SMD of droplets was sampled within a single probe volume defined by two laser beams, whereas in simulations the SMD was calculated by calculating all the droplets within a ring. Second, the mass flow rate of the injector is unknown in the current simulation. Experimental data on SMD at p_{inj}=125 bar are not shown in Figure 3.50 because these data were not reported by Hemdal et al. [21].

A comparison of the measured (symbols) and calculated (lines) gasoline liquid penetration for different ambient and fuel temperatures is shown in Figure 3.51. The calculated liquid penetrations show acceptable agreement with the measurements, with the ambient and fuel temperatures weakly affecting the computed liquid penetration in line with the experiments. No comparison of the measured and calculated SMD for gasoline at different ambient and fuel temperatures is shown because such experimental data were not reported by Hemdal et al. [21].

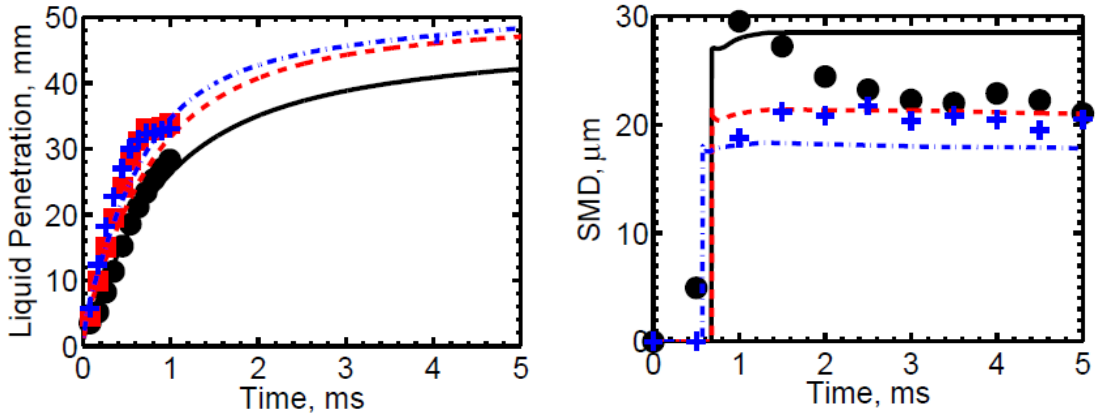

(a)Liquid penetration *(b)SMD at plane*

Figure 3.50: *Comparison of measured (symbols) and calculated (lines) gasoline liquid penetration and SMD for different injection pressures. Black circles and solid lines: p_{inj}=50 bar; red squares and dashed lines: p_{inj}=125 bar; blue pluses and dot-dashed lines: p_{inj}=200 bar. Uniform droplet size distribution (r=15 μm) and Reitz-KHRT-2 model (B_1=40, C_τ=1, C_{RT}=5.33, $msLimit$=0.03).*

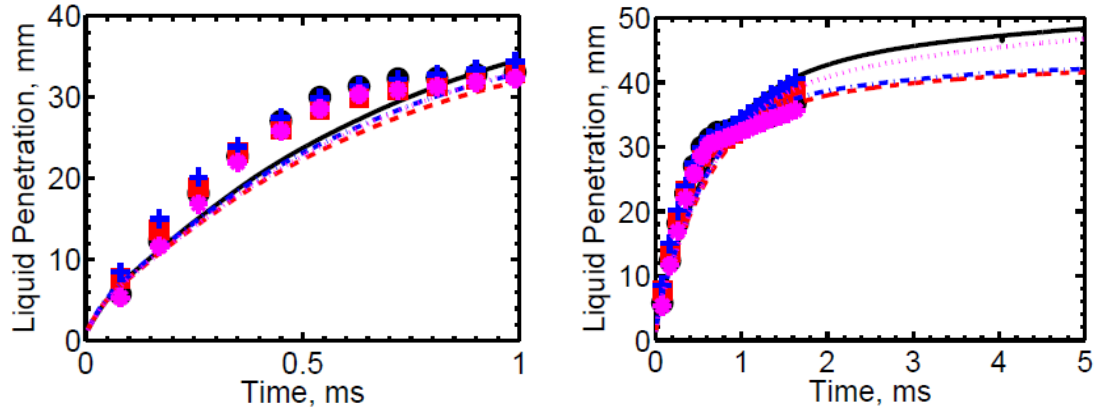

(a)Liquid penetration *(b)SMD at plane*

Figure 3.51: *Comparison of measured (symbols) and calculated (lines) gasoline liquid penetration and SMD for different ambient and fuel temperatures. Black circles and solid lines: T_a=350 K, T_f=243 K; red squares and dashed lines: T_a=295 K, T_f=295 K; blue pluses and dot-dashed lines: T_a=350 K, T_f=320K; magenta stars and dotted lines: T_a=295 K, T_f=243 K. Uniform droplet size distribution (r=15 μm) and Reitz-KHRT-2 model (B_1=40, C_τ=1, C_{RT}=5.33, $msLimit$=0.03).*

A comparison of the measured (symbols) and calculated (lines) liquid penetration and SMD of ethanol at different injection pressures, i.e. p_{inj}=50, 125, 200 bar, is shown in Figure 3.52. The calculated liquid penetrations are higher than those measured experimentally after 1 ms. The calculated SMD for p_{inj}=200 bar agrees well with the measurements, whereas the calculated SMD for p_{inj}=50 bar is overpredicted at the end of the spray. Experimental data on SMD at p_{inj}=125 bar are not shown in Figure 3.52 (b) because such data were not reported by Hemdal et al. [21].

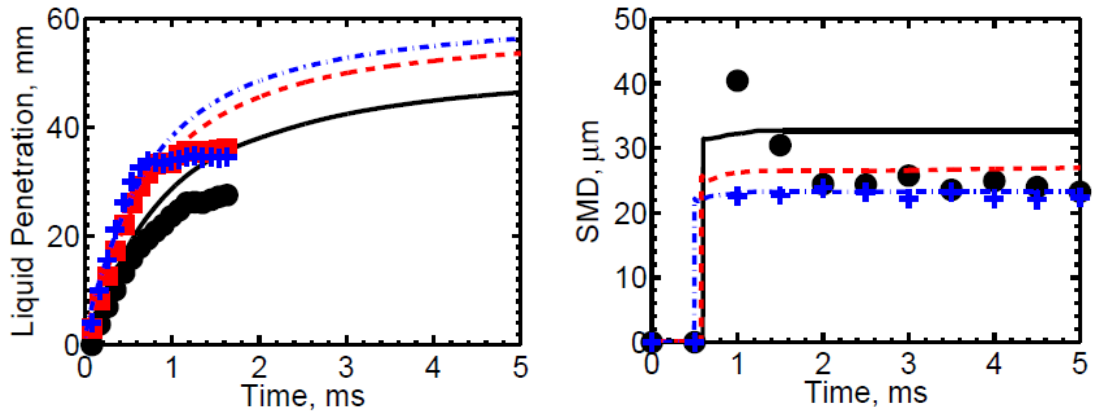

(a)Liquid penetration *(b)SMD at plane*

Figure 3.52: *Comparison of the measured (symbols) and calculated (lines) liquid penetration and SMD of ethanol for different injection pressures. Black circles and solid lines: p_{inj}=50 bar; red squares and dashed lines: p_{inj}=125 bar, blue pluses and dot-dashed lines: p_{inj}=200 bar. Uniform droplet size distribution (r=15 µm) and Reitz-KHRT-2 model (B_1=40, C_τ=1, C_{RT}=5.33, $msLimit$=0.03).*

Figure 3.53 shows a comparison of the measured (symbols) and calculated (lines) liquid penetration and SMD of ethanol at different ambient and fuel temperatures. The calculated liquid penetrations and SMDs show acceptable agreement with experimental data. In keeping with the experimental findings, the fuel temperature has only a modest effect on the computed liquid penetration. At lower air and higher fuel temperatures, the computed results agree well with the available experimental data (cf. dashed lines with squares). Under cold start conditions, the computed liquid penetration is overpredicted at 1 ms as was previously noted when discussing Figure 3.52.

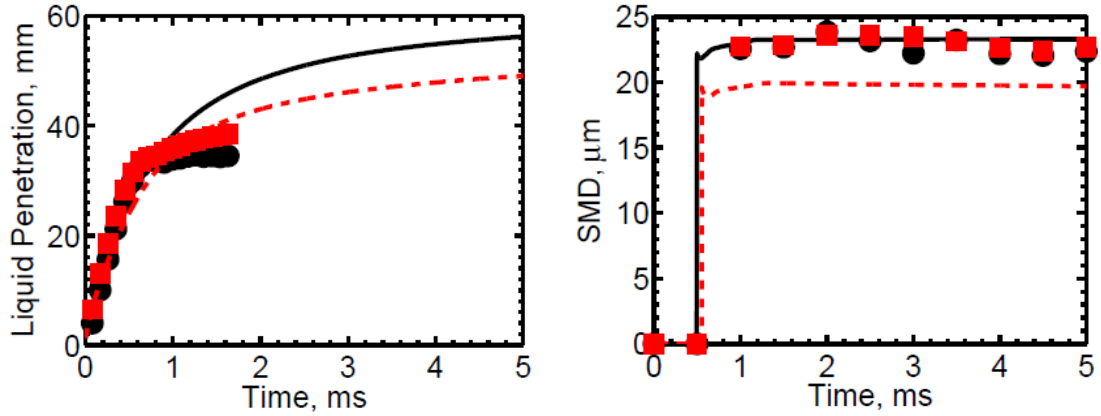

(a)Liquid penetration *(b)SMD at plane*

Figure 3.53: *Comparison of the measured (symbols) and calculated (lines) liquid penetration and SMD of ethanol for different ambient and fuel temperatures. Black circles and solid lines: T_a=350 K, T_f=243 K; red squares and dashed lines: T_a=295 K, T_f=295 K. Uniform droplet size distribution (r=15 µm) and Reitz-KHRT-2 model (B_1=40, C_τ=1, C_{RT}=5.33, $msLimit$=0.03).*

The calculated velocity vector field for an ethanol hollow cone spray at 1 ms after the start of injection is shown in Figure 3.54. A double-vortex with the form of a figure

eight is observed. A similar vortex was observed with a uniform droplet distribution + the Reitz-KHRT-3 model (see Figure 3.63), whereas a single strong vortex on each side was observed with the Rosin-Rammler + standard Reitz-Diwakar models (see Figure 3.58), the LISA + Reitz-Diwakar models (see Figure 3.68), and the VSB2 model (see Figure 3.73).

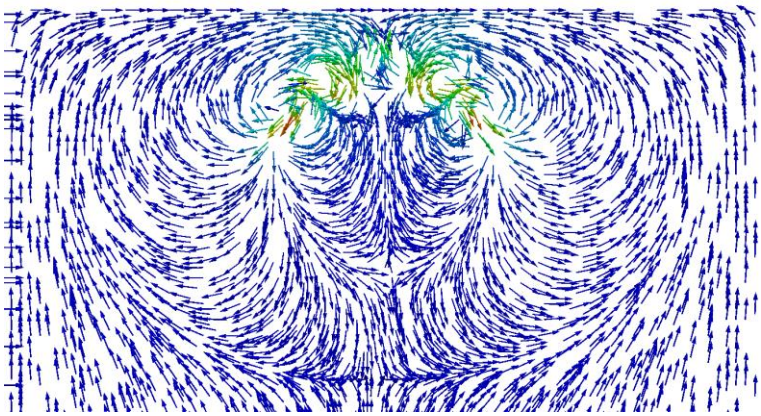

Figure 3.54: *The calculated velocity vector field at 1 ms after start of injection, using ethanol with a uniform droplet size distribution (r=15 μm) and the Reitz-KHRT-2 model (B_1=40, C_τ=1, C_{RT}=5.33, $msLimit$=0.03).*

Rosin-Rammler distribution + standard Reitz-Diwakar model

A comparison of the measured (symbols) and calculated (lines) liquid penetration and SMD of gasoline at different injection pressures, i.e. p_{inj}=50, 125, 200 bar, is shown in Figure 3.55. The calculated liquid penetrations show acceptable agreement with the experimental data, at least at p_{inj}=200 bar, and both simulation and measurement indicate that the liquid penetration increases as the injection pressure rises. The calculated SMDs are lower than those measured, and they decrease as the injection pressure rises. In contrast, the measured SMDs are almost independent of the injection pressure at the end of the measurement.

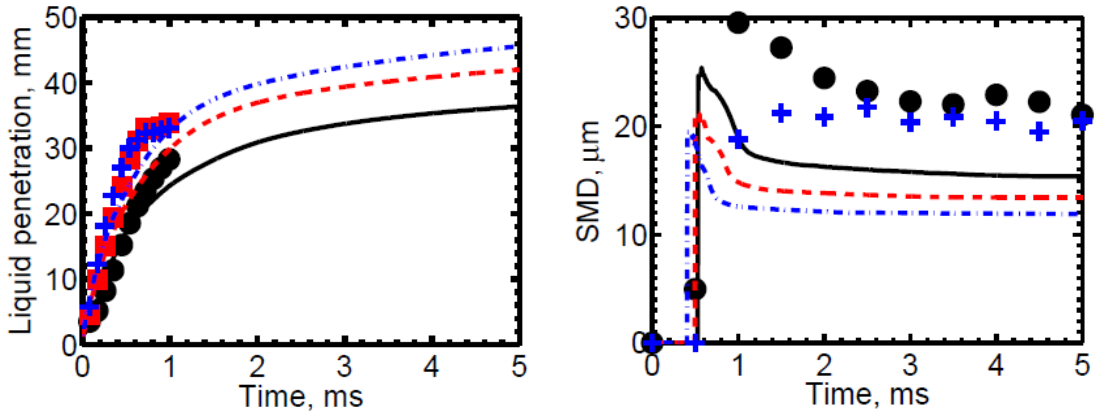

(a)Liquid penetration *(b)SMD at plane*

Figure 3.55: *Comparison of the measured (symbols) and calculated (lines) liquid penetration and SMD of gasoline at different injection pressures. Black circles and solid lines: p_{inj}=50 bar; red squares and dashed lines: p_{inj}=125 bar; blue pluses and dot-dashed lines: p_{inj}=200 bar. Rosin-Rammler distribution and standard Reitz-Diwakar model.*

The measured (symbols) and calculated (lines) liquid penetration of gasoline at different ambient and fuel temperatures are compared in Figure 3.56. The calculated liquid penetrations are in good agreement with the experimental data; in both cases, the depth of liquid penetration is found to be only weakly dependent on the ambient and fuel temperatures.

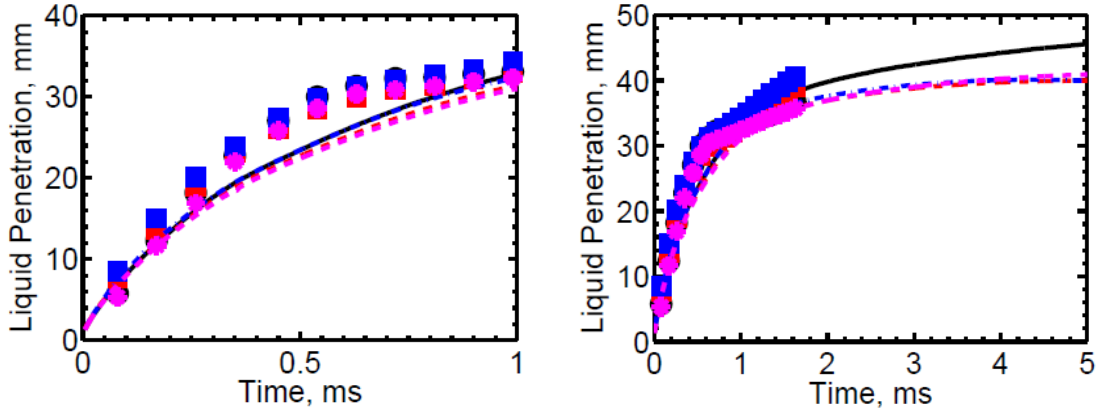

(a)Liquid penetration *(b)SMD at plane*

Figure 3.56: *Comparison of the measured (symbols) and calculated (lines) liquid penetration and SMD of gasoline at different ambient and fuel temperatures. Black circles and solid lines: T_a=350 K, T_f=243 K; red squares and dashed lines: T_a=295 K, T_f=295 K; blue pluses and dot-dashed lines: T_a=350 K, T_f=320K; magenta stars and dotted lines: T_a=295 K, T_f=243 K. Rosin-Rammler distribution and standard Reitz-Diwakar model.*

Figure 3.57 compares the measured (symbols) and calculated (lines) liquid penetration and SMD of ethanol at different injection pressures, i.e. p_{inj}=50, 200 bar. The calculated liquid penetrations agree well with the measurements, and both simulation and measurement indicate that the liquid penetration increases with an increase in the injection pressure. The calculated SMDs are lower than those that were measured. The computed SMDs decrease as the injection pressure rises, whereas the

measured SMDs are almost the same for different injection pressures at the end of the measurement.

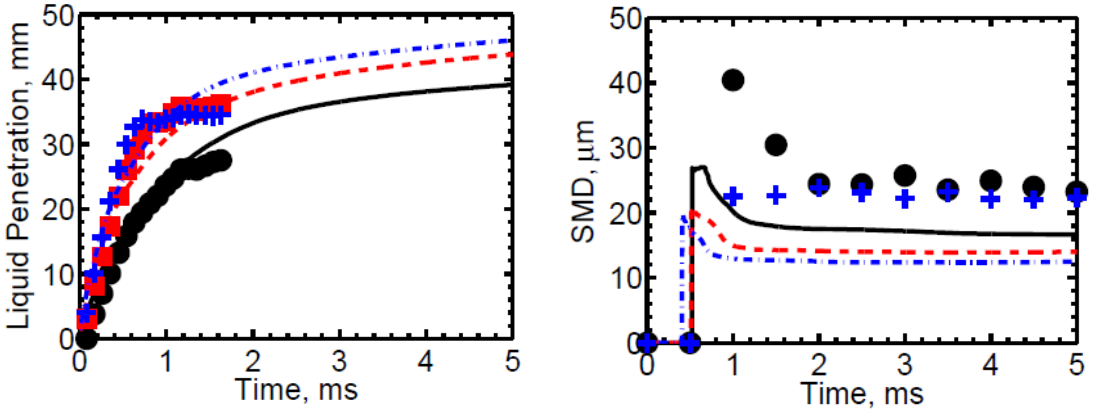

(a)Liquid penetration *(b)SMD at plane*

Figure 3.57: *Comparison of measured (symbols) and calculated (lines) liquid penetration and SMD of ethanol at different injection pressures. Black circles and solid lines: p_{inj}=50 bar; red squares and dashed lines: p_{inj}=200 bar. Rosin-Rammler distribution and standard Reitz-Diwakar model.*

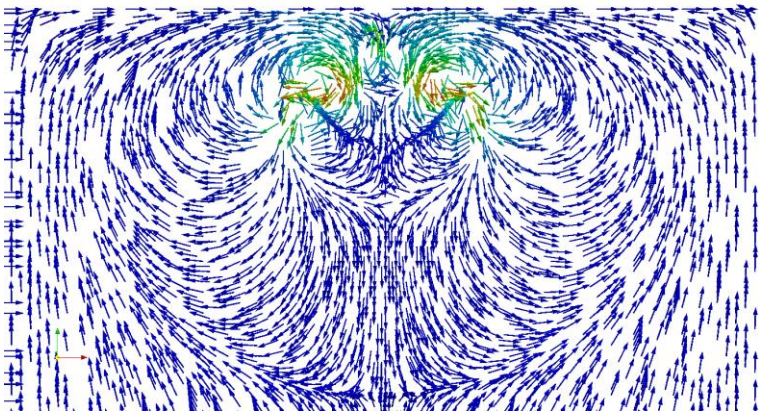

Figure 3.58: *The calculated velocity vector field at 1 ms after start of injection, using ethanol with a uniform droplet size distribution (r=15 µm) and the Reitz-KHRT-2 model (B_1=40, C_τ=1, C_{RT}=5.33, $msLimit$=0.03).*

A comparison of the measured (symbols) and calculated (lines) liquid penetration and SMD of ethanol for different ambient and fuel temperatures is shown in Figure 3.59. The calculated values agree well with the measurements; in both cases, the ambient and fuel temperatures only weakly affect the liquid penetration. The calculated SMD is lower than was measured.

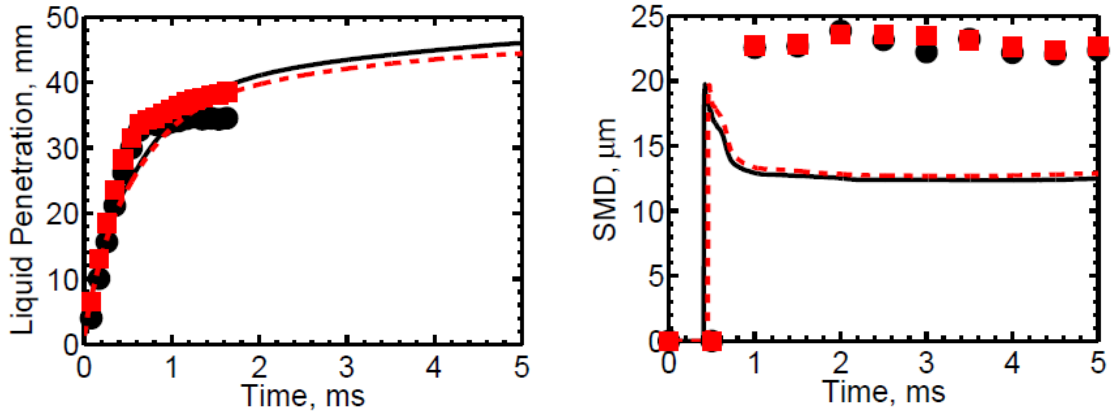

(a)Liquid penetration *(b)SMD at plane*

Figure 3.59: *Comparison of the measured (symbols) and calculated (lines) liquid penetration and SMD of ethanol at different ambient and fuel temperatures. Black circles and solid lines: T_a=350 K, T_f=243 K; red squares and dashed lines: T_a=295 K, T_f=295 K. Rosin-Rammler distribution and standard Reitz-Diwakar model.*

Uniform droplet size distribution (r=15 µm) + Reitz-KHRT-3 model

The measured (symbols) liquid penetration and SMD of gasoline for injection pressures of p_{inj}=50 and 200 bar are compared to those calculated (lines) using a uniform droplet size distribution (r=15 µm) and the Reitz-KHRT-3 model in Figure 3.60. The calculated liquid penetrations are lower than those that were measured, and both simulation and measurement indicate that the liquid penetration increases as the injection pressure rises.

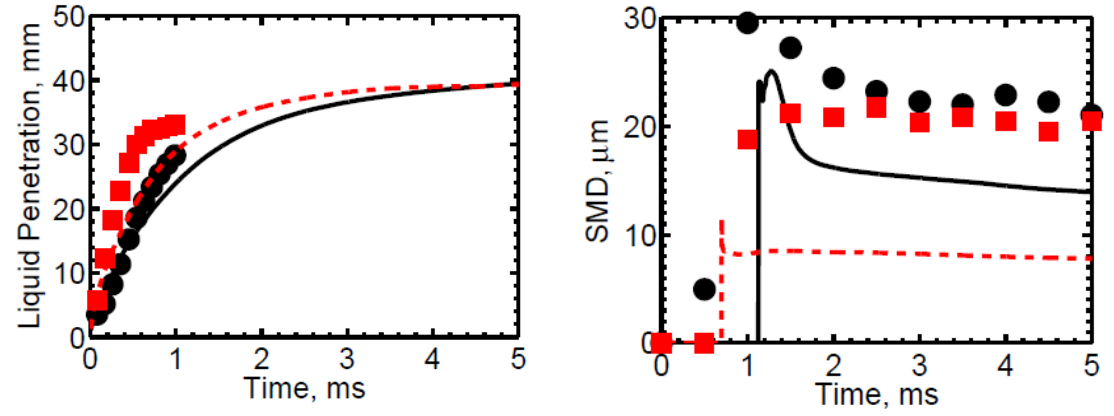

(a)Liquid penetration *(b)SMD at plane*

Figure 3.60: *Comparison of measured (symbols) and calculated (lines) gasoline liquid penetration and SMD for different injection pressures. Black circles and solid lines: p_{inj}=50 bar; red squares and dashed lines: p_{inj}=200 bar. Uniform droplet size distribution (r=15 µm) and the Reitz-KHRT-3 model (B_1=40, C_τ=10, C_{RT}=0.1, $msLimit$=0.03).*

The measured (symbols) and calculated (lines) liquid penetration and SMD of gasoline for different ambient and fuel temperatures are compared in Figure 3.61. The calculated liquid penetrations are lower than those that were measured, and the ambient and fuel temperatures only weakly affect the liquid penetration. The calculated SMD is sensitive to the ambient and fuel temperatures.

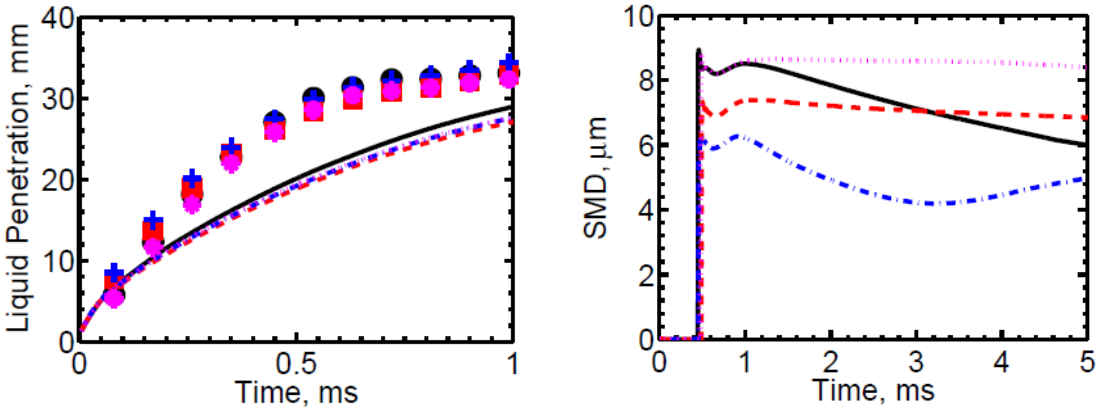

(a)Measured (symbols) and calculated (lines) liquid penetration

(b)Calculated (lines) SMD at plane

Figure 3.61: *Calculated and measured liquid penetration and SMD of gasoline at different ambient and fuel temperatures. Black circles and solid lines: T_a=350 K, T_f=243 K; red squares and dashed lines: T_a=295 K, T_f=295 K; blue pluses and dot-dashed lines: T_a=350 K, T_f=320K; magenta stars and dotted lines: T_a=295 K, T_f=243 K). Uniform droplet size distribution (r=15 µm) and the Reitz-KHRT-3 model (B_1=40, C_τ=10, C_{RT}=0.1, $msLimit$=0.03).*

A comparison of the measured (symbols) and calculated (lines) liquid penetration and SMD of ethanol for different injection pressures, i.e. p_{inj}=50, 200 bar, is shown in Figure 3.62. The calculated liquid penetration for p_{inj}=50 bar is higher than that which was measured, whereas the calculated liquid penetration for p_{inj}=200 bar is lower than was measured. Both simulation and experiment indicate that liquid penetration increases with an increase in the injection pressure. The calculated SMD for p_{inj}=50 bar agrees well with the experimental result, whereas the SMD for p_{inj} =200 bar is underpredicted.

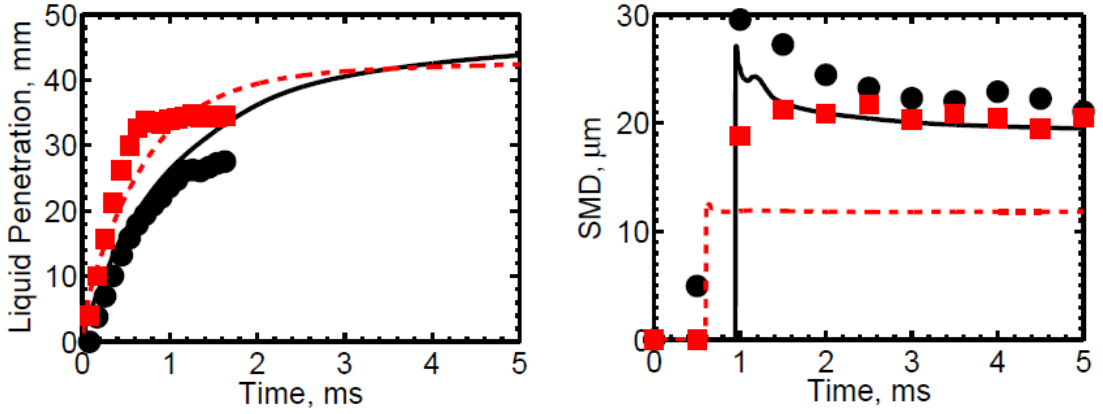

(a)Liquid penetration

(b)SMD at plane

Figure 3.62: *Comparison of measured (symbols) and calculated (lines) liquid penetration and SMD of ethanol for different injection pressures. Black circles and solid lines: p_{inj}=50 bar; red squares and dashed lines: p_{inj}=200 bar. Uniform droplet size distribution (r=15 µm) and the Reitz-KHRT-3 model (B_1=40, C_τ=10, C_{RT}=0.1, $msLimit$=0.03).*

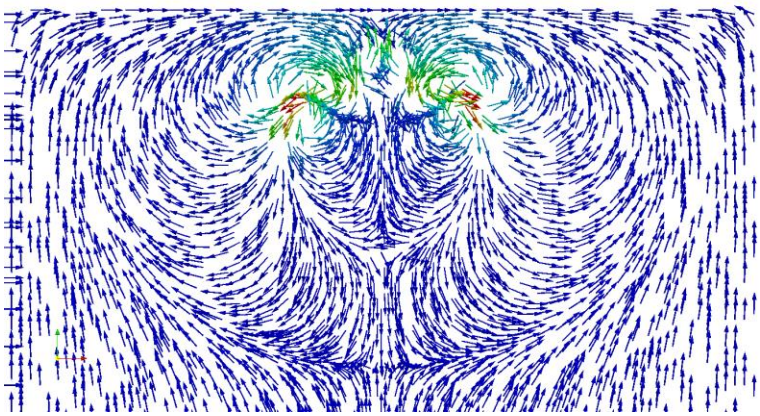

Figure 3.63: *The calculated velocity vector fields for an ethanol hollow cone spray at 1ms after the start of injection, simulated using a uniform droplet size distribution (r=15 μm) and the Reitz-KHRT-3 model (B_1=40, C_τ=10, C_{RT}=0.1, $msLimit$=0.03).*

A comparison of the measured (symbols) and calculated (lines) liquid penetration and SMD of ethanol for different ambient and fuel temperatures is shown in Figure 3.64. The calculated liquid penetrations and SMDs are lower than the measurements. As was observed experimentally, the fuel temperatures weakly affect the computed liquid penetration.

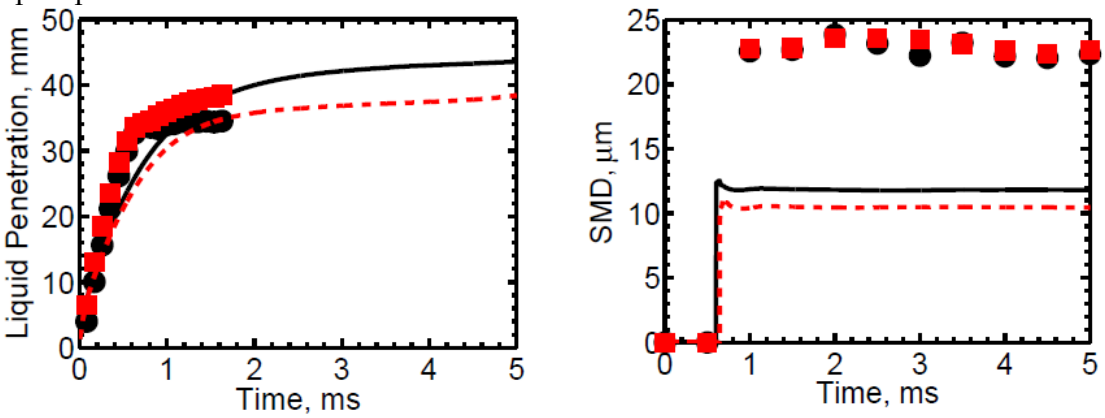

(a)Liquid penetration *(b)SMD at plane*

Figure 3.64: *Comparison of measured (symbols) and calculated (lines) liquid penetration and SMD of ethanol for different ambient and fuel temperatures. Black circles and solid lines: T_a=350 K, T_f=243 K; red squares and dashed lines: T_a=295 K, T_f=295 K. Uniform droplet size distribution (r=15 μm) and the Reitz-KHRT-3 model (B_1=40, C_τ=10, C_{RT}=0.1, $msLimit$=0.03).*

LISA + Reitz-Diwakar models

A comparison of the measured (symbols) and calculated (lines) liquid penetration and SMD of gasoline for different injection pressures, i.e. p_{inj}=50, 200 bar, is shown in Figure 3.65. The calculated liquid penetrations are lower than the measurements, and simulation shows the liquid penetration for p_{inj}=50 bar is higher than that for p_{inj}=200 bar after 2.5 ms. The calculated SMD for p_{inj} =50 bar agrees well with the measurements, whereas the calculated SMD for p_{inj}=200 bar is underpredicted.

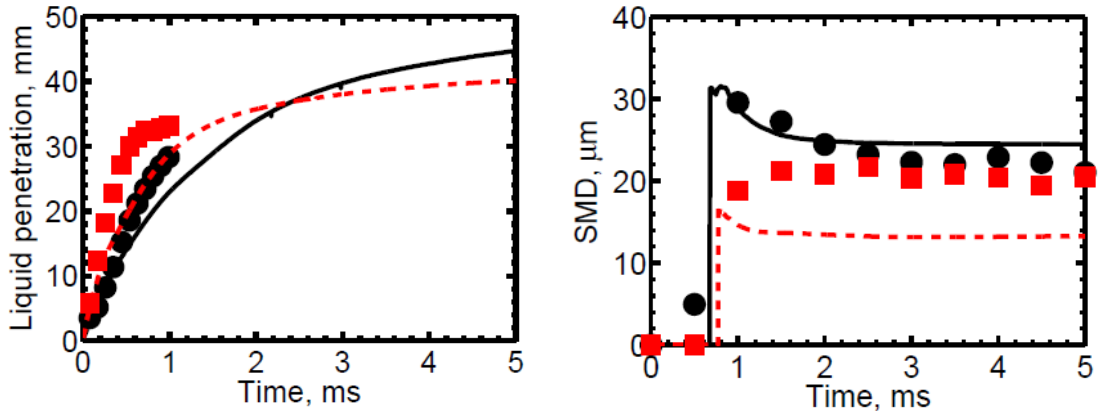

(a)Liquid penetration *(b)SMD at plane*

Figure 3.65: *Comparison of the measured (symbols) and calculated (lines) liquid penetration and SMD of gasoline for different injection pressures. Black circles and solid lines: p_{inj}=50 bar; red squares and dashed lines: p_{inj}=200 bar. LISA and standard Reitz-Diwakar models.*

A comparison of the measured (symbols) and calculated (lines) liquid penetration of gasoline for different ambient and fuel temperatures is shown in Figure 3.66. The calculated liquid penetrations are lower than the measurements; in both the experiments and the simulations, the liquid penetration was only weakly dependent on the ambient temperature and fuel temperature. The calculated SMD is sensitive to the ambient and fuel temperatures.

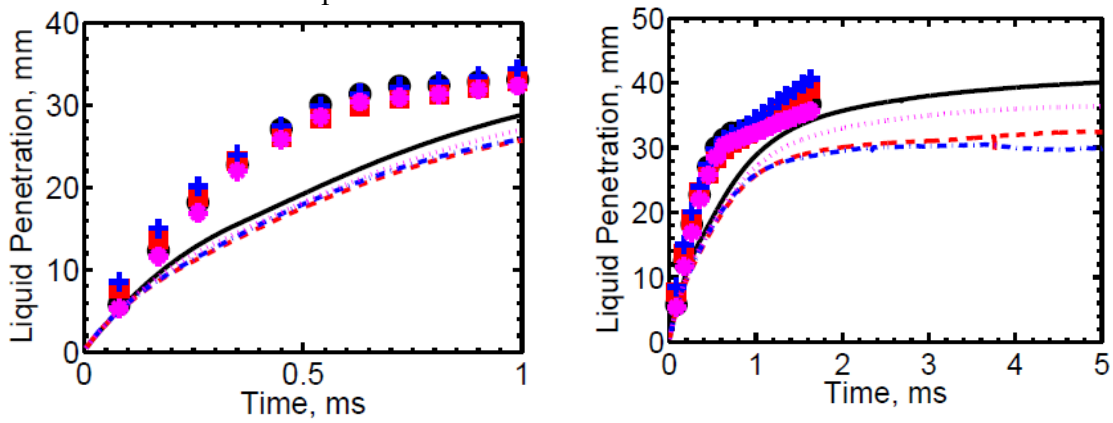

(a)0-1 ms *(b)0-5 ms*

Figure 3.66: *Comparison of measured (symbols) and calculated (lines) gasoline liquid penetration for different ambient and fuel temperatures. Black circles and solid lines: T_a=350 K, T_f=243 K; red squares and dashed lines: T_a=295 K, T_f=295 K; blue pluses and dot-dashed lines: T_a=350 K, T_f=320K; magenta stars and dotted lines: T_a=295 K, T_f=243 K. LISA and standard Reitz-Diwakar models.*

A comparison of the measured (symbols) and calculated (lines) liquid penetration and SMD of ethanol for different injection pressures, i.e. p_{inj}=50, 200 bar, is shown in Figure 3.67. The calculated liquid penetrations agree well with the measurements at p_{inj}=200 bar. The computed liquid penetration for p_{inj}=50 bar is higher than that for p_{inj}=200 bar after 2.2 ms. The SMD for p_{inj}=50 bar is overpredicted, whereas that for p_{inj}=200 bar agrees well with the measurement.

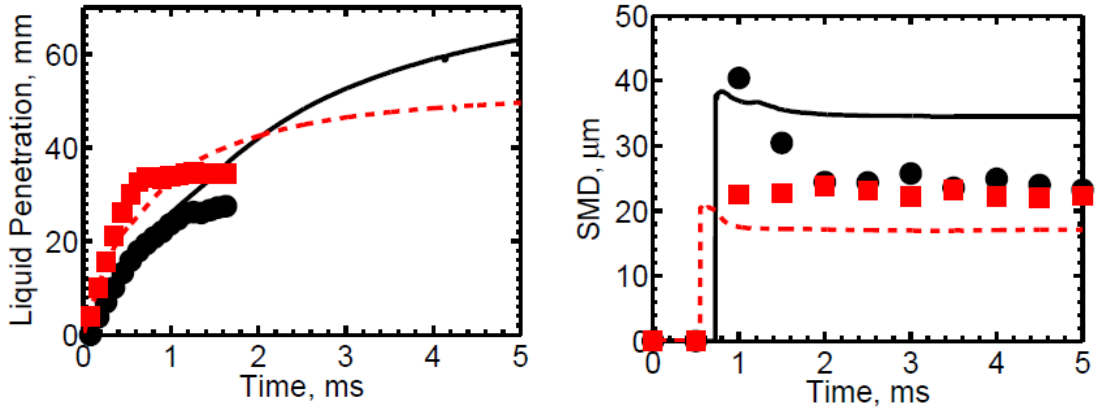

(a)Liquid penetration *(b)SMD at plane*

Figure 3.67: *Comparison of measured (symbols) and calculated (lines) ethanol liquid penetration and SMD for different injection pressures. Black circles and solid lines: p_{inj}=50 bar; red squares and dashed lines: p_{inj}=200 bar. LISA and standard Reitz-Diwakar models.*

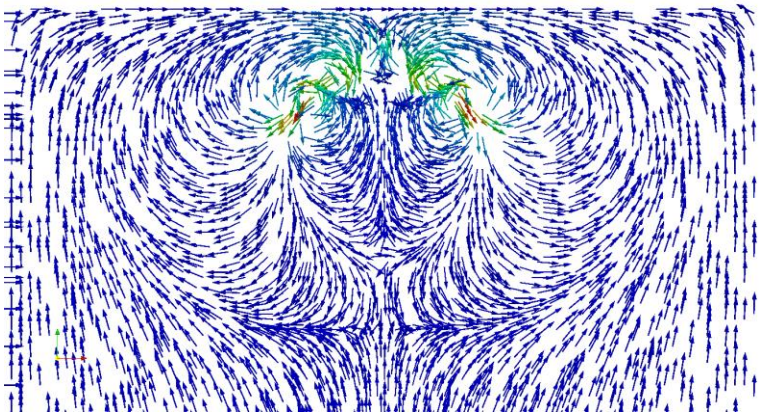

Figure 3.68: *The calculated velocity vector field for ethanol hollow cone spray at 1 ms after start of injection. LISA and standard Reitz-Diwakar models.*

A comparison of the measured (symbols) and calculated (lines) liquid penetration and SMD of ethanol for different ambient and fuel temperatures is shown in Figure 3.69. The calculated liquid penetrations agree well with the measurements; in both simulation and experiment, the ambient temperature and fuel temperature only weakly affect the liquid penetration. The computed SMDs are lower than the measurements.

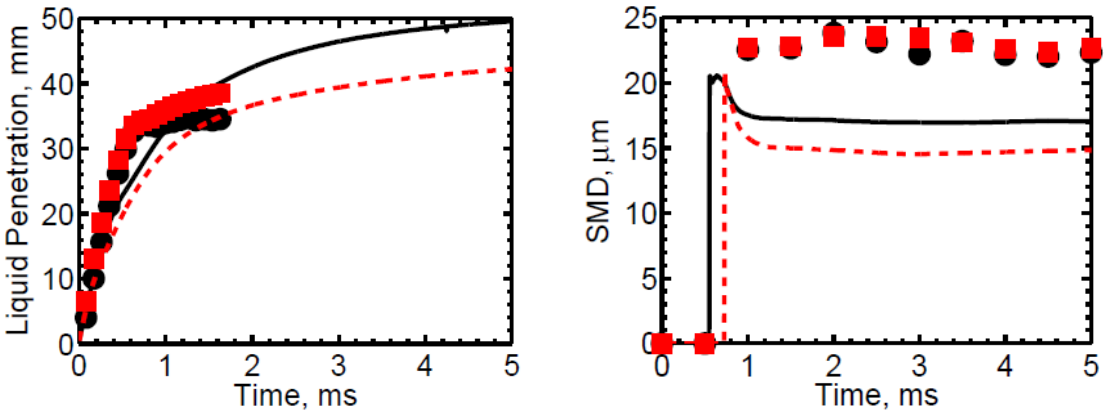

(a)Liquid penetration *(b)SMD at plane*

Figure 3.69: *Comparison of the measured (symbols) and calculated (lines) liquid penetration and SMD of ethanol for different ambient and fuel temperatures. Black circles and solid lines: T_a=350 K, T_f=243 K; red squares and dashed lines: T_a=295 K, T_f=295 K. LISA and standard Reitz-Diwakar models.*

Rosin-Rammler distribution (r_m=7.5 μm, q=3) + VSB2 model

The experimental (symbols) liquid penetration of ethanol and gasoline at different injection pressures, i.e. p_{inj}=50, 200 bar, are compared to those calculated using the Rosin-Rammler distribution (r_m=7.5 μm, q=3) and the VSB2 model in Figure 3.70. The calculated liquid penetrations agree well with the measurements, and both simulation and measurement show the liquid penetration increases as the injection pressure rises. The calculated SMDs are underpredicted.

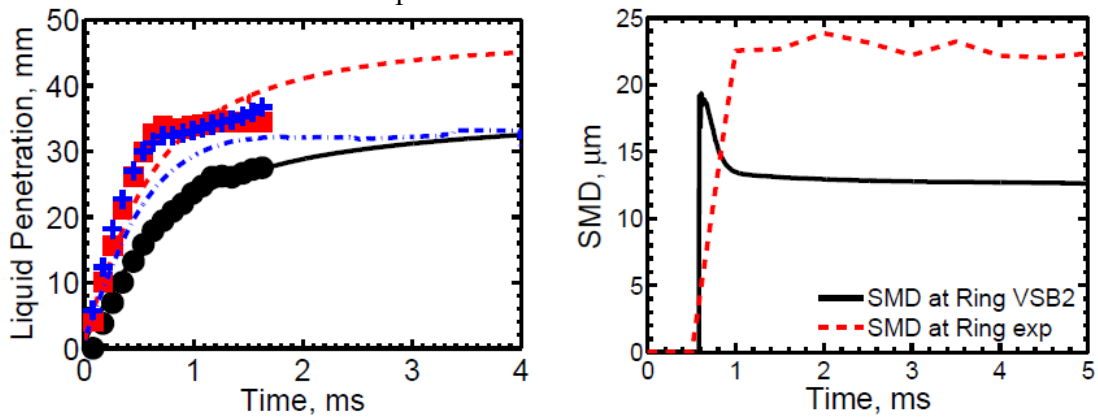

(a)Liquid penetration *(b)SMD at plane*

Figure 3.70: *Comparison of measured (symbols) and calculated (lines) gasoline and ethanol liquid penetration and SMD for different injection pressures. Black circles and solid lines: ethanol, p_{inj}=50 bar; red squares and dashed lines: ethanol, p_{inj}=200 bar; blue pluses and dot-dashed lines: gasoline, p_{inj}=200 bar. Rosin-Rammler distribution (r_m=7.5 μm, q=3), VSB2 model.*

A comparison of the measured (symbols) and calculated (lines) liquid penetration of gasoline for different ambient and fuel temperatures is shown in Figure 3.71. The calculated liquid penetrations are lower than the measurements; both the simulated

and the experimental data indicate that the ambient temperature and fuel temperature only weakly affect the liquid penetration.

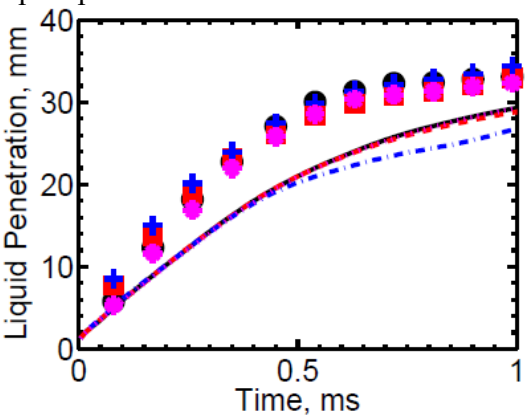

Figure 3.71: *Comparison of measured (symbols) and calculated (lines) liquid penetration of gasoline for different ambient and fuel temperatures. Black circles and solid lines: T_a=350 K, T_f=243 K; red squares and dashed lines: T_a=295 K, T_f=295 K; blue pluses and dot-dashed lines: T_a=350 K, T_f=320K; magenta stars and dotted lines: T_a=295 K, T_f=243 K. Rosin-Rammler distribution (r_m=7.5 μm, q=3), VSB2 model.*

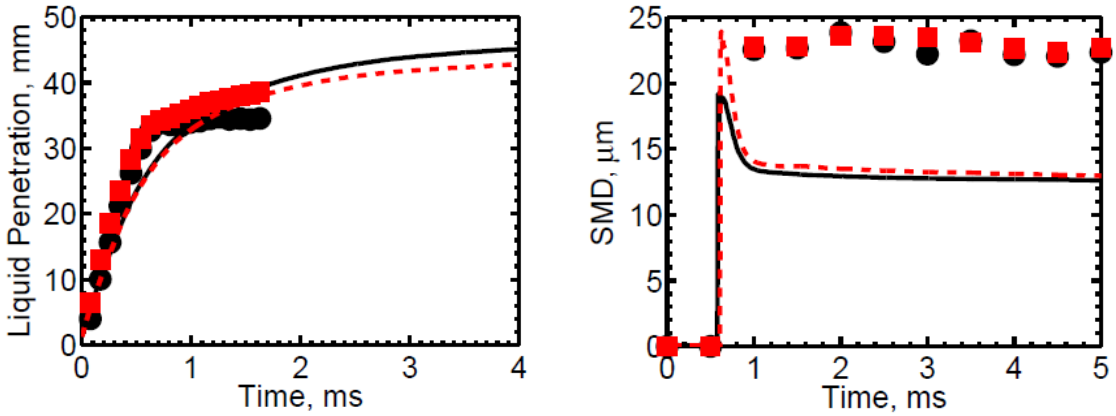

(a)Liquid penetration *(b)SMD at plane*

Figure 3.72: *Comparison of measured (symbols) and calculated (lines) liquid penetration of gasoline for different ambient and fuel temperatures. Black circles and solid lines: T_a=350 K, T_f=243 K; red squares and dashed lines: T_a=295 K, T_f=295 K; blue pluses and dot-dashed lines: T_a=350 K, T_f=320K; magenta stars and dotted lines: T_a=295 K, T_f=243 K. Rosin-Rammler distribution (r_m=7.5 μm, q=3), VSB2 model.*

A comparison of the measured (symbols) and calculated (lines) liquid penetration and SMD of ethanol for different ambient and fuel temperatures is shown in Figure 3.72. The calculated liquid penetrations agree well with the measurements; both the experimental and the simulated data indicate that the ambient temperature and fuel temperature only weakly affect the liquid penetration. The computed SMDs are lower than those that were measured.

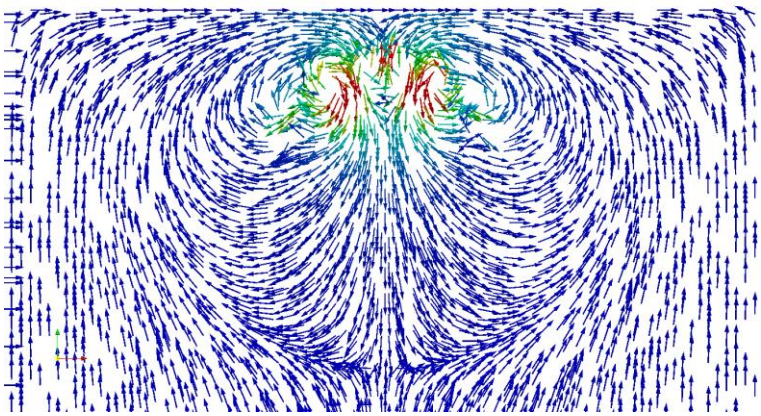

Figure 3.73: *The calculated velocity vector field for ethanol hollow cone spray at 1 ms after start of injection. Rosin-Rammler distribution (r_m=7.5 μm, q=3), VSB2 model.*

3.5. Conclusions

A pintle injector model was implemented into OpenFOAM® in order to simulate sprays discharged by an outward-opening piezo injector. The flow field calculated using the pintle injector model is more realistic than that obtained using the default unit injector model implemented in the standard version of OpenFOAM®.

It was found that a number of the spray models available in the standard version of OpenFOAM® (specifically, the Rosin-Rammler PDF, LISA, TAB, and KHRT breakup models, and the O'Rourke and trajectory collision models) had been implemented in a way that was not consistent with the intentions of their creators. Consequently, several modifications were made to OpenFOAM® so as to correct these errors. Of the various modifications made, that which had the most pronounced effect on the computed depths of penetration and SMD was the implementation of the correct version of the KHRT model; the effect on the calculated SMD values was especially profound. This modification greatly improved the agreement between the computed and measured results at high injection pressures. Moreover, a bug in the original implementation of the O'Rourke collision model in OpenFOAM® caused the code to crash when this model was activated; using the corrected implementation, it was possible to run simulations using the O'Rourke model.

Extensive sensitivity studies were carried out to examine the influence of various parameters (including initial and boundary conditions, spray model constants, and others) on the predicted behaviour of the hollow cone sprays. When using the Rosin-Rammler PDF to simulate primary breakup, the PDF's diameter was found to have a strong influence on the computed liquid penetration and SMD.

Model validation studies demonstrated that several combinations of spray submodels yield acceptable results for liquid penetration and SMD, including the Rosin-Rammler + Reitz-Diwakar models and the uniform droplet size + Reitz-KHRT models. The latter combination exhibited the best performance under the conditions examined, especially at high pressures and when predicting the SMD.

Chapter 4

Modelling of Stratified Turbulent Combustion in a DISI Engine

4.1. Combustion models for premixed and stratified turbulent combustion

In a direct-injection spark-ignition engine, a precisely but small amount of liquid fuel is released into the combustion chamber. This is followed by sparking, which occurs just downstream of the injector nozzle; the spark is fired shortly after the start of injection. Consequently, an ignitable fuel-air mixture is formed around the spark plug; after its ignition, a flame kernel propagates through the surrounding inhomogeneous mixture, which is globally lean but has substantial variation in its local equivalence ratios.

In DISI engines, burning can be characterized as a two-stage combustion mode. The first mode involves the propagation of an inhomogeneously premixed flame while the second involves the mixing-controlled afterburning of lean and rich combustion products as a result of the turbulent mixing. The amount of heat released during the premixed burning mode is greater than for the afterburning diffusion mode [18][100].

It is widely acknowledged that premixed turbulent combustion is inherently more complicated than turbulent diffusion combustion because of the much stronger coupling between the chemistry and turbulence in the former burning mode [100][16]. Consequently, the predictive capabilities of contemporary premixed turbulent combustion models are weaker than those of the corresponding models for turbulent diffusion combustion [18]. Accurate modelling of the premixed burning mode is therefore of crucial importance for simulations of combustion in a DISI engine. The first part of this chapter discusses some of the most widely used premixed turbulent combustion models in existence today before describing a series of sub-models of stratified turbulent combustion.

4.1.1. Premixed turbulent combustion models

In a premixed turbulent flame, the heat release from the flame affects the local density and flow field, and hence the turbulence. In turn, the turbulence affects the heat release rate. Many researchers have tried to describe this phenomenon using different methods. Here, several widely used premixed turbulent combustion models are discussed, including the classical Eddy Break-Up (EBU) model [101][102], Bray-Moss-Libby (BML) model, the Coherent Flame Model (CFM) and many of its variants, and the level-set G-equation model. The Flame Speed Closure (FSC) model is not included in this section because it is discussed at length in Section 4.2. The EBU, BML, CFM, and G-equation models address similar conditions involving high Reynolds ($Re \gg 1$) and

Damköhler ($Da \gg 1$) numbers. Note that the Damköhler number Da is the ratio of the characteristic turbulent time and the characteristic reaction time, $Da = \tau_t/\tau_c$.

Eddy-Break-Up model

The Eddy-Break-Up model was originally introduced by Spalding [101] for simulating premixed turbulent combustion. This model is based on the fast-chemistry assumption, meaning that once the fuel and air are mixed, they are burned immediately. Accordingly, the mean chemical reaction rate

$$\widetilde{\omega_f} = -C_{EBU}\frac{\sqrt{\widetilde{Y_f''^2}}}{\tau_t} \tag{4.1}$$

is considered to be controlled by a characteristic turbulent time τ_t, which is equal to

$$\tau_t = \frac{\tilde{k}}{\tilde{\varepsilon}} \tag{4.2}$$

within the framework of the standard $k-\varepsilon$ model. Here, C_{EBU} is a model coefficient; $\widetilde{Y_f''^2}$ is the variance of the mixture fraction of the fuel; the $\tilde{k}$ and $\tilde{\varepsilon}$ are the Favre-averaged turbulent kinetic energy and its dissipation rate, respectively.

Later, Magnussen and Hjertager [102] introduced a similar model for diffusion flames called the Eddy Dissipation Model (EDM) in which the $\sqrt{\widetilde{Y_f''^2}}$ term is replaced by the mass fraction of the deficient species, i.e. fuel for a lean mixture and oxygen for a rich mixture,

$$\widetilde{\omega_f} = -C_{EDM}\frac{min\left[\widetilde{Y_f}, \frac{\widetilde{Y_o}}{s}, \frac{\widetilde{Y_p}}{1+s}\right]}{\tau_t} \tag{4.3}$$

where C_{EDM} is a model coefficient; $\widetilde{Y_f}$, $\widetilde{Y_o}$ and $\widetilde{Y_p}$ are the Favre-averaged mass fractions of the fuel, oxidizer and products, respectively; and s is the stoichiometric mass ratio of oxidizer to fuel.

The Eddy-Break-Up model has been used widely in turbulent combustion simulations because (i) it yields a plausible dependence of global burning rate on rms turbulent velocity fluctuations u' [103] and (ii) it can be easily implemented into CFD codes since the mean reaction rate depends on known quantities. Accordingly, this model is available in almost every commercial CFD code. However, researchers have often complained that it ignores the effect of mixture composition and therefore requires constant tuning. When simulating the influence of mixture stratification on the burning rate, the neglect of the mixture composition effects becomes unacceptable.

Bray-Moss-Libby model

The Bray-Moss-Libby model is a classic model of premixed turbulent combustion [104]. It is based on the flamelet concept, in which the combustion region is divided into reactants and products separated by a thin flame front that is usually less than 1 mm thick. Accordingly, the thermochemical state of the mixture is characterized by a single scalar combustion progress variable c, which is defined either as a normalized temperature or a normalized mass fraction of a deficient reactant as follows

$$c = \frac{T - T_u}{T_b - T_u} = \frac{Y_u - Y}{Y_u - Y_b} \tag{4.4}$$

where subscripts u and b represents the properties in the unburned and burned mixture, respectively. Note that for reactants c =0 while for products c =1. Since the BML model is focused on the flamelet region where the flame front is very thin and the probability of finding intermediate states of the mixture is very low, two Dirac delta functions are commonly used to represent the probability of finding unburned and burned mixtures as follows

$$P(\mathbf{x},t) = \underbrace{\alpha(\mathbf{x},t)\delta(c)}_{unburned} + \underbrace{\beta(\mathbf{x},t)\delta(1-c)}_{burned} + \underbrace{\gamma(\mathbf{x},t)P_f(\mathbf{x},t)}_{burning} \tag{4.5}$$

where, α, β and γ represent the probabilities of finding the unburned, burned and burning gases, respectively at location $\mathbf{x}$ and time instant t, see Figure 4.1(a). Normalization of the probability density function leads to the following relation

$$\alpha(\mathbf{x},t) + \beta(\mathbf{x},t) + \gamma(\mathbf{x},t) = 1 \tag{4.6}$$

Equation (4.5) is of less interest since the probability of finding burning mixture γ is unknown. In the case of a thin-flame with low γ, it can be disregarded when evaluating certain quantities such as the progress variable, as shown in equation below and Figure 4.1(b):

$$P(\mathbf{x},t) \approx \alpha(\mathbf{x},t)\delta(c) + \beta(\mathbf{x},t)\delta(1-c) \tag{4.7}$$

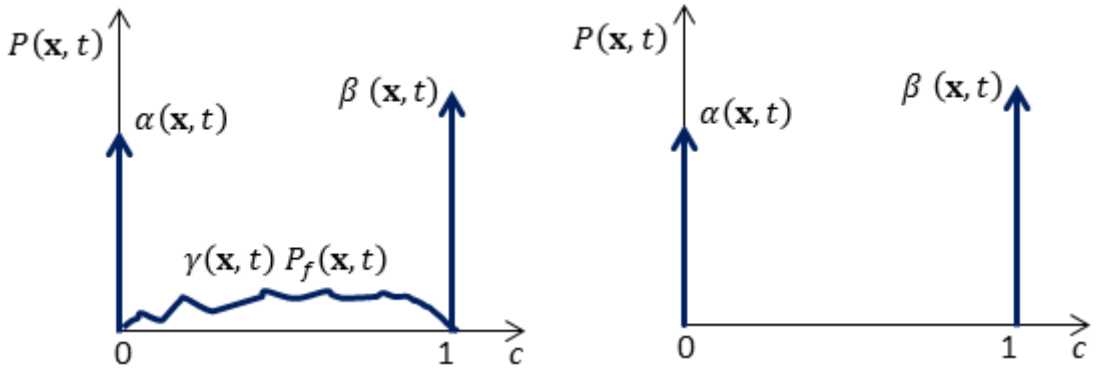

(a)PDF in flamelet region *(b)Purely bimodal approximation*

Figure 4.1: *Probability density functions (PDFs) for progress variable in the flamelet region with the probability of finding a burning mixture included (a) and using the purely bimodal approximation (b).*

Many classical correlations can be derived using Equation (4.7). For the sake of brevity, the time t and spatial coordinates $\mathbf{x}$ will not be specified later. For instance, the Reynolds-averaged progress variable $\bar{c}$ can be derived as

$$\bar{c} = \int_0^1 cP(c)dc = \int_0^1 [c\alpha\delta(c) + c\beta\delta(1-c)]dc = \beta \tag{4.8}$$

Equation (4.8) indicates that the physical meaning of $\bar{c}$ is the probability of finding the burned mixture. Likewise, the Reynolds-averaged regress variable $\bar{b}$ represents the probability of finding the fresh mixture

$$\bar{b} = 1 - \bar{c} = \alpha \tag{4.9}$$

By using Equation (4.7), the following relation can be derived

$$\overline{\rho c} = \bar{\rho}\tilde{c} = \int_0^1 \rho c P(c) dc = \rho_b \beta = \rho_b \bar{c} \tag{4.10}$$

Similarly,

$$\overline{\rho(1-c)} = \int_0^1 \rho(1-c) P(c) dc = \rho_u \alpha = \rho_u (1 - \bar{c}) \tag{4.11}$$

Combining Equations (4.10) and (4.11) we can get a classical relation between the Favre-averaged progress variable $\tilde{c}$ and the mean density $\bar{\rho}$

$$\bar{\rho} = \frac{\rho_u}{1 + (\sigma - 1)\tilde{c}} \tag{4.12}$$

where $\sigma = \rho_u / \rho_b$ is the density ratio. Equation (4.12) is commonly used in CFD codes to address the effect of heat release from a premixed flame on the flow.

By substituting Equation (4.12) into Equation (4.10), one obtains

$$\bar{c} = \frac{\sigma \tilde{c}}{1 + (\sigma - 1)\tilde{c}} \tag{4.13}$$

Equation (4.13) reminds us that the Reynolds- and Favre-averaged progress variables differ substantially. The Reynolds-averaged progress variable is usually larger than the Favre-averaged one at the same location in the flame brush.

In the framework of BML, many turbulent combustion characteristics q can be written as follows

$$\bar{q} = (1 - \bar{c}) q_u + \bar{c} q_b \tag{4.14}$$

$$\tilde{q} = (1 - \tilde{c}) q_u + \tilde{c} q_b \tag{4.15}$$

For example, the Favre-averaged temperature $\tilde{T}$ can be written as

$$\tilde{T} = (1 - \tilde{c}) T_u + \tilde{c} T_b \tag{4.16}$$

However, Equations (4.14) and (4.15) do not hold for certain quantities such as the reaction rate and reactant concentration gradient, which vanish in unburned and burned zones but are finite within flamelets. Accordingly, the use of Equation (4.7) does not allow us to model the mean reaction rate $\bar{\dot{\omega}}$. While a number of expressions for evaluating this rate have been proposed, as reviewed elsewhere, none of them have yet been validated against a representative set of experimental data for flames of different types in a range of simple well-defined test cases.

Coherent Flame models

A Coherent Flame Model (CFM) is based on the concept that the mean chemical reaction rate $\bar{\dot{\omega}}_Y$ is a the product of two quantities: the consumption rate of fuel per unit area of the flamelets $\omega_{L,Y}$ and the average flamelet area per unit volume or the Flame Surface Density (FSD) Σ, i.e.

$$\bar{\dot{\omega}} = \omega_L \Sigma \tag{4.17}$$

where

$$\omega_L = \rho_u S_L (Y_b - Y_u) \tag{4.18}$$

Y_u and Y_b are the mass fractions of the studied species in the unburned and burned mixture, respectively. To close Equation (4.17), a balance equation for the flame surface density Σ is solved. The source and sink terms in the FSD balance equation [105] are associated with the production of Σ by stretching and the annihilation of flamelet surface area due to collisions of flamelets, respectively. Various CFM models have been used to simulate premixed and stratified turbulent combustion in internal combustion engines [106]-[110].

G-equation model

Within the framework of this approach, the flame surface is associated with a particular level set $G(\mathbf{x}, t) = G_0$ of a monotonous function $G(\mathbf{x}, t)$ such that $G(\mathbf{x}, t) = G_0$ and the flame thickness is not resolved. The unburned and burned regions in the flow are represented by $G < G_0$ and $G > G_0$ respectively. A kinematic equation for the level set G is solved to track the propagation of the mean flame front by invoking an expression for its speed. This approach was documented in detail in a book [16], and has been used to simulate both premixed and stratified combustion in engines [111][112].

4.1.2. Stratified turbulent combustion models

In practical systems such as direct-injection spark-ignition engines, the highly inhomogeneous and turbulent fuel-air mixture formed by direct fuel injection is ignited and propagates throughout the combustion chamber. This type of combustion mode is neither purely premixed nor purely diffusion burning; instead, it is a stratified combustion mode involving premixed flame propagation through a highly inhomogeneous and turbulent mixture followed by mixing-controlled afterburning.

To model stratified turbulent combustion, at least three phenomena must be described: (i) the propagation of the premixed flame in the inhomogeneous turbulent mixture, (ii) the influence of turbulent fluctuations in mixture composition on the burning process and (iii) the evolution of the afterburning diffusion flame driven by turbulent mixing of lean and rich burned products.

The propagation of a premixed flame in inhomogeneous turbulent mixtures can be described by solving the following combustion progress variable equation:

$$\frac{\partial \bar{\rho}\tilde{c}}{\partial t} + \nabla.(\bar{\rho}\tilde{u}\tilde{c}) = -\nabla.\left(\overline{\rho u'' c''}\right) + \bar{\dot{\omega}} \tag{4.19}$$

This expression is closed by invoking a model of the premixed burning mode. The invoked model should properly address the effect of mixture inhomogeneity on the turbulent burning rate. For example, the mean reaction rate $\bar{\dot{\omega}}$ depends on the laminar flame speed, which in turn depends on the local conditions of the unburned mixture (i.e. its pressure, temperature and composition).

Another problem that must be addressed when simulating stratified turbulent combustion is that of modelling the effects of turbulent fluctuations in the mixture composition on the burning process. This effect can be very importance under certain

conditions. For example, if the mean local equivalence ratio is equal to 1.15, i.e. $\tilde{\phi} = 1.15$, the local laminar flame speed evaluated using the mean equivalence ratio is equal to the maximum value, i.e. $S_L(\tilde{\phi}) = \max[S_L(\phi)]$, see Figure 4.2 (c). Under such conditions, any increase or decrease in the equivalence ratio will reduce the laminar flame speed $S_L(\phi)$ relative to $S_L(\tilde{\phi})$, as shown in Figure 4.2 (a, b). Consequently, the turbulent flame speed is reduced.

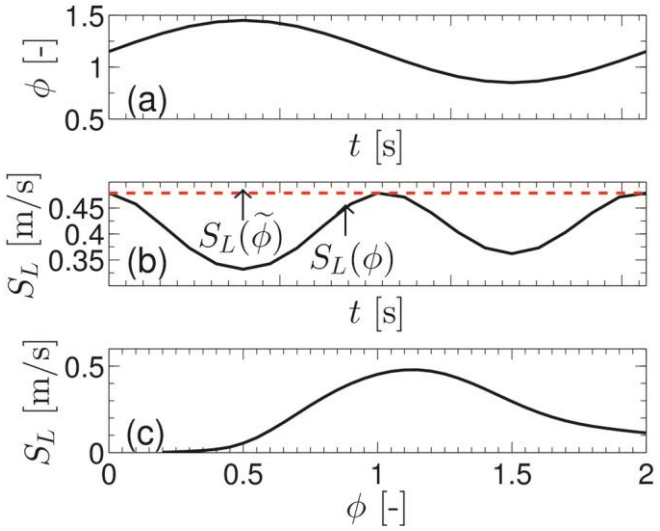

Figure 4.2: *The effect of fluctuations in equivalence ratio on the laminar flame speed. (a) The equivalence ratio fluctuates around the value of 1.15 with a magnitude of 0.3. (b) The laminar flame speed fluctuates due to the pulsations in the equivalence ratio. (c) A plot of the laminar flame speed against the equivalence ratio calculated for T_u= 500 K, p= 15 bar using the Chalmers approximation [114][67].*

A common approach to modelling the effect of turbulent fluctuations in the mixture fraction on the burning process consists of introducing a presumed mixture fraction PDF P when calculating the averaged characteristics $\overline{q(f)}$ as follows [108][111][112]

$$\overline{q(f)} = \int_0^1 q(f)P(f)df \tag{4.20}$$

The mean quantity $\overline{q(f)}$ could be the mean turbulent burning velocity $\overline{U_t(f)}$, mean burned temperature $\overline{T_b(f)}$, or the mean reaction rate $\overline{W(f)}$, among other things. The mixture fraction is directly related to the equivalence ratio and can be defined in different ways, with $f = 0$ for pure air and $f = 1$ for pure fuel. In this work, the mixture fraction is defined as the total (both burned and unburned) fuel mass fraction.

In URANS simulations, one usually solves balance equations for the Favre-averaged first $\tilde{f}$ and second $\widetilde{f''^2}$ moments of the mixture fraction field. Subsequently, one can define a presumed Favre PDF $\tilde{P}(f)$ that yields the computed $\tilde{f}$ and $\widetilde{f''^2}$. Using this PDF, one can evaluate various mean quantities used in turbulent burning calculations. A more detailed description of this approach is given in Section 4.2.4.

It is worth noting that the PDF used in Equation (4.20) is a canonical PDF $P(f)$, which differs from the Favre PDF $\tilde{P}(f)$ modelled using $\tilde{f}$ and $\widetilde{f''^2}$ according to the URANS equations. To the best of the author's knowledge, there has not yet been any

target-directed research into the differences between these two PDFs when dealing with stratified turbulent combustion. This issue is discussed further in Section 4.2.4.

Finally, during stratified or premixed/non-premixed turbulent combustion in a DISI engine, there is high probability that the premixed flame will propagate through a lean or rich mixture and thus create locally lean or rich products. These products re-mix due to turbulent diffusion and subsequently re-burn in a process known as diffusion-controlled afterburning. When modelling this effect, it is quite common to assume that after premixed burning has occurred in a lean or rich mixture, the mixture consists of locally equilibrated lean or rich products. The afterburning of such products can be addressed by assuming that the afterburning rate is controlled solely by turbulent mixing [18][112][113][115]. This very simplified model of turbulent diffusion combustion is satisfactory for many purposes because its accuracy is often comparable to that achieved using more advanced models of premixed turbulent combustion. However, it is necessary to incorporate flamelet libraries into models of mixing-controlled afterburning in order to reliably predict emissions profiles.

Many researchers have simulated stratified turbulent combustion using various approaches. Here, we restrict ourselves to multidimensional URANS simulations of stratified turbulent combustion in DISI engines.

Drake et al. [116] studied combustion in a SG DISI engine by comparing the results of CFD simulations to optical measurements. Two-stage stratified turbulent combustion including a premixed flame and mixing-controlled diffusion flame was modelled using a modified BML model and the Eddy Dissipation Model. First, the fuel spray was calibrated against shadow images in the optical engine, and then the heat release rate images were compared to OH* luminosity images. It was found that most of the fuel was burned in the premixed mode rather than the diffusion mode.

Wallesten et al. [115] simulated combustion in a DISI engine using the Flame Speed Closure model after reformulating the progress variable equation in terms of the fuel mass fraction to facilitate the model's implementation into the FIRE code. Reasonable agreement between simulations and measurements was obtained for various engine speeds and different engine loads.

Baritaud et al. [107] extended the CFM model to simulate stratified turbulent combustion in a spark-ignited engine using the KIVA 2 code. Their extended model included balance equations for the mean mass fractions of unburned fuel and unburned oxidant, flame surface density, and unburned enthalpy, and was also supplemented with the reaction rate Equation (4.18). Mixture stratification was modelled by artificially specifying fuel equivalence ratios in the horizontal or vertical directions. CO and NOx emissions were addressed using simple chemistry. These authors' simulations were used to investigate the effects of stratification but their results have yet to be verified by comparison with experimental data.

Hélie et al. [108] investigated combustion in a commercial DISI engine using an extended CFM model. The effect of fluctuation in mixture fraction was addressed by invoking the common presumed beta-PDF approach and the afterburning mode was treated using the Eddy-Break-Up model. Similar extended CFM models were also used in multidimensional URANS simulations of stratified combustion in DISI engines using commercial CFD code FIRE [109] [110].

Dahms et al. [111] combined a complicated ignition model (SparkCIMM) with a level-set G Equation model to simulate combustion in a Spray-Guided DISI engine. The

initial and boundary conditions for the combustion modelling were obtained by running 3D CFD simulations of the gas exchange processes in the engine. The initial flame propagation was compared to experimental flame propagation probability contours as well as pressure traces and heat release rate curves. Like Dahms et al. [111], Kim et al. [112] used a commercial code (Star-CD) to simulate stratified combustion and emissions in a DISI engine. A flamelet library computed using a chemical mechanism for a three-component gasoline surrogate was combined with the G Equation model, and a presumed beta-PDF was introduced to allow for turbulent fluctuations in the mixture fraction. Simple emission mechanisms including NO and soot were included.

Kim et al. [117] studied the effects of variable charge motion and injection timing on turbulent combustion in a SG DISI engine using Star-CD. The spray sub-model used in this work was calibrated against high speed images from spray chamber measurements. The classical Eddy-Break-Up model and simple ignition model were used in the simulations, but the output of the integrated model was not compared to any experimental data. Liu et al. [118] took similar approach, using the Eddy-Break-Up model to simulate stratified combustion with a combustion chamber bowl offset.

Yang et al. [119] studied combustion in a SG DISI engine using the Arrhenius fast-chemistry combustion model with the commercial code Converge. Based on their simulations, they argued that SG DISI combustion occurred in the thickened flame combustion regime where the Damköhler number is low ($Da \ll 1$) and the Karlovitz number is high ($Ka \gg 1$). Both the spark energy decomposition rate and amount were treated as input parameters in these CFD simulations.

4.2. Flame Speed Closure model

The Flame Speed Closure (FSC) model was selected to simulate the stratified turbulent combustion in a DISI engine for the following reasons. First, as reviewed elsewhere [18][120], it quantitatively predicts the effects of mixture composition on the turbulent burning rate. Within the model's framework, such effects are mainly controlled by the dependence of the local laminar burning velocity on the local mixture composition. Second, it describes the transient nature of combustion in a SI engine, including the formation of a small flame kernel, transition to turbulent combustion, and development of premixed turbulent flames. In the FSC model, the transient effects are addressed by two transient terms – one for the turbulent flame speed and another for the turbulent diffusivity. Third, it correctly predicts the effects of pressure on the turbulent burning velocity because it accounts for the dependence of the burning velocity on both the laminar flame speed and the laminar heat diffusivity. Fourth, it is readily combined with the simplest afterburning diffusion combustion model can easily be combined with the FSC model by solving the mixture fraction equation and using the BML approach. Finally, the FSC model has been extensively quantitatively validated against experimental data obtained by various research groups for premixed turbulent flames expanding in fan-stirred bombs. Such flames are more relevant to combustion in SI engines than other kinds of laboratory flames. More detailed descriptions of the FSC model can be found in Ref. [18][120].

4.2.1. The FSC model for premixed burning

The model characterizes the state of the mixture in a flame using a single combustion progress variable c introduced by Bray and Moss [121] and is based on the following balance equation

$$\frac{\partial \bar{\rho}\tilde{c}}{\partial t} + \nabla.(\bar{\rho}\tilde{\mathbf{u}}\tilde{c}) = \nabla.[\bar{\rho}(\kappa + D_t)\nabla\tilde{c}] + \rho_u U_t|\nabla\tilde{c}| + Q \tag{4.21}$$

where t is the time, $\mathbf{u}$ is the flow velocity vector, ρ is the density, κ is the molecular heat diffusivity, D_t and U_t are the turbulent diffusivity and burning velocity, respectively, and Q is a source term discussed later. Subscripts u and b refer to the unburned and burned mixture, respectively. Overlines denote the Reynolds average ($\bar{q} = q - q'$), while $\tilde{q} = \overline{\rho q}/\bar{\rho}$ is the Favre-averaged value of q ($\tilde{q} = q - q''$).

Within the framework of the FSC model, D_t and U_t are given by the following equations

$$D_t = D_{t,\infty}\left[1 - \exp\left(-\frac{t_{fd}}{\tau_L}\right)\right] \tag{4.22}$$

$$U_t = U_{t,\infty}\left[1 - \frac{\tau_L}{t_{fd}} + \frac{\tau_L}{t_{fd}}\exp\left(-\frac{t_{fd}}{\tau_L}\right)\right]^{1/2} \tag{4.23}$$

where t_{fd} is the flame development time counted starting from spark ignition, $\tau_L = D_{t,\infty}/u'^2$ is the Lagrangian time scale of turbulence, and $D_{t,\infty}$ and $U_{t,\infty}$ are the fully developed turbulent diffusivity and burning velocity, respectively. The two time-dependent terms allow us to simulate the early stages of premixed turbulent flame development, including the formation of a small flame kernel after the spark ignition (see also the source term Q), the transition to turbulent burning and development of the turbulent flame.

To evaluate the fully developed turbulent diffusivity $D_{t,\infty}$, a turbulence model should be invoked, e.g.

$$D_{t,\infty} = \frac{C_\mu}{Pr_t}\frac{\tilde{k}^2}{\tilde{\varepsilon}} \tag{4.24}$$

within the framework of the standard $k-\varepsilon$ model [122]. Here, k and ε are the turbulent kinetic energy and its dissipation rate, respectively; $C_\mu = 0.09$ is a constant, and Pr_t is the turbulent Prandlt number (a ratio of the turbulent transport of momentum to that of heat), which is equal to 1.0 in this work.

Within the framework of the FSC model, the fully developed turbulent burning velocity is given by the following expression [123]

$$U_{t,\infty} = Au'Da^{1/4} = Au'^{3/4}L^{1/4}S_L^{1/2}\kappa_u^{-1/4} \tag{4.25}$$

where A is the only constant of the FSC model; $u' = 2\tilde{k}^{1/2}/3$, $L = C_\mu^{3/4}\tilde{k}^{3/2}/\tilde{\varepsilon}$, and $\tau_t = L/u'$ are the rms turbulent velocity fluctuations, integral length scale, and eddy-turn-over time, respectively; and $\tau_c = \delta_L/S_L$, $\delta_L = \kappa_u/S_L$, and S_L are the chemical time scale, laminar flame thickness and laminar flame speed, respectively. The evaluation of S_L under engine operating conditions will be discussed later.

It is worth emphasizing that Equation (4.25) accurately predicts the effect of pressure on the turbulent burning velocity [18][120]. In particular, it is well known that

for heavy paraffins, the turbulent burning velocity increases with the pressure despite the associated decrease in S_L [120][124]. Equation (4.25) reproduces this trend because the decrease in the molecular heat diffusivity κ_u with pressure is much more pronounced than the decrease in S_L.

In order to (i) simulate the early stages of flame kernel growth after spark ignition and (ii) obtain an appropriate balance equation in the limit case of $u' \to 0$, the FSC model invokes an extra source term [120][125]

$$Q = \frac{\bar{\rho}(1-\tilde{c})}{t_r(1+D_t/\kappa_b)} \exp\left(-\frac{\Theta}{\tilde{T}}\right) \tag{4.26}$$

where $\Theta = 20000$ K is the activation temperature for a single reaction to which the combustion chemistry is reduced, the Favre-averaged temperature $\tilde{T}$ is evaluated using the simplest form of the ideal gas state equation ($\bar{\rho}\tilde{T} = \rho_u T_u$), and the reaction time scale t_r is set so that in the case of $u' = 0$, the burning velocity yielded by stationary, one-dimensional Equations (4.21) and (4.26) is equal to the laminar flame speed S_L, which is an input parameter of the model. As discussed in Appendix A, this constraint results in

$$t_r = \Psi^2\left(\frac{T_b}{T_u}, \frac{\Theta}{T_u}\right)\frac{\kappa_u}{S_L^2} \tag{4.27}$$

where the non-dimensional function Ψ approximates the calculated values of $S_L\sqrt{t_r/\kappa_u}$, computed for various $T_b/T_u$and Θ/T_u ratios by numerically integrating the stationary, one-dimensional Equations (4.21) and (4.26) with $D_t = U_t = 0$. If the laminar speed is considered to be a known input parameter of the FSC model then the function Ψ does not feature any empirical or tuning parameters.

4.2.2. Laminar flame speed and combustion temperature

In order for the FSC model to predict the turbulent burning rate in the combustion chamber of a DI SI engine, appropriate values of S_L must be specified for a wide range of mixture fractions, pressures, and temperatures. Due to the lack of experimental data on the laminar flame speeds of gasoline-air mixtures at elevated pressures and temperatures, we were forced to rely on results from simulations of stationary, planar, one-dimensional laminar premixed flames using well-validated combustion chemistry. These simulations and their results are discussed in Chapter 2, where an approximation of $S_L = S_L(f, T_u, p)$ for gasoline-air mixtures is reported for engine applications. When modelling stratified turbulent burning using the FSC model, this approximation was substituted into Equation (4.25).

In the standard version of OpenFOAM®, the combustion temperature is evaluated based on an assumption of ideal and complete combustion, i.e. the combustion products are assumed to consist only of CO_2, H_2O, N_2, and excess O_2 or fuel depending on the local equivalence ratio. In the present work, the equilibrium combustion temperature is calculated for combustion products that consist of more species. For example, the burned products from a rich mixture contain substantial quantities of CO, and the equilibrium adiabatic flame temperature in such cases may be up to 150 K lower than in situations involving complete combustion. The equilibrium combustion temperatures T_b computed for various equivalence ratios ϕ (or mixture fractions f),

pressures p, and unburned gas temperatures T_u were approximated by expressions of the form $T_b = T_b(f, T_u, P)$, which are presented in Chapter 2.

4.2.3. Mean stratification

In order to simulate the mean stratification of the unburned gas, the following well-known transport equation for the Favre-averaged fuel-air mixture fraction $\tilde{f}$

$$\frac{\partial(\bar{\rho}\tilde{f})}{\partial t} + \nabla.\left(\bar{\rho}\tilde{\mathbf{u}}\tilde{f}\right) - \nabla.\left(\bar{\rho}D_t\nabla\tilde{f}\right) = \overline{\rho S} \tag{4.28}$$

was implemented and solved numerically. Here, the source term $\overline{\rho S}$ is associated with the evaporation of fuel droplets after injection of the fuel spray into the combustion chamber.

The simplest method of modelling the influence of mixture stratification on combustion involves using the computed three-dimensional field $\tilde{f}(\mathbf{x}, t)$ to evaluate the local characteristics of the combustion products and the local turbulent burning velocity as follows

$$\begin{aligned} T_b(\mathbf{x}, t) &= T_b\left[\tilde{f}(\mathbf{x}, t)\right] \\ \rho_b(\mathbf{x}, t) &= \rho_b\left[\tilde{f}(\mathbf{x}, t)\right] \\ U_{t,\infty}(\mathbf{x}, t) &= U_{t,\infty}\left\{S_L\left[\tilde{f}(\mathbf{x}, t)\right]\right\} \end{aligned} \tag{4.29}$$

4.2.4. Turbulent fluctuations in the mixture fraction

Equation (4.29) cannot describe the effects of turbulent fluctuations in the mixture composition on the mean characteristics of stratified burning. These effects are commonly modelled by invoking a presumed Probability Density Function (PDF) $P_f(f)$ for the mixture fraction. Within the framework of this approach, which was introduced into the combustion literature by Janicka and Kollmann [126] in a study of non-premixed flames, the general shape of the function $P_f(f)$ is chosen arbitrarily**.** However, the particular expression for the PDF features a few (typically two) unknown parameters $a(\mathbf{x}, t)$, $b(\mathbf{x}, t)$ etc., which are locally determined from the following constraints

$$\overline{\rho f^m}(\mathbf{x}, t) = \int_0^1 \rho f^m P_f[(\mathbf{x}, t), b(\mathbf{x}, t), \ldots]df \tag{4.30}$$

where $m = 1, \ldots, m_{\max}$ is an integer and $m_{\max}$ is equal to the number of the unknown parameters $a(\mathbf{x}, t)$, $b(\mathbf{x}, t)$, etc. The moments on the Left Hand Side (LHS) are evaluated by numerically solving the corresponding balance equations. Note that if $m_{\max} = 1$, the presumed PDF $P_f(f)$ is associated with the Dirac delta function $\delta\left[f - \tilde{f}(\mathbf{x}, t)\right]$ and the influence of fluctuations in the mixture composition on ρ_b, T_b, S_L, U_t, etc. is neglected.

In this work, I implement the presumed PDF approach using the most common value of $m_{\max} = 2$. This leaves two subtasks that must be addressed: (i) computation of the second Favre moment $\overline{\rho f^2}(\mathbf{x}, t)$ or $\overline{\rho f"^2}(\mathbf{x}, t) = \overline{\rho f^2}(\mathbf{x}, t) - \bar{\rho}(\mathbf{x}, t)\tilde{f}^2(\mathbf{x}, t)$ and (ii) modeling of the PDF shape.

The former subtask has been studied in depth in the context of simulating non-premixed turbulent flames and the appropriate balance equation is well known [16]. However, the problem becomes more complex when considering combustion in a DISI engine due to the influence of fuel evaporation on the instantaneous mixture fraction field. This process is addressed by introducing the mean evaporation source term $\bar{\rho}\widetilde{S_v}$ on the RHS of the following balance equation

$$\frac{\partial(\bar{\rho}\widetilde{f''^2})}{\partial t} + \nabla.\left(\bar{\rho}\tilde{\mathbf{u}}\widetilde{f''^2}\right) - \nabla.\left(\bar{\rho}D_t\nabla\widetilde{f''^2}\right) = 2\bar{\rho}D_t\left|\nabla\tilde{f}\right|^2 - \bar{\rho}\chi_f + \tilde{b}\bar{\rho}\widetilde{S_v} \tag{4.31}$$

where the evaporation term is multiplied by the regress variable $\tilde{b}$, because evaporation occurs in the unburned flow. χ_f is the scalar dissipation rate, which is commonly modeled as follows

$$\chi_f = C_\chi \frac{\tilde{\varepsilon}}{\tilde{k}}\widetilde{f''^2} \tag{4.32}$$

and C_χ is a constant whose value is taken to be 1 in this work. As shown elsewhere [127][128], the evaporation source term can be modelled as follows

$$\widetilde{S_v} = 2\widetilde{fS} - \widetilde{f^2S} - 2\tilde{f}\tilde{S} + \tilde{f}^2\tilde{S} \tag{4.33}$$

where the mean terms $\widetilde{fS}$ and $\widetilde{f^2S}$ are unclosed. The following closure relations are invoked in this work [127][128]:

$$\bar{\rho}\widetilde{fS} = \frac{1}{V}\sum_k Y_k^* \dot{m}_k \tag{4.34}$$

$$\bar{\rho}\widetilde{f^2S} = \frac{1}{V}\sum_k Y_k^{*2} \dot{m}_k \tag{4.35}$$

are invoked.

The simplest method of addressing the effects of the turbulent fluctuations in the mixture fraction is to use mass-averaged presumed beta-PDF when dealing with the following mean characteristics [108][111]

$$\bar{\tilde{q}} = \int_0^1 q(f)\tilde{P}_f(f)df \tag{4.36}$$

where overbar and tilde are jointly used to stress that the Reynolds-averaged value of a quantity $q = \{\rho_b, T_b, S_L, U_t, \dots\}$ is estimated by invoking the mass-weighted presumed beta-PDF

$$\tilde{P}_f = \frac{\Gamma(a)\Gamma(b)}{\Gamma(a+b)} f^{a-1}(1-f)^{b-1} \tag{4.37}$$

where a ratio of gamma functions $\Gamma(z) = \int_0^\infty \eta^{z-1}\mathrm{e}^{-\eta}d\eta$ is used to satisfy the normalizing constraint of $\int_0^1 \tilde{P}_f df = 1$. The parameters a and b in Equation (4.37) are evaluated using the following expressions:

$$a = \tilde{f}\left[\frac{\tilde{f}(1-\tilde{f})}{\widetilde{f''^2}} - 1\right] \tag{4.38}$$

$$b = \left(1 - \tilde{f}\right)\left[\frac{\tilde{f}\left(1 - \tilde{f}\right)}{\widetilde{f''^2}} - 1\right]$$

Because the first and second moments of the presumed PDF are computed by solving Favre-averaged balance equations, the obtained PDF is mass-weighted.

A more sophisticated approach consists of averaging $q = \{\rho_b, T_b, S_L, U_t, \dots\}$ using the canonical PDF $P_f(f)$ as follows

$$\bar{q} = \int_0^1 q(f) P_f(f) df \tag{4.39}$$

In the present work, the mass-weighted $\tilde{P}_f(f)$ modelled by Equations (4.37) and (4.38) is transformed to the canonical $P_f(f)$ by invoking the following joint PDF for the combustion regress variable b and mixture fraction

$$P(b, f) = P_b(b) P_f(f) = \left[\bar{b}\delta(1 - b) + \left(1 - \bar{b}\right)\delta(b)\right] \tag{4.40}$$

where $\delta(b)$ is a Dirac delta function. Equation (4.40) is based on two assumptions. First, fluctuations in combustion regress variable and mixture fraction are hypothesized to be statistically independent. While this assumption is difficult to substantiate, it is widely used even though some recent studies have identified issues arising from correlation $\overline{\rho b'' f''}$ between the two fluctuations [129]. Second, the regress-variable PDF $P_b(b)$ is modeled in a way that builds on the classical Bray-Moss-Libby (BML) approach [121][130], which is based on the hypothesis that the probability of finding intermediate states of the reacting mixture (i.e. states partway between unburned reactants and equilibrium combustion products) is much less than unity in a premixed turbulent flame. Note that Equation (4.40) deals with the regress variable $b = 1 - c$ rather than the widely used combustion progress variable c, because it is the balance equation for $\tilde{b} = 1 - \tilde{c}$ that is implemented in OpenFOAM®.

Using Equation (4.40), the canonical PDF can be determined as follows

$$P_f = \left[\int_0^1 \frac{\tilde{P}_f(\phi) d\phi}{\bar{b}\rho_u + \left(1 - \bar{b}\right)\rho_b(\phi)}\right]^{-1} \frac{\tilde{P}_f(f)}{\bar{b}\rho_u + \left(1 - \bar{b}\right)\rho_b(f)} \tag{4.41}$$

as discussed in Appendix B.

4.3. Implementation of FSC model into OpenFOAM®

An advantage of using an open source code when implementing new models and methods is that users have full access to the source code including libraries and solvers. This gives more freedom when implementing models than is typically possible with commercial CFD codes, in which users have only limited access to the code via user-defined functions. However, OpenFOAM® is written in the object orientated language C++ and the hierarchies of its classes are not easy to understand. Consequently users must dig deep into the code in order to understand some of the member functions, and great care should be taken when modifying the code.

This section describes the implementation of the important parts of the Flame Speed Closure model including the regress variable equation, mean density and mean temperature calculation, and the Favre and Canonical beta-PDF approaches.

4.3.1. Implementation of regress variable equation

OpenFOAM® is written in the object orientated language C++ and it is intended to be a flexible, programmable environment for simulation whose top-level code is a direct representation of the equations used in the models of interest. This section discusses the current implementation of the core of the FSC model – the regress variable equation – into OpenFOAM®.

The transport equation for the regress variable b of the FSC model is similar to the progress variable Equation (4.21), and it is written as follows:

$$\underbrace{\frac{\partial \bar{\rho}\tilde{b}}{\partial t}}_{1} + \underbrace{\nabla.\left(\bar{\rho}\tilde{\mathbf{u}}\tilde{b}\right)}_{2} + \underbrace{\nabla.\left[\bar{\rho}(\kappa + D_t)\nabla\tilde{b}\right]}_{3} + \underbrace{\rho_u U_t\left|\nabla\tilde{b}\right|}_{4} + \underbrace{Q}_{5} = 0 \tag{4.42}$$

The first term in Equation (4.42) is a transient term and can be represented in OpenFOAM® language as *fvm::ddt(rho,b)*; the second term is a convection term that can be written as *mvConverction->fvm(phi,b)*; the third term is a diffusion or Laplacian term and can be written as *fvm::laplacian(alphaTurbRealTimeDependent,b)*; the fourth term is a sink term and it is represented by two terms as shown below in order to facilitate the model's implementation:

$$\rho_u U_t\left|\nabla\tilde{b}\right| = \rho_u U_t \nabla.\left(\tilde{b}\mathbf{n}\right) - \rho_u U_t \tilde{b}\nabla.\mathbf{n} = \nabla.\left(\rho_u U_t \tilde{b}\mathbf{n}\right) - \tilde{b}\nabla.\left(\rho_u U_t \mathbf{n}\right) \tag{4.43}$$

In the language of OpenFOAM®, this split term can be expressed as *fvm::div(phiSt, b, "div(phiSt,b)") - fvm::Sp(fvc::div(phiSt), b)*. Here, $\mathbf{n} = \nabla\tilde{b}/\left|\nabla\tilde{b}\right|$ is the unit vector locally normal to the mean flame brush. The last term Q modelled by Equation (4.42) is a source term that simulates the early stage of flame kernel growth after spark ignition. It can be written as *rho*b/tr/(1+alphaTurbRealTimeDependent/thermo.alphab())*exp(-Ta/T)*.

4.3.2. Implementation of the mean density and mean temperature

In the standard library of OpenFOAM®, the Favre-averaged temperature $\tilde{T}$ is calculated by interpolating the JANAF thermodynamic polynomial as follows

$$\tilde{h} = \frac{R^0}{W}\left(\sum_{k=1}^{5}\frac{a_k}{k}\tilde{T}^k + a_6\right) \tag{4.44}$$

where the mean specific enthalpy $\tilde{h}$ [J/kg] is computed by solving the relevant Favre-averaged balance equation. Here, $R^0 = 8.314$ [J/(mole K)] is the universal gas constant. The molecular weight W of the mixture and the coefficients a_k in Equation (4.44) are calculated using a mixing rule based on weighing factors of $\tilde{b}$ and $1-\tilde{b}$ within the turbulent flame brush as follows

$$\frac{1}{W} = \frac{1}{W_u}\tilde{b} + \frac{1}{W_b}\left(1-\tilde{b}\right) \tag{4.45}$$

$$\frac{a_k}{W} = \frac{a_{u,k}}{W_u}\tilde{b} + \frac{a_{b,k}}{W_b}\left(1-\tilde{b}\right) \tag{4.46}$$

Here, the coefficients $a_{u,k}$ and $a_{b,k}$ characterize the unburned gas and combustion products, respectively, and $k = 1,2,\ldots 6$. If $\tilde{b}$ and $1-\tilde{b}$ are substituted with the mass fractions Y_u and Y_b then Equations (4.45) and (4.46) describe a two-component mixture, i.e. OpenFOAM® seems to consider the mean state of a burning mixture within a turbulent flame brush to be a two-component "super-mixture" of unburned reactants Y_u and equilibrium combustion products Y_b. However, the intermittency of reactants and products in a turbulent premixed flame is not equivalent to the co-existence of species Y_u and Y_b in a two-component mixture. For example, the two species have the same temperature in the two-component mixture, but the temperatures of reactants and products are significantly different in a turbulent flame. As a result, Equations (4.44)-(4.46) are inconsistent with premixed turbulent combustion, as discussed in detail elsewhere [131][114].

In the present work, the conditioned burned enthalpy $\bar{h}_b$, Favre-averaged temperature $\tilde{T}$ and Reynolds-averaged density $\bar{\rho}$ within the flame brush are evaluated within the BML framework as follows

$$\bar{h}_b = \frac{\tilde{h} - \tilde{b}\bar{h}_u}{1-\tilde{b}} \tag{4.47}$$

$$\tilde{T} = T_u\tilde{b} + T_b\left(1-\tilde{b}\right) \tag{4.48}$$

$$\frac{1}{\bar{\rho}} = \frac{1}{\rho_u}\tilde{b} + \frac{1}{\rho_b}\left(1-\tilde{b}\right) \tag{4.49}$$

Note that Equation (4.48) results straightforwardly from Favre-averaging of quantity $q = 1/\rho$, i.e. Equation (4.48) holds independently of the BML assumptions.

In OpenFOAM® the density is calculated by introducing a parameter called compressibility psi

$$psi = \frac{1}{R_{spec}T} \tag{4.50}$$

where $R_{spec} = R^0/W$ is the specific gas constant in units of J/(K kg). Therefore, the density can be calculated as follows

$$\rho = p\, psi \tag{4.51}$$

Thus, the calculation of density is straight forward if the compressibility is known in OpenFOAM®. The following discussion therefore deals with the evaluation of the compressibility rather than the density.

When the local mixture composition is outside the flammability limit, i.e. $\tilde{\phi} > 2.0$ or $\tilde{\phi} < 0.2$ in the present work, the standard OpenFOAM® option is activated, i.e. the mean temperature is calculated using Equations (4.44))-(4.46), and the mean compressibility is then evaluated using Equation (4.50). When the mean local equivalence ratio is within the pre-defined flammability limit, i.e. $0.2 \leq \tilde{\phi} \leq 2.0$, the Equations (4.47)-(4.49) are used, with $T_b = T_b\left(\tilde{f}, \bar{h}_b, p\right)$ being given by approximations reported in Appendix B. By combining such an approach with a presumed mixture fraction PDF, effects of turbulent fluctuations in the mixture composition on the mean

temperature and density can be addressed. However, modelling of turbulent fluctuations in the enthalpy was beyond the scope of the present work. The CFD solver is only used to solve the mean enthalpy and unburned enthalpy equations; the burned enthalpy $\tilde{h}_b$ within the flame brush is calculated using Equation (4.47). Note that the BML approach is only applied within the flame brush, i.e. in regions where $0.001 < \tilde{b} < 0.999$. The process used to calculate the mean temperature and density is shown schematically in Figure 4.3.

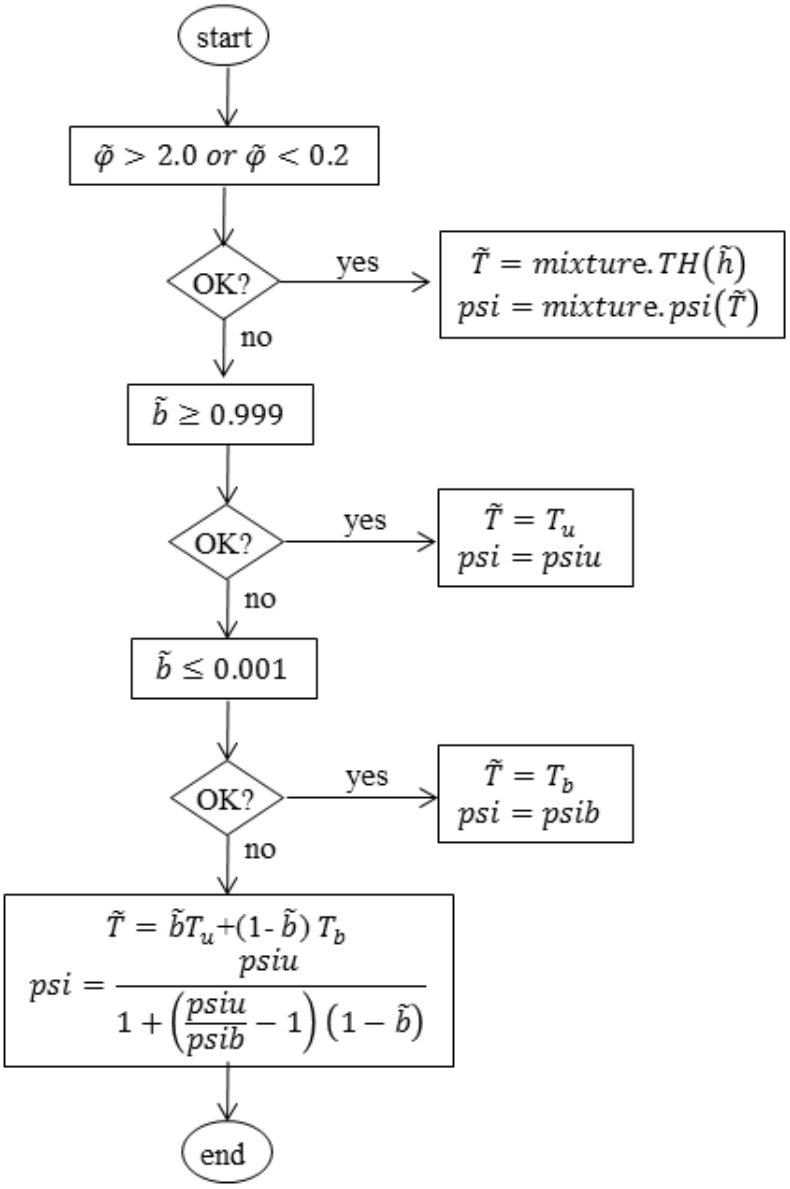

Figure 4.3: *Schematic illustration of the process used to calculate the Favre-averaged temperature and Reynolds-averaged compressibility during premixed combustion*

4.3.3. Implementation of Favre and canonical beta-PDFs

The mean characteristics of turbulent flame propagation, e.g. $\overline{T_b}$ and $\overline{S_L^{1/2}}$ were evaluated by invoking a presumed beta-PDF which was determined by the first and

second moments of the mixture fraction, i.e. $\tilde{f}$ and $\widetilde{f''^2}$. The calculation of those mean characteristics is shown in Figure 4.4. The mean characteristics are only evaluated using the presumed PDF for regions that are: (i) within the flammability limit; (ii) within the flame brush region; and (iii) where the segregation factor $g = \widetilde{f''^2}/\tilde{f}(1-\tilde{f})$ is large enough, otherwise turbulent fluctuations in the mixture fraction are neglected. All mean characteristic $\bar{q}$ are evaluated as follows

$$\bar{q} = \frac{\int_{f_{min}}^{f_{max}} T_b \widetilde{P_f}\, df}{\int_{f_{min}}^{f_{max}} \widetilde{P_f}\, df} \tag{4.52}$$

where f_{min} and f_{max} correspond to the lower and upper flammability limits, respectivley.

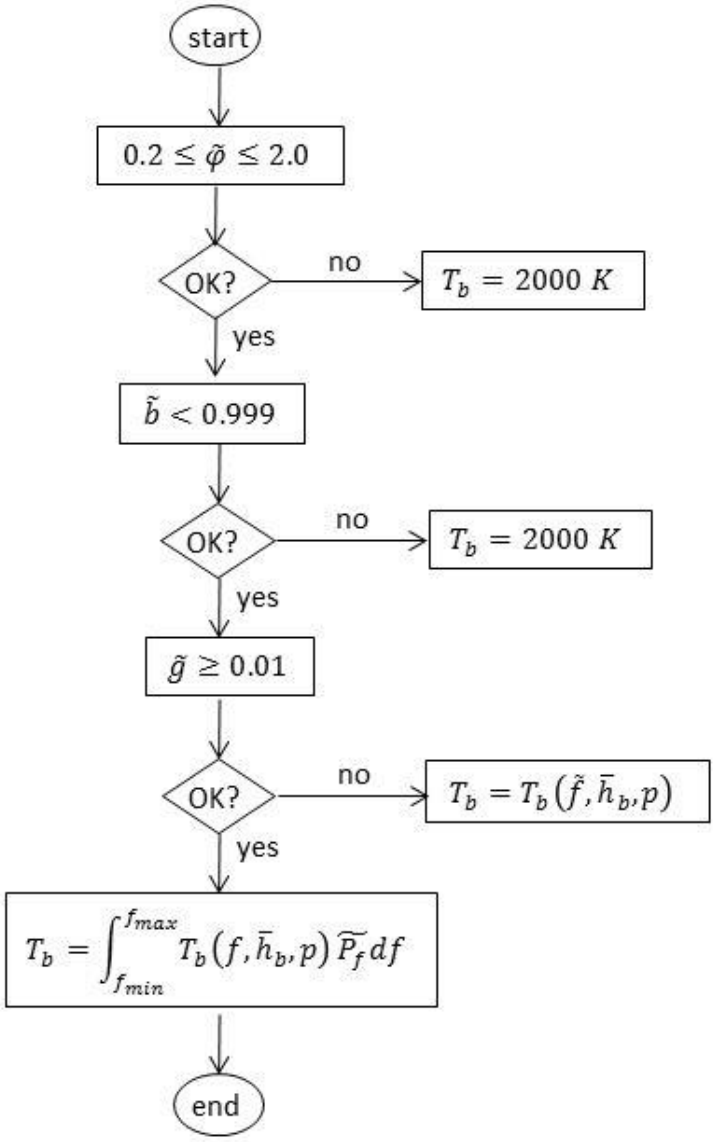

Figure 4.4: *Schematic illustration of the process used to calculate the averaged temperature using Favre and canonical beta-PDFs.*

4.4. Other sub-models

The methodology and the implementations of spray sub-models used in the present simulations are described at length in Chapter 3 as well as in reference [132], where simulated results are validated against experimental data obtained by Hemdal et al. [21]. Gasoline liquid properties were taken from the KIVA fuel library; a uniform droplet size distribution was assumed at the nozzle exit; and the KHRT breakup model was used with modelling constants adjusted for gasoline low pressure gasoline sprays as discussed in Chapter 3. The constants are reported in Table 4.1.

Other relevant processes such as mean flow evolution, energy balance, droplet evaporation, spray-wall interaction, turbulence and turbulent mixing and spark ignition were addressed using models implemented into the standard version of OpenFOAM®. These models are summarized in Table 4.1. A target-directed study of these processes is beyond the scope of the present thesis. It is worth noting, however, that the simple ignition model implemented in the standard version of OpenFOAM® involves (i) specifying the ignition location, diameter and strength (a time-independent constant) and (ii) decreasing the regress variable in the cells located within the ignition sites when solving the transport equation for $\tilde{b}$. Such an oversimplified model cannot properly represent the discharge of high voltage and current between the electrode gaps and the heating-up of the ignition kernel by the current. However, because this work focuses on the modelling of stratified turbulent burning, the simple ignition model was used.

Table 4.1: *Summary of models used in the simulations and their constants.*

Type	Name	constants
Turbulence	standard $k-\varepsilon$	$C_\mu = 0.09, C_1 = 1.44, C_2 = 1.92, C_3 = -0.33, \sigma_k = 1.0, \sigma_\varepsilon = 1.3, Pr_t = 1.0$
Energy balance	Two-enthalpy equations	
Injector	Hollow cone	Inner cone angle 80°; outer cone angle 90°
Primary breakup	Uniform droplet size	40 μm
Secondary breakup	KHRT	$B_0 = 0.61, B_1 = 40, C_\tau = 10, C_{RT} = 0.1$
Droplet evaporation	standard	
Heat transfer	RanzMarshall	
Spray-wall interaction	reflect	
Ignition	Step function	Ignition strength: 16; ignition diameter 3mm
Chemistry	Chalmers chemical mechanism for gasoline surrogate	
Stratified turbulent combustion	Flame speed closure + presumed beta-PDF	A=0.5

4.5. Experimental and numerical setups

The CFD studies presented in this thesis were conducted in parallel with experimental investigations on an SG DISI engine performed by my colleagues at Chalmers. The experiments were conducted on a single-cylinder research engine (AVL 5411.018) operated in the stratified mode. The engine was run at fixed rotational speed of 1500 rpm and under three load cases with target imep values of 3.6, 3.8 and 5 bar. The engine specifications are listed in Table 4.2. A blend of 95 octane gasoline with 10% ethanol was directly injected into the cylinder using an outward opening piezo actuated injector and the resulting fuel cloud was ignited by a three-electrode spark plug. The injector and spark plug were mounted between the intake and exhaust valves in a close couple configuration, and they were positioned at an angle with respect to the vertical line of the cylinder. The angle was equal to 20 degrees for the injector and 5 degrees for the spark plug. The fuel was discharged at an injection pressure of 200 bar using a single injection strategy; the injection duration was set to 420 μs for the low load case and 550 μs for the medium load case. Table 4.3 shows operating parameters of the engine such as injection timing t_{inj}, ignition timing t_{ign}, injection duration t_{dur}, air excess ratio λ, and indicated mean effective pressure (IMEP) in three studied cases.

Table 4.2: *Engine specifications*

Bore [mm]	83
Stroke [mm]	90
Compression ratio	10.2
Displacement volume [cm^3]	487
Dead volume [cm^3]	53
Intake valve diameter [mm]	33
IVO/IVC [CAD]	340/600
Exhaust valve diameter [mm]	28
EVO/EVC [CAD]	105/365

Table 4.3: *Parameters for three cases.*

parameters	Case 1	Case 2	Case 3
t_{inj} [CAD bTDC]	18	20	32
t_{ign} [CAD bTDC]	15	16	20
t_{dur} [CAD]	4	4	5
λ	2.6	2.6	1.85
Imep [bar]	3.6	3.8	5

The in-cylinder pressure was measured using a pressure transducer over 100 firing cycles. Fuel injection, spark ignition, and subsequent flame propagation were captured using a colour high speed video. Images were recorded during seven individual cycles at a frame rate of 9000 images per second. In addition to capturing the natural flame emission a second set of measurements were preformed where the OH chemiluminescence were filtered out using optics (308 nm mirror and 310 ± 10 nm filter) and captured onto a high speed camera with an image intensifier coupled in front of it. The OH chemiluminescence of the ignition and flame was captured for 20

individual cycles at a frame rate of 10000 images per second. Both the images of the natural flame emission and the OH chemiluminescence were processed to make average images at subsequent crank angle degrees.

Because (i) this investigation focuses on the modelling of stratified combustion modelling and (ii) manipulating moving valves in the OpenFOAM® code is complicated and computationally demanding, the present 3D URANS simulations conducted in this work were performed for a closed cycle, i.e. they only cover the period between Intake Valve Closing (IVC) and Exhaust Valve Opening (EVO). However, a full cycle simulation including the intake process was performed using the KIVA code by my former college Dr. A. Imren in order to estimate the initial turbulence level (see Table 4.4). Based on the results of this full-cycle simulation, a tumbling motion was introduced at the start of the OpeanFOAM® simulations by placing a tumble center with a maximum absolute velocity of 15 m/s at the point (-0.02 m, 0, 0) in the simulated combustion chamber; see Figure 4.20. Fixed temperature boundary conditions were set at the piston, cylinder linear, and cylinder head, with the wall temperature at each boundary being 500K, 480K, and 450K, respectively. The initial and boundary conditions are listed in Table 4.4.

Table 4.4: *Initial and boundary conditions*

Parameters	Initial value	Boundary type
k [m²/s²]	3.6	kqRWallFunction
ε [m²/s³]	1210	epsilonWallFunction
T_{IVC} [K]	400	fixedValue
p_{IVC} [bar]	1.1	zeroGradient
$\bar{c}$ [-]	0	fixedValue: 0

A computational mesh with 62 756 cells and the same combustion chamber geometry as the optical engine was generated by Dr. A. Imren using ICEM CFD meshing program and converted into OpenFOAM® format using a utility supplied with the code – see Figure 4.5. During compression (expansion) strokes, the mesh cells were compressed (expanded) in the direction of piston motion [133][134]. The time step was equal to 0.1 CAD. Computations were run on AMD Opteron 6220 CPUs, on a single node with 16 cores and 32/64 GB of RAM. Depending on the complexity of the sub-models, the computational time ranged from 7 hours to 3 days.

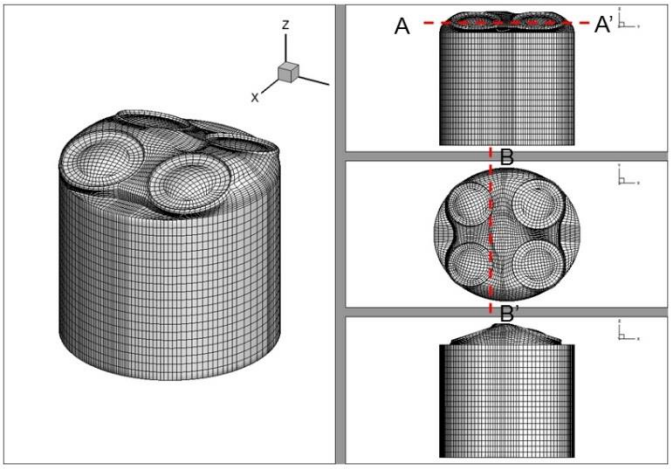

Figure 4.5: *Computational mesh for the research engine at IVC. Sections A-A' and B-B' cut through the centers of the ignition kernel and the hollow-cone spray, respectively.*

4.6. Effect of different sub-models

The stratified turbulent combustion model was implemented and extended in a stepwise fashion, and the effects of different sub-models on the simulated global burning characteristics were likewise studied step-by-step. Particular attention was paid to the sub-models for the laminar flame speed approximation, the calculation of the mean density and combustion temperature, the effects of turbulent fluctuations in the mixture fraction, and the evaporation source term in the mixture fraction variance equation.

4.6.1. Laminar flame speed

The laminar flame speed S_L is one of the key factors in determining the turbulent burning rate. It depends on the type of fuel that is used, unburned temperature, pressure and equivalence ratio. It can be measured or calculated using a well validated chemical mechanism. The present author is aware of a limited number of approximations [65][114][135][136] that can be used to estimate the laminar flame speed for gasoline-air mixtures. Figure 4.6 compares the laminar flame speeds calculated using these approximations to the experimental data of Zhao et al. [13] for flames formed at T_u=500 K and p=1 atm. The approximations by Rhodes and Keck [135] and Huang et al. [114] agree well with the measured values [13], with the latter approximation covering a wider range of operating conditions relevant to engine conditions. The approximation of Kwon et al. [136] over-predicts the measured data while that of Metghalchi and Keck [65] slightly under-predicts them.

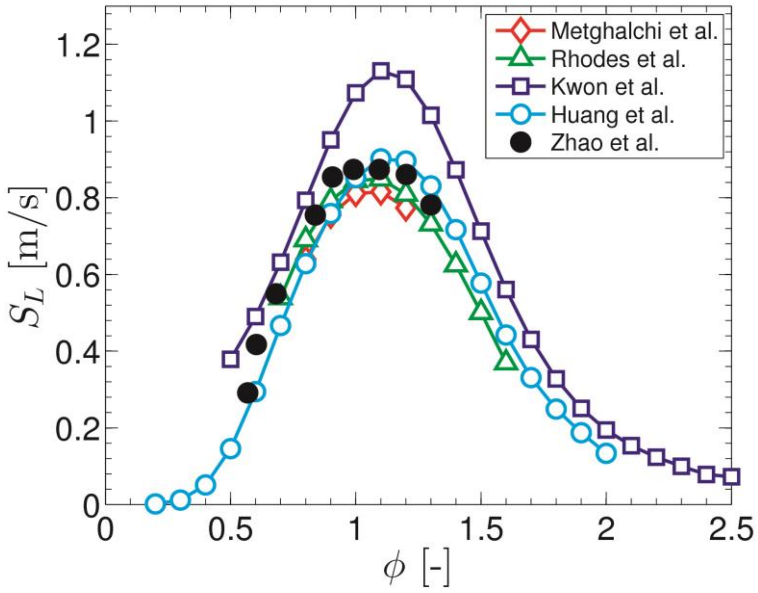

Figure 4.6: *Computed and measured laminar flame speeds for gasoline-air mixtures at T_u=500 K and p=1 atm. The red line with open diamonds shows the results obtained using the approximation of Metghalchi and Keck [65]; the green line with open triangles shows the approximation of Rhodes and Keck [135]; the blue line with open squares shows the approximation of Kwon et al. [136]; the cyan line with open circles shows the approximation of Huang et al. [114]; and the filled circles show the experimental measurements of Zhao et al.[13].*

To study the effect of different approximations of S_L on the global burning rate in the studied SG DISI engine, four runs were performed in which different expressions of S_L were substituted into Equation (4.25) for the fully-developed turbulent burning velocity, with all other things variables being held constant. In these simulations, the influence of turbulent fluctuations in the mixture composition on the burning rate was taken into account by using the presumed Favre beta-PDF and the mean density and temperature were computed using the BML method represented by Equations (4.48) and (4.49). The results obtained are shown in Figure 4.7. It can be seen that different approximations of S_L yield similar results in terms of burning rate and in-cylinder pressure under the simulated conditions. However, this does not mean that the combustion rate is insensitive to S_L. The combustion rate and in-cylinder pressure increase substantially if the speed S_L computed by approximation [114] is doubled, and decreased substantially if it is halved (see Figure 4.7). It is also worth noting that using the semi-detailed chemical mechanism discussed in Chapter 2 will offer an opportunity to simulate emissions in future work.

The CFD results discussed in the rest of the thesis were obtained using the approximation of Huang et al. [114], which is described in section 2.3.2.

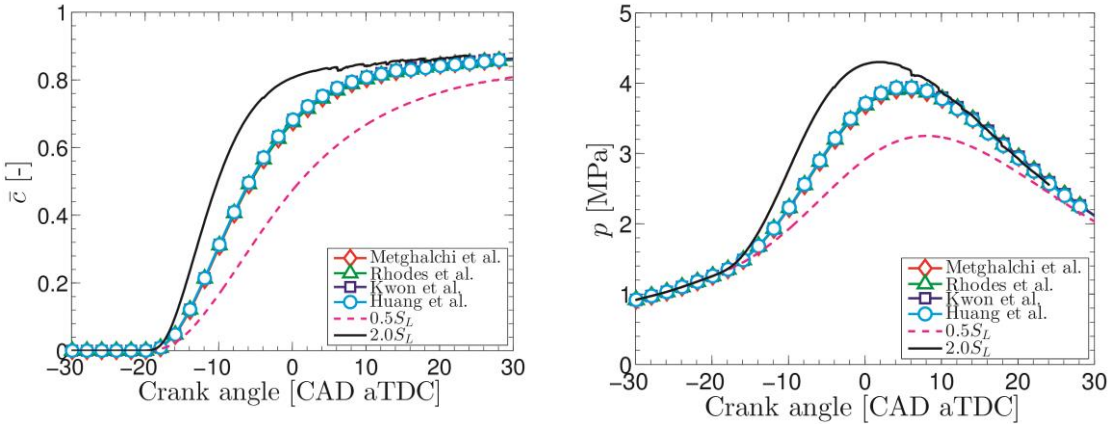

(a) Reynolds-averaged progress variable *(b) in-cylinder pressure*

Figure 4.7: *Comparison of volume-averaged $\bar{c}$ and pressure p computed using different approximations and in cases where S_L is doubled or halved for case 3 in Table 4.3.*

4.6.2. Mean density and temperature

As discussed in section 4.3.2, the expressions used to calculate the mean density $\bar{\rho}$ and mean temperature $\tilde{T}$ in the standard version of OpenFOAM® are Equations (4.44)-(4.46), which are flawed; the widely used BML method uses Equations (4.48) and (4.49). The calculated global burning characteristics obtained using the two approaches are compared in Figure 4.8. Under the conditions considered in this work, the OpenFOAM® method yielded a slightly faster combustion rate and higher pressure than the widely used BML method.

The CFD results discussed in the remainder of the thesis were obtained using the BML method rather than the standard method implemented in the unmodified version of OpenFOAM®.

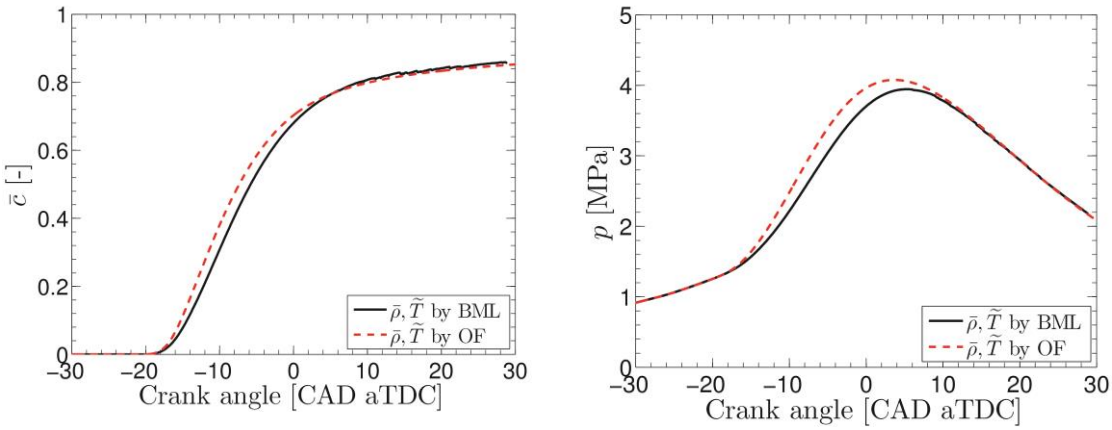

(a) Reynolds-averaged progress variable *(b) in-cylinder pressure*

Figure 4.8: *Comparison of volume-averaged $\bar{c}$ and pressure p computed using different methods for evaluating the mean density $\bar{\rho}$ and temperature $\tilde{T}$. The black solid line shows results obtained using the BML approach, i.e. Equations (4.48) and (4.49); the red dashed line shows results obtained using the OpenFOAM® approach, i.e. Equations (4.44)-(4.46). Data shown are for case 3 in Table 4.3.*

4.6.3. Combustion temperature

Figure 4.9 shows that the combustion temperature T_b obtained in the equilibrium calculations is substantially lower than that predicted when complete combustion is assumed, i.e. when using the standard version of OpenFOAM®. This is because the equilibrium combustion products contain substantial amounts of CO formed by CO_2 dissociation but this important process is neglected when complete combustion is assumed. The difference in the combustion temperatures has a straightforward effect on the in-cylinder mean pressure and temperature as shown in Figure 4.10 (b) and (c). However, the combustion temperature has a weaker effect on the Reynolds-averaged progress variable as shown in Figure 4.10 (a) because the progress variable is only affected indirectly via the mean density. Modifying OpenFOAM® by implementing the temperature approximation described in section 2.3.2 to improve its calculation of the combustion temperature is likely to be very important when modelling NO_x emissions because the well-known Zel'dovich mechanism predicts that the rate of thermal NO formation is highly sensitive to the product temperature, as discussed in by Miller and Bownman [137].

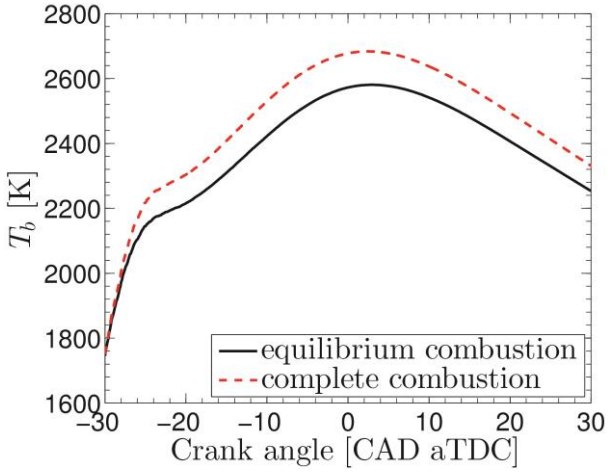

Figure 4.9: *Comparison of the volume-averaged combustion temperature (T_b) evaluated using the equilibrium assumption and the assumption of complete combustion. t_{inj}=-100 CAD aTDC, t_{ign}=-33 CAD aTDC, ϕ=1.15.*

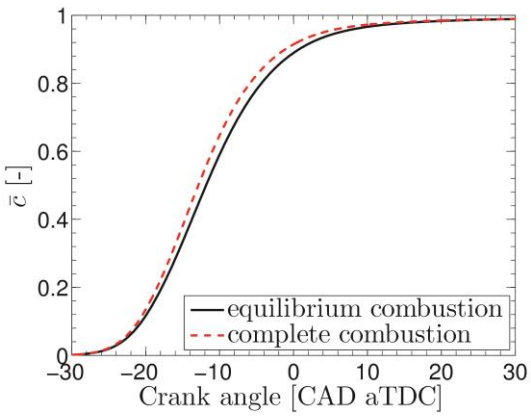

(a) Reynolds-averaged progress variable

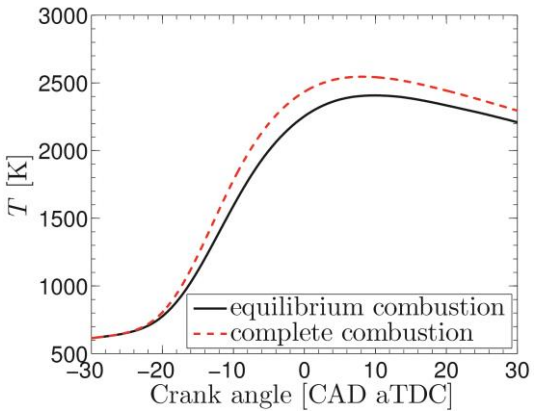

(b) in-cylinder temperature

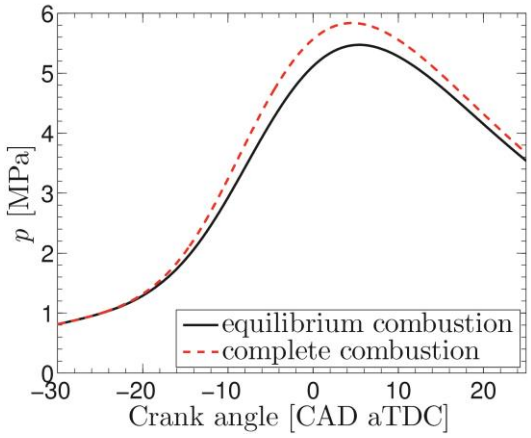

(c) in-cylinder pressure

Figure 4.10: *Comparison of volume-averaged progress variable $\bar{c}$, temperature $\tilde{T}$ and pressure p evaluated assuming equilibrium (solid lines) or complete (dashed lines) combustion. t_{inj}=-100 CAD aTDC, t_{ign}=-33 CAD aTDC, ϕ=1.15.*

4.6.4. Turbulent fluctuations in mixture composition

A widely used approach to modelling the influence of turbulent fluctuations in mixture composition on the mean characteristics of stratified burning (e.g. ρ_b, T_b, S_L, U_t, etc.) is based on invoking a presumed Probability Density Function (PDF) $P_f(f)$ for the mixture fraction. Three approaches to modelling this influence are compared in Figure 4.11, which shows the effects of turbulent fluctuations in the mixture fraction on the computed volume-averaged $\bar{c}$ and pressure p. The solid curves in Figure 4.11 were generated by evaluating the laminar flame speed $S_L(\tilde{f})$ and combustion temperature $T_b(\tilde{f})$ using the local Favre-averaged value $\tilde{f}$ of the mixture fraction, i.e. neglecting the turbulent fluctuations in f. Conversely, the red dashed curves were computed using the Favre beta-PDF $\tilde{P}_f$ given by Equations (4.37) and (4.38) and using Equation (4.36) to average the local combustion temperature and turbulent burning velocity, which depends on the mixture fraction due to dependence of U_t on $S_L(f)$. Finally, the blue dot-dashed curves were computed by invoking the canonical beta-PDF P_f given by Equation (4.41) and using Equation (4.39) to average the local characteristics.

The two presumed PDF approaches yield a slower combustion rate for a global equivalence ratio of 1.15, which is the equivalence ratio that maximizes the magnitude of this effect. Indeed, because the peak value of the laminar flame speed $S_L(\varphi)$ for the gasoline surrogate is computed at $\varphi \cong 1.15$, both positive and negative turbulent fluctuations in the mixture fraction reduce the local laminar flame speed and, hence, the local rate of turbulent burning.

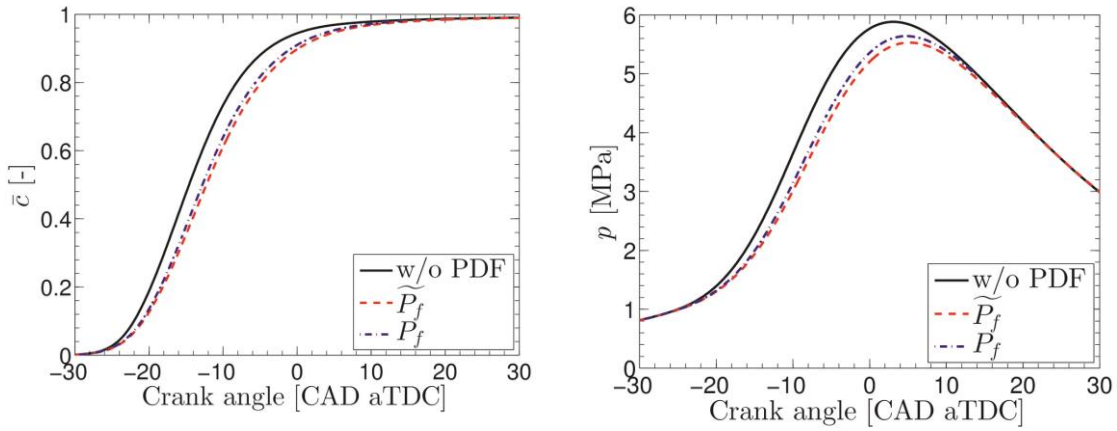

(a) Reynolds-averaged progress variable *(b) in-cylinder pressure*

Figure 4.11: *Comparison of volume-averaged $\bar{c}$ and pressure p computed without any beta-PDF for the mixture fraction, with the Favre beta-PDF, and with the canonical beta-PDF for the mixture fraction. t_{inj} =100 CAD bTDC, t_{ign}=33 CAD bTDC, the mean equivalence ratio is equal to 1.15.*

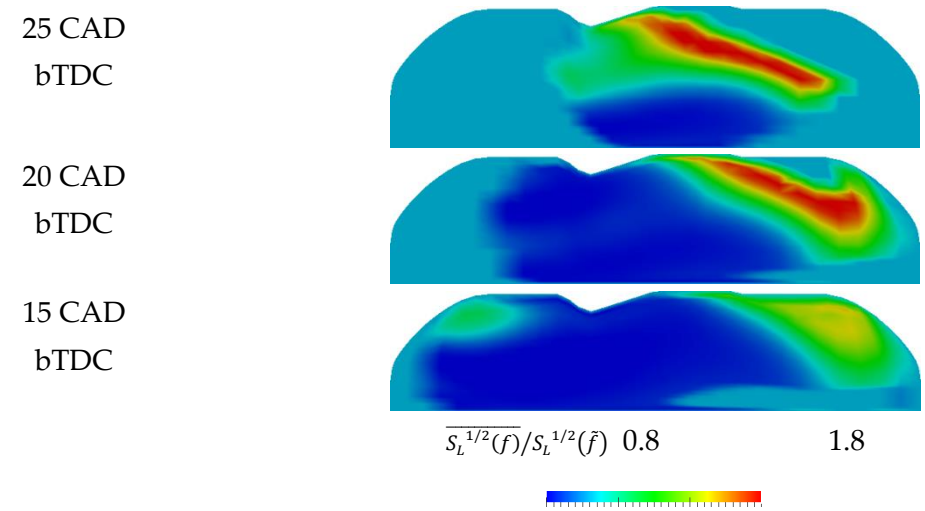

Figure 4.12: *Distribution of $\overline{S_L^{1/2}(f)}/S_L^{1/2}(\tilde{f})$ at different time points, computed using the Favre beta-PDF for the mixture fraction. t_{inj} =100 CAD bTDC, t_{ign}=33 CAD bTDC, the mean equivalence ratio is equal to 1.15.*

Ratios of $\overline{U_t(f)}/U_t(\tilde{f}) = \overline{S_L^{1/2}(f)}/S_L^{1/2}(\tilde{f})$ computed in the same run at various instants are shown in Figure 4.12. In keeping with the reasoning outlined above, this ratio is below unity in the most of the engine cylinder's volume. The ratio may be greater than unity in locally very lean mixtures, where positive fluctuations in the

mixture fraction increase the local laminar flame speed more strongly than negative fluctuations due to the highly non-linear dependence on $S_L(f)$ in very lean mixtures.

Under the conditions of the present simulations, the canonical and Favre beta-PDF yield similar results but the computational cost of the former is almost four times that of the latter.

4.6.5. The effect of including an evaporation source term in the mixture fraction variance equation

The discussions of the mixture fraction variance equation in Refs. [138][139] do not mention an evaporation source term. However, the use of such a term was addressed in Ref. [128]. Figure 4.13 compares the volume-averaged $\bar{c}$ and pressure obtained by substituting either $\widetilde{S_v} = 0$ (dashed curves) or the term obtained using Equations (4.33)-(4.35) (solid curves) into Equation (4.31). Under the simulated conditions, the evaporation source term affects the overall combustion process weakly.

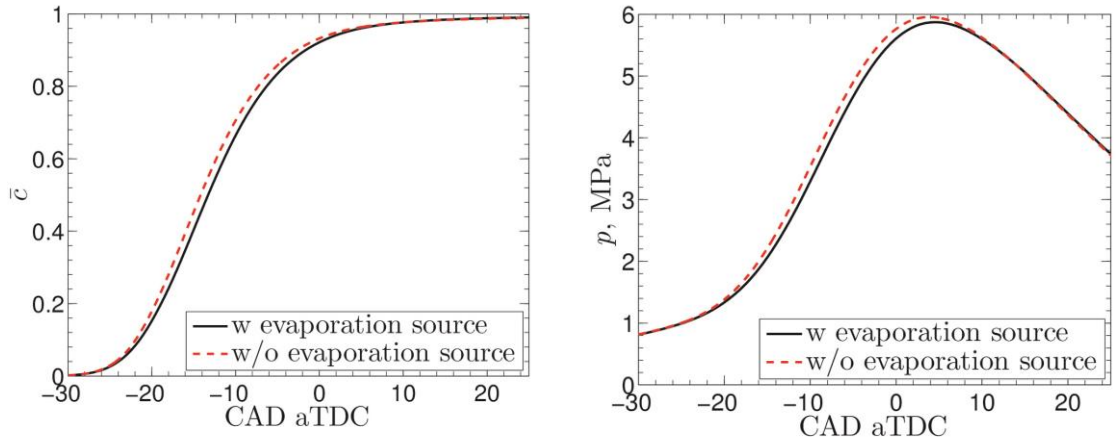

(a) Reynolds-averaged progress variable *(b) in-cylinder pressure*

Figure 4.13: *Comparison of the Reynolds-averaged progress variable $\bar{c}$ and pressure p calculated with and without the extra source term in the mixture fraction variance equation. t_{inj}=-100 CAD aTDC, t_{ign}=-33 CAD aTDC, ϕ=1.15.*

Figure 4.14 shows the effect of the evaporation source term on the normalized mixture fraction variance field $\frac{\widetilde{f''^2}}{f_{st}^2}$ at different instants, where f_{st} equals the stoichiometric fuel air ratio. The first row in Figure 4.14 clearly shows that magnitude of $\frac{\widetilde{f''^2}}{f_{st}^2}$ calculated with evaporation source term is nearly eight times greater than that without immediately after the end of injection, with significant difference in the scale legends. However, the normalized mixture fraction variance fields calculated with and without the evaporation source term at the start of combustion are very similar, as shown by the plots in the second row of Figure 4.14.

In these simulations, the influence of turbulent fluctuations in the mixture composition on the burning rate was taken into account by invoking the Favre beta-PDF.

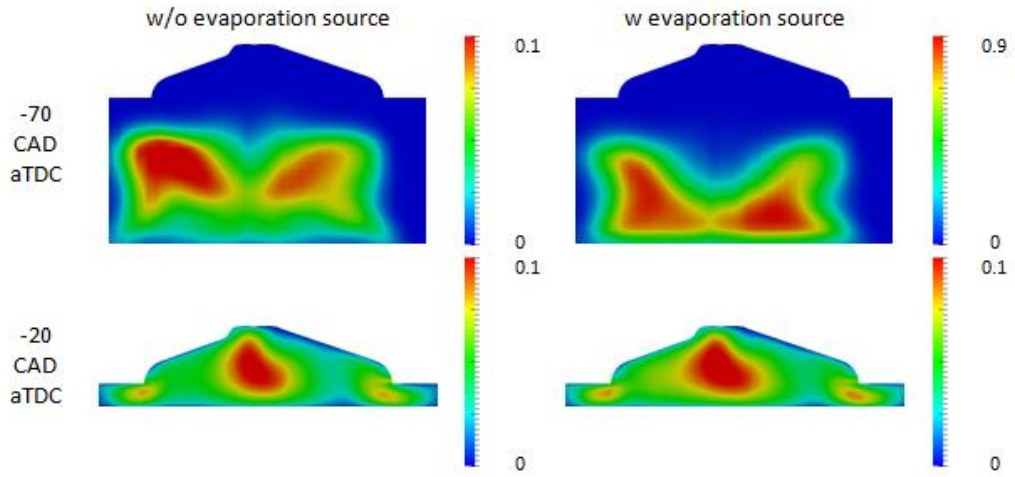

Figure 4.14: *Comparison of normalized mixture fraction variance* $\frac{\widetilde{f''^2}}{f_{st}^2}$ *with and without the extra source term in the mixture fraction variance equation.* t_{inj}*=-100 CAD aTDC,* t_{ign}*=-33 CAD aTDC,* ϕ*=1.15.*

4.7. Sensitivity study

A sensitivity study was conducted to assess the model's robustness. Because the accurate prediction of turbulence and turbulent mixing is essential in the calculation of turbulent combustion rates, a range of relevant input parameters were initially varied in the study, including the turbulence model, turbulent Prandtl number, initial turbulent kinetic energy, initial turbulent dissipation rate, fuel injection timing, fuel injection pressure, the amount of injected fuel and injection position. Second, the ignition process involves a number of phenomena such as the build-up of an extremely high voltage and current between the electrode gaps; the break-down of the electric arc; the heating of the gas phase, and so on. However, the ignition model implemented into the standard version of OpenFOAM® and used in this work was a simple step-function which substantially oversimplifies the real ignition process. The influence of the input parameters of the ignition model on the major global characteristics of the combustion process was investigated by varying the ignition timing, strength, duration, diameter and position. Finally, the model's sensitivity to numerical input parameters was studied by varying the grid size, differential schemes, and so on. All of the simulations in the sensitivity study were performed for a single set of operating conditions corresponding to case 3 in Table 4.3.

4.7.1. Turbulence model

Engineering turbulence models are necessary in CFD research on combustion engines, because resolving every motion at every scale is still computationally unfeasible under typical engine operating conditions. Such engineering models typically involve two transport equations that simulate the spatial and temporal evolution of two large-scale characteristics of turbulence. The most widely used model

of this sort in CFD R&D is the standard $k-\varepsilon$ model implemented in the original version of OpenFOAM® due to its robustness, computational economy, and reasonable reproduction of experimental trends. The $k-\varepsilon$ turbulence model was the most heavily used turbulence model in this work.

In addition to the standard $k-\varepsilon$ model, various other two-equation turbulence models that are implemented in the official version of OpenFOAM® were tested, namely (i) the Launder and Sharma $k-\varepsilon$ turbulence model [105], (ii) the RNG $k-\varepsilon$ model [98], (iii) the realizable $k-\varepsilon$ model [140] and (iv) the $k-\omega$ SST model [99]. The Launder and Sharma $k-\varepsilon$ turbulence model was developed for low-Reynolds number, compressible and combusting flows [105]. The RNG model was developed by renormalizing the Navier-Stokes equations to account for the effects of smaller scales of motion [98]. The realizable $k-\varepsilon$ turbulence model satisfies certain mathematical constraints on the Reynolds stresses that are consistent with the physics of turbulent flows. It is suggested to provide superior performance for flows involving rotation, boundary layers under strong adverse pressure gradients, separation, and recirculation [140]. The $k-\omega$ SST model is a blended model that addresses both regions near walls and regions far from walls. This model is fairly robust and generally does a good job near solid boundaries. It also is often found to do a better job at capturing recirculation regions than other models [99].

The effect of using the above-mentioned turbulence models on the calculated results averaged over the ignition kernel, i.e. a spherical volume with a diameter of 3 mm, is shown in Figure 4.15. It is obvious that the turbulence models affect the fuel-air mixing and combustion process substantially. The standard $k-\varepsilon$ model predicted a slightly rich fuel-air mixture in the ignition zone whereas the other investigated turbulence models predicted leaner fuel-air mixtures in this same location, as shown in Figure 4.15 (a). The local turbulent kinetic energy reached its maximum value at around 10 CAD bTDC for most of the turbulence models. The standard, Launder Sharma and realizable $k-\varepsilon$ models yielded relatively high local turbulent kinetic energies whereas the RNG $k-\varepsilon$ and $k-\omega$ SST model gave relatively low local turbulent kinetic energies, as shown in Figure 4.15 (b). It is worth noting that all of the investigated turbulence models yielded a strong peak in the local turbulent kinetic energy at around -25 CAD aTDC due to fuel injection, as shown in Figure 4.15 (b). Therefore, the turbulence level before combustion in a DISI engine is mainly controlled by the fuel injection process.

The standard $k-\varepsilon$ model predicted the fastest burning rate as well as the highest in-cylinder pressure, as shown in Figure 4.16. This is associated with higher turbulent kinetic energy and the slightly rich local fuel-air mixture calculated using the standard $k-\varepsilon$ turbulence model. It is worth remembering that both laminar and turbulent burning velocities peak at slightly rich conditions. The other investigated turbulence model yielded incomplete combustion. The standard $k-\varepsilon$ turbulence model was used in all of the other simulations discussed in this Chapter, but Figure 4.16 clearly shows that a choice of turbulence model is of substantial importance and this issue should definitely be addressed in future work. Accurately predicting the evolution of turbulence in combustion chambers remains challenging, as clearly shown in a recent comprehensive study by Darmstadt group [141][142].

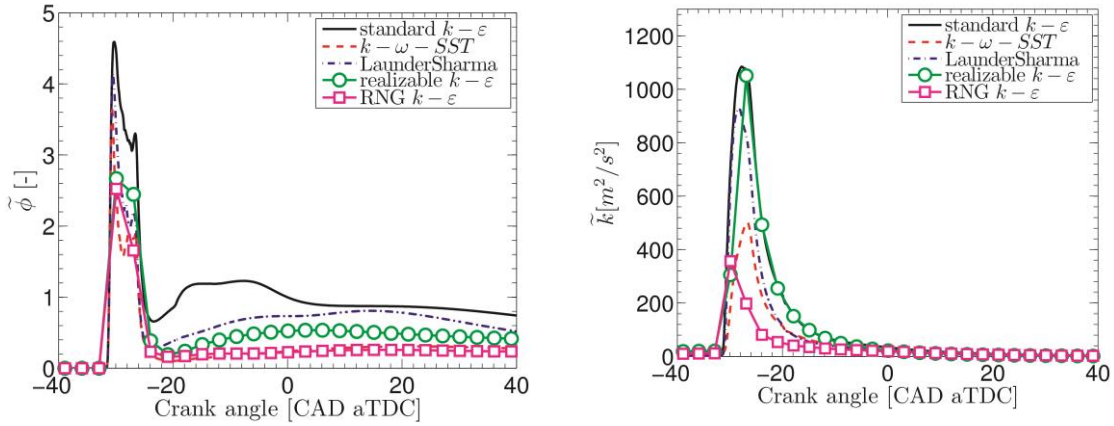

(a)local equivalence ratio *(b)local turbulent kinetic energy*

Figure 4.15: *The effect of various turbulence models on the mean local equivalence ratio and turbulent kinetic energy within the ignition kernel. Both quantities were averaged over a sphere with a diameter of 3 mm.*

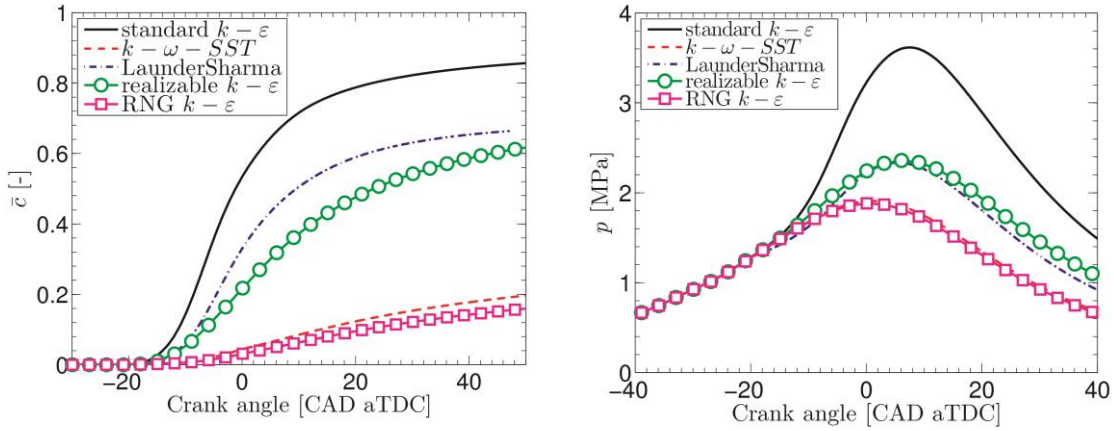

(a) Reynolds-averaged progress variable *(b) in-cylinder pressure*

Figure 4.16: *The effect of various turbulence models on the volume-averaged Reynolds-averaged progress variable and mean in-cylinder pressure.*

4.7.2. Turbulent Prandtl number

The turbulent Prandtl number Pr_t is defined as the ratio of the turbulent/eddy viscosity μ_t and the turbulent heat diffusivity α_t

$$Pr_t = \frac{\mu_t}{\alpha_t} \tag{4.53}$$

where

$$\mu_t = C_\mu \rho \frac{\tilde{k}^2}{\tilde{\varepsilon}} \tag{4.54}$$

within the framework of the standard $k-\varepsilon$ model. In OpenFOAM®, the turbulent Prandtl number is used to evaluate α_t when solving the transport equations for the following quantities: Favre-averaged enthalpy, enthalpy conditioned to unburned gas,

Favre-averaged mixture fraction and mixture fraction variance. The values of Pr_t reported in the CFD literature range typically range from 0.7 to 0.9 depending on the type of flow being considered, but can be much lower (e.g. 0.35) in some cases [143]-[145].

The effect of the turbulent Prandtl number on the turbulent combustion was investigated by conducting simulations in which Pr_t was set to 0.3, 0.5, 0.7 and 0.9. As shown in Figure 4.17, variation within this range had very little effect on local parameters such as the local equivalence ratio, segregation factor and turbulent kinetic energy. However, the average combustion rate and pressure were increased by decreasing Pr_t as shown in Figure 4.18. This was due to the decrease of the turbulent Laglangian time scale $\tau_L = D_{t,\infty}/u'^2$ associated with the decrease of turbulent diffusivity $D_{t,\infty}$ when Pr_t increases according to Equation (4.24). This raises theτ_{fd}/τ_L ratio and thus increases the turbulent burning velocity (Equation (4.23)) leading an increase in the combustion rate.

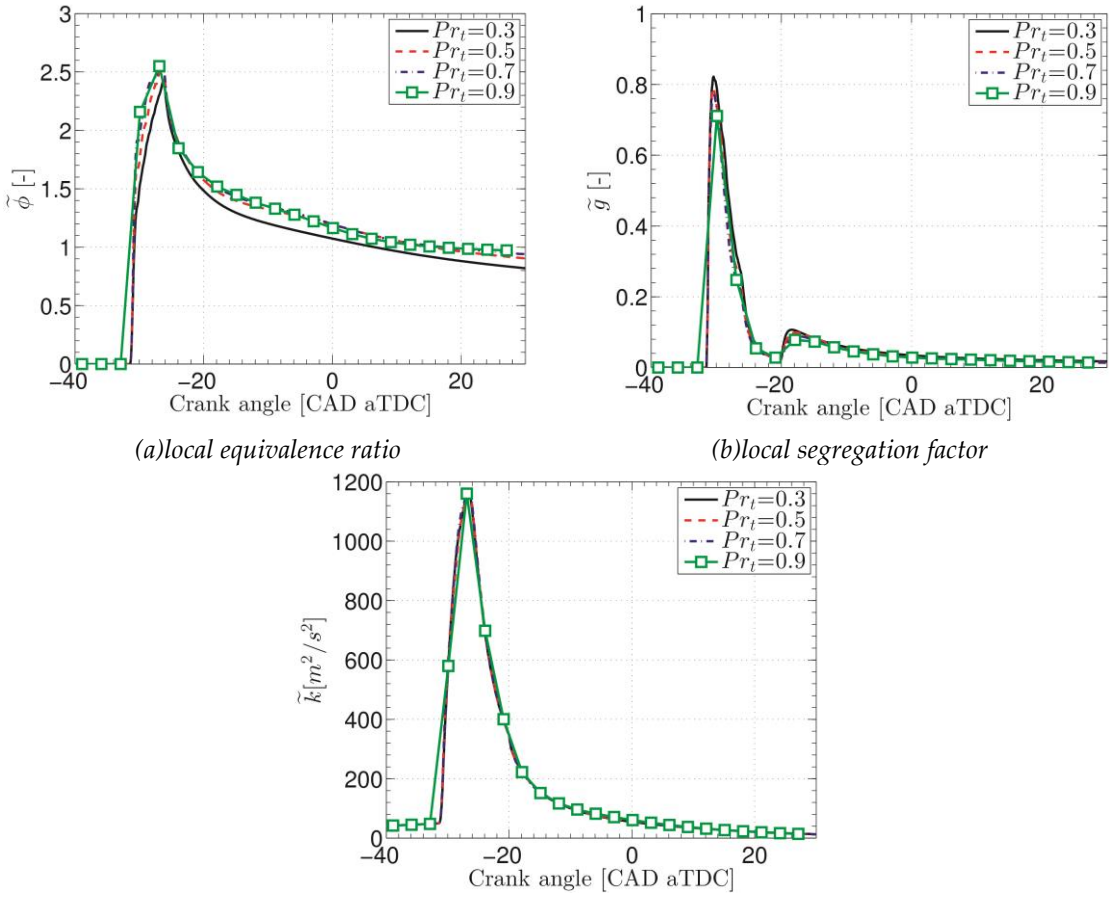

(a)local equivalence ratio *(b)local segregation factor*

(c)local turbulent kinetic energy

Figure 4.17: *The effect of varying the turbulent Prandtl number on the mean local equivalence ratio, segregation factor and turbulent kinetic energy within the ignition kernel. These quantities were averaged over a sphere with a diameter of 3 mm.*

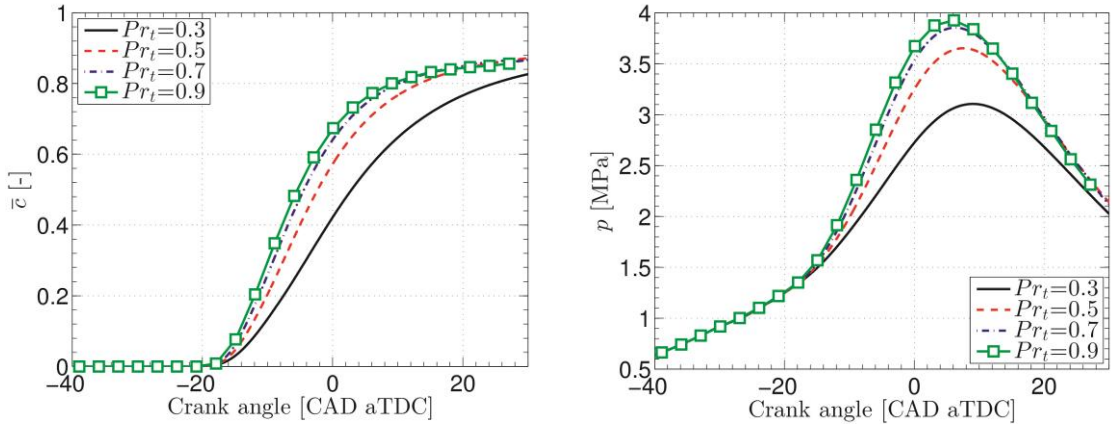

(a) Reynolds-averaged progress variable *(b) in-cylinder pressure*

Figure 4.18: *The effect of varying the turbulent Prandtl number on the volume-averaged Reynolds-averaged progress variable and mean in-cylinder pressure.*

4.7.3. The initial turbulent kinetic energy and its dissipation rate

The manipulation of moving valves in the OpenFOAM® code is complicated and time-consuming, and the studies presented herein were focused on combustion modelling. Therefore, the URANS simulations were performed over a closed cycle, i.e. from ICV to EVO. The initial turbulence level and tumble motion were specified based on a full cycle KIVA calculation and simulations were performed to investigate the dependence of the computed combustion rate on variables associated with the initial turbulence including the initial turbulent kinetic energy, turbulent dissipation rate, tumble position and tumble strength.

The effects of varying the initial turbulent kinetic energy and its dissipation rate on the Reynolds-averaged progress variable and in-cylinder pressure is shown in Figure 4.19. The overall combustion rate is only weakly affected by these two variables.

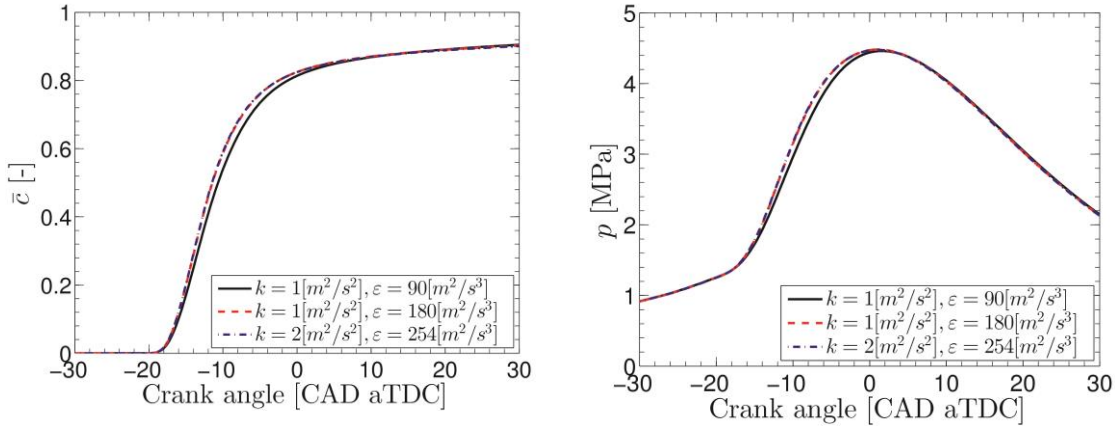

(a) Reynolds-averaged progress variable *(b) in-cylinder pressure*

Figure 4.19: *The effect of varying the initial turbulent kinetic energy and its dissipation rate on the volume-averaged Reynolds-averaged progress variable and mean in-cylinder pressure.*

4.7.4. Initial tumble position and its maximum velocity

The initial tumble position and its maximum velocity were selected based on the results of prior studies, so a series of simulations were performed using different initial values of these variables to determine the effect of their variation on the combustion process. The coordinates of the tested initial positions of the tumble center are indicated by the red dots in Figure 4.20, and the effects of varying the position of the tumble center and its maximum velocity on the overall combustion rate are shown in Figure 4.21-Figure 4.23. It is clear that neither of these variables has a strong effect on the volume-averaged Reynolds-averaged combustion progress variable or the in-cylinder pressure, which justifies the assumption of initial tumble position rather than performing the full cycle simulation.

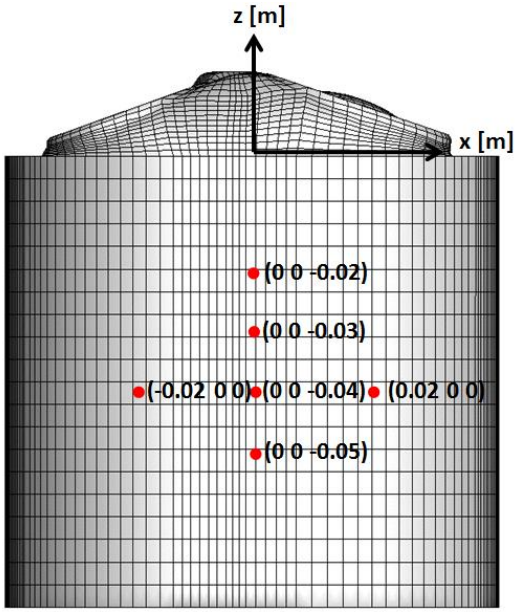

Figure 4.20: *The tested initial tumble center positions.*

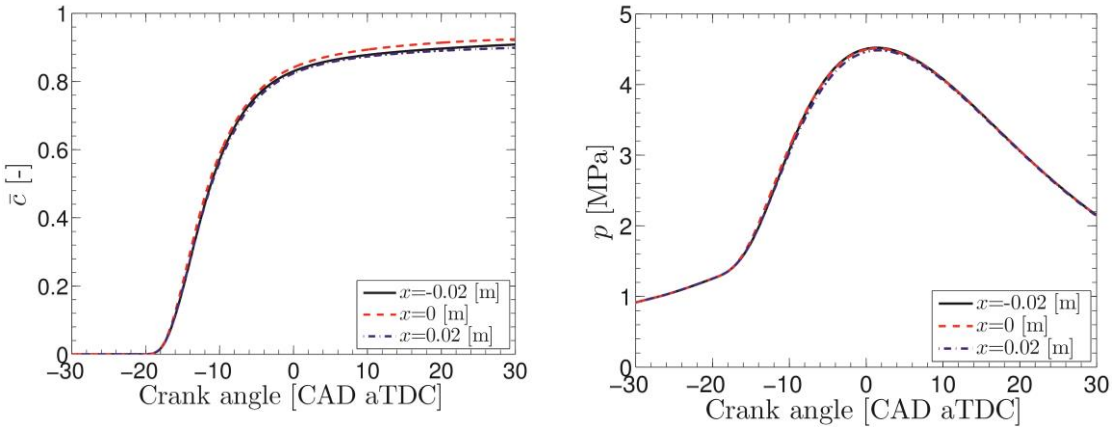

(a) Reynolds-averaged progress variable *(b) in-cylinder pressure*

Figure 4.21: *The effect of varying the initial tumble centre position on the volume-averaged Reynolds-averaged progress variable and mean in-cylinder pressure.*

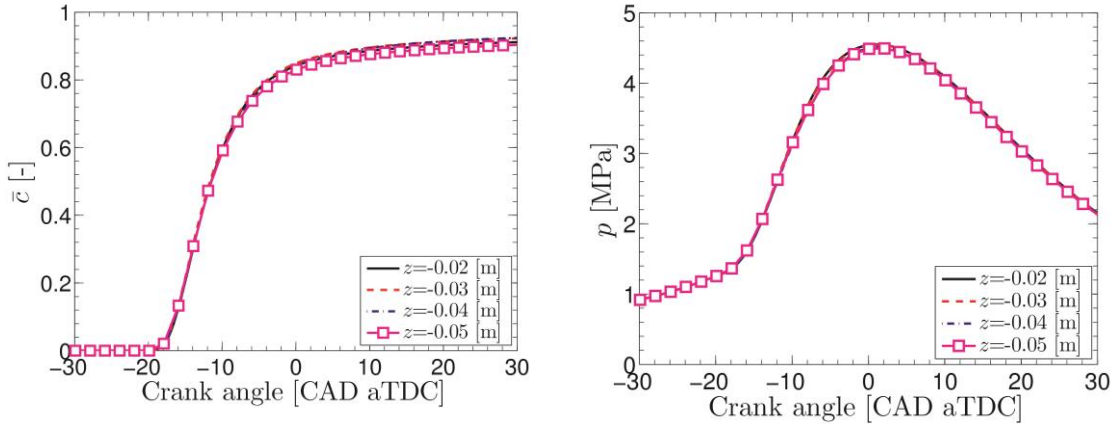

(a) Reynolds-averaged progress variable *(b) in-cylinder pressure*

Figure 4.22: *The effect of varying the initial tumble centre position on the volume-averaged Reynolds-averaged progress variable and mean in-cylinder pressure.*

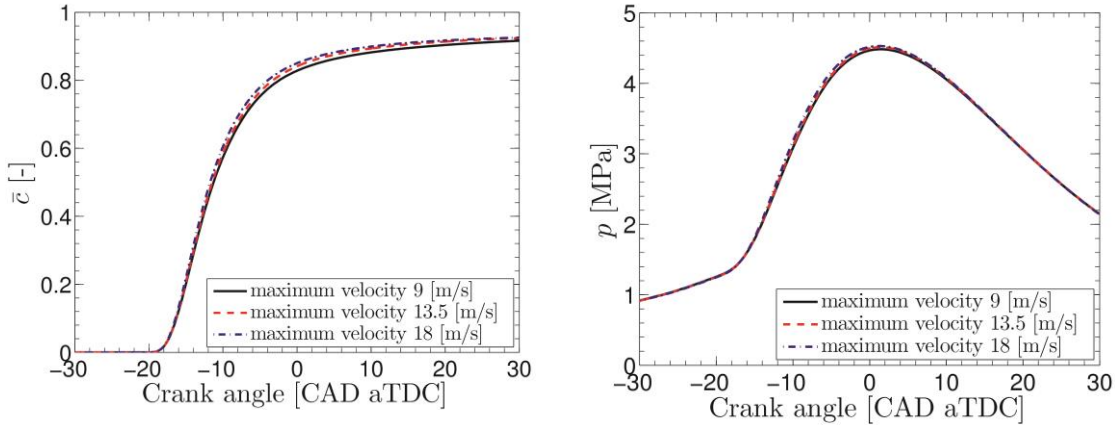

(a) Reynolds-averaged progress variable *(b) in-cylinder pressure*

Figure 4.23: *The effect of varying the maximum tumble velocity on the volume-averaged Reynolds-averaged progress variable and mean in-cylinder pressure.*

4.7.5. Fuel injection

The fuel injection process is essential for the generation of turbulence and the formation of a combustible fuel-air mixture, and therefore flame propagation. In the SG DISI engine measurements, the timing of the electric signal for fuel delivery was controlled by an ECU (Engine Control Unit), but the real injection timing was slightly delayed relative to the signal timing. Therefore, studies were conducted to assess the sensitivity of the computed fuel-air mixing characteristics and combustion processes to the timing of fuel injection and the fuel injection pressure.

The effect of fuel injection timing on the computed mean local equivalence ratio and segregation factor within the ignition kernel is shown in Figure 4.24. The local equivalence ratio for an early injection was lower than for a late injection. In other words, an early injection resulted in more extensive mixing of fuel and air. The degree of inhomogeneity in the fuel-air mixture was represented by the segregation factor. The timing of the peak $\tilde{g}$ was delayed for a late injection, but after -20 CAD aTDC, the

mean local segregation factor was only weakly affected by the injection timing. Delaying the injection timing slightly decreased the local turbulent kinetic energy as shown in Figure 4.25. Nevertheless, Figure 4.26 shows that varying the injection timing had negligible effects on the computed combustion progress variable and mean in-cylinder pressure was negligible, probably due to mutual compensation between the effects of the ignition timing on the mean local equivalence ratio and the turbulent kinetic energy.

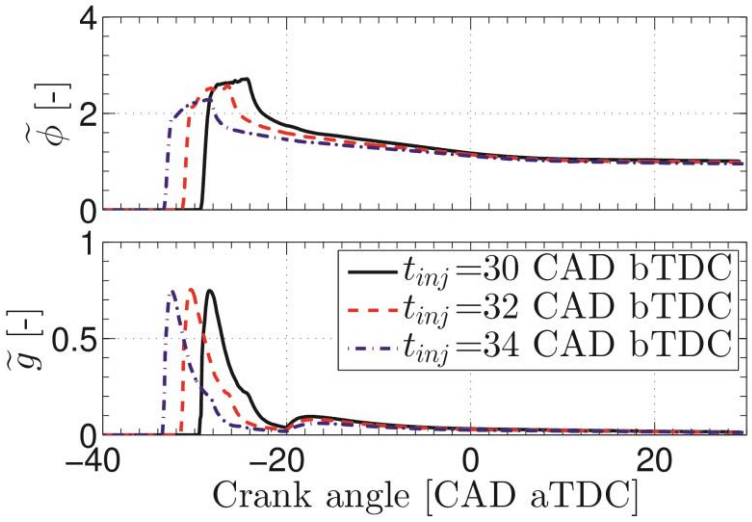

Figure 4.24: *The effect of the fuel injection timing on the mean local equivalence ratio and segregation factor within the ignition kernel. Both quantities were averaged over a sphere with a diameter of 3 mm.*

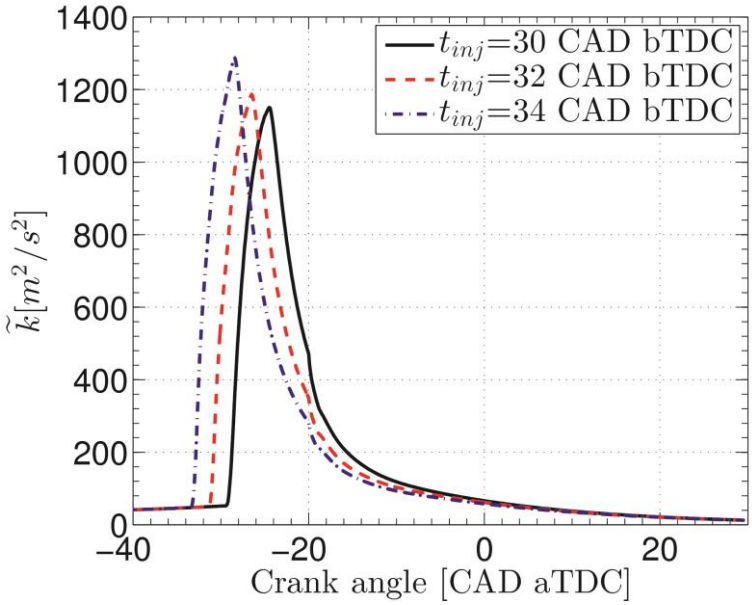

Figure 4.25: *The effect of the fuel injection timing on the mean local turbulent kinetic energy within the ignition kernel. This quantity was averaged over a sphere with a diameter of 3 mm.*

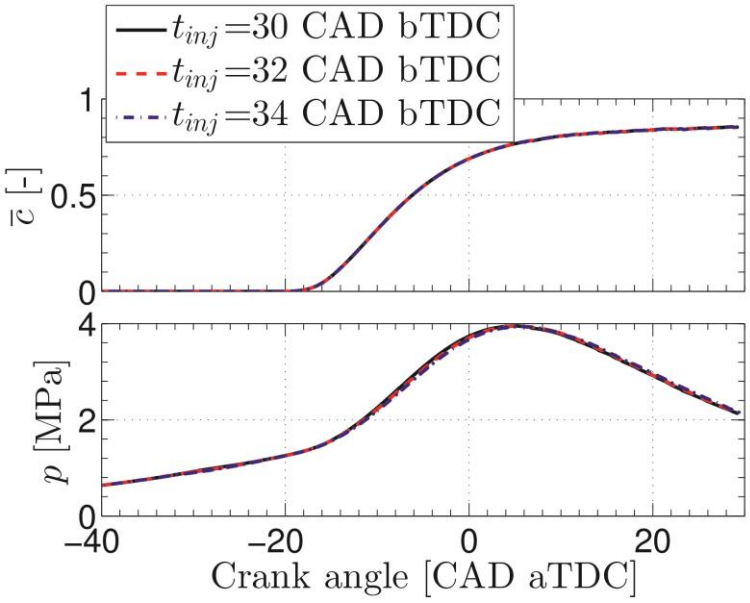

Figure 4.26: *The effect of the fuel injection timing on the volume-averaged Reynolds-averaged progress variable and mean in-cylinder pressure.*

The effect of the injection pressure on the mean local equivalence ratio and segregation factor within the ignition kernel is shown in Figure 4.27. The injection pressure had a noticeable impact on the fuel-air mixing process: the higher the injection pressure, the lower the mean local equivalence ratio was. However, it had only a weak impact on the segregation factor. Increasing in the injection pressure substantially enhanced the local turbulent kinetic energy immediately after the injection, but the effect was much less pronounced at the ignition timing (see Figure 4.28). The global Reynolds-averaged progress variable and in-cylinder pressure were weakly affected by the injection pressure, as shown in Figure 4.29.

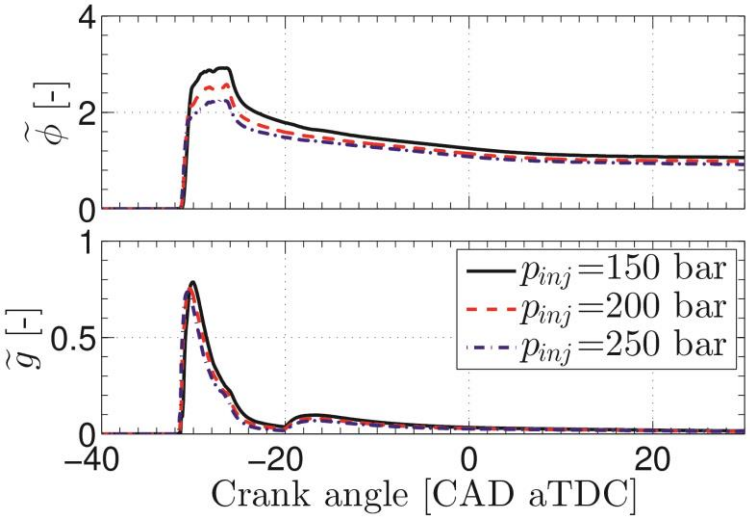

Figure 4.27: *The effect of the fuel injection pressure on the mean local equivalence ratio and segregation factor within the ignition kernel. Both quantities were averaged with a sphere of a diameter of 3 mm.*

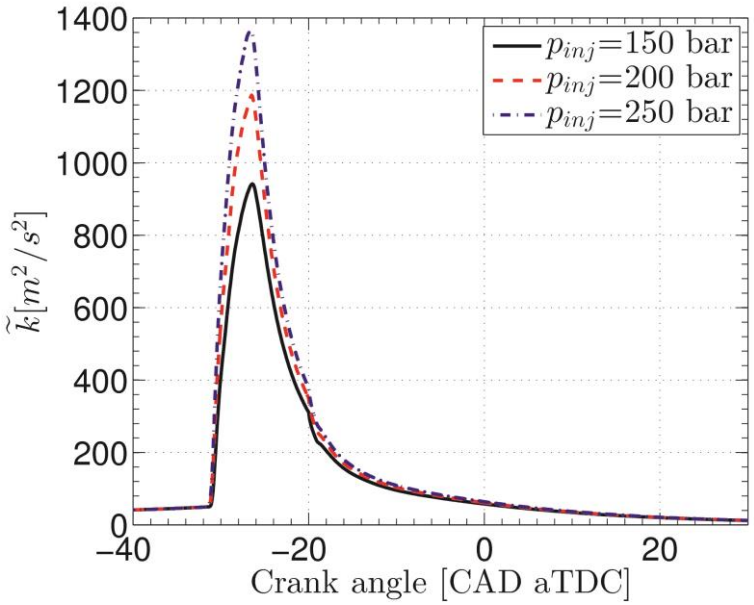

Figure 4.28: *The effect of the fuel injection pressure on the mean local turbulent kinetic energy within the ignition kernel. This quantity was averaged over a sphere with a diameter of 3 mm.*

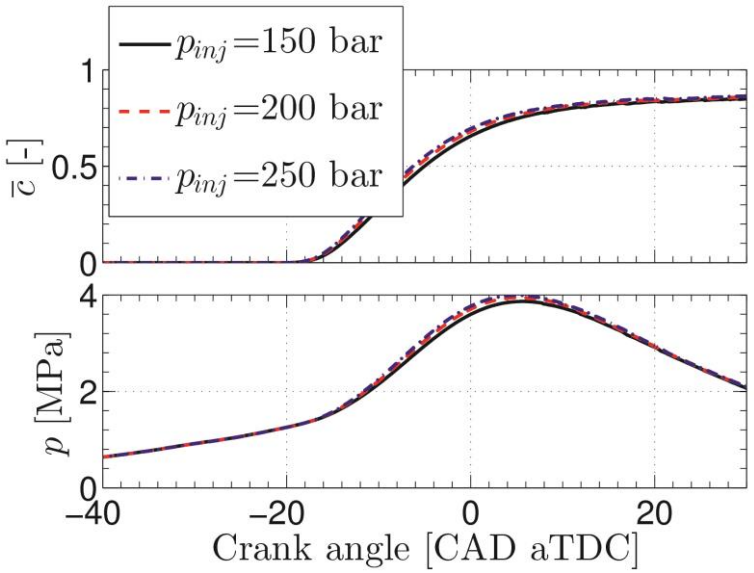

Figure 4.29: *The effect of the fuel injection pressure on the volume-averaged Reynolds-averaged progress variable and mean in-cylinder pressure.*

The 3D URANS simulations of combustion in a DISI engine were performed using a primary breakup model that assumes a uniform droplet size distribution at the nozzle exit; the secondary breakup model was described using the KHRT model, which is discussed in detail in Chapter 3. The sensitivity of the computed results to the initial droplet size at the nozzle exit, which is an input parameter of the primary breakup model, was investigated by varying the droplet size from 10 to 40 μm. The results presented in Figure 4.30 show that the initial droplet size strongly influences the mean local parameters (i.e. parameters associated with processes occurring within

the ignition kernel) such as the equivalence ratio, segregation factor and turbulent kinetic energy. Increasing the droplet size reduced the mean local equivalence ratio but increased the mean local segregation factor and turbulent kinetic energy. Because both decreases in $\tilde{\phi}$ and increases in $\tilde{k}$ are beneficial for the mean local burning rate, the highest overall combustion rate was obtained using the largest initial droplets as shown in Figure 4.31.

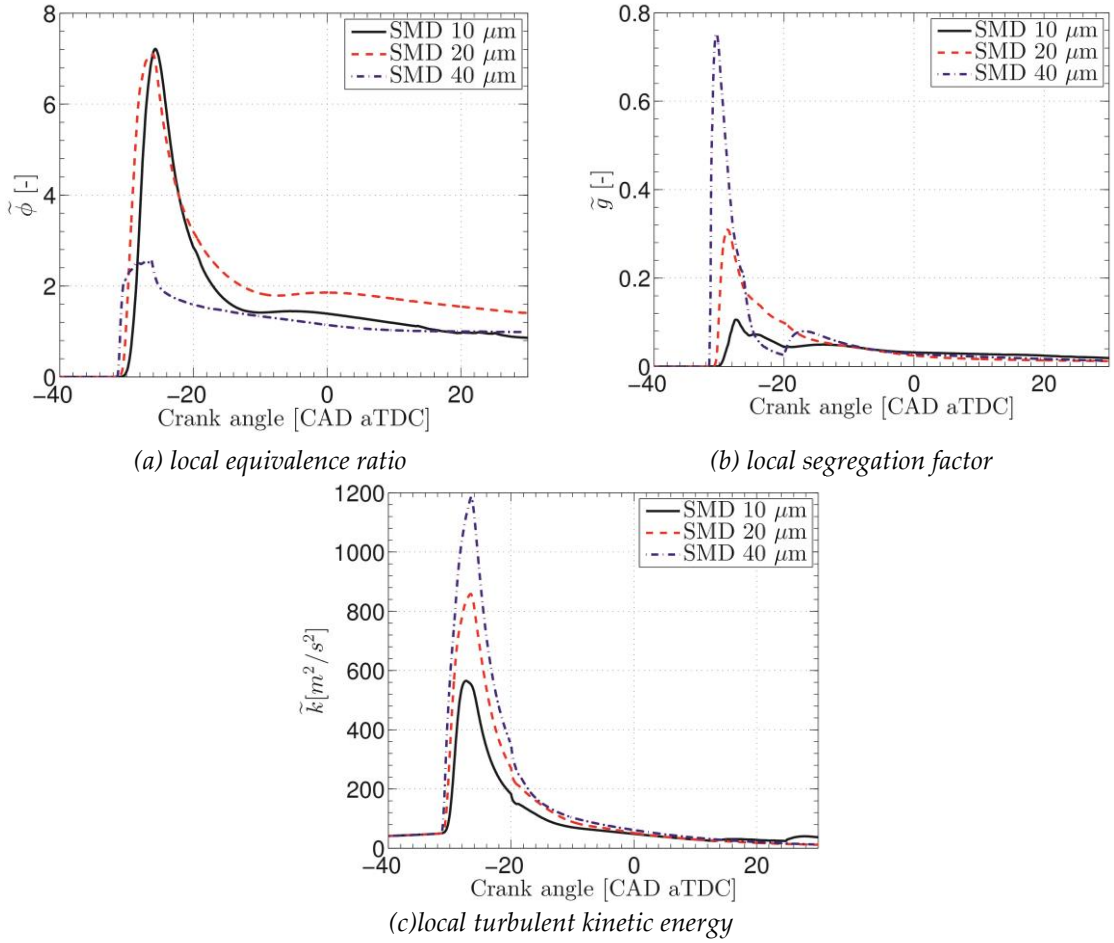

(a) local equivalence ratio

(b) local segregation factor

(c)local turbulent kinetic energy

Figure 4.30: *The effect of initial droplet size on the mean local equivalence ratio, segregation factor and turbulent kinetic energy within the ignition kernel. These quantities were averaged over a sphere with a diameter of 3 mm.*

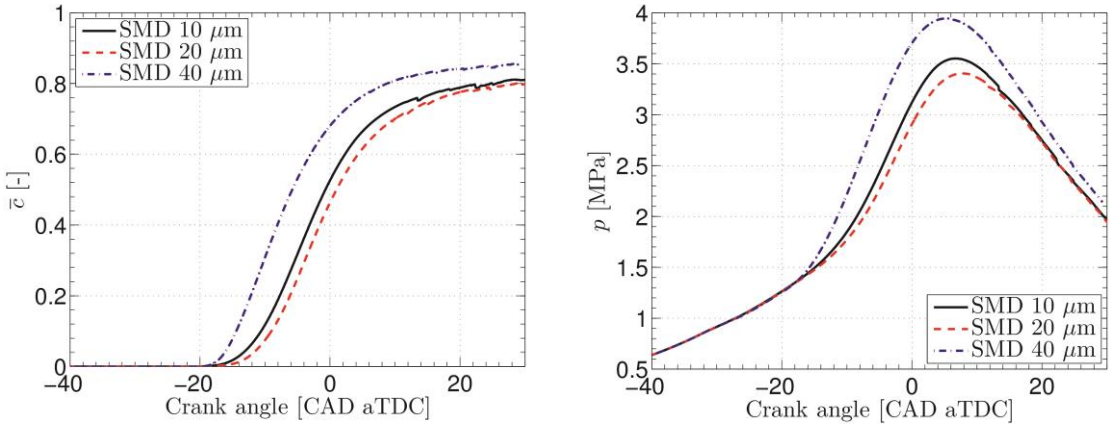

(a) Reynolds-averaged progress variable *(b) in-cylinder pressure*

Figure 4.31: *The effect of initial droplet size on the volume-averaged Reynolds-averaged progress variable and mean in-cylinder pressure.*

4.7.6. Ignition parameters

The simple ignition model implemented in the standard version of OpenFOAM® and used in the simulations presented herein relies on three input parameters: the ignition strength, ignition diameter and ignition duration.

The ignition strength controls the regress variable's rate of decrease in the ignition cells. The effects of varying the ignition strength on the computed volume-averaged Reynolds-averaged combustion progress variable and mean in-cylinder pressure are shown in Figure 4.32. The overall combustion rate increased with the ignition strength but the predicted effect was weak when the ignition strength was greater than 8.

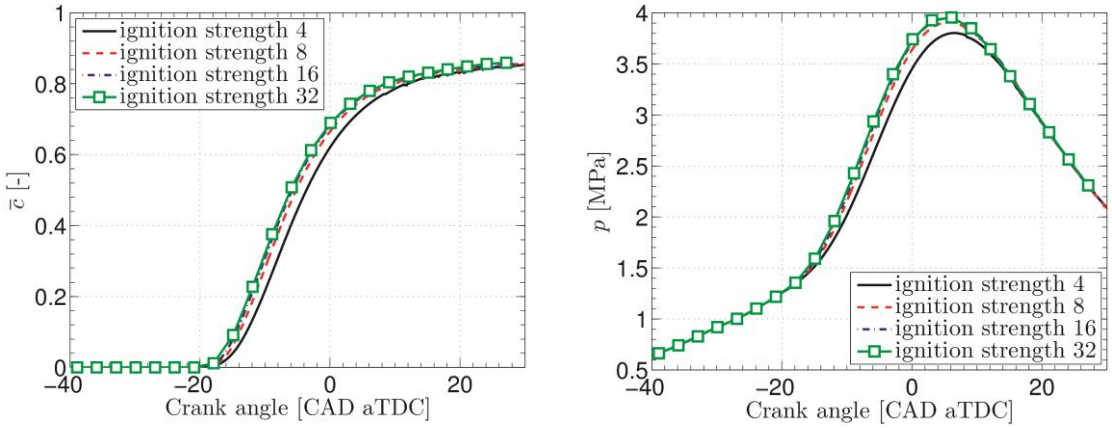

(a) Reynolds-averaged progress variable *(b) in-cylinder pressure*

Figure 4.32: *The effect of ignition strength on the volume-averaged Reynolds-averaged progress variable and mean in-cylinder pressure.*

The ignition diameter controls the size of the ignition kernel. Its effect on the overall combustion rate is shown in Figure 4.33, which indicates that increasing the ignition diameter caused a modest increase in the combustion rate.

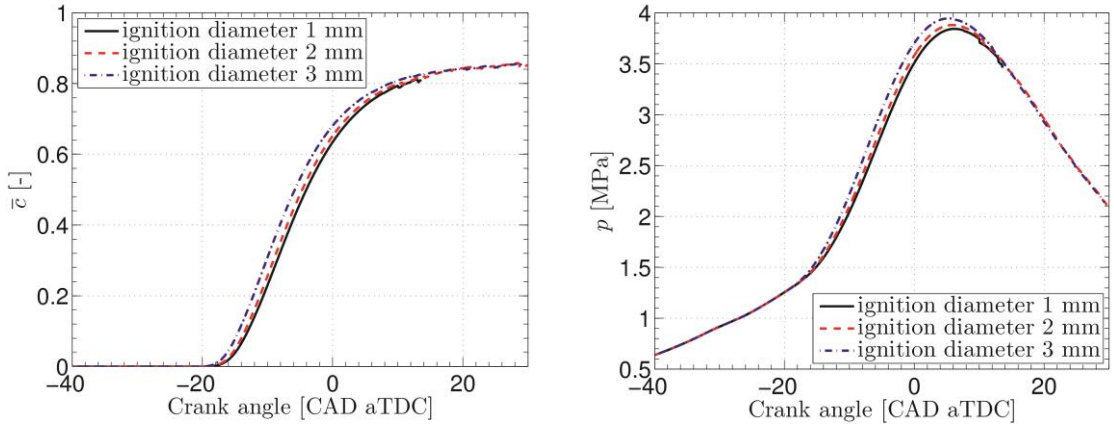

(a) Reynolds-averaged progress variable *(b) in-cylinder pressure*

Figure 4.33: *The effect of ignition diameter on the volume-averaged Reynolds-averaged progress variable and mean in-cylinder pressure.*

The ignition duration controls the duration of time interval during which the ignition model is active. As shown in Figure 4.34, varying in the ignition duration had very modest effects on the computed combustion rate.

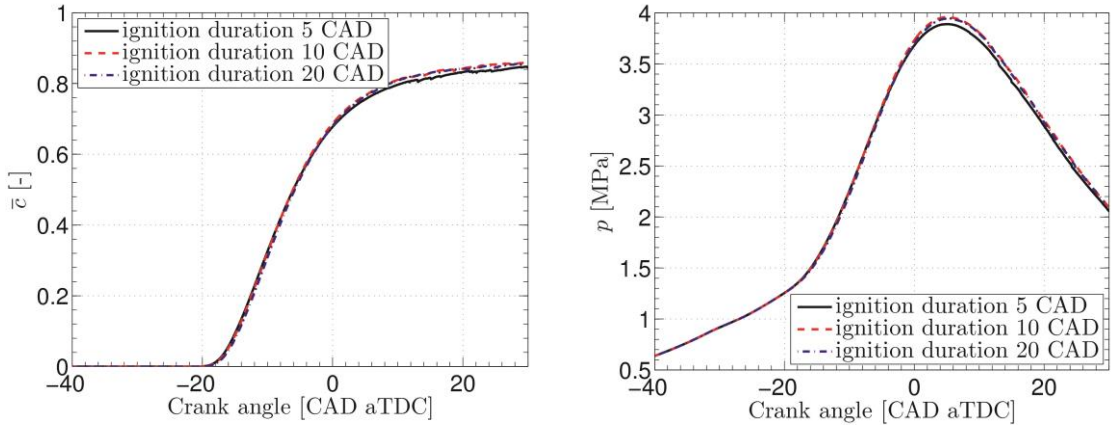

(a) Reynolds-averaged progress variable *(b) in-cylinder pressure*

Figure 4.34: *The effect of ignition duration on the volume-averaged Reynolds-averaged progress variable and mean in-cylinder pressure.*

4.7.7. Mesh aspect ratio

Grid size dependency is a commonly discussed problem in spray and combustion simulations. The modelling of spray and combustion in a piston engine, the problem is complicated by the piston's motion, which necessitates the use of a moving mesh. The moving mesh technique adopted in this thesis involves extending and compressing the grid in the direction of piston motion. Accordingly, the mesh can be strongly extended or compressed in one direction and the mesh aspect ratio, i.e. the ratio of the cells' longest edges to that of their shortest edges, can be substantially changed. When using unstructured grids, the aspect ratio is generally considered to be an important mesh characteristic and a common goal is to make the aspect ratio as close to unity as possible. However, due to the complexity of the combustion chamber geometries considered in applied CFD studies, researchers must use meshes that are characterized

by substantially greater aspect ratios. Nevertheless, it is generally advisable to make the aspect ratio as close to unity as possible when performing studies using a commercial CFD code. For instance, the Fluent manual recommends avoiding aspect ratios in excess of 5:1 [146]. However, this is not a strict requirement because the acceptability of a given aspect ratio is determined by the type of flow under consideration and the scheme being used. As long as a grid-independent solution is obtained, the quality of the grid can be considered acceptable.

In order to investigate the sensitivity of results computed within the framework of the present thesis to the aspect ratio, three sets of meshes were generated with 10, 20 and 30 grid layers in the cylinder's linear zone. These three meshes had very different maximum aspect ratios of 13, 28 and 42, respectively, at TDC. The numerical solutions obtained in the simulations were only weakly sensitive to the aspect ratio of the mesh as shown in Figure 4.35 and Figure 4.36. The mean local equivalence ratio calculated within the ignition kernel using 10 grid layers was slightly lower than those obtained with 20 or 30 grid layers, but the mean local segregation factor and local turbulent kinetic energy were not affected by the grid's aspect ratio (see Figure 4.35). Similarly, the volume-averaged Reynolds-averaged progress variable and in-cylinder pressure were not affected by the aspect ratio of the grid as shown in Figure 4.36.

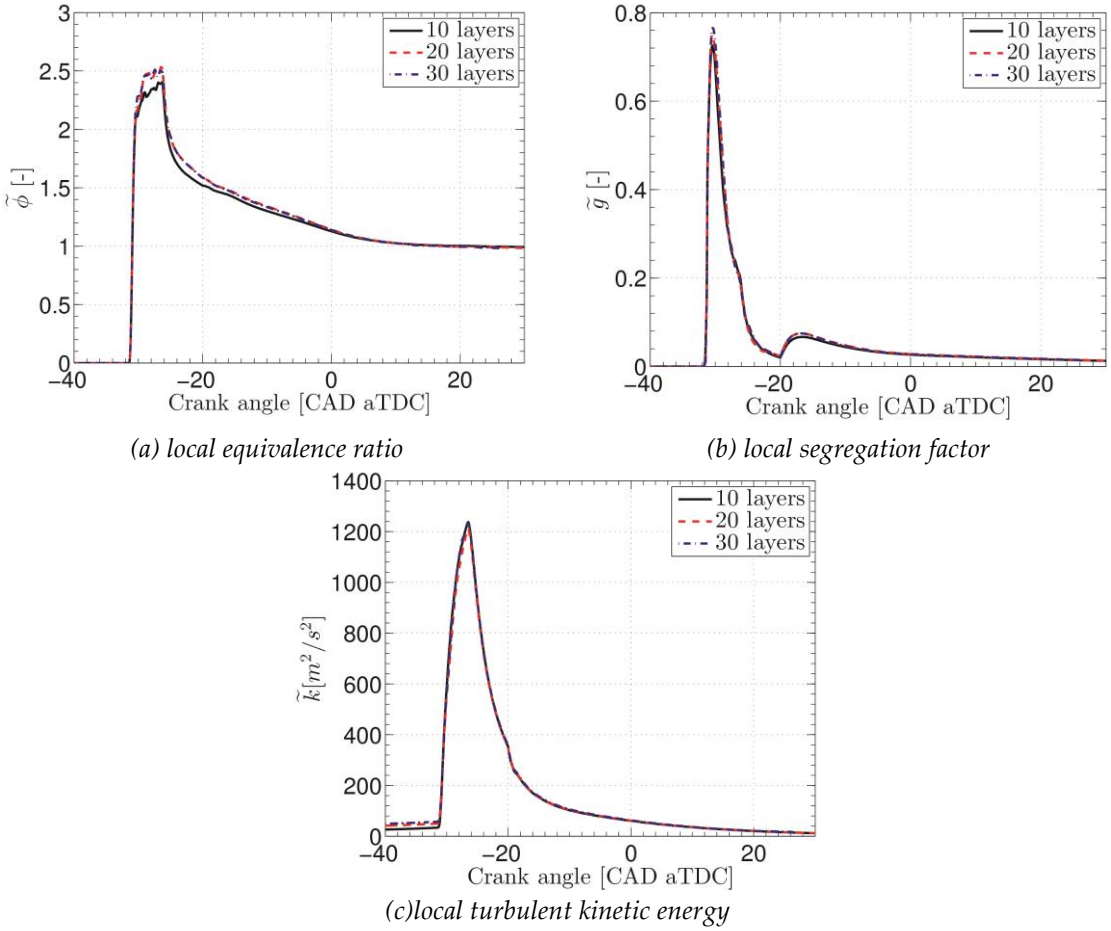

(a) local equivalence ratio

(b) local segregation factor

(c)local turbulent kinetic energy

Figure 4.35: *The effect of changing the grid mesh on the mean local equivalence ratio, segregation factor and turbulent kinetic energy within the ignition kernel. These quantities were averaged over a sphere with a diameter of 3 mm.*

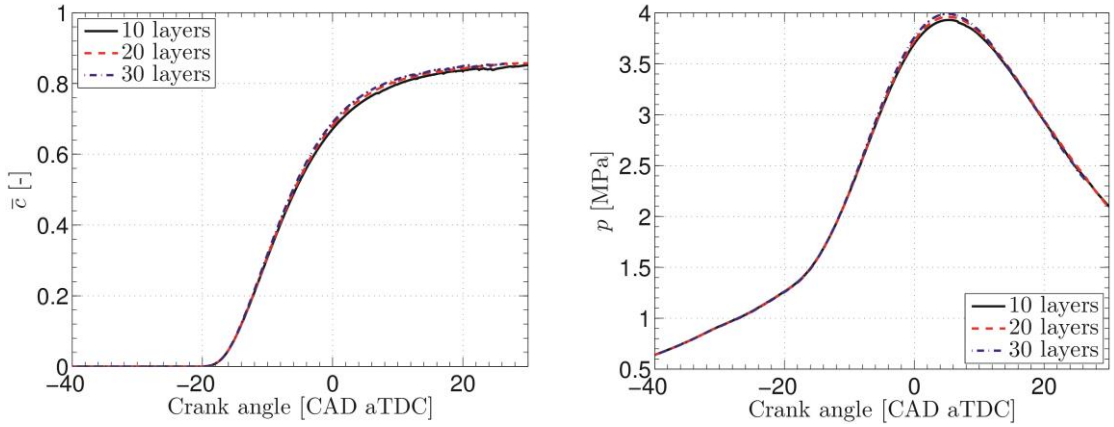

(a) Reynolds-averaged progress variable *(b) in-cylinder pressure*

Figure 4.36: *The effect of changing the grid mesh on the mean local Reynolds-averaged progress variable and mean in-cylinder pressure.*

4.7.8. Time step

The effects of changing the numerical integration time step size on the calculated results are shown in Figure 4.37 and Figure 4.38. Three test runs were performed for a medium load case (imep = 5 bar) with t_{inj}= 32 CAD bTDC and t_{ign}= 20 CAD bTDC using time steps of 0.05 CAD, 0.1 CAD, and 0.5 CAD. When the time step was too large, i.e. 0.5 CAD, the calculated mean local (within the ignition kernel) equivalence ratio and turbulent kinetic energy were significantly lower than those obtained using the two smaller time steps as shown in Figure 4.37 (a) and (b). In addition, the evolution of the segregation factor $\tilde{g}$ was slightly delayed as shown in Figure 4.37 (c). These results indicate that the species and turbulence transportation were poorly resolved when the time step was set to 0.5 CAD. The combustion rate and in-cylinder pressure calculated using the largest time step of 0.5 CAD were slightly greater than those obtained using a smaller time step such as 0.1 CAD (see Figure 4.38). The results obtained using time steps of 0.1 CAD and 0.05 CAD were very similar but the latter value was more computationally expensive. Therefore, most of results discussed in the present thesis were obtained using a time step of 0.1 CAD.

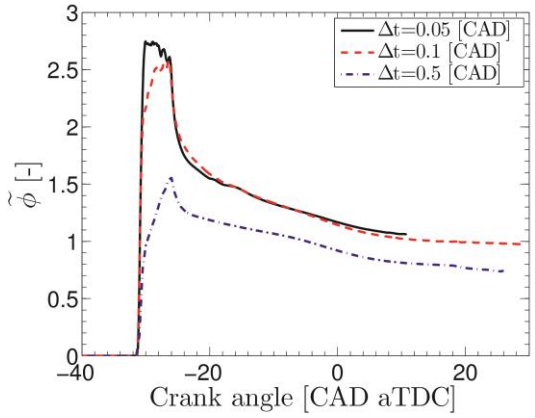

(a) local equivalence ratio

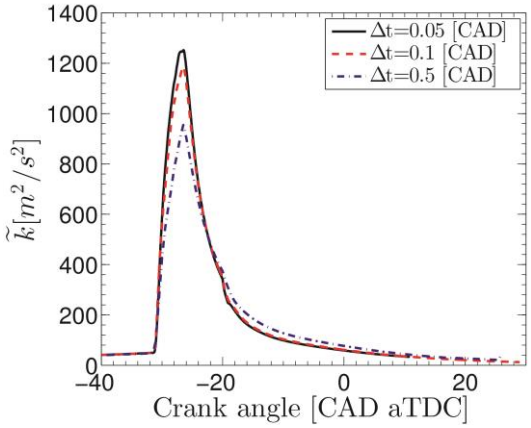

(b) local segregation factor

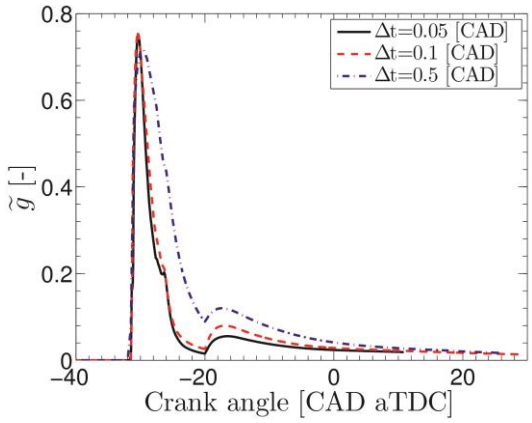

(c)local turbulent kinetic energy

Figure 4.37: *The effect of the integration time step on the mean local equivalence ratio, turbulent kinetic energy and segregation factor within the ignition kernel. These quantities were averaged over a sphere with a diameter of 3 mm.*

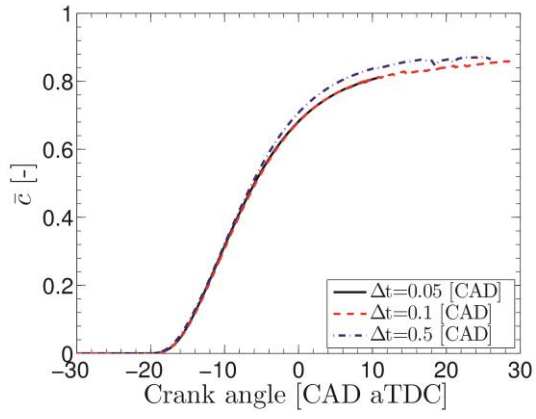

(a) Reynolds-averaged progress variable

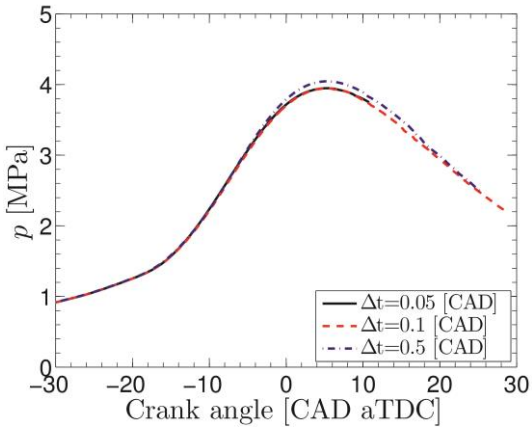

(b) in-cylinder pressure

Figure 4.38: *The effect of the integration time step on the volume-averaged Reynolds-averaged progress variable and mean in-cylinder pressure.*

4.7.9. Numerical schemes

Numerical schemes are used to discretize of Partial Differential Equations (PDE) and transform them into sets of algebraic equations. OpenFOAM® offers a wide range of discretization schemes for various nonlocal terms that are often used in transport equations.

In the present work, three numerical schemes for the discretization of divergence terms such as $\nabla.\left(\rho_u U_t \tilde{b}\right)$ from Equation (4.42), were tested: the first order Gauss upwind 0 1, second order Gauss Gamma01, and second order Gauss LimitedLinear01 schemes. When applied to Equation (4.42), all three schemes were bounded because the regress variable was a bounded scalar, i.e. $0 \leq \tilde{b} \leq 1$. Figure 4.39 illustrates the effect of the divergence scheme on the computed progress variable and in-cylinder pressure. The first order Gauss upwind scheme yielded a slightly slower combustion rate and lower pressure than the two other schemes, both of which produced similar results.

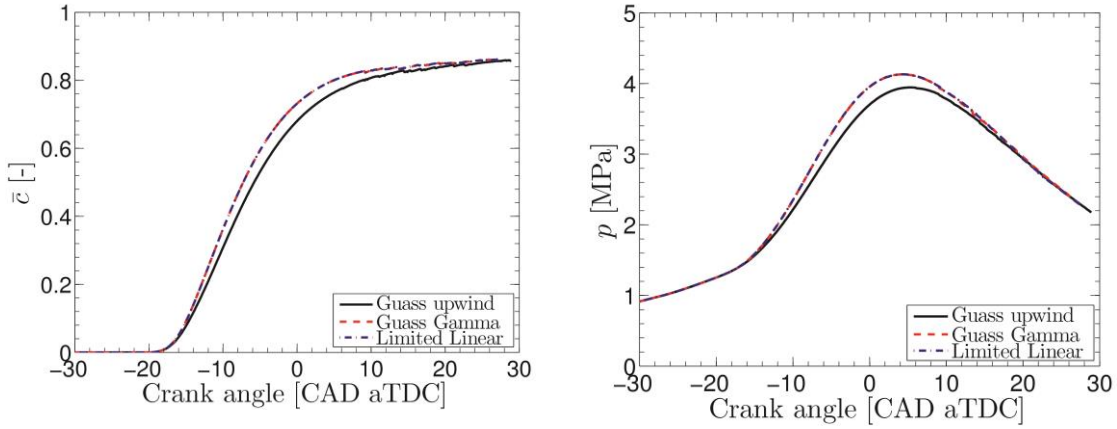

(a) Reynolds-averaged progress variable *(b) in-cylinder pressure*

Figure 4.39: *The effects of three different divergence schemes on the volume-averaged Reynolds-averaged progress variable and mean in-cylinder pressure.*

A Laplacian discretization schemes are used to discretize Laplacian terms such as $\nabla.[\bar{\rho}(\kappa + D_t)\nabla\tilde{b}]$ from Equation (4.42). Two Laplacian schemes were tested in this work: the second order conservative Gauss linear corrected scheme and the first order non-conservative Gauss linear uncorrected scheme. Figure 4.40 shows that both yielded near-identical results.

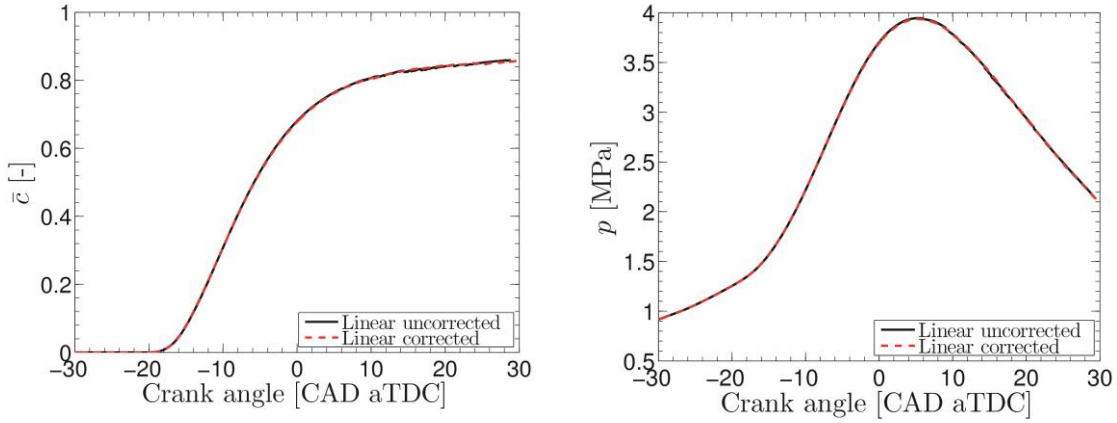

(a) Reynolds-averaged progress variable *(b) in-cylinder pressure*

Figure 4.40: *The effects of two different Laplacian schemes on the volume-averaged Reynolds-averaged progress variable and mean in-cylinder pressure.*

Most of results discussed in the present thesis were obtained using the Gauss upwind divergence scheme and the Gauss linear uncorrected Laplacian scheme.

4.8. Comparison with measurements

Figure 4.41 compares the in-cylinder pressure traces from two experiments conducted at different engine loads to the simulated in-cylinder pressure curves for the corresponding engine operating conditions obtained using the newly implemented Flame Speed Closure model in OpenFOAM®. It should be noted that both pressure traces determined from measurements conducted over around 100 cycles (black solid lines) and ensemble-averaged results (yellow solid lines with circles) are shown in Figure 4.41. In general, the computed pressure traces agree quite well with the measurements in terms of the pressure rise rate during the combustion phase. For the medium load case, i.e. imep=5 bar, the computed pressure trace rises slightly earlier than the experimental curve. This difference is probably largely due to the oversimplified description of the ignition process in the simulations, which was performed using a step function; in reality, ignition is much more complex than this approach assumes. Another factor that may have contributed to the discrepancy is the unknown delay between the signal timing and the timing of the spark plug's activation in the experimental apparatus. Despite these minor issues, the good agreement between the simulated and experimental combustion rates under different engine operating conditions with short time intervals between injection and ignition was very encouraging.

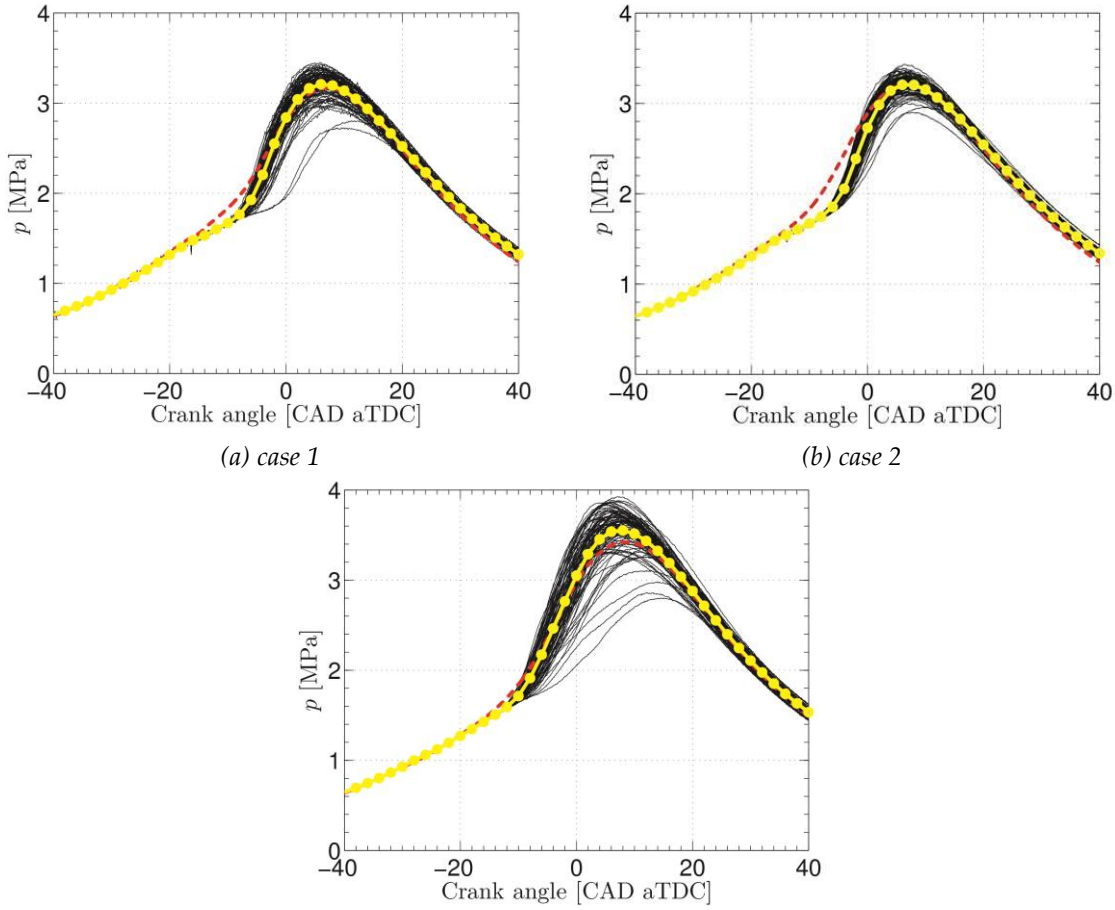

Figure 4.41: *Comparison of calculated (red dashed lines) and experimental (cycles 1-100: black solid lines; ensemble-averaged: yellow solid line with circles) pressure traces for three cases shown in Table 4.3.*

4.9. Conclusions

The Flame Speed Closure (FSC) model of premixed turbulent combustion was implemented into the OpenFOAM® code and extended in a stepwise fashion to enable the simulation of stratified turbulent combustion in DI SI engines. The key results arising from the extension of the combustion model and its subsequent use in various simulations are:

1. The Chalmers combustion mechanism of gasoline was approximated and implemented into OpenFOAM® to describe the influence of the equivalence ratio, pressure, and temperature of the unburned gas on the burning rate and flame temperature.
2. A correct method for calculating the mean density based on the BML concept has been implemented in OpenFOAM®. This approach predicts a lower in-cylinder pressure than is obtained using the method currently implemented in OpenFOAM®.
3. The equilibrium combustion temperature of gasoline burning under engine-like conditions was implemented into the CFD code. Simulations using this

temperature yielded slightly lower in-cylinder pressures and temperatures than those predicted by assuming complete combustion. This should improve the prediction of NO emissions in future studies.

4. To address the influence of turbulent fluctuations in the mixture composition on the mean burning rate, density and temperature, a Favre (mass-weighted) beta-PDF approach was implemented in OpenFOAM®. This model predicts a lower combustion rate and in-cylinder pressure than the standard OpenFOAM® model for a global equivalence ratio of 1.15.
5. The evaporation source term in the mixture fraction variance equation has been implemented in OpenFOAM® and was found to strongly affect the normalized variance fields during the injection phase. However, it has only weak effects on the combustion rate and in-cylinder pressure for different injection timings.

In addition, extensive sensitivity studies were performed to evaluate the robustness of the integrated model and identify the important factors in modelling DISI engines. The key findings of these studies are:

6. The predicted combustion rate is very sensitive to the turbulence model used in the simulation and the turbulent Prandtl number.
7. The simulations' results are only weakly dependent on the initial turbulence values, and parameters relating to fuel injection and ignition.

Experimental pressure traces generated under a range of engine operating conditions were found to be very accurately reproduced by simulations performed using the newly implemented model. In particular, the simulations described the pressure rise rates very well. However, the current ignition model is not entirely satisfactory and requires improvement.

Chapter 5

Conclusions and Future Work

5.1. Conclusions

The scientific results presented in this thesis relate to four different but closely linked objectives: (i) the development of effective models for simulating stratified turbulent combustion in a DISI engine, (ii) the implementation of these models and others presented in the literature into an open source code, (iii) the validation of these models against experimental measurements, and (iv) the application of the integrated models to the simulation of stratified turbulent combustion in a SGDI engine.

5.1.1. Modle development

A semi-detailed (120 species, 677 reactions) chemical mechanism for the combustion of gasoline-ethanol blends in air was developed and validated by treating gasoline as a blend of *iso*-octane, toluene, and *n*-heptane in a volumetric ratio of 55%:35%:10%.

A correlation for evaluating gasoline laminar flame speeds under engine-like conditions was developed in order to model flame propagation in a SGDI engine using the aforementioned mechanism.

To address the influence of non-uniformities and fluctuations in mixture composition on the mean burning rate, density and temperature, the FSC model of premixed turbulent combustion was combined with balance equations for the Favre-averaged mixture fraction and its variance, as well as a presumed mixture-fraction PDF in the form of beta function. A method for computing the canonical PDF based on its mass-weighted counterpart was also developed for this purpose.

5.1.2. Implementation of models

The developed models as well as relevant models for simulating stratified turbulent combustion in a SGDI engine were implemented into the open source CFD code OpenFOAM®. Specifically, OpenFOAM® was modified in the following ways:

1. A pintle injector model was implemented that makes it possible to simulate sprays discharged by an outward-opening piezo-controlled pintle-type injector. This model offers more accurate descriptions of the resulting flow fields than can be achieved using the default unit injector model in OpenFOAM®.
2. A modified version of the KHRT model was implemented, which significantly improved the predictions of the liquid penetration length and SMD.
3. Due to bugs in the original implementations of the O'Rourke and trajectory collision models in OpenFOAM®, the code crashed when either of these models was activated. Corrected versions of these models were implemented, enabling their successful use in OpenFOAM®. The new pintle injector model, modified

KHRT model, and the corrected O'Rourke and trajectory models were subsequently incorporated into all official releases of OpenFOAM® from v2.0.0 onwards.

4. Liquid properties for gasoline were implemented in order to properly simulate gasoline spray breakup and evaporation.
5. A correlation for the laminar flame speed during gasoline combustion under engine-like conditions was implemented to facilitate the modelling of flame propagation through steeply stratified mixtures in GDI engines.
6. The method for evaluating the temperature of combustion products implemented in the standard version of OpenFOAM® was improved to allow for the dissociation of the products and heat losses. Specifically, the temperatures of equilibrium products arising from the combustion of gasoline-air mixtures were computed at various equivalence ratios, pressures, and burned gas enthalpies typical of combustion in a DISI engine. The computed results were approximated and this approximation was implemented into OpenFOAM®.
7. An incorrect method for evaluating the mean density and temperature of a premixed turbulent flame brush was replaced with the widely used BML thermochemistry.
8. The FSC model of premixed turbulent combustion with an approximation of the relevant reaction time scale as a function of the laminar flame speed, pressure, and unburned gas temperature was implemented into OpenFOAM®.
9. A balance equation for the variance of the mixture fraction and a model of the evaporation source term in this equation were implemented into OpenFOAM®.
10. A method for computing a mass-weighted beta-function PDF for the mixture fraction was implemented into OpenFOAM®.
11. A newly developed method for transforming the aforementioned mass-weighted PDF into the corresponding canonical PDF was implemented into OpenFOAM®.

5.1.3. Validation of models

The combustion chemistry of a gasoline surrogate was extensively validated against a wide range of experimental data on both ignition delays and laminar flame speeds under various conditions. More specifically, the mechanism was validated, first, against experimental data on ignition delay times for pure toluene, pure *iso*-octane, pure *n*-heptane, gasoline surrogate, a ternary mixture of the three components, and PRF + toluene. The experimental measurements were acquired over the following ranges of conditions: $0.5 \leq \phi \leq 1.0$, $13\ atm \leq p \leq 60\ atm$, $600K \leq T_u \leq 1500K$ and 0-30% EGR. Second, computed laminar flame speeds were validated against experimental data obtained under the following ranges of conditions: $0.6 \leq \phi \leq 1.6$, $1\ atm \leq p \leq 25\ atm$ and $298K \leq T_u \leq 500K$.

Numerical simulations of gasoline and ethanol sprays discharged by an outward-opening piezo-actuated pintle-type injector into quiescent air were performed using various spray models at different fuel and air temperatures and injection pressures. The numerical results were quantitatively compared to experimental data obtained by my colleagues using the Chalmers spray rig. The results obtained using the modified implementation of the KHRT model yielded the best agreement with the experimental

liquid penetration length and SMD under the studied conditions. Based on these results, the KHRT model was selected for use in subsequent numerical studies on combustion in DISI engines.

5.1.4. Application to a DISI engine

The numerical modelling of stratified turbulent combustion in a DISI engine was investigated by examining the effects of individual sub-models on the predicted combustion rate in a step-wise fashion. Under the studied conditions, the importance of these sub-models can be ranked as follows (from the highest to the lowest): (i) the model predicting the temperature of the combustion products, (ii) the mass-weighted presumed PDF, (iii) the model predicting the mean density and temperature, (iv) the evaporation source term, (v) the approximation of the laminar flame speed and (vi) the canonical presumed PDF.

The sensitivity of the computed overall burning rate to various initial/boundary conditions and the input parameters of selected models available in the standard version of OpenFOAM was also investigated. The formation of a near-stoichiometric fuel-air mixture within the ignition kernel at the ignition timing was found to be very important for the description of the overall combustion process. In particular, the following model/input parameters were found to be important: (i) the initial droplet diameter, (ii) the turbulence model, (iii) the turbulent Prandtl number and (iv) the ignition strength used in the ignition model.

The numerical research tool resulted from the present thesis, i.e. OpenFOAM® with newly implemented models, was validated by quantitatively comparing computed pressure traces to experimental data obtained by my colleagues for two different sets of operating conditions and loads.

5.2. Future work

The work described in this thesis addressed certain important phenomena relevant to numerical modelling of stratified turbulent combustion in DISI engines. Although the good quantitative agreement between the simulations' results and experimental measurements was encouraging, the significance of this agreement should not be overstated. The sensitivity of the computed results to the sub-models that were used and the initial/boundary conditions that are imposed means that further work will be required to establish OpenFOAM® as a predictive R&D tool for the design and refinement of advanced GDI engines. In particular, the following important issues should be addressed:

1. The ignition model in the standard version of OpenFOAM® should be substantially improved.
2. The simulations presented herein focused on the closed cycle of a GDI engine, i.e. the period between IVC and EVO, and were conducted within the URANS framework by invoking a two-equation engineering turbulence model. Full cycle simulations including the intake and exhaust processes should be performed in the future, probably within the LES framework, in order to better describe turbulence levels and the tumble motion at IVC, which is closely related to the fuel-air mixing

and combustion processes. It is worth remembering, however, that the prediction of turbulence inside the combustion chambers of piston engines remains challenging, and even the most advanced LES simulations performed by leading research groups cannot yet quantitatively predict experimentally observed fluctuations in the rms turbulent velocity for non-reacting flows [141][142]. A full description of such processes in the more complex reacting case is therefore likely to be some way off. In the short term, it is not clear whether any plausible increase in the predictive capabilities of full-cycle URANS or even LES calculations will be sufficient to justify their routine use given the high computational costs of such simulations.

3. Although the spray sub-models were validated against measurements made using a constant volume spray rig at relatively low ambient temperatures and pressures, they should also be validated against experimental measurements acquired under engine-like conditions because spray characteristics have profound effects on ignition and flame propagation.
4. Although the simulated combustion process was not found to be very sensitive to the choice of laminar flame speed approximation, it will still be necessary to test the model's description of high temperature combustion chemistry under high temperature and high pressure conditions as appropriate experimental data become available. Such investigations are required both to improve the prediction of laminar flame speeds under the operating conditions of DISI engines and to enable reliable modelling of their emissions.
5. The use of alternative fuels such as blends of gasoline and ethanol could potentially improve the thermal efficiency of GDI engines while also reducing their NOx and soot emissions. It would be interesting to conduct numerical studies on stratified combustion using such fuels would can be considered in a later stage of this project.

Most of the items listed above relate to improving the predictive capabilities of models that are currently implemented in OpenFOAM®. Improvements of this sort will eventually allow us to better predict the overall burning rate in DISI engines. However, they could also be extended further to improve the prediction of emissions profiles, which are very important in engine R&D but were beyond the scope of this present thesis. In particular,

1. A model of thermal NO formation should be implemented into OpenFOAM in the near future.
2. Spray-wall interactions, wall-film formation, and the initiation of pool fires strongly affect soot emissions from DISI engines. Because the reduction of soot emissions is a major design goal for engines of this sort, advanced models of these phenomena should be developed, validated, and implemented into OpenFOAM®.
3. The new semi-detailed chemical mechanism of gasoline combustion presented herein offers an opportunity not only to evaluate the laminar flame speed, but also to model emissions of species such as CO or prompt NO. In order to take full advantage of this mechanism, the FSC model with the presumed PDF approach for stratified turbulent burning should be further extended by properly addressing emissions from both locally inhomogeneously premixed and mixing-controlled flames.

4. Modelling of flammability limits under conditions associated with combustion in SIDI engines is very important for the prediction of unburned hydrocarbon emissions, among other things. This issue represents a major challenge for the combustion community due to well documented but poorly understood phenomena such as back-supported burning and transient effects [18].

Appendix A

Parameterization of the Reaction Time Scale in Equation (4.27)

If $u' = 0$, then the FSC balance Equation (4.21) becomes

$$\frac{\partial}{\partial t}(Rc) + \frac{\partial}{\partial x}(Ruc) = \frac{\partial}{\partial x}\left(R\kappa\frac{\partial c}{\partial t}\right) + \frac{R(1-c)}{t_r}\exp\left(-\frac{\theta}{\mathrm{T}}\right) \tag{A.1}$$

in the planar one-dimensional case. Here, $\theta = \Theta/T_u$ is the normalized activation temperature, the normalized temperature $T = T/T_u$ and density $R = \rho/\rho_u$ are equal to

$$\begin{aligned} \mathrm{T} &= 1 - c + c(1+\Delta) \\ R &= (1+\Delta c)^{-1} \end{aligned} \tag{A.2}$$

respectively, and $\Delta = T_b/T_u - 1$ is the heat-release parameter. Let us assume that $\kappa/\kappa_u = T^q$.

The goal is to determine a value of the time scale t_r such that the flame speed with respect to the unburned gas obtained using Equations (A.1) and (A.2) supplemented with the continuity equation

$$\frac{\partial R}{\partial t} + \frac{\partial}{\partial x}(Ru) = 0 \tag{A.3}$$

is equal to the laminar flame speed S_L, which is considered to be a known input parameter. For this purpose, I must solve Equations (A.1)-(A.3) supplemented with the following boundary conditions,

$$\begin{aligned} c(-\infty, t) &= 0 \\ c(\infty, t) &= 1 \\ u(-\infty, t) &= 0 \end{aligned} \tag{A.4}$$

which stipulate that the flame propagates from right to left, and the initial conditions below:

$$\begin{aligned} c(x \le x_1, 0) &= 0 \\ 0 < c(x_1 < x < x_2, 0) &< 1 \\ c(x \ge x_2, 0) &= 1 \\ \frac{dc}{dx}(x_1 < x < x_2, 0) &> 0 \end{aligned} \tag{A.5}$$

The problem stated above involves a single parameter $(\kappa_u/t_r)^{1/2}$ that has the dimension of velocity and two non-dimensional parameters, $\theta = \Theta/T_u$ and $\Delta = T_b/T_u - 1$. Therefore, for dimensional reasons, I have

$$S_L = \left(\frac{\kappa_u}{t_r}\right)^{1/2} \Psi(\theta, \Delta) \tag{A.6}$$

which yields Equation (4.27).

The function $\Psi(\theta, \Delta)$ was determined by numerically integrating Equations (A.1)-(A.5) for various values of θ and Δ. For this purpose, (i) a chemical time scale t_r was set, (ii) the corresponding flame speed S_L was computed, and (iii) Ψ was set equal to $S_L(t_r/\kappa_u)^{1/2}$. The results obtained in these simulations are indicated by the symbols in Figure A.1. The curves plotted in this figure approximate the computed results using the following parameterization

$$\Psi = \left[\sum_{k=0}^{4} a_k \left(\frac{T_b}{T_u}\right)^k\right]\left[\sum_{k=0}^{4} b_k \left(\frac{\Theta}{T_u}\right)^k\right] \exp\left(-\frac{1}{2}\frac{\Theta}{T_u}\frac{T_u}{T_b}\right) \tag{A.7}$$

with the coefficients a_k and b_k being reported in Table A.1.

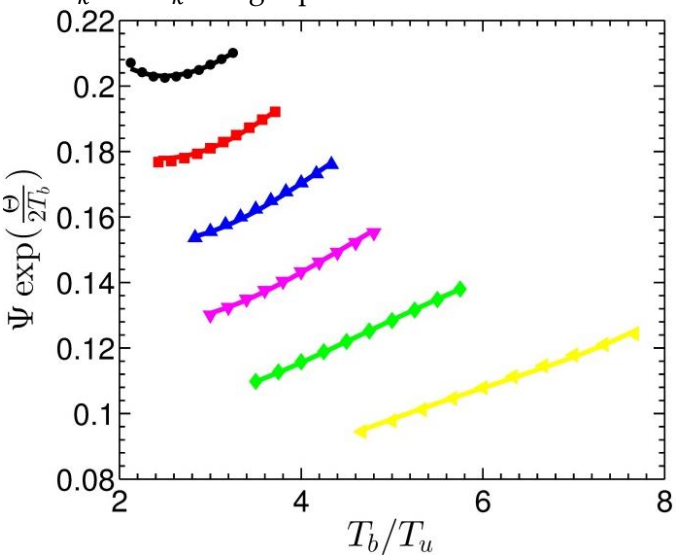

Figure A.1: *Comparison of the computed $\Psi exp\left(\frac{\theta}{2T_b}\right)$ values (symbols) and its approximations (lines) for different $\frac{\theta}{T_u}$ values. Black line and circles: $\frac{\theta}{T_u} = 25$; red line and squares: $\frac{\theta}{T_u} = 28.57$; blue line and upward triangles: $\frac{\theta}{T_u} = 33.33$; magenta line and downward triangles: $\frac{\theta}{T_u} = 40$; green line and diamonds: $\frac{\theta}{T_u} = 50$; yellow line and triangles left: $\frac{\theta}{T_u} = 66.67$.*

Table A.1: *Coefficients for approximating Ψ*

k	0	1	2	3	4
a_k	3.15E-05	-1.42E-05	4.75E-06	-6.02E-07	2.80E-08
b_k	4.01E+04	-2.15E+03	5.57E+01	-6.97E-01	3.36E-03

Appendix B

Canonical and Mass-Weighted Mixture Fraction PDFs

In a stratified turbulent flame, on the one hand, the Favre-averaged value of an arbitrary quantity $q = q(f)$ can be determined by invoking the joint PDF for the combustion regress variable and mixture fraction as follows

$$\begin{aligned}\tilde{q} = \frac{1}{\bar{\rho}}\int_0^1\int_0^1 \rho(b,f)q(f)P(b,f)db\,df &= \frac{1}{\bar{\rho}}\int_0^1 q(f)\left[\int_0^1 \rho(b,f)P(b,f)db\right]df \\ &= \frac{1}{\bar{\rho}}\int_0^1 q(f)\langle\rho|f\rangle P_f(f)df\end{aligned} \tag{B.1}$$

On the other hand,

$$\tilde{q} = \int_0^1 q(f)\tilde{P}_f(f)df \tag{B.2}$$

Therefore,

$$\tilde{P}_f(f) = \frac{\langle\rho|f\rangle}{\bar{\rho}}P_f(f) \tag{B.3}$$

where $\langle\rho|f\rangle$ is the density conditionally averaged density provided that the mixture fraction is equal to f.

If Equation (4.40) is invoked, then,

$$\langle\rho|f\rangle = \bar{b}\rho_u + \left(1-\bar{b}\right)\rho_b(f) \tag{B.4}$$

where the dependence of the unburned density on the mixture fraction is disregarded for simplicity. Subsequently, Equations (B.3) and (B.4) result in

$$\frac{1}{\bar{\rho}} = \frac{1}{\bar{\rho}}\int_0^1 P_f(f)df = \int_0^1 \frac{\tilde{P}_f}{\langle\rho|f\rangle}df = \int_0^1 \frac{\tilde{P}_f}{\bar{b}\rho_u + \left(1-\bar{b}\right)\rho_b(f)}df \tag{B.5}$$

and Equations (B.3)-(B.5) yield Equation (4.41).

This result can be used straightforwardly provided that the Reynolds-averaged value of the combustion regress variable is known. The FSC and most other models of premixed turbulent combustion yield the Favre-averaged value of b, but the mean density must be known in order to evaluate $\bar{b}$ based on $\tilde{b}$, whereas $\bar{b}$ is required in order to average the density, see Equation (B.5). Accordingly, Equation (4.41) should be supplemented with an equation that yields $\tilde{b} = \tilde{b}\left(\bar{b}\right)$ and the two equations should be solved iteratively, followed by evaluation of the mean density using Equation (B.5).

A link between the Favre- and Reynolds-averaged combustion regress variables is required to close the problem, and can be obtained as follows. Because

$$\bar{\rho}\tilde{b} = \overline{\rho b} = \int_0^1 P_f(f)\left\{\int_0^1 \rho(b,f)b\left[\bar{b}\delta(1-b) + \left(1-\bar{b}\right)\delta(b)\right]db\right\}df$$
$$= \int_0^1 P_f(f)\bar{b}\rho_u df = \rho_u\bar{b} \tag{B.6}$$

we have

$$\frac{1}{\bar{\rho}} = \frac{\tilde{b}}{\rho_u\bar{b}} \tag{B.7}$$

This equality and Equation (B.5) allow us to determine the Favre-averaged regress variable based on its Reynolds-averaged value, i.e.

$$\tilde{b} = \int_0^1 \frac{\rho_u\bar{b}\tilde{P}_f(f)df}{\bar{b}\rho_u + \left(1-\bar{b}\right)\rho_b(f)} \tag{B.8}$$

Equations (4.41) and (B.8) were solved iteratively.

Bibliography

[1] U.S. Census Bureau. World POPClock projection, www.census.gov/popclock. (accessed August 4, 2014).

[2] United States Energy Information Administration. International energy outlook 2013, www.eia.gov/forecasts/ieo/pdf/0484(2013).pdf. (2013, accessed August 4, 2014).

[3] BP. BP statistical review of world energy, June 2014. www.bp.com/content/dam/bp/pdf/Energy-economics/statistical-review-2014/BP-statistical-review-of-world-energy-2014-full-report.pdf. (2014, accessed August 4, 2014).

[4] International Council on Clean Transportation. Global transportation energy and climate roadmap 2012, www.theicct.org/sites/default/files/publications/ICCT%20Roadmap%20Energy%20Report.pdf. (2012, accessed August 4, 2014).

[5] United States Energy Information Administration. Annual energy outlook 2014, www.eia.gov/forecasts/aeo/pdf/0383(2014).pdf. (2014, accessed August 4, 2014).

[6] EU. 2007. Regulation (EC) No 715/2007 of the European parliament and of the council, official journal of the european union, 29.6.2007, L 171, 1-16, http://eur-lex.europa.eu/LexUriServ/LexUriServ.do?uri=OJ:L:2007:171:0001:0016:EN:PDF

[7] Emission standards. European Union, cars, greenhouse gas emissions, https://www.dieselnet.com/standards/eu/ghg.php, Retrieved August 13, 2014.

[8] EU, 2009. Regulation (EC) No 443/2009, Official Journal of the European Union, 5.6.2009, L 140/1, http://eur-lex.europa.eu/legal-content/EN/TXT/?uri=celex:32009R0443.

[9] EU, 2014a. Regulation (EU) No 333/2014, Official Journal of the European Union, 5.4.2014, L 103/15, http://eur-lex.europa.eu/legal-content/EN/TXT/?uri=CELEX:32014R0333.

[10] Emission standards, US, cars, greenhouse gas emissions and fuel economy, https://www.dieselnet.com/standards/us/fe_ghg.php.

[11] European vehicle market statistics, 2013, www.theicct.org/sites/default/files/publications/EU_vehiclemarket_pocketbook_2013_Web.pdf. (2013, accessed August 6, 2014).

[12] United States Environmental Protection Agency. EPA staff technical report: cost and effectiveness estimates of technologies used to reduce light-duty vehicle carbon dioxide emissions, www.epa.gov/otaq/climate/420r08008.pdf. (2008, accessed August 8, 2014).

[13] Zhao F, Lai M-C and Harrington DL. Automotive spark-ignited direct-injection gasoline engines. *Prog Energ Combust* 1999; 25(5): 437-562.

[14] Wirth et al. The next generation of gasoline direct injection: improved fuel economy and optimized system cost. In: *Aachener Kolloquium Fahrzeug- und Motorentechnik*, 6-8 Oct 2003.

[15] Wärnberg J. *Hollow cone gasoline/ethanol sprays under cold start conditions*. Licentiate thesis, Chalmers University of Technology, Sweden, 2009.

[16] Peters N. *Turbulent combustion*. Cambridge university press, 2000.

[17] Poinsot T and Veynante D. *Theoretical and Numerical Combustion*. 2nd ed. Philadelphia: Edwards, 2005.

[18] Lipatnikov, AN. *Fundamentals of premixed turbulent combustion*. London: CRC, 2012, p.548.

[19] Ogink R and Golovitchev V. Gasoline HCCI modeling: an engine cycle simulation code with a multi-zone combustion model. SAE paper 2002-01-1745, 2002.

[20] Jasak H, Weller H and Nordin N, In-cylinder CFD simulation using a C++ object-oriented toolkit. SAE paper 2004-01-0110, 2004.

[21] Hemdal S, Denbratt I, Dahlander P and Warnberg J. Stratified cold start sprays of gasoline-ethanol blends. *SAE Int J Fuels Lubr* 2009; 2(1): 683-696.

[22] Cohn DR, Bromberg L and Heywood JB. *Direct injection ethanol boosted gasoline engines: biofuel leveraging for cost-effective reduction of oil dependence and CO2 emissions*. MIT Laboratory for Energy and the Environment Report LFEE 2005-001 RP, 2005.

[23] Stein RA, House CJ, Leone TG, Optimal use of E85 in a turbocharged direct injection engine. SAE paper 2009-01-1490, 2009.

[24] Norton TS and Dryer FL. An experimental and modeling study of ethanol oxidation kinetics in an atmospheric pressure flow reactor. *Int J Chem Kinet* 1992; 24(4): 319-344.

[25] Egolfopoulos FN, Du DX, Law CK. A study on ethanol oxidation kinetics in laminar premixed flames, flow reactors, and shock tubes. *Proc Combust Inst* 1992; 24: 833-841.

[26] Marinov NM. A detailed chemical kinetic model for high temperature ethanol oxidation. *Int J Chem Kinet* 1999; 31(3): 183-220.

[27] Li J, Kazakov A and Dryer FL. Ethanol pyrolysis experiments in a variable pressure flow reactor. *Int J Chem Kinet* 2001; 33(12): 859-867.

[28] Saxena P and Williams FA. Numerical and experimental studies of ethanol flames. *Proc Combust Inst* 2007; 31(1): 1149-1156.

[29] Seiser R, Humer S, Seshadri K and Pucher E. Experimental investigation of methanol and ethanol flames in nonuniform flows. *Proc Combust Inst* 2007; 31(1): 1173-1180.

[30] Pitz WJ, Cernansky NP, Dryer FL, Egolfopoulos FN, Farrell JT, Friend DG and Pitsch H. Development of an experimental database and kinetic models for surrogate gasoline fuels. SAE paper 2007-01-0175, 2007.

[31] Andrae J, Johansson D, Björnbom P, Risberg P and Kalghatgi GT. Co-oxidation in the auto-ignition of primary reference fuels and n-heptane/toluene blends. *Combust Flame* 2005; 140(4): 267-286.

[32] Buda F, Bounaceur R, Warth V, Glaude PA, Fournet R and Battin-Leclerc F. Progress towards an unified detailed kinetic model for the autoignition of alkanes from C4 to C10 between 600 and 1200 K. *Combust Flame* 2005; 142(1-2): 170-186.

[33] Callahan CV, Held TJ, Dryer FL, Minetti R, Ribaucour M, Sochet LR, Faravelli T, Gaffuri P and Ranzi E. Experimental data and kinetic modelling of primary reference fuel mixtures. *Proc Combust Inst* 1996; 26: 739-746.

[34] Chaos M, Kazakov A, Zhao Z and Dryer FL. A high-temperature chemical kinetic model for primary reference fuels. *Int J Chem Kinet* 2007; 39(7): 399-414.

[35] Tanaka S, Ayalaa F and Keck JC. A reduced chemical kinetic model for HCCI combustion of primary reference fuels in a rapid compression machine. *Combust Flame* 2003; 133(4): 467-481.

[36] Ra Y and Reitz RD. A reduced chemical kinetic model for IC engine combustion simulations with primary reference fuels. *Combust Flame* 2008; 155(4): 713-738.

[37] Huang C, Lu XC and Huang Z. New reduced chemical mechanism for homogeneous charge combustion ignition combustion investigation of primary reference fuels. *Energ Fuel* 2008; 22(2): 935-944.

[38] Jerzembeck S, Peters N, Pepiot-Desjardins P and Pitsch H. Laminar burning velocities at high pressure for primary reference fuels and gasoline: experimental and numerical investigation. *Combust Flame* 2009; 156(2): 292-301.

[39] Andrae J, Björnbom P, Cracknell RF and Kalghatgi GT. Autoignition of toluene reference fuels at high pressures modeled with detailed chemical kinetics. *Combust Flame* 2007; 149(1-2): 2-24.

[40] Chaos M, Zhao Z, Kazakov A, Gokulakrishnan P, Angioletti M and Dryer FL. A PRF+toluene surrogate fuel model for simulating gasoline kinetics. In: *5th US combustion Meeting*, San Diego, California, 2007.

[41] Pires da Cruz A, Pera C, Anderlohr JM, Bounaceur R, Battlin-Leclerc A. A complex chemical kinetic mechanism for the oxidation of gasoline surrogate fuels: n-heptane, iso-octane and toluene - mechanism development and validation. In: *Proceedings of the Third European Combustion Meeting*, Chania, 2007.

[42] Anderlohr JM, Bounaceur R, Pires da Cruz A and Battlin-Leclerc A. Modeling of autoignition and NO sensitization for the oxidation of IC engine surrogate fuels. *Combust Flame* 2009; 156(2): 505-521.

[43] Bounaceur R, Glaude PA, Fournet R, Warth V and Battlin-Leclerc A. Detailed kinetic models for the low-temperature auto-ignition of gasoline surrogates. In: *Proceedings of the fourth European combustion meeting*, Wien, 2009.

[44] Mehl M, Curran HJ, Pitz WJ and Westbrook CK. Detailed kinetic model of gasoline surrogate mixtures. In: *Proceedings of the fourth European combustion meeting*, Wien, 2009.

[45] Naik CV, Pitz WJ, Sjöberg M, Dec JE, Orme J, Curran HJ, et al. Detailed chemical kinetic modeling of a surrogate fuels for gasoline and application to an HCCI engine. In: *Proceedings of the fourth joint meeting of the US sections of the combustion institute*, Philadelphia, 2005.

[46] Naik CV, Pitz WJ, Westbrook CK, Sjöberg M, Dec JE, Orme J, et al. Detailed chemical kinetic modeling of a surrogate fuels for gasoline and application to an HCCI engine. SAE paper 2005-01-3741, 2005.

[47] Golovitchev VI, Rinaldini CA and Cantore G. Development and application of gasoline/EtOH combustion mechanism: modeling of direct injection ethanol boosted gasoline engine. In: *COMODIA*, SI-15, 2008.

[48] Frassoldati A, Cuoci A, Faravelli T and Ranzi E. Kinetic modeling of the oxidation of ethanol and gasoline surrogate mixtures. In: *Proceedings of the sixth Mediterranean combustion symposium*, Porticcio-Ajaccio, Corsica-France, June 7-11,2009.

[49] Andrae JCG, Brink T and Kalghatgi GT. HCCI experiments with toluene reference fuels modeled by a semidetailed chemical kinetic model. *Combust Flame* 2008; 155(4): 696-712.

[50] Gauthier BM, Davidson DF and Hanson RK. Shock tube determination of ignition delay times in full-blend and surrogate fuel mixtures. *Combust Flame* 2004; 139(4): 300-311.

[51] Westbrook C and Dryer F. Chemical kinetic modeling of hydrocarbon combustion. *Prog Energy Combust Sci* 1984; 10(2): 1–57.

[52] Ranzi E, Faravelli T, Gaffuri P and Sogaro A. Low-temperature combustion: automatic generation of primary oxidation reactions and lumping procedures. *Combust Flame* 1995; 102(1-2): 179–192.

[53] Dagaut P, Pengloan G and Ristori A. Oxidation, ignition and combustion of toluene: experimental and detailed chemical kinetic modelling. *Phys Chem Chem Phys* 2002; 4: 1846-1854.

[54] Glaude PA, Warth V, Fournet R, Battin-Leclerc F, Côme GM and Scacchi G. Modeling of n-heptane and isooctane gas-phase oxidation at low temperature by using computer-aided designed mechanism. *Bull Soc Chim Belg* 1997; 106(6): 343-348.

[55] Lutz AE, Kee RJ and Miller JA. SENKIN: a Fortran program for predicting homogeneous gas phase chemical kinetics with sensitivity analysis. Sandia National Laboratories Tech. Rep. SAND87-8248, 1988.

[56] Kee RJ, Crcar JF, Smooke MD and Miller JA. PREMIX: a Fortran program for modeling steady laminar one-dimensional premixed flames. Sandia National Laboratories Report SAND85-8249, 1985.

[57] Kee RJ, Miller JA and Jefferson TH. CHEMKIN: a general-purpose, problem-independent, transportable, Fortran chemical kinetics code package. Sandia National Laboratories Report SAND80-8003, 1980.

[58] Marinov NM. A detailed chemical kinetic model for high temperature ethanol oxidation. *Int J Chem Kinet* 1999; 31(3): 183-220.

[59] Lawrence Livermore National Laboratory. Detailed chemical mechanism for dimethyl ether. www-pls.llnl.gov/data/docs/science_and_technology/chemistry/combustion/dme_24_mech.txt, (accessed August 2009).

[60] Lawrence Livermore National Laboratory. Thermodynamic and transport parameters for n-heptane, iso-octane, and ethanol. www-pls.llnl.gov/?url=science_and_technology-chemistry-combustion-mechanisms, (accessed August 2009).

[61] Israel Institute of Technology. Third millennium thermodynamic database for combustion and air-pollution use with updates from active thermochemical, ftp.technion.ac.il/pub/supported/aetdd/thermodynamics/BURCAT.THR, (accessed August 2009).

[62] Massachusetts Institute of Technology. Chemical mechanism, thermodynamic and transport parameters for toluene, web.mit.edu/anish/www/MITcomb.html, (accessed August 2009).

[63] Curran HJ, Pitz WJ, Westbrook CK, Callahan CV and Dryer FL. Oxidation of automotive primary reference fuels at elevated pressures. *Proc Combust Inst* 1998; 27: 379-387.

[64] Ciezki HK and Adomeit G. Shock-tube investigation of self-ignition of n-heptane-air mixtures under engine relevant conditions. *Combust Flame* 1993; 93(4): 421-433.

[65] Metghalchi M and Keck JC. Burning velocities of mixtures of air with methanol, isooctane, and indolene at high pressure and temperature. *Combust Flame* 1982; 48: 191-210.

[66] Zhao ZW, Conley JP, Kazakov A, Dryer FL. Burning velocities of real gasoline fuel at 353 K and 500 K. SAE paper 2003-01-3265, 2003.

[67] Huang C, Golovitchev V and Lipatnikov A. Chemical model of gasoline-ethanol blends for internal combustion engine applications. SAE paper 2010-01-0543, 2010.

[68] Sileghem L, Alekseev VA, Vancoillie J, van Geem KM, Nilsson EJK, Verhelst S and Konnov AA. Laminar burning velocity of gasoline and the gasoline surrogate components iso-octane, n-heptane and toluene. *Fuel* 2013; 122: 355-365.

[69] Dirrenberger P, Claude PA, Bounaceur R, le Gall H, Pires da Cruz A, Konnov AA and Battin-Leclerc F. Laminar burning velocity of gasolines with addition of ethanol. *Fuel* 2014; 115: 162-169.

[70] Reitz RD and Bracco FV. Mechanisms of breakup of round liquid jets. In: *Encyclopedia of Fluid Mechanics*, Gulf Pub, NJ 3, 1986.

[71] Reitz RD. Modeling atomization processes in high-pressure vaporizing sprays. *Atomization Sprays* 1987; 3: 309-337.

[72] Reitz RD and Diwakar R. Effect of drop breakup on fuel sprays. SAE paper 860469, 1986.

[73] Reitz RD and Diwakar R. Structure of high-pressure fuel sprays. SAE paper 870598, 1987.

[74] Su TF, Patterson MA, Reitz RD and Farrell PV. Experimental and numerical studies of high pressure multiple injection sprays. SAE paper 960861, 1996.

[75] Patterson MA and Reitz RD. Modeling the effects of fuel spray characteristics on diesel engine combustion and emission. SAE paper 980131, 1998.

[76] Beale JC and Reitz RD. Modeling spray atomization with the Kelvin-Helmholtz/Rayleigh-Taylor model. *Atomization Sprays* 1999; 9: 623-650.

[77] Senecal RK, Schmidt DP, Nouar I, Rutland CJ, Reitz RD and Corradini ML. Modeling high-speed viscous liquid sheet atomization. *Int J Multiphase Flow* 1999; 25: 1073-1097.

[78] Schmidt DP, Nouar I, Senecal RK, Rutland CJ, Reitz RD and Hoffman JA. Pressure-swirl atomization in the near field. SAE paper 1999-01-0496, 1999.

[79] Dombrowski N and Johns WR. The aerodynamic instability and disintegration of viscous liquid sheets. *Chem Eng Sci* 1963; 18: 203-214.

[80] Clark CJ and Dombrowski N. Aerodynamic instability and disintegration of inviscid liquid sheets. *Proc R Soc Lond A* 1972; 329(1579): 467-478.

[81] Weber C. On the breakdown of a fluid Jet. *Z A M P* 1931; 11: 136-159.

[82] Chryssakis CA, Assanis DN, Lee J-K and Nishida K. Fuel spray simulation of high-pressure swirl-injector for DISI engines and comparison with laser diagnostic measurements. SAE paper 2003-01-0007, 2003.

[83] Gao J, Huang JZ and Wang X. Experimental and numerical study of high-pressure-swirl injector sprays in a direct injection gasoline engine. *Proc IMechE A* 2005; 219: 617-629.

[84] Park SH, Kim HJ, Suh HK and Lee CS. Atomization and spray characteristics of bioethanol and bioethanol blended gasoline fuel injected through a direct injection gasoline injector. *Int J Heat Fluid Flow* 2009; 30: 1183-1192.

[85] Lucchini T, D'Errico G and Nordin N. CFD modelling of gasoline sprays. SAE paper 2005-24-086, 2005.

[86] Zuo B, Gomes AM and Rutland CJ. Modeling superheated fuel sprays and vaporization. *Int J Engine Research* 2000; 1: 321-336.

[87] O'Rourke PJ and Amsden AA. The Tab method for numerical calculation of spray droplet breakup. SAE paper 872089, 1987.

[88] Han Z, Parrish S, Farrell PV and Reitz RW. Modeling atomization processes of pressure-swirl hollow-cone fuel sprays. *Atomization Sprays* 1997; 7: 663-684.

[89] Bellman R and Pennington RH. Effects of surface tension and viscosity on Taylor instability. *Q Appl Math* 1954; 12: 151-162.

[90] Liu AB, Mether D and Reitz RD. Modeling the effects of drop drag and breakup on fuel sprays. SAE paper 930072, 1993.

[91] Kösters A and Karlsson A. A comprehensive numerical study of diesel fuel spray formation with OpenFOAM. SAE paper 2011-01-0842, 2011.

[92] O'Rourke, PJ. *Collective drop effects on vaporizing liquid sprays*. PhD Thesis, Princeton University, 1981.

[93] O'Rourke PJ and Bracco FV. Modeling drop interaction in thick sprays and a comparison with experiments. *Proc I Mech E* 1980; 9: 101-116.

[94] Amsden AA, O'Rourke PJ, Butler TD. KIVA-II: A computer program for chemically reactive flows with sprays. LA-11560-MS, Los Alamos national Laboratories, 1989.

[95] Nordin N. *Complex chemistry modeling of diesel spray combustion*. PhD Thesis, Chalmers University of Technology, 2001.

[96] Schetz JA and Fuhs AE. *Handbook of fluid dynamics and fluid machinery, volume one fundamentals of fluid dynamics*. Wiley-Interscience, 1996.

[97] Reid RC, Prausnitz JM and Poling BE. *The properties of gases and liquids*. Fourth edition. McGraw-Hill, 1987.

[98] Yakhot V and Orszag SA. Renormalization group analysis of turbulence: I. basic theory. *SIAM J Sci Comput* 1986; 1(1): 1-51.

[99] Menter F and Esch T. Elements of industrial heat transfer prediction. In: *16th Brazilian Congress of Mechanical Engineering (COBEM)*, Nov, 2001.

[100] Bilger RW, Pope, SB, Bray KNC and Driscoll JF. Paradigms in turbulent combustion research. *P Combust Inst* 2005; 30(1): 21-42.

[101] Spalding DB. Mixing and chemical reaction in steady confined turbulent flames, *P Combust Inst* 1971; 13(1): 649–657.

[102] Magnussen BF and Hjertager BH. On the mathematical modeling of turbulent combustion with special emphasis on shoot formation and combustion. *P Combust Inst* 1976; 16(1): 719–729.

[103] Haworth D. A review of turbulent combustion modeling for multidimensional in-cylinder CFD. SAE paper 2005-01-0993, 2005.

[104] Libby PA and William FA. *Turbulent Reacting Flows*. Springer, pp42.

[105] Launder BE and Sharma BI. Application of the energy-dissipation model of turbulence to the calculation of flow near a spinning disc. *Heat Mass Transfer* 1974; 1(2): 131-138.

[106] Boudier P, Henriot S, Poinsot T and Baritaud T A model for turbulent flame ignition and propagation in spark ignition engines. *P Combust Inst* 1992; 24(1): 503-510.

[107] Baritaud TA, Duglos JM and Fusco A. Modeling turbulent combustion and pollutant formation in stratified charge SI engines. *P Combust Inst* 1996; 26(2): 2627-2635.

[108] Hélie J, Duclos J, Baritaud T, Poinsot T, et al. Influence of mixture fluctuations on combustion in direct injection spark ignition engines simulations. SAE paper 2001-01-1226, 2001.

[109] Fontana G, Galloni E, Palmaccio R and Torella E. Numerical and experimental analysis of different combustion chambers for a small spark-ignition engine. SAE paper 2004-01-1998, 2004.

[110] Fan Q, Hu Z, Deng J, Li L, et al. Stratified mixture formation and combustion process for wall-guided stratified-charge DISI engines with different piston bowls by simulation. SAE paper 2010-01-0595, 2010.

[111] Dahms R, Drake M, Grover JrR, Solomon A. et al. Detailed simulations of stratified ignition and combustion processes in a spray-guided gasoline engine using the sparkCIMM/G-equation modeling framework. *SAE Int J Engines* 2012; 5(2): 141-161.

[112] Kim J, Kim G, Lee H and Min K. Numerical analysis of pollutant formation in direct-injection spark-ignition engines by incorporating the G-equation with a flamelet library. SAE paper 2014-01-1145, 2014.

[113] Hentschel W. Optical diagnostics for combustion process development of direct-injection gasoline engines. *P Combust Inst* 2000; 28(1): 1119-1135.

[114] Huang C, Yasari E and Lipatnikov A. A numerical study on stratified turbulent combustion in a direct-injection spark-ignition gasoline engine using an open-source code. SAE paper 2014-01-1126, 2014.

[115] Wallesten J, Lipatnikov A and Chomiak J. Modeling of stratified combustion in a direct-ignition, spark-ignition engine accounting for complex chemistry. *P Combust Inst* 2002; 29(1): 703-709.

[116] Drake MC, Fansler TD and Lippert AM. Stratified-charge combustion: modeling and imaging of a spray-guided direct-injection spark-ignition engine. *P Combust Inst* 2005; 30(2): 2683-2691.

[117] Kim S, Kim Y and Lee J. Analysis of the in-cylinder flow, mixture formation and combustion processes in a spray-guided GDI engine. SAE paper 2008-01-0142, 2008.

[118] Liu J, Gong J, Cai L, Tan L, et al. Multi-dimensional simulation of air/fuel premixing and stratified combustion in a gasoline direct injection engine with combustion chamber bowl offset. SAE paper 2006-32-0006, 2006.

[119] Yang X, Solomon A and Kuo T. Ignition and combustion simulations of spray-guided SIDI engine using Arrhenius combustion with spark-energy deposition model. SAE paper 2012-01-0147, 2012.

[120] Lipatnikov AN and Chomiak J. Turbulent flame speed and thickness: phenomenology, evaluation, and application in multi-dimensional simulations. *Prog Energy Combust Sci* 2002; 28(1): 1-73.

[121] Bray KNC and Moss JB. A unified statistical model of the premixed turbulent flame. *Acta Astronautica* 1977; 4: 291-319.

[122] Launder BE and Spalding DB. *Mathematical models of turbulence*. London: Academic press, 1972.

[123] Zimont V. Theory of turbulent combustion of a homogeneous fuel mixture at high Reynolds number. *Combust Explo Shock* + 1979; 15: 305-311.

[124] Lipatnikov A and Chomiak J. Modeling of pressure and non-stationary effects in spark ignition engine combustion: a comparison of different approaches. SAE paper 2000-01-2034, 2000.

[125] Lipatnikov A and Chomiak J. A simple model of unsteady turbulent flame propagation. SAE paper 972993, 1997.

[126] Janicka J and Kollmann W. A two-variables formalism for the treatment of chemical reactions in turbulent H2-air diffusion flames. *P Combust Inst* 1979; 17(1): 421-430.

[127] Demoulin FX and Borghi R. Modeling of turbulent spray combustion with application to diesel like experiment. *Combust Flame* 2002; 129(3): 281-293.

[128] Colin O and Benkenida A. A new scalar fluctuation model to predict mixing in evaporating two-phase flows. *Combust Flame* 2003; 134(3): 207-227.

[129] Darbyshire OR and Swaminathan N. A presumed joint PDF model for turbulent combustion with varying equivalence ratio. *Combust Sci Tech* 2012; 184: 2036-2067.

[130] Libby PA and Bray KNC. Variable density effects in premixed turbulent flames. *AIAA J* 1977; 15: 1186-1193.

[131] Yasari E. *Extension of OpenFOAM library for RANS simulation of premixed turbulent combustion*. Licentiate thesis, Chalmers University of Technology, Sweden, 2013.

[132] Huang C and Lipatnikov A. Modelling of gasoline and ethanol hollow-cone sprays using OpenFOAM. SAE paper 2011-01-1896, 2011.

[133] Lucchini T, D'Errico G, Onorati A, Bonandrini G, et al. Development of a CFD approach to model fuel-air mixing in gasoline direct-injection engines. SAE paper 2012-01-0146, 2012.

[134] Lucchini T, Fiocco M, Onorati A, Montanaro A, et al. Full-cycle CFD modeling of air/fuel mixing process in an optically accessible GDI engine. *SAE Int J Engines* 2013; 6(3): 1610-1625.

[135] Rhodes D and Keck J. Laminar burning speed measurements of indolene-air-diluent mixtures at high pressures and temperatures. SAE paper 850047, 1985.

[136] Kwon H, Choi H, Kim J, Min K. Combustion and emission modelling of a direct-injection spark-ignition engine by combining flamelet models for premixed and diffusion flames. *Combust Theor Model* 2012; 16(6): 1089-1108.

[137] Miller JA and Bowman CA. Mechanism and modeling of nitrogen chemistry in combustion. *Prog Energy Combust Sci* 1989; 15(4): 287-338.

[138] Dahms RN, Drake MC, Fansler TD, Kuo T-W and Peters N. Understanding ignition processes in spray-guided gasoline engines using high-speed imaging and the extended spark-ignition model SparkCIMM: part A: spark channel processes and the turbulent flame front propagation. *Combust Flame* 2011; 158: 2229–2244.

[139] Dahms RN, Drake MC, Fansler TD, Kuo T-W and Peters N. Understanding ignition processes in spray-guided gasoline engines using high-speed imaging and the

extended spark-ignition model SparkCIMM: part B: importance of molecular fuel properties in early flame front propagation. *Combust Flame* 2011; 158: 2245–2260.

[140] Shih T-H, Liou WW, Shabbir A, Yang Z and Zhu J. A new k-epsilon eddy-viscosity model for high Reynolds number turbulent flows - model development and validation. *Comput Fluids* 1995; 24(3): 227-238.

[141] Baum E, Peterson B, Böhm B and Dreizler A. On the validation of LES applied to internal combustion engine flows: Part 1: comprehensive experimental database. *Flow Turbl Combust* 2014; 92:269-297.

[142] Baumann M, di Mare F, Janicka J. On the validation of LES applied to internal combustion engine flows: Part II: Numerical analysis. *Flow Turbl Combust* 2014; 92: 299-317.

[143] Spalding DB. Concentration fluctuations in a round turbulent free jet. *Chem Eng Sci* 1971; 26(1): 95-107.

[144] Launder, B.E., Heat and Mass Transport, 1976, 978-3-662-22570-7, Turbulence, V 12, Topics in Applied Physics, Bradshaw, Peter, Springer Berlin Heidelberg, 231-287.

[145] Bilger RW, Saetran LR and Krishnamoorthy LV. Reaction in a scalar mixing layer. *J Fluid Mech* 1991; 233: 211-242.

[146] Ansys. Ansys Fluent user's guide, 2009.